ELECTRON BEAM INDUCED DEPOSITION OF RHODIUM NANOSTRUCTURES

THÈSE N^{O} 2528 (2002)

PRÉSENTÉE Á LA FACULTÉ STI SECTION DE MICROTECHNIQUE

ÉCOLE POLYTECHNIQUE FÉDÉRALE DE LAUSANNE

POUR L'OBTENTION DU GRADE DE DOCTEUR ÈS SCIENCES

PAR

Fabio CICOIRA

Laurea in chimica, Università degli Studi di Bologna, Italie
et de nationalité italienne

acceptée sur proposition du jury:

Dr P. Hoffmann, directeur de thèse
Dr J. Gobrecht, rapporteur
Prof. E. Kapon, rapporteur
Dr H. Koops, rapporteur
Prof. H. Mathieu, rapporteur

Lausanne, EPFL
2002

Svakoga dana u svakom pogledu sve vishe napredujem

Every day in each direction I improve more and more

Ogni giorno sotto ogni profilo progredisco sempre di più

(Dino Zolja in *Do You Remember Dolly Bell* by E. Kusturica)

To my family

Abstract

Electron Beam Induced Deposition (EBID) allows deposition of three-dimensional micro- and nano-structures of conductive and insulating materials on a wide range of substrates. The process is based on the decomposition of molecules of a pre-selected precursor by a focused electron beam. In recent decades EBID of several metals, namely Au, W, Cu and Pt, from different families of precursors, has been achieved and the technique has found some application for small-scale production of laboratory devices and for repair of masks and micro-opto-electronic devices. The weak point of the technique is at present the low purity of the deposited material, caused by metal-organic precursors and by the lack of selectivity of the electron-induced decomposition process.

This work is dedicated to EBID of Rh nanostructures from the precursor $[RhCl(PF_3)_2]_2$. High metal content deposits are expected because the precursor does not contain C atoms and because Rh is one of the less reactive metals.

$[RhCl(PF_3)_2]_2$ as EBID precursor has been characterized by vapor pressure, mass spectrometry and surface residence time measurements.

The vapor pressure of 7.5 Pa at room temperature reveals that the precursor is sufficiently volatile for room temperature EBID. The knowledge of the vapor pressure allows also to estimate the number of precursor molecules delivered to the reaction area per unit time.

Mass spectrometry measurements allow to know the decomposition path of the precursor under electron impact in the gas phase. The measured spectrum indicates that the molecule decomposes by successive loss of PF_3 groups, as confirmed by density functional theory calculations. This is compatible with a high metal content deposit.

Residence time measurements show that $[RhCl(PF_3)_2]_2$ does not decompose on stainless steel surfaces. The measured residence time of 2 ms allows to estimate that the activation energy for desorption of $[RhCl(PF_3)_2]_2$ on stainless steel is about 0.6 eV and that precursor molecules can travel distances in the micrometer range before being desorbed.

EBID structures obtained from $[RhCl(PF_3)_2]_2$ have been characterized with a wide range of techniques for a better knowledge of the material properties and the deposition process. The deposit morphology has been studied by Transmisssion Electron Microscopy (TEM) and Scanning Electron Microscopy (SEM) to characterize the different steps of the deposition

process. Crystallographic analysis is carried out by TEM in diffraction mode. Chemical analysis is carried out by Auger Electron Spectroscopy (AES) and Electron Energy Loss Spectroscopy (EELS).

Morphological analysis of deposits carried out at different exposure times reveals that the first phase of the growth process, in close proximity to the substrate, is characterized by an increase of the deposit height and the deposit diameter. On the other hand the second phase of the growth process is characterized by increasing height and constant diameter.

TEM contrast profiles of dots and Atomic Force Microscopy (AFM) sections of lines have clearly shown that the EBID rate is highest in the center of the beam and decreases in the peripheral regions.

Deposition at variable distances from the precursor source allowed to obtain hollow structures, whose morphology reveals that the precursor reaches the reaction area mainly by direct gas phase transport.

Structural analysis and TEM revealed that, independently of the deposition conditions, the deposited material is made up of Rh nanocrystals immersed in a lighter amorphous matrix. Chemical analysis by Auger Electron Spectroscopy revealed that, after removal of the C rich contamination layer by Ar ion sputtering, the average composition of the deposits is about: 60 at.% Rh, 20 at.% P, 5 at.% Cl, 7 at.% N, 8 at.% O. The absence of C and the presence of N and O in the deposit bulk have been confirmed by Electron Energy Loss Spectroscopy. This technique allowed also to prove that Rh is dominant also in deposits of sub-micrometer size (not analyzable with AES) and to determine the elemental distribution in the deposit with nanometer resolution.

Comparison of the deposit composition and the positive ions detected by mass spectrometry revealed that EBID, compared to low pressure gas phase ionization, involves a higher number of events, i.e. multi-electron decomposition and rearrangements of partially decomposed species.

Riassunto

La deposizione indotta da fascio di elettroni (*Electron Beam Induced Deposition, EBID*) permette di depositare micro e nanostrutture tridimensionali di materiali conduttori ed isolanti su di una vasta gamma di substrati. La tecnica é basata sulla decomposizione di molecole di un opportuno precursore ad opera di un fascio di elettroni focalizzato. Nel corso degli ultimi decenni è stata realizzata la deposizione di diversi metalli, principalmente Au,W, Cu e Pt, da varie famiglie di precursori. EBID ha trovato applicazioni nella produzione di devices di laboratorio su piccola scala. Il punto debole di questa tecnica è senza dubbio la bassa purezza dei materiali depositati, causata dai precursori organo-metalici e dalla scarsa selettivita del processo.

Questo lavoro è dedicato alla deposizione di nanostrutture in rodio dal precursore $[RhCl(PF_3)_2]_2$ potenzialmente adatto alla deposizione di strutture ad alto contenuto metallico in quanto non contenente carbonio.

Il precursore$[RhCl(PF_3)_2]_2$ è stato caratterizzato tramite misure di pressione di vapore, spettroscopia di massa e tempo di residenza in superficie.

La pressione di vapore del precursore, 7.5 Pa a temperatura ambiente, lo rende adatto per deposizioni a temperatura ambiente. La conoscenza della pressione di vapore permette di stimare anche il numero di molecole di precursore che raggiungono la zona di reazione.

Misure di spettrometria di massa permettono di conoscere la frammentazione della molecola indotta da impatto elettronico. Lo spettro di massa dimostra che la molecola viene decomposta per successiva perdita di gruppi PF_3, come confermato anche da calcoli DFT (Density Funtional Theory).

Le misure di tempo di residenza dimostrano che $[RhCl(PF_3)_2]_2$ non reagisce chimicamente con superfici di acciaio inossidabile, ma viene reversibilmente adsorbito con un tempo di residenza di 2 ms. Tale valore corrisponde ad una energia di attivazione per il desorbimento di 0.6 eV.

Le strutture EBID depositate da $[RhCl(PF_3)_2]_2$ sono state caratterizzate con varie tecniche per conoscere le proprieta del materiale e per studiare le varie fasi del processo di deposizione. La morfologia dei depositi é stata studiata tramite microscopia elecronica a trasmissione (TEM) e microscopia elettronica a scansione (SEM). L'analisi cristallografica è stata effettuta tramite microscopia elecronica a trasmissione in modo di diffrazione. Per studiare La composizione

chimica dei depositi è stata studiata tramite le tecniche di spettroscopia per elettroni Auger e spettroscopia per perdita di energia di elettroni (EELS).

L'analisi morfologica di strutture EBID depositate con un diverso tempo di esposizione al fascio di elettroni rivela che la prima fase del processo di deposizione è caratterizzata da un aumento dello spessore e del diametro del deposito. La seconda fase di crescita è invece caratterizzata da crescita tridimensionale con diametro costante.

Curve di contrasto TEM dimostrano che la velocità di crescita del processo è più alta al centro del fascio di elettroni che nelle regioni periferiche.

Deposizioni a distanza variabile dalla sorgente di precursore permettono di ottenere strutture cave e dimostrano che il precursore raggiunge la zona di reazione principalmente per trasporto dalla fase gas.

L'analisi strutturale ha dimostrato che, indipendentemente dai parametri di deposizione, il materiale costituente le strutture EBID é costituitio da nanocristalli di rodio immersi in una matrice amorfa di piu basso *Z*. L' analisi chimica con AES ha dimostrato che, dopo rimozione dello strato di contaminazione per mezzo di sputtering ionico, la composizione media del materiale é 60 at.% Rh, 20 at.% P, 5 at.% Cl, 7 at.% N, 8 at.% O. L'assenza di C e la presenza di N e O nel volume del deposito è stata confermata anche dalla tecnica EELS. Quest'ultima tecnica ha permesso anche di provare la presenza di Rh in strutture sub-micrometriche.

Un confronto tra i frammenti ottenuti dallo spettro di massa e la composizione del deposito dimostra che il processo EBID ha un meccanismo diverso dalla decomposizione per impatto di elettroni in fase gas.

Table of contents

CHAPTER 1 *Introduction*

In this chapter I give a survey of the most important micro and nano-fabrication techniques. The main aspects of each method, such us minimum feature size, range of applicability, throughput and material purity, are discussed and compared.

1.1 NEED FOR NANO-FABRICATION

Nano-fabrication is the construction of materials, structures and devices on a nanometric scale. There are many opportunities which can be realized by making new types of small structures or by downsizing existing ones. The needs for nano-fabrication come mainly from microelectronics, where downsizing has meant lower cost, more components per chip, faster operation, higher performance, and lower power consumption [1]. In addition many interesting quantum effects occur at nanometer dimensions. Examples are electronic effects such us Coulomb blockades [2] and single electron tunneling (SET) [3].

The techniques for micro- and nano- fabrication are based mainly on imaging with light or particle beams. Alternative techniques can involve contact printing and selective chemical etching. In this chapter I discuss and compare the techniques based on irradiation by light and particle beams and describe briefly some alternative techniques.

1.2 MICRO- AND NANO-FABRICATION TECHNIQUES BASED ON LIGHT AND PARTICLE BEAMS

Irradiation by light or particle beams allows micro- and nano-structure generation by lithographic or direct deposition techniques. In lithographic techniques structuring is achieved with a multi-step process (e.g. involving resist coating, exposure, development, and eventually metallization and stripping) while direct deposition techniques are in general single step processes.

1.2.1 PHOTOLITHOGRAPHY

Photolithography (PL) is the technique presently used for micro-fabrication in microelectronics and it has been the work horse of the semiconductor industry since its beginning. The photolithographic techniques currently used are based on a projection printing system

(stepper) in which the image of a mask is reduced and projected, through a high numerical aperture lens system, onto a thin film of photoresist previously spin coated on a wafer. The irradiation changes the solubility of the resist. The exposed zones are then developed, to obtain a polymeric mask on the substrate. The resist-free parts of the substrate can be covered with metal, etched or implanted. The final removal off of the polymer leaves on the substrate the negative image of the mask. The repetition of such lithography steps allows the fabrication of multi-layered structures. The minimum distance between the structures, i.e. the resolution of the stepper, is subject to the limitations set by optical diffraction. Although the theoretical limit set by optical diffraction is about $\lambda/2NA$, the minimum feature size that can be obtained is approximately the wavelength of the light used [4]. For this reason, illuminating sources with shorter wavelength are progressively introduced to generate structures with smaller feature sizes. As structures become increasingly small, they also become increasingly difficult and expensive to produce.

In the early 1970s Gorden Moore, founder of Intel, projected that the number of transistors in an integrated circuit would double every 18 months. This prediction was later known as Moore's Law [5]. Over the past three decades many trends in the semiconductor industry have followed this law, thanks to continuous development in photolithography, and have allowed the feature size to decrease by a factor of almost one half every three years. It is plausible that features as small as 100 nm could be manufactured optically in the future by employing advanced mask/resist technologies and deep UV radiation. Below this size, however, the current strategies for photolithography may be blocked by optical diffraction and by the opacity of the materials used for making lenses or supports of photomasks. New approaches must be developed if Moore's Law is to extend to the sub-100 nm range. At present, several alternative techniques allow fabrication of sub-100 nm structures for laboratory and research applications, on a wide range of substrates (semiconductor, ceramic, glass, metals, plastic). Some of these techniques are discussed in the next paragraphs.

1.2.2 LITHOGRAPHY BY PARTICLE BEAMS

Lithographic techniques involving particle beams are Electron Beam Lithography (EBL), Focused Ion Beam Lithography (FIBL), Electron Projection Lithography (EPL) and Ion Projection Lithography (IPL).

Electron and Ion Beam Lithography are resist-based techniques capable of generating sub-100 nm patterns. The process steps are essentially the same as those described for photolithography, except that the pattern on the resist is obtained by scanning the focused electron or ion beam across the surface. The simplest EBL systems are based on Scanning Electron Microscopes, which will be discussed in more detail in Chapter 2; ion beam lithography systems are based on focused ion beams, described in Section 1.2.5.

Common characteristics of the processes are the high resolution (below 100 nm), the possibility to work with a variety of materials and the high flexibility of patterns. On the other hand both techniques are far too slow for production lithography: current photolithography tools project up to 10^{10} pixels in parallel (exposure time 1s), while e-beam systems expose one pixel

at a time (exposure time 0.1 μs) [6]. To reach a high throughput, a large number of direct write machines would be required, but electron or ion beam lithography tools are both expensive (a few millions of dollars) and require frequent service.

EBL is at present in a more advanced state of development than ion beam lithography. At present it is used principally in support of the integrated circuit industry for production of masks for optical and X-ray lithography, for rapid prototyping of integrated circuits and for specific small volume products, like GaAs integrated circuits and optical waveguides. On a research scale EBL is used for studies of quantum effects and other novel phenomena at very small dimensions [7, 8]. The weak point of the EBL technique is the low speed and also the presence of proximity effect, which causes pattern- specific line width variations due to electron scattering. This effect can be reduced by working at very high (100 keV) or at very low (500 eV) electron energy in order to minimize, in the first case, backward scattering, or, in the second case, electron range. Other correction methods are dose modulation and pattern biasing [7].

FIBL has potentially the same application as EBL.

The main advantages of electron beams over ion beams are: reduced shot noise effects (there are typically a factor 100 more electrons than ions needed to produce exposure, thus statistical fluctuations are less likely to play a role); the absence of implantation effects; the more advanced state of development. Conversely the advantages of ion beams over electron beams are: higher sensitivity (two orders of magnitude) of the resists to ion beams, low ion scattering in the resist and in the substrate, which reduces proximity effects because of reduced scattering, and better stability of the beam [9].

Electron or ion projection systems, which employ a mask to produce a large array of beams, can provide both small minimum dimensions and high throughput. Different solutions have been envisaged in recent decades to improve EPL, such as SCALPEL (SCattering with Angular Limitation in Projection ELectron beam) [10], PREVAIL (PRojection Exposure with Variable Axis Immersion Lenses) and IPL [11], but the use of these techniques is still limited to laboratory applications.

1.2.3 LIGHT-INDUCED CHEMICAL VAPOR DEPOSITION (LICVD)

The decomposition of precursor molecules by a laser beam to give a solid deposit is known as Laser Induced Chemical Vapor Deposition (LICVD). The two main approaches to LICVD are direct laser writing and mask projection patterning [12]. Direct writing techniques involve laser beams focused on a surface to induce localized chemical reactions. In mask projection patterning an entire pattern is deposited onto a substrate surface by illuminating a mask and projecting the image onto the substrate by a series of lenses. We focus here on laser direct writing.

Direct writing LICVD systems consist of a laser, a focusing optics and a vacuum cell containing the substrate. The laser light enters the cell through a window and is focused onto the

substrate surface usually with a microscope objective lens. Patterning is usually obtained by moving the substrate with a precisely controlled motor, in contrast with techniques based on particle beams, in which the beam itself is moved.

The decomposition of the precursor can be induced by heat (pyrolytic CVD), light (photolytic CVD) or by a combination of both (photo-physical CVD) [13]. Deposition rates are several orders of magnitude higher in pyrolytic than in photolytic processes, therefore pyrolytic CVD is very efficient for patterning at high speeds and for generating three dimensional structures. The thermal decomposition of the precursor molecules allows also to obtain materials with crystalline structure and high metal content. The main limitation of the process is its dependence on the substrate material, i.e. on its reflectivity, absorption coefficient and thermal conductivity. Photolytic CVD presents the advantages of a low local processing temperature and low sensitivity to the substrate's thermal properties, which allows uniform writing on materials with different thermal properties. Drawbacks of the process are the lower purity of the deposited material and the low speed of the process. In most of the real cases both pyrolysis and photolysis reactions are involved in the deposition mechanism, therefore the advantages of the two processes can be combined.

Precursor	*P (Torr)*	*T (°C)*	LASER, wavelength (nm), power	Metal content (at.%)	R_R	Ref.
WF_6 Ar carrier	0.625	320-475	Ar+, 488, 30-60 mW	pure W	-	Table 3-12 in [14]
WF_6/ H_2/Ar carrier	4	25-450	ArF, 133		2	Table 3-12 in [14]
W $(CO)_6$	High Vacuum	800	cw Ar^+, 514, MW/ cm^2	pure W	-	Table 3-12 in [14]
$Me_2Au(acac)$	$\approx 10^{-2}$	RT	Ar+, 514, 1-1.5 x10^5 W/cm^2	97	3	[15]
$Cu(hfa)_2$	$\approx 10^{-2}$	RT	Ar+, 514, 2-1.5x10^5 W/cm^2	90	2	[16]

Table 1-1: *Properties and deposition conditions of some metallic deposits obtained with LICVD. P and T indicate the precursor pressure and the substrate temperature during deposition respectively, and R_R is the electrical resistivity ratio between deposit and pure metal ($\rho_{deposit}/\rho_{pure\ metal}$).*

A wide range of metals, semiconductors and oxides have been deposited with LICVD using different families of precursors: halides, silanes, hydrocarbons, ß-diketonates, alkyls and carbonyls [13]. The deposits show high purity and electrical resistivities of the same order of magnitude as those of bulk metals, as shown in the examples reported in Table 1-1 for W, Au

and Cu deposition. The composition, the electrical properties and the structure of the deposits depend mainly on the precursor and on the power of the laser beam.

The ultimate resolution of LICVD is limited by the wavelength of the incident photons and by thermal diffusion processes at surfaces. At present features with a lateral resolution of some hundreds of nm have been demonstrated [17]. LICVD allows also deposition of three-dimensional high aspect ratio objects, such as rods, fibers, helixes and micro-springs [13].

Application of laser direct writing in micro-fabrication are electrical contacts, electrical circuit and mask repair [14].

1.2.4 ELECTRON BEAM INDUCED DEPOSITION (EBID)

Electron Beam Induced Deposition (EBID) is the result of local decomposition, by a focused electron beam, of precursor molecules adsorbed on a surface. The decomposition process is non-thermal, since the power dissipated by the electron beam at the surface (at the energy and current values generally used) induces only a negligible temperature increase [18] [19] [20]. EBID represents a single-step direct writing technique.

EBID experiments are usually performed in the vacuum chamber of a conventional or modified Scanning Electron Microscope (SEM) or Transmission Electron Microscope (TEM), with primary electron energies ranging in most of the cases from 1 to 100 keV. Focused electron beams and EBID systems will be discussed in detail in Chapter 2.

The materials obtained with this technique have in general nanocomposite structure, with metal nano crystals of variable size (a few nm depending on the precursor and deposition conditions) embedded in an amorphous matrix. The main constituents of the amorphous matrix are carbon, oxygen or other light elements present in the precursor molecule. As a consequence of such chemical composition and structure, the electrical conductivity of the material can be several orders of magnitude lower than that of bulk materials. The metal content (and the electrical conductivity) of the deposits can be increased by choosing particular deposition conditions, i.e. choosing the appropriate precursor molecule, increasing the electron current, heating the substrate during deposition, introducing reactive gases into the deposition system, or by ex-situ annealing of the deposit. Some properties of W, Au, Pt and Cu deposits are reported in Table 1-2. A more detailed review of the state of the art of this technique will be given in Chapter 5.

EBID is very interesting for nano-fabrication since it combines high resolution and high growth rate in the beam axis (three dimensional). Other advantages of EBID are the possibility to deposit locally on substrates of different thickness and shape, and low substrate damage (heating, sputtering, implantation). High resolution and high growth rates allow to build high aspect ratio structures of a wide range of shapes. Local deposition enables to introduce specific chemical, electrical or magnetic functionalities on nanometric objects and pre-deposited structures.

EBID has recently found a commercial application for production of special high aspect ratio carbon tips (curvature radius < 100 nm, height > 1 μm) for Atomic Force Microscopy [21]. Laboratory applications are X-ray mask repair [22], micro electrical devices [23], micro-field emitters [24] [20], micro switches [23], conducting lines [25] and photonic crystals [26]. EBID carbon lines have been used to connect biomolecules to pre-structured electrodes in electron transport experiments [27].

Precursor	*T (°C)*	*E, I_P*	Remarks	Deposit properties	Ref.
WF_6, WCl_6, $W(CO)_6$	- 180	3 keV, 18.4 μA	frozen layer	90 at.% W	[28]
$(CH_3)_2Au(hfa)^{(1)}$	20	10-30 keV. -	ESEM O_2 gas	50 at.%.	[29]
$CpPt(CH_3)_3^{(2)}$	25	15 keV, -	-	21 at.% Pt	[30]
hfaCu(I)TMVS$^{(3)}$	25	30 keV, 600 pA	ESEM precursor gas	10 at.% Cu, 35 at.% Si R_R = 2 (to pure Cu)	[31]

Table 1-2: *Properties and deposition conditions of some metallic deposits obtained with EBID. T indicates the substrate temperature during deposition; E and I_P, respectively, the electron energy and current used for deposition; R_R the electrical resistivity ratio between deposit and pure metal ($\rho_{deposit}/\rho_{pure\ metal}$). [1]hfa: hexa fluoro acetylacetonate; [2]Cp: cyclopentadienil; [3] TMVS: tri-methyl-vinyl-silane.*

1.2.5 FOCUSED ION BEAM INDUCED DEPOSITION (FIBID)

In Focused Ion Beam Induced Deposition (FIBID), the deposits are obtained by decomposition of precursor molecules adsorbed at the substrate surface by means of a focused beam of positive ions. The technique is similar to EBID but the process mechanisms and the deposit properties are different. The essential elements of a FIBID system are the ion gun and the focusing column [32]. The most common ion gun is a liquid metal (generally gallium) ion source [9]. A system of electrostatic lenses in the column focuses the ions into a point on the sample. Gallium sources can operate stably for many hours and, with an appropriate design of the lenses, can achieve beam diameters down to 8 nm [9]. The precursor molecules used in FIBID are the same as those used in EBID and other CVD techniques.

FIB systems can also be used for etching, doping and direct deposition. FIB etching can be of two types: physical sputter (or milling) and Gas Assisted Etching (GAE), which uses chemical reactions between the substrate surface and a halogen containing gas [32]. Milling finds its main applications in failure analysis of multi-layered structures, fabrication of cross sectional

Precursors	*T (°C)*	Ions	*E (keV)*	Deposit properties	Ref.
$Me_2Au(hfa)$[1]	RT	Ar^+ (broad beam)	750	98 at.% Au $R_R \approx 10$	[33]
$(MeCp)Pt(Me)_3$	RT	Ga^+	25	37 at.% Pt $R_R \approx 40$	[34]
$Fe(CO)_5$	130	Ga^+	25	85 at.% Fe	[35]
Al $Al(C_4H_9)_3$	370	Ga^+	50	85 at.% Al	[35]
(hfa)CuTMVS[2]	100	Ga^+	35	100 at.% Cu $R_R \approx 1.1$	[36]
W/WF_6	-	-	50	93%W $R_R \approx 25$	[37]

Table 1-3: *Characteristics of materials obtained with focused ion beam deposition. T indicates the substrate temperature during deposition; E is the ion energy used for deposition; R_R the electrical resistivity ratio between deposit and pure metal ($\rho_{deposit}/\rho_{pure\ metal}$). (1)hfa: hexa-fluoro-acetylacetonate; (2) TMVS: tri-methyl-vinyl-silane.*

TEM specimens and micro-machining. Gas assisted etching is faster and cleaner than milling since the formation of volatile products by the gas-substrate reaction avoids redeposition of the sputtered material. The technique has the same applications as ion milling but can also be used to etch deep trenches in semiconductor surfaces [38]. FIB doping is obtained by implantation of source ions in a semiconductor. Ga^+ FIB doping can enhance the resistivity of GaAs epitaxial layers by more than five orders of magnitude [39]. Direct deposition with a FIB consists in depositing structures of the material used as ion source [40].

The main virtue of FIBID is the possibility to combine deposition, milling and implantation. Further advantages over EBID are higher deposition rate and better material purity [36] [41] (compare Tables 1-2 and 1-3). The metal content can reach values close to 100% if the substrate temperature is increased by resistive [36] or laser induced (local) heating [42]. In addition, deposition rates in FIBID can be more than a factor 10 higher than in EBID, as shown by experiments carried out with two techniques using the same precursors [43]. This can be explained by an enhancement of the surface reactivity induced by ion bombardment [43], confirmed by the observation of spontaneous precursor decomposition on surfaces bombarded by ions [44]. The main disadvantages of FIBID are high surface damage, undesired implantation of source ions [43] and the high cost of the FIB equipment.

FIBID and EBID from spin coated layers

In these techniques electron [45, 46] or ion [47] beams decompose locally a layer of precursor pre-deposited on the substrate material. The process involves four steps: 1) deposition of the precursor by spin coating or by thermal vapor deposition under vacuum, 2) electron or ion beam irradiation; 2) removal of the unreacted precursor by rinsing in organic solvent, 4) evaporation of the solvent in dry atmosphere. FIBD and EBID from spin coated layers are therefore placed between direct deposition and classical lithography. For electron beam deposition the most important works with this technique have been performed by J.A. Cairns and his team [48] [45, 46]. The precursors were organometallic compounds containing gold, palladium or both elements, namely tetrakis isobutyl-diaurum-difluoride (TIDD), dicyclohexyl dipalladium-difluoride (DCPD) and bis-isobutyl aurum (III) cyclohexyl palladium (II) difluoride. EBID lines were obtained by irradiation of a 30 keV beam in a SEM. The dimension of the lines depended on the electron beam size, as for conventional EBID. Electron Dispersive X-ray (EDX) analysis detected the presence of only small quantities of contaminants, mostly chlorine. Resistivity measurements of lines obtained from TIDD gave a value very close to that of pure Au (2.44 $\mu\Omega$ cm).

Compared to conventional EBID, the advantage of this method is the independence of the vapor pressure of the precursor, which allows to work with high molecular weight species, which can be specially designed to be spin coated without decomposition and to decompose under electron irradiation. The disadvantages are the impossibility to generate three-dimensional features and the necessity of a multistep process, as in conventional PL/EBL.

1.3 SCANNING PROBE BASED METHODS

Soon after the invention of the Scanning Tunnelling Microscope (STM) and the Atomic Force Microscope (AFM) researchers found that scanning could alter the scanned surface; hence controlled scanning probe surface modification, named Scanning Probe Lithography (SPL), was started [49-51]. SPL can occur via three different modification modes: mechanical, optical and electrical [52].

Mechanical modification is usually achieved with AFM; it can occur by scratching or by pick up and put down. In the first case the probe tip of an AFM is employed to mechanically displace material on a sample surface. In the second particles are picked up from one region of a surface and subsequently transferred to another. Optical modification occurs through irradiation of a light sensitive material with a Scanning Near-field Optical Microscope (SNOM). The SNOM tip functions either as light detector or light source. Electrical modification consists of chemical or physical changes that take place on the sample surface exposed to the electric field, for applied voltages above a certain threshold. Electrical SPL methods, mainly based on STM, involve: direct modification of surfaces, patterning [53], etching [54], material transfer between tip and surface [55, 56], atomic scale polymerization [57] and chemical vapor deposition [58-63]. We discuss here scanning probe assisted chemical vapor deposition since it is the technique most related to the subject of this work.

Scanning probe assisted CVD occurs when gas phase (CVD like) precursors are decomposed in the region between the tip and the sample in a STM.

The decomposition can be caused by the tunnelling electrons or, according to most authors by the tip-surface voltage gap [52], but it is not straightforward to distinguish between the two contributions. The bias applied between the tip and the sample in deposition experiments ranges from 10 to -40 eV [52]. The properties of the deposited materials depend on the tip material, on the voltage bias and on the precursor compound.

The main virtue of this technique is the high resolution which can allow the deposition of sub-10 nm features [62, 63]. Negative aspects are the small scan range of the probes (max. 150 μm), the fact that the technique is limited to conducting substrates, the low writing speed, and the limited three-dimensional range (max. 10 μm).

1.4 OTHER TECHNIQUES

1.4.1 MICRO CONTACT PRINTING (μCP)

Micro Contact Printing (μCP) belongs to a family of techniques known under the name of soft lithography, originally developed in the group of G. Whitesides at Harvard University [64]. The name soft lithography comes from the fact that an elastomeric stamp or mold, previously shaped on a master, is the key element which transfers the pattern to the substrate [65]. The master can be produced with any serial technique and can contain details much smaller than those obtainable with photolithographic techniques. Therefore with such techniques sub-100 nm structures can be obtained.

Micro Contact Printing forms patterned Self Assembled Monolayers (SAMs) containing regions terminated by different chemical functionalities with submicron lateral dimensions. An elastomeric polydimethylsiloxane (PDMS) master stamp transfers a pattern to the surface of the substrate by contact. After printing, a different SAM can be formed on the non-functionalized regions by washing the patterned substrate with a dilute solution containing another molecule. μCP was first demonstrated for SAMs of alkanethiolates on gold but has been extended to other systems of SAMs [65]. The most useful systems are patterrned SAMs of alkenethiolates on evaporated thin films of Au and Ag, because in both cases highly ordered monolayers are obtained. Au is interesting since it is the material for electrodes in many applications and it is compatible with GaAs technology. Ag is attractive as it is an excellent thermal and electrical conductor, chemically more reactive than Au and therefore easier to etch.

Patterned SAMs can be used as ultrathin resists in selective wet etching or as templates to control the wetting, dewetting, nucleation growth, and deposition of other materials. They have also been used to control both azimuthal and polar orientations of nematic liquid crystals. The smallest features generated to date with a combination of μCP and selective etching are trenches etched in Au with lateral dimensions of approximately 35 nm [64].

The major virtues of μCP are simplicity and low cost of the equipment, and the possibility to form patterns over large areas (>50 cm^2) in a single impression. The main drawbacks are the fact that the technique works only with a limited number of materials and substrates, the impossibility to process the substrate locally and the low capability for three-dimensional structuring. Today μCP finds its main applications in plastic electronics, integrated optics, micro-reactors, micro-mechanics and Micro Electro-Mechanical Systems (MEMS) [65].

1.4.2 REACTIVE ION ETCHING (RIE)

Reactive Ion Etching allows generation of three-dimensional high aspect ratio structures on Si. The process consists in etching deep trenches on a substrate covered with an etch mask. The etching gases used are SF_6, CF_4, CHF_3 for Si; $CHCl_3$ and CCl_4 for GaAs. The masks can be made by electroplated nickel or SiO_2 [66]. The mask used in this process should hold up during the etch and be eroded at the end, therefore its width and height should be chosen in accordance with the vertical and lateral etch rates, as well as the final base width of the desired 3D structure.

In modern Reactive Ion Etching (RIE) systems the reactive species in the plasma are generated with an electron cyclotron resonance source (ECR), as described in ref. [67]. The etch rate, the selectivity and resolution depend on the plasma parameters (gas pressure, ion flux, ion energy) and the mask shape [67] [66, 68]. The etch rate decreases in general with decreasing spacing between mask elements, i.e. with increasing aspect ratio of the etched trenches.

RIE has been used to build high-density sharp Si field emitter arrays [67]. Using a 1 μm thick high resolution (1.5 μm line widths) SiO_2 etch mask it is possible to obtain tips with a base diameter of 2.2 μm, a height of 11 μm and a tip diameter of 70 nm. Further sharpening in Cl_2 plasma can reduce the radius to 22 nm. Tip sharpening can be obtained also by low temperature oxidation in O_2 plasma and subsequent removal of the oxide in buffered HF [68]. For a plasma oxidation time of 70, 200 and 500 minutes the Si field emitter was sharpened to 25, 18 and 8 nm, respectively [66].

The main virtues of RIE is that it allows to obtain high aspect ratio structures with parallel processing and a low number of steps. Drawbacks are the fact that the process is limited to Si and GaAs technology and the impossibility to process the substrate locally.

1.4.3 THE LIGA PROCESS

The acronym LIGA generates from the German expression for the major process steps: X-ray lithography with synchrotron radiation (LI), electroforming (G, *Galvanoformung*) and molding (A, *Abformung*) [69]. The technique is used in making microstructures with lateral dimensions of the order of several micrometers and high aspect ratio.

In the first step a thick layer of a resist (in general Poly Methyl Meta Acrylate, PMMA) deposited on a metallic substrate is irradiated with synchrotron light through the pattern of an X-ray

mask. The resist is then developed. By means of electroplating metals such us Cu, Ni, or Au, the complementary microstructure is plated up using the metallic substrate as a cathode. The remaining resist is dissolved, leaving the patterned metal structure as the end product. Alternatively, the electroplating can be extended to reach a thickness of 4-5 mm above the height of the primary structure, producing a robust mold insert. The insert can be replicated by molding techniques (i.e. injection molding, hot embossing), offering nearly the same quality but at lower cost and higher quantities compared with the primary patterning. The secondary polymer structures may form the final polymer component, be used as a template in a second electroforming process, or serve as disposable molds for the fabrication of ceramic microstructures [69].

The exposure station, separated from the X-ray beamline with a Be window, is a vacuum chamber which houses a linear stage which moves the mask/substrate holder vertically and at a constant velocity through the synchrotron beam. The membranes of the masks for LIGA are made of low-Z material (such as Be, C, Ti, Si) while the adsorber pattern is usually made of high Z material, usually Au, W, Ta. The most used resist is PMMA, which is modified in the exposed regions, which are removed by a special mixture of deionized water and organic solvents [70].

The main advantage of LIGA lies in the microstructures being molded out of plastic, metals and ceramic in nearly any lateral geometry and high aspect ratio (more than 60:1), with the walls having a roughness of less than 50 nm and nearly vertical side walls along the entire height of the structure [69]. Disadvantages are the low resolution (some microns), and the high number of process steps.

1.4.4 SELECTIVE LASER CLADDING (SLC)

3D structuring can be achieved by laser rapid prototyping [71]. In this process the original 3D geometrical part is decomposed into 2D profile layers, then material is added layer by layer by selective laser cladding (SLC). The most attractive metal fabrication system is Laser Engineered Net Shaping (LENS). In general LENS systems use a focused Nd:YAG high power laser to melt an area on a metal target while one or more nozzles simultaneously delivers metal powder. With an opportune choice of the powder delivering system the composition and the properties of the material can be very similar to those of the target. At present the technique is not interesting for micro- and nano-fabrication since it allows fabrication of objects in the cm/mm range.

1.5 CONCLUSIONS

Direct deposition techniques are very interesting for micro and nano fabrications since they involve a low number of steps, allow selective area modification and deposition and in some cases generation of three dimensional high aspect ratio structures.

The intrinsic limit of direct deposition techniques is that they are all serial, therefore the writing processes are limited by the scanning speed of the probe on the sample. To compete with the optical lithography throughput a single beam or probe system should have a writing speed of about 20 km/s. Numerous efforts are being undertaken to speed up direct write systems, especially STM lithography and EBL, which permit almost atomic resolution to be combined with a parallel processing [10, 72].

In Table 1-4 the most important characteristics of the discussed techniques are compared. The high resolution, the high aspect ratio, the good flexibility and capability of local deposition lead us to focus on EBID. High resolution is due to the fact that electron beams can be focused into nanometer-sized probes while at present focused ions beams have a minimum probe size of about 8 nm and photon optics cannot do better than about 120 nm [9, 73]. High aspect ratio generation is possible due to the practically unlimited height range. Scanning probe CVD can reach better resolutions but suffers the limited height (z) range which does not allow high aspect ratio generation. Another advantage of EBID over scanning probe methods is the wider xy scanning range (some cm versus 150 μm).

Technique	Serial/ Parallel S/P	Minimum feature size	Aspect /ratio	Flexibility	Purity	Cost
PL	P	-	-	-	+++	++
μCP	P	++	-	+	+	++
EBL/IBL	S	++	-	++	+++	-
LICVD	S/P	-	++	+	+++	-
FIBID	S	+	++	++	+	-
EBID	S	++	+++	++	-	+
SPL	S	+++	-	-	+	+
LIGA	P	-	++	-	+	-
RIE	P	--	++	+	+	-
SLC	S		+	+	+	+

Table 1-4: *Comparison of techniques for nano-structure generation, + means advantage, - disadvantage.*

In this work I test new precursor molecules and try to gain insight into the decomposition process in order to improve the purity of the EBID structure. In parallel I investigate the suitable methods for chemical and structural characterization of the deposits.

1.6 REFERENCES

[1] H. Rohrer; *Nanoengineering beyond Nanoelectronics*; Microelectron. Engin., 41/42 (1998); p. 31-36.

[2] C.W.J. Beenakker; *Theory of Coulomb-Blockade Oscillations in the Conductance of a Quantum Dot*; Phis. Rev. B, 44 (1991); p. 1646-1656.

[3] T.A. Fulton, G.J. Dolan; *Observation of single electron Charging Effects in Small Tunnell Junctions*; Phys. Rev. Lett., 59 (1987); p. 109-112.

[4] H.J. Levinson, W.H. Arnold; *Optical Lithography*, in *Microlithography, Micromachining, and Microfabrication*; P. Rai-Choudry, Editor; SPIE, 1997, p. 13-127.

[5] G. Moore; *Crossing the chasm*; Harperbussiness, 1999.

[6] H.C. Pfeiffer, W. Stikel; *PREVAIL: An E-Beam Stepper with Variable Axis Immersion Lenses*; Microelectron. Engin., 27 (1995); p. 143-146.

[7] M.A. McCord, M.J. Rooks; *Electron Beam Lithography*, in *Microlithography, Micromachining, and Microfabrication*; P. Rai-Choudry, Editor; SPIE, 1997, p. 142-232.

[8] B. Dwir, I. Utke, D. Kaufman, E. Kapon; *Electron-beam lithography of V-groove quantum wire devices*; Microelectron. Engin., 53 (2000); p. 295-298.

[9] J. Melngailis; *Focused Ion-Beam Lithography*; Nucl. Inst. Meth. Phys. Res. B, 80-1 (1993); p. 1271-1280.

[10] J.A. Liddle, L.R. Harriot, A.E. Novembre, W.K. Waskiewicz; *SCALPEL: A projection electron-beam approach to sub-optical lithography*; 1999, Bell Laboratories, Lucent Technologies, www.bell-labs.com/project/SCALPEL.

[11] J. Melngailis, A.A. Mondelli, I.L. Berry, R. Mohondro; *A review of ion projection lithography*; J. Vac. Sci. Technol. B, 16 (1998); p. 927-957.

[12] M.L. Hitchmann, K.F. Jensen; *Chemical Vapor Deposition (Principles and Applications)*; Academic Press, Inc., 1993.

[13] D. Bäuerle; *Laser processing and chemistry*; Springer-Verlag, 1996.

[14] T. Kodas, M. Hampden-Smith; *The Chemistry of Metal CVD*; VCH, 1995.

[15] T.H. Baum, C.R. Jones; *Laser chemical vapor deposition of gold (part II)*; J. Electrochem. Soc., 134 (1987); p. 2616-2619.

[16] F.A. Houle, C.R. Jones, T. Baum, C. Pico, C.A. Kovac; *Laser chemical vapor deposition of copper*; Appl. Phys. Lett., 46 (1985); p. 204-206.

[17] D.J. Ehrlich, J.Y. Tsao; *Spatial resolution limits of laser patterning: submicrometer projection microchemistry*; Mat. Res. Soc. Symp. Proc., 29 (1984); p.

[18] L. Reimer; *Scanning Electron Microscopy*; Springer, 1998.

[19] H. Hiroshima, M. Komuro; *High growth rate for slow scanning in electron-beam-induced deposition*; Jpn. J. App. Phys. 1, 36 (1997); p. 7686-7690.

[20] M. Weber, M. Rudolph, J. Kretz, H.W.P. Koops; *Electron-Beam-Induced-Deposition for fabrication of vacuum field emitter devices*; J. Vac. Sci. Technol. B, 13 (1995); p. 461-464.

[21] Website of Nanotools GmbH, www.nanotools.de.

[22] K.T. Kohlmann, M. Thiemann, W.H. Brünger; *E-beam induced X-ray mask repair with optimized gas nozzle geometry*; Microelectron. Engin., 13 (1991); p. 279-282.

[23] H.W.P. Koops, E. Munro, J. Rouse, J. Kretz, M. Rudolph, M. Weber, G. Dahm; *Miniature low-voltage beam systems producable by combined lithographies*; Nucl. Inst. Meth. Phys. Res. B, 363 (1995); p. 1-9.

[24] C. Schössler, H.W.P. Koops; *Nanostructured Integrated Electron Source*; J. Vac. Sci. Technol. B, 16 (1998); p. 862-865.

[25] H.W.P. Koops, C. Schossler, A. Kaya, M. Weber; *Conductive dots, wires, and supertips for field electron emitters produced by Electron-Beam-Induced Deposition on samples having increased temperature*; J. Vac. Sci. Technol. B, 14 (1996); p. 4105-4109.

[26] H.W.P. Koops; *Photonic crystals built by three-dimensional additive lithography enable integrated optics of high density*; Proc. SPIE, 2849 (1996); p. 248-56.

[27] W. Fritzsche, K. Bohm, E. Unger, M. Kohler; *Making electrical contact to single molecules*; Nanotechnology, 9 (1998); p. 177-83.

[28] D.A. Bell, J.L. Falconer, L. Zhiming, C.M. McConica; *Electron beam-induced deposition of tungsten*; J. Vac. Sci. Technol. B, 12 (1994); p. 2976-2979.

[29] A. Folch, J. Tejada, C.H. Peters, M.S. Wrighton; *Electron-Beam Deposition of Gold Nanostructures in a Reactive Environment*; Appl. Phys. Lett., 66 (1995); p. 2080-2082.

[30] O. Yavas, C. Ochiai, M. Takai, Y.K. Park, C. Lehrer, S. Lipp, L. Frey, H. Ryssel, A. Hosono, S. Okuda; *Field emitter array fabricated using focused ion and electron beam induced reaction*; J. Vac. Sci. Technol. B, 18 (2000); p.

[31] Y. Ochiai, J. Fujita, S. Matsui; *Electron-beam-induced deposition of copper compound with low resistivity*; J. Vac. Sci. Technol. B, 14 (1996); p. 3887-3891.

[32] D.K. Stewart, J.D.J. Casey; *Focused Ion Beams for Micromachining and Microchemistry*, in *Microlithography, Micromachining, and Microfabrication*; P. Rai-Choudry, Editor; SPIE, 1997, p. 155-191.

[33] G.M. Shedd, H. Lezec, A.D. Dubner, J. Melngailis; *Focused ion beam induced deposition of gold*; Appl. Phys. Lett., 49 (1986); p. 1584-1586.

[34] J. Puretz, L.W. Swanson; *Focused Ion-Beam deposition of Pt containing films*; J. Vac. Sci. Technol. B, 10 (1992); p. 2695-2698.

[35] R.L. Kubena, F.P. Stratton, T.M. Mayer; *Selective area nucleation for metal chemical vapor deposition using focused ion beams*; J. Vac. Sci. Technol. B, 6 (1988); p. 1865-1868.

[36] A.D. Della Ratta, J. Melngailis, C.V. Thompson; *Focused-Ion Beam-Induced deposition of copper*; J.Vac. Sci. Technol. B, 11 (1993); p. 2195-2199.

[37] K. Gamo, S. Namba; *Ion beam assisted etching and deposition*; J. Vac. Sci. Technol. B, 8 (1990); p. 1927-1931.

[38] S. Matsui, Y. Ochiai; *Focused ion beam applications to solid state devices*; Nanotechnology, 7 (1996); p. 247-58.

[39] K. Gamo; *Recent Advances of Focused Ion-Beam Technology*; Nucl. Inst. Meth. Phys. Res. B, 121 (1997); p. 464-469.

[40] S. Nagamachi, M. Ueda, J. Ishiwaka; *Focused ion beam direct deposition and its applications*; J. Vac. Sci. Technol. B, 16 (1998); p. 2515-2521.

[41] H.W.P. Koops, J. Kretz, M. Rudolph, M. Weber, G. Dahm, K.L. Lee; *Characterization and application of materials grown by Electron-Beam-Induced Deposition*; Jpn. J. Appl. Phys. 1, 33 (1994); p. 7099-7107.

[42] J. Funatsu, C.V. Thompson, J. Melngailis, J.N. Walpole; *Laser-Assisted Focused-Ion-Beam-Induced Deposition of Copper*; J. Vac. Sci. Tech. B, 14 (1996); p. 179-180.

[43] S. Lipp, L. Frey, C. Lehrer, B. Frank, E. Demm, S. Pauthner, H. Ryssel; *Tetramethoxysilane as a precursor for focused Ion-Beam and Electron-Beam assisted insulator (SiOx) deposition*; J. Vac. Sci. Technol. B, 14 (1996); p. 3920-3923.

[44] S.J. Kirch, A. Wagner; *Spontaneous decomposition of dimethyl gold hexafluoroacetylacetonate on ion bombarded surfaces*.; J. Vac. Sci. Technol., A 8 (5) (1990); p. 3701-3706.

[45] G.J. Berry, J.A. Cairns, J. Thomson; *New Material for the Production of Fine Line Interconnects in Integrated-Circuit Technology*; J. Mater. Sci. Lett., 14 (1995); p. 844-846.

[46] G.J. Berry, J.A. Cairns, J. Thomson; *The production of fine metal tracks from a new range of organometallic compounds*; Sensors and Actuators A, 51 (1995); p. 47-50.

[47] P. Hoffmann, G. Ben Assayag, J. Gierak, J. Flicstein, M. Maar-Stumm, H. van den Bergh; *Direct writing of gold nanostructures using a gold-cluster compound and a focused ion beam*; J. Appl. Phys., 74 (1993); p. 7588-7591.

[48] M.R. Davidson, G.J. Berry, J.A. Cairns, A.G. Fitzgerald, B. Lawrenson, J. Thomson, I.C.E. Turcu, W. Shaikh, N. Spencer, R.M. Allott, N. Takeyasu; *Novel route for the production of X-ray masks from a range of organometallic films*; Microelectron. Engin., 42 (1998); p. 279-282.

[49] E.E. Ehrichs, R.M. Silver, A.L. de Lozanne; *Direct writing with the scanning tunnelling microscope*; J.Vac. Sci. Technol. A, 6 (1987); p. 540-542.

[50] G.M. Shedd, P.E. Russel; *The scanning tunnelling microscope as a tool for nanofabrication*; Nanotechnology, 1 (1990); p. 67-80.

[51] M. Baba, S. Matsui; *Nanostructure fabrication by scanning tunneling microscope*; Jpn. J. Appl. Phys. 1, 29 (1990); p. 2854-2857.

[52] R.M. Nyffenegger, R.M. Penner; *Nanometer-scale surface modification using the scanning probe microscope-Progress Since 1991*; Chem. Rev., 97 (1997); p. 1195-1230.

[53] D.P. Adams, T.M. Mayer, B.S. Swartzentruber; *Selective area growth of metal nanostructures*; Appl. Phys. Lett., 68 (1996); p. 2210-2212.

[54] M. Baba, S. Matsui; *Atomic desorption of chlorine adsorbed on Si(111) with a scanning tunneling microscope*; Appl. Phys. Lett., 64 (1994); p. 2852-4.

[55] D.H. Huang, T. Nakayama, M. Aono; *Platinum nanodot formation by atomic point contact with a scanning tunnelling microscope platinum tip*; Appl. Phys. Lett., 73 (1998); p. 3360-3362.

[56] D. Fuijta, Q. Jiang, H. Nejoh; *Fabrication of gold nanostructures on a vicinal Si (111) 7x7 surface using ultrahigh vacuum scanning tunnelling microscope and a gold-coated tungsten tip*.; J. Vac. Sci. Technol. B, 14 (1996); p.

[57] L.P. Ma, W.J. Yang, S.S. Xie, S.J. Pang; *Ultrahigh density data storage from local polymerization by a scanning tunnelling microscope*.; Appl. Phys. Lett., 73 (1998); p. 3303-3305.

[58] D.S. Saulys, A. Ermakov, E.L. Garfunkel, P.A. Dowben; *Electron-beam-induced patterned deposition of allylcyclopentadienyl palladium using scanning tunneling microscopy*; J. Appl. Phys., 76 (1994); p. 7639-7641.

[59] M.A. McCord, D.P. Kern, T.H.P. Chang; *Direct deposition of 10-nm metallic features with the scanning tunnelling microscope*; J. Vac. Sci. Technol. B, 6 (1988); p. 1877-1880.

[60] D. Samara, J.R. Williamson, C.K. Shih, S.K. Banerjee; *Scanning tunnelling microscopy induced chemical vapor deposition of semiconductor quantum dots*; J. Vac. Sci. Technol. B, 14 (1995); p. 1344-1348.

[61] M.A. McCord, D.D. Awschalom; *Direct deposition of magnetic dots using scanning tunnelling microscope*; Appl. Phys. Lett., 57 (1990); p.

[62] F. Marchi, D. Tonneau, H. Dallaporta, V. Safarof, V. Bouchiat, P. Doppelt, R. Even, L. Beitone; *Direct patterning of noble mertal nanostructure with a scanning tunnelling microscope*; J. Vac. Sci. Technol. B, 18 (2000); p. 1171-1176.

[63] T.M.H. Wong, S.J. O'Shea, A.W. McKinnon, M.E. Welland; *Direct writing of nanostructures from silane on silicon (111)*; Appl. Phys. Lett., 67 (1995); p. 786-788.

[64] Y. Xia, J.A. Rogers, K.E. Paul, G.M. Whitesides; *Unconventional methods for fabricating and patterning nanostructures*; Chem. Rev., 99 (1999); p. 1823-1848.

[65] Y. Xia, M.W. Whitesides; *Soft Lithography*; Angew. Chem. Int. Ed., 37 (1998); p. 550-575.

[66] S.J. Pang; *Applications of dry etching to microsensors, field emitters, and optical devices*, in *Microlithography, Micromachining, and Microfabrication*; P. Rai-Choudry, Editor; SPIE, 1997, p. 99-149.

[67] M.R. Rakhshandehroo, S.W. Pang; *Fabrication of Si field emitters by dry etching and mask erosion*; J. Vac. Sci. Technol. B, 14 (1996); p. 612-616.

[68] K.T. Sung, S.W. Pang; *Oxidation of silicon in an oxigen plasma generated by a multipolar electron cyclotron resonance source*; J. Vac. Sci. Technol. B, 10 (1992); p. 2211-2216.

[69] C.R. Friedrich, R. Warrington, W. Bacher, W. Bauer, P.J. Coane, J. Göttert, T. Hanemann, J. Hausselt, M. Heckele, R. Knitter, J. Mohr, V. Pioter, H.J. Ritzhaupt-Kleiss, R. Ruprecht; *High Aspect Ratio Processing*, in *Microlithography, Micromachining and Microfabrication*; P. Rai-Choudry, Editor; SPIE, 1997, p. 301-369.

[70] W. Ehrfeld, H.J. Baving, D. Beets, P. Bley, F. Götz, J. Mohr, D. Münchmeyer, W. Schelb; J. Vac. Sci. Technol. B, 6 (1988); p. 178.

[71] J.Y. Jeng, S.C. Peng, C.J. Chou; *Metal Rapid Prototype Fabrication Using Selective Laser Cladding Technology*; Int. J. Adv. Manuf. Technol., 16 (2000); p. 681-687.

[72] R. Lüti, R.R. Schlitter, J. Brugger, P. Vettiger, M.E. Welland, J.K. Gimzewski; *Parallel nanodevice fabrication using a combination of shadow mask and scanning probe methods*; Appl. Phys. Lett., 75 (1999); p. 1314-1316.

[73] S. Matsui; *Nanostructure fabrication using electron beam and its application to nanometer devices*, in IEEE Proc., 1997, p.629-43.

CHAPTER 2 *Focused electron beam in SEMs*

EBID deposition systems are generally based on scanning electron microscopes (SEMs). Here I describe briefly the structure of a SEM and give an overview on the properties of focused electron beams. Further on the geometrical theory of probe formation, useful to understand some of the factors affecting the ultimate resolution of the EBID process, is discussed. At the end of the chapter I present the measurement of the electron probe size of the system used in this work.

2.1 THE SCANNING ELECTRON MICROSCOPE (SEM)

In a Scanning Electron Microscope *(*SEM) the electron beam is generated by an electron emitter (cathode), then accelerated through the anode grid and concentrated in a point called the first crossover. The voltage between the anode and the cathode can be set between 0.3 and 50 keV. The first crossover is demagnified by one or two sets of condenser lenses and finally focused as a very fine spot on the specimen by the objective lenses.

2.2 ELECTRON GUNS

An electron gun is characterized by the size of the first cross over, the energy dispersion (full width at half maximum of the energy profile of the electron beam) and the brightness. The brightness (current density per solid angle) β is defined by:

$$\beta = \frac{j_p}{\pi\alpha^2} \tag{2.1}$$

where $j\,(\Delta I/\Delta S)$ is the current density and α the beam aperture angle.

The simplest electron guns are based on the thermionic effect: an emitter is heated to allow the electrons to overcome the metal work function by thermionic excitation; the emission current density follows Richardson's law:

$$j_p = BT_c^2 exp(-\phi_w / kT_T) \tag{2.2}$$

where A indicates a constant depending on the cathode material, T_T the temperature at the cathode tip, ϕ_w the work function of the cathode material and k Boltzmann's constant. A typical example of thermionic emitter is the tungsten filament (Fig. 2-1), made of a hairpin bent wire, heated by Joule effect at 2700-2800 K operating temperature. Tungsten filaments have a relatively low brightness due to the low current density, as a consequence of a high work function and a high crossover diameter. The advantages of this emitter are the low cost and the possibility to work in a relatively low vacuum (10^{-5}-10^{-6} Torr). A different thermionic emitter is the LaB_6 cathode, made by a LaB_6 crystal with a polished tip mounted on a filament heated by Joule effect. Compared to the tungsten filament, this emitter has a smaller crossover diameter, which results in a gain of brightness, and a lower operation temperature (1850 K). High vacuum is needed (10^{-7} Torr) to prevent the formation of oxides, which shorten the lifetime considerably.

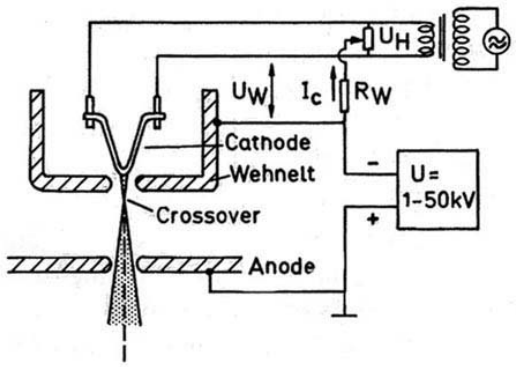

Figure 2-1: *The tungsten hairpin filament [1].*

Filament	ßx10^{-5} (A/cm^{2}sr)	Energy spread (eV)	Operating pressure (Torr)	Lifetime	Crossover diameter	Cost (CHF)
W	1	1-3	10^{-5}	40-200 hrs	20-50 μm	10
LaB_6	20-50	0.5-2	10^{-7}	1000 hrs	10-20 μm	1000
FEG	100-500	0.2-0.5	10^{-9}-10^{-10}	>1500 hrs	3-5 nm	12000

Table 2-1: *Properties and characteristics of different types of electron guns [1, 2].*

Field emission guns (FEG) consist of a tungsten tip with a curvature radius $r \approx 100$ nm. From such a tip the emission starts when the potential gradient $Y = U/r$ (where U is the potential difference between the cathode tip and the first extraction electrode) reaches values larger than 10^7 V/cm. Such high fields decrease the width of the potential wall in front of the tip to a few

nanometers so that electrons from the Fermi level can penetrate the potential barrier by tunnelling effect. These guns require Ultra High Vacuum (UHV) to avoid ion sputtering of the emitting tip. FEGs can work at room temperature (cold FEG) or at 1000-1500 K (hot FEG) to prevent gas adsorption during operation. The main advantages of a FEG are the very high brightness and the small crossover diameter (3-5 nm), which requires only one demagnifying lens to get the electron probe diameter below 1nm. The most important features of the different types of electron guns are reported in Table 2-1.

2.3 ELECTRON OPTICS

After the electron beam has been formed and concentrated by the Wehnelt cylinder to the first crossover (Fig. 2-1), it is controlled by a system of electron lenses (Fig. 2-2). Electron lenses are of two types: condenser and objective, both consisting of an axial magnetic field with rotational symmetry. Condenser lenses condense the beam to the second (and eventually the third) crossover, objective lenses focus the beam on the specimen. At the exit of each electron lens the beam passes through an aperture (from 100 to 10 μm in diameter), which in condenser lenses eliminates widely scattered electrons (spray diaphgrams) and in objective lenses (final aperture) defines the aperture angle. The aperture angle α is the angle formed by the edge of the electron beam as it exits the lens aperture and the center of the electron probe.

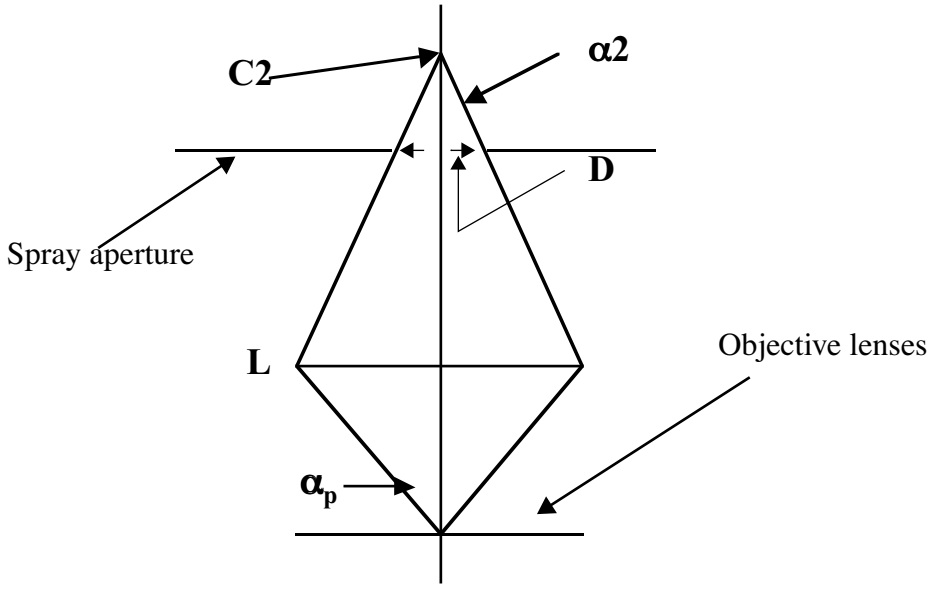

Figure 2-2: *Schematic view of the electron optics of the SEM Cambridge S100, used in this work as deposition system. C2: second crossover, α2: aperture angle after the second crossover, D: spray aperture, L: condenser lens, α_p: final aperture angle.*

2.4 GEOMETRICAL THEORY OF PROBE FORMATION AND ABERRATIONS

A small electron probe on the specimen is produced after demagnification of the crossover of diameter d_{cr} by means of two or three lenses. The geometrical diameter of the spot d_0 is given by

$$d_0 = \frac{f_1 f_2 f_3}{L_1 L_2 L_3} d_{cr} = m d_{cr} \tag{2.3}$$

where L_i represent the distances between the lenses, f_i the focal distances and m the demagnification. Thermionic cathodes have typically a crossover diameter of 20-50 μm, so a demagnification $m < 1/5000$ is needed to obtain a probe of about 10 nm.

The aperture angle defined by an aperture of radius r after a lens of focus f is:

$$\alpha = \frac{r}{f}. \tag{2.4}$$

An important feature of SEMs is that the electron probe current, the aperture angle and the geometrical probe diameter cannot be changed independently. The electron current density j_p and the probe aperture α are related by the gun brightness β:

$$j_p = \pi \beta \alpha . \tag{2.5}$$

If we assume that the current density is uniform over a circle of diameter d_0, the total probe current is given by:

$$I_p = \frac{\pi}{4} d_0^{\,2} j_p \qquad \text{which determines} \qquad d_0 = \left(\frac{4 I_p}{\pi \beta}\right)^{\frac{1}{2}} \alpha^{-1} = C_0 \alpha^{-1} \tag{2.6}$$

with $C_0 = (4I_p/\pi\beta)^{1/2}$, representing the geometric probe coefficient.

The geometric probe diameter d_0 is broadened by aberrations of the objective lenses. Typical lens aberrations are spherical and chromatic aberration, diffraction error and astigmatism (Fig. 2-3). To estimate the influence of the aberrations we assume that the geometric electron probe profile of half width d_o and the error disc of widths d_s, d_c, d_d follow Gaussian distribution. This has the advantage that a convolution of two Gaussian widths a_1 and a_2 results in a blurred Gaussian of width $a_1^2 + a_2^2$. This estimation of the effective probe diameter gives a good indication of the orders of magnitude involved and shows how different parameters influence the real probe size.

- **Spherical aberration**

If parallel rays pass through an electron lens, those further from the optical axis are focused closer to the lens. The effect can be described by the equation

$$d_s = 0.5 C_s \alpha^3 \tag{2.7}$$

where d_s represents the beam diameter in the plane of least confusion, C_s the spherical aberration coefficient and α the aperture angle. Spherical aberration cannot be completely eliminated but it can be minimized by reducing the focal length of the lens and the diameter of the aperture. Typical values of C_s for SEM weak lenses are in the range 20-100 mm.

- **Chromatic aberration**

Chromatic aberration is the result of the electrons having different velocities and thus different wavelengths. The differing wavelengths cause the electrons to be focused at different points, which blurs the image. The diameter of the error disc d_c is given by

$$d_c = \frac{\Delta E}{E} C_c \alpha \tag{2.8}$$

where C_c represents the chromatic aberration coefficient, $\Delta E/E$ the energy dispersion and α the aperture angle. This defect can be reduced by minimizing the energy spread ΔE (advantage of a FEG), reducing the focal length of the lenses, the angular aperture and the lens current. C_c values are similar to the focal length of the electron lenses (around 10 mm).

- **Diffraction**

The diffraction error is caused by a diffraction pattern formed at the exit of the diaphragms after the objective lens, which limits the aperture to keep the spherical and chromatic aberrations small. The disc of least confusion is

$$d_d = 0.6 \frac{\lambda}{\alpha} \tag{2.9}$$

where λ is the de Broglie wavelength of the electrons ($\lambda = 38.8\ pm$ for $E = 1\ keV$, $\lambda = 6.58\ pm$ for $E = 30\ keV$).

- **Astigmatism**

Astigmatism is an asymmetry in the focusing field, resulting from magnetic inhomogeneities of the polepieces. Electrons incident in the sagittal and meridional planes are focused at different distances from the lenses, forming focal lines separated by a distance Δf. Astigmatism can be corrected adding stigmator coils, consisting of eight small electromagnets around the column, the current of which can be varied by controls on the microscope. The coils are wired

so that the electromagnetic field from them can be shifted around the cross-sectional axis of the column. Adjusting the controls forces the distorted beam of electrons back into a round shape.

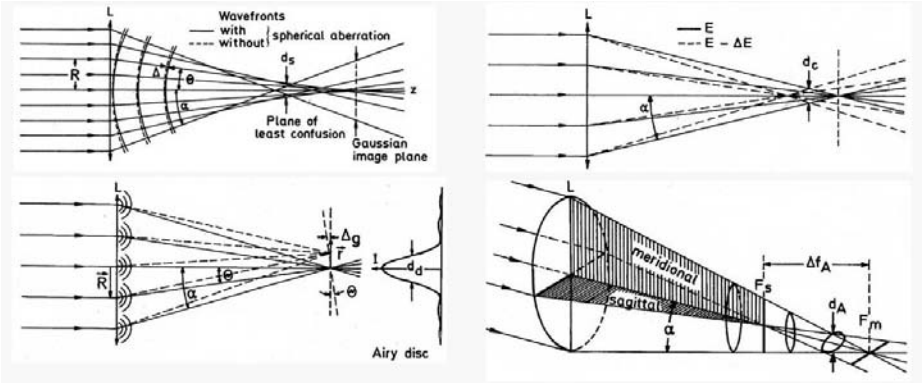

Figure 2-3: *Defects of a focused electron beam [1]: spherical aberration (a), chromatic aberration (b), diffraction (c), astigmatism (d).*

By taking into account all the lens distortions, assuming a Gaussian distribution of the geometric electron probe profile and the error discs, the final probe diameter d_p will be given by

$$d_p^2 = d_0^2 + d_d^2 + d_s^2 + d_c^2 = [C_0^2 + (0.6\lambda)^2]\alpha^{-2} + \frac{1}{4}C_s^2\alpha^6 + \left(C_c\frac{\Delta E}{E}\right)^2\alpha^2 . \qquad (2.\,10)$$

In thermionic cathodes $C_0 >> \lambda$, so the diffraction error can be neglected. When operating at sufficiently high voltage (>10 kV) the chromatic aberration term also becomes negligible; therefore the dominant terms in Eq. 2. 10 are the ones containing C_0 and C_s. The minimum probe diameter of a W thermionic electron gun as a function of the current and of the electron energy, calculated with the Eq. 2. 10, is reported in Fig. 2-4.

The optimum aperture angle α_{opt}, at which the smallest electron probe diameter is produced, can be obtained by setting the derivative $\partial d_p/\partial\alpha_p = 0$ and solving for $\alpha_p = \alpha_{opt}$:

$$\alpha_{opt} = \left(\frac{4}{3}\right)^{\frac{1}{8}}(C_s C_0^3)^{\frac{1}{4}} . \qquad (2.\,11)$$

Optimum aperture angles for electron energies of 2 and 25 keV are reported in Fig. 2-5 a and b. Introducing α_{opt} in the terms of the Eq. 2. 10 containing C_0 and C_s (diffraction and chromatic aberration negligible) gives:

$$d_{p,\,min} = \left(\frac{4}{3}\right)^{\frac{3}{8}}(C_s C_0^3)^{\frac{1}{4}} \propto \mathrm{I_p}^{\frac{3}{8}} . \qquad (2.\,12)$$

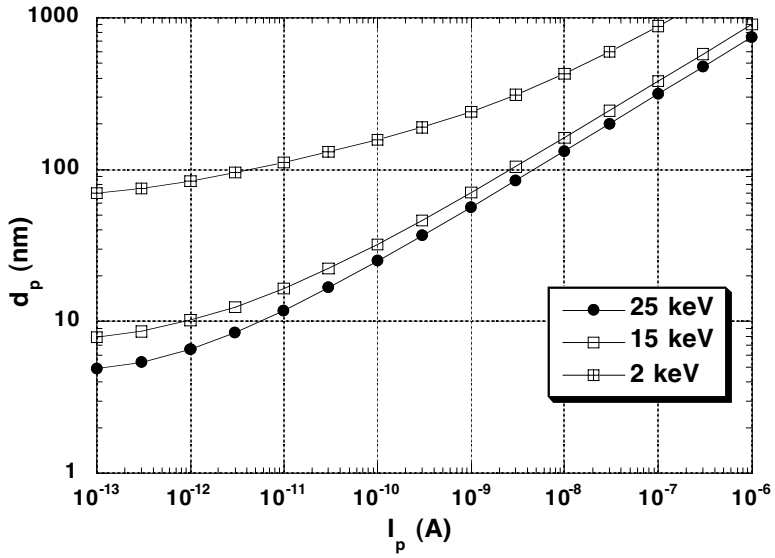

Figure 2-4: *Electron probe diameter (d_p) of a W thermionic emitter operating at 2820 K plotted against the probe current (I_p) for three different values of the electron voltage (E). The values of d_p are calculated from the Eq. 2. 10, assuming C_s = 20 mm and C_c = 8 mm.*

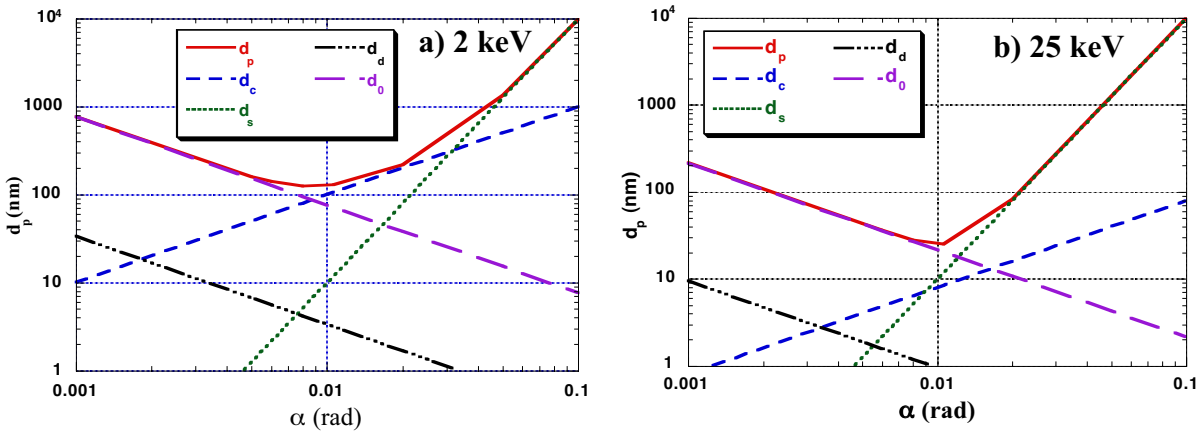

Figure 2-5: *Electron probe diameter as a function of the electron probe aperture for a W filament operating at 2820 K with I_p = 100 pA and E = 2 keV (a) and E = 25 keV (b). The values are calculated using Eq. 2. 11, with C_s = 20 mm and C_c= 8 mm. The minimum theoretical beam diameter is 120 nm at 2 keV and 25 nm at 25 keV.*

The term C_0 contains the electron current, therefore the maximum possible current for a probe diameter $d_{p,min}$ is obtained by solving Eq. 2. 12 for I_p using Eq. 2. 6

$$I_p = \frac{3\pi^2}{16}\beta C_s^{-\frac{2}{3}} d_{p,min}^{\frac{8}{3}}, \quad (2.13)$$

which in case of constant value of C_s gives the relation between current and probe diameter for thermionic electron guns:

$$d_p \propto I_p^{0.375} \quad (2.14)$$

In reality the optimum angle α is fixed by the final aperture. Thus, Eq. 2. 11 defines one optimum current for which Eqs. 2. 12 and 2. 13 are true. For all other currents the aperture is not optimized and the beam diameter (spot size) is larger than given in Eq. 2. 10. Therefore an experimental determination of the real focal beam diameter has been carried out and the results discussed are the following sections.

2.5 MEASUREMENTS OF PROBE SIZE AND DISTRIBUTION

A knowledge of the electron probe size and distribution is important to investigate the mechanism of EBID. There is no way of measuring these parameters directly but an estimation can be obtained making use of two indirect methods: resolution standard imaging and measurement of the diameter of EBID dots deposited with short exposure time.

2.5.1 RESOLUTION STANDARD IMAGING

In SEMs the resolving power, i.e. the resolution (smallest measurable distance between two objects), is related to the probe size. The simplest and quickest method to measure the resolution consists in imaging a commercial resolution standard, in general Au particles deposited on carbon. This method does not allow an absolute measurement of the beam size since the resolving power of a SEM varies from specimen to specimen and it depends not only on the interaction between the sample and the electron beam, but also on the secondary emission from the sample which is used to form the image. In addition, the quality of the measurements depends on the operator and the definition of resolution itself is not absolute. Nevertheless, these measurements are useful for an estimation of the beam size and distribution.

In this work the SEM resolution is defined as the shortest measurable distance between two gold particles on a Au on C resolution standard (Agar ltd., UK). Such distance is measured from digital SEM images using the commercial software Digital Micrograph (Gatan, USA). The measured resolution values (*dR*) of the SEM Cambridge S100 (measured at 25 keV) are plotted as a function of the probe current in Fig. 2-9. The measurements show good agreement with the theoretical values of the probe diameter calculated with Eq. 2. 14 and reported in Fig. 2-4.

The measured resolution values can also be used for an estimation of the electron beam distribution. If a Gaussian distribution is assumed, the electron beam current density *j(x,y)* has the form:

$$j(x,y) = \frac{I_p}{2\pi\sigma^2} e^{-\frac{x^2+y^2}{2\sigma^2}} = j_0 e^{-\frac{x^2+y^2}{2\sigma^2}} \qquad (2.15)$$

where I_p represents the total electron probe current (number of electrons per second), j_0 the peak current density, σ the width parameter (half width at $1/\sqrt{e}$) and $1/2\pi\sigma^2$ the normalization constant. According to the Rayleigh criterion [1] two points at a distance dR apart are resolved if their current distributions *j(r)* overlap at half their separation with an intensity drop of 75% (Fig. 2-6).

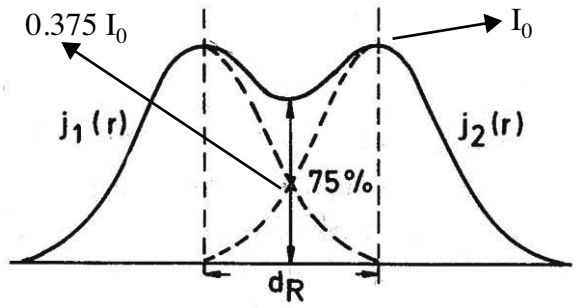

Figure 2-6: *Definition of resolving power (dR) according to the Rayleigh criterion [1].*

Solving Eq. 2. 15 (for $I_p = 0.375\ I_0$, $x = dR/2$ and $y = 0$) gives σ as a function of *dR*:

$$\sigma = (0.356)dR\,. \qquad (2.16)$$

The measured values of *dR*, the calculated values of σ and of the beam width at $1/e$ and $1/e^2$ of the maximum for different values of the electron current (acceleration voltage 25 kV), measured with an accuracy of ±20%, are reported in Table 2-2.

Measurements of dR allow calculation of σ for different electron currents. Substitution of the calculated width parameters in Eq. 2. 15 (with $y = 0$) gives the radial electron density for an electron beam following a Gauss distribution. The Gaussian distributions for the electron beam of the SEM Cambridge S100 at 5 pA, 25 pA, 100 pA and 500 pA are shown in Fig. 2-7.

I_p (pA)	dR(nm)	σ (nm)	w(1/e)(nm)	w(1/e^2)(nm)	d_{1000e}(nm)	d_{1e}(nm)
5	7	2.5	7.1	10	9	13
25	14	5	14.1	20	18	26
100	25	9.1	25.7	36.4	35	48
500	40	14.2	40.2	56.8	56	77

Table 2-2: *Measured resolution (dR), width (w) at 1/√e, 1/e, 1/e^2 of the Gaussian distribution for the electron beam of the microscope Cambridge S100 at different electron currents (acceleration voltage 25 keV). Values obtained by imaging a resolution standard (Au particles on C). d_{xe}: distance from the peak value to which x electrons are found.*

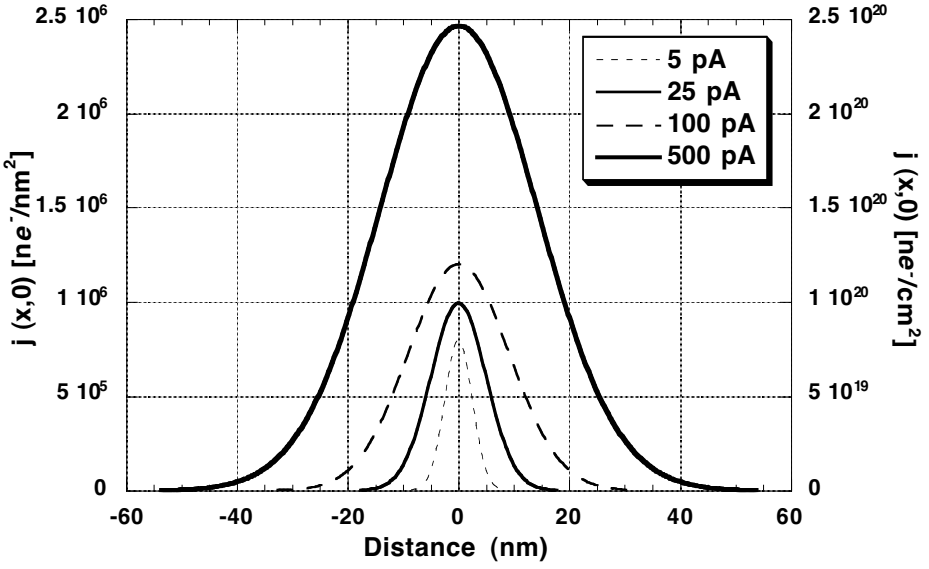

Figure 2-7: *Radial electron densities for a Gauss distribution, as calculated from resolution standard measurements, for four different electron currents with an electron energy of 25 keV, for the electron microscope Cambridge S100.*

2.5.2 SHORT TIME EBID

EBID experiment can also be used for an estimation of the beam size, as already shown by other authors [3]. The method applied here consists in measuring the diameter of EBID dots deposited at very short exposure times (3 s-0.05 s) from DF TEM images and contrast profiles. The values refer to dots deposited on 20 nm thick carbon foil (carbon TEM grid), to minimize the effect of secondary and backscattered emission from the substrate. The experiment will be discussed in detail in Chapter 7.

The measurements show that the smallest obtained dot diameter is about 100 nm. This value is higher than expected for the electron beam distribution calculated from resolution measurements. For example, at I_p = 25 pA the electron density drops to less than one percent at a distance of 25 nm from the peak of the distribution (as shown in Fig. 2-7 and in Table 2-2); this means that a deposit with a diameter of around 50 nm is expected. The experimental results indicate therefore that the beam distribution is different than that calculated from the resolution measurements. The real beam distribution at the surface can be evaluated from the contrast profiles in DF TEM pictures of the short time deposits. These contrast profiles have a close to Gaussian shape, with a deviation in the zone around the center of the beam. Gaussian fitting of profiles measured on deposit carried out at different currents allows to obtain the width parameter of the beam distribution. The values of the width parameter, for I_p = 1000 pA, I_p = 330 pA, I_p = 110 pA, I_p = 25 pA are listed in Table 2-3. These values are used to plot the electron beam density (using Eq. 2. 15) reported in Fig. 2-8.

I_p (pA)	σ (nm)	w(1/e)(nm)	w(1/e^2)(nm)	d_{1000e}(nm)	d_{100e}(nm)	d_{1e}(nm)
25	42±20	60±20	84±20	100	132	180
110	67±20	95±20	134±20	170	227	300
330	116±20	165±20	233±20	300	385	520
1000	173±20	245±20	346±20	470	585	> 600

Table 2-3: *Width (w) at 1/√e, 1/e and 1/e^2 of the Gauss distribution for the electron microscope Cambridge S100 at different electron currents (acceleration voltage 25 keV). The values have been calculated from the diameter and the DF contrast profiles of EBID dots. d_{xe}: distance from the peak value to which x electrons are found.*

The values listed in Table 2-3 (width at 1/e) are plotted versus the probe current in Fig. 2-9, together with the theoretical values calculated from Eq. 2. 10 and the measured resolution dR. The graph shows that the deposit diameter increases as $I_p^{0.366}$. This value is very close to the theoretical value $I^{0.375}$ expected for the increase of the beam diameter (Eq. 2. 14) and found for the plotted resolution values (*dR*). The result indicate that the diameter of the deposits depends on the probe current with the same law as the beam diameter. The beam diameters are about a factor 8 higher than the measured resolution values. This can be explained by the fact that the Rayleigh criterion does not take into account the base width of the Gauss function, by mechanical instability of the microscope during deposition and by aberration or astigmatism errors. The last are more probable in deposition experiments than in resolution standard imaging due to major difficulties in focusing and astigmatism adjusting.

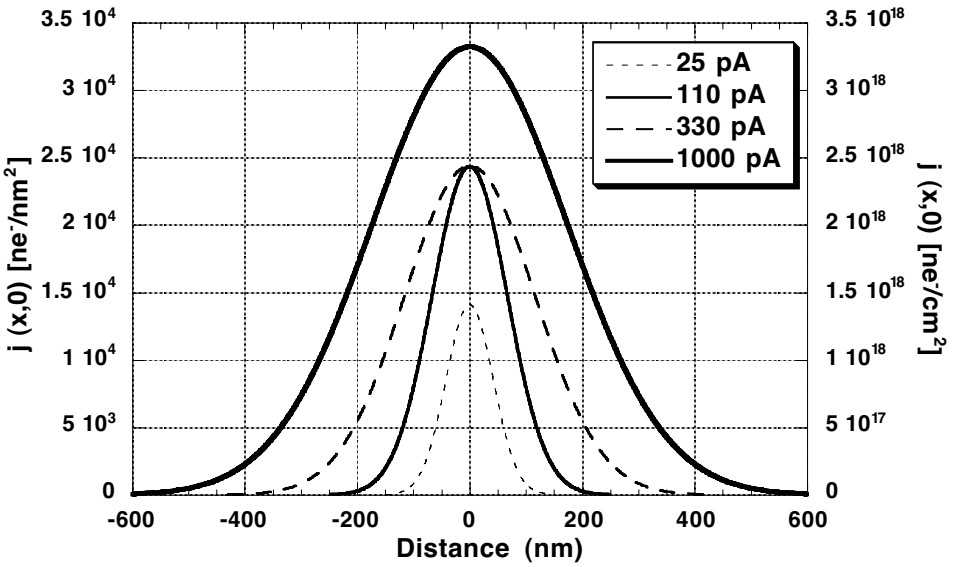

Figure 2-8: *Radial electron densities for a Gauss distribution, as calculated from DF contrast profiles of EBID dots deposited with the electron microscope Cambridge S100 at four different electron currents, with an electron energy of 25 keV.*

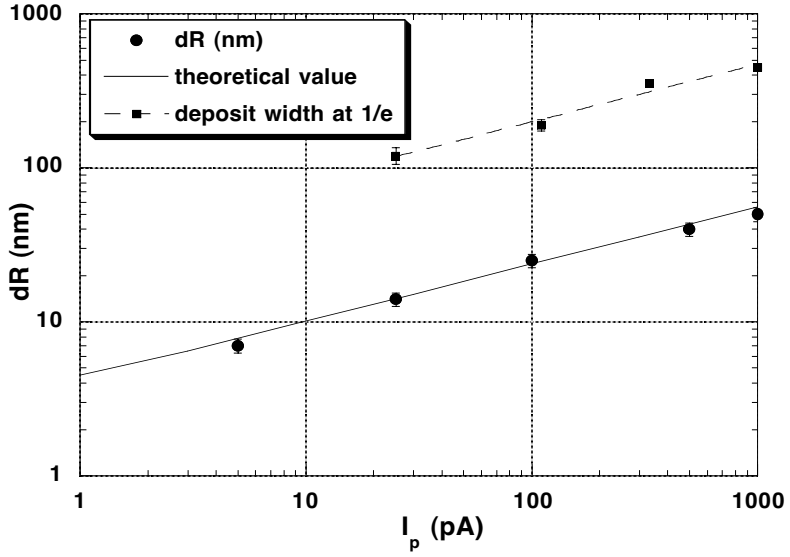

Figure 2-9: *Resolution (dR) and diameter of EBID dots (E=25 keV, 1 second exposure time). versus probe current (I_p) for the SEM Cambridge S100, measured at E=25 keV. The data are in good agreement with the theoretical results obtained from Eq. 2. 10.*

2.6 CONCLUSIONS

The diameter of a focused electron beam increases with decreasing electron energy and increasing probe current. The final value of the probe diameter is affected by the contribution of the lens aberration. The beam size and distribution for the SEM used in this work, have been measured, with two different experimental techniques: resolution standard imaging and short time EBID. In both cases the values increase with the electron current with the power law expected from theory. The electron beam diameter measured with short time EBID is a factor of eight higher than that measured from resolution standard imaging and gives a better estimation of the real probe size.

2.7 REFERENCES

[1] L. Reimer; *Scanning Electron Microscopy*; Springer, 1998.

[2] S. Flegler, J.W.J. Heckman, K.L. Klomparens; *Scanning and Transmission Electron Microscopy, an Introduction*; Oxford University Press, 1993.

[3] M. Weber, H.W.P. Koops, W. Gortz; *Scanning probe microscopy of deposits employed to image the current-density distribution of electron beams*; J. Vac. Sci. Technol. B, 10 (1992); p. 3116-3119.

CHAPTER 3 *Physical and chemical properties of precursor molecules*

After having presented the different CVD precursor families and their suitability, the selection criteria for the EBID precursor used in this work, di-eta-chloro tetrakis (phosphorous trifluoride) di-Rhodium [$RhCl(PF_3)_2]_2$, are discussed. Further on the chemical and physical properties of the compounds are presented. In particular, I focus on vapor pressure, mass spectrometry and residence time measurements, which give information on the volatility, the electron beam induced decomposition and the surface reactivity of the compound. Finally, an approximate model for calculation of precursor flow through capillary tubes is presented.

3.1 PRECURSORS FOR CHEMICAL VAPOR DEPOSITION (CVD) OF METALS

In order to be appropriate for use in CVD techniques, and in particular in EBID, the precursor molecules should fulfil the following requirements [1].

1. Volatility: the precursor should be easy to handle (ideally solid or liquid) and sufficiently volatile to vaporize at room temperature (vapor pressure >1 Pa).

2. Reactivity: the precursor should react under electron bombardment to give the pure material and highly volatile byproducts.

3. Synthesis: the synthesis should involve as few steps as possible.

4. Purity: the resulting deposit is required to be clean and free of contaminants.

5. Environment and cost: it is advisable that precursors be non-toxic and recyclable; the price must be as low as possible.

The volatility of a molecule depends on its charge, polarity and size. Ionic and polar molecules tend to be less volatile due to the presence of electrostatic forces. Larger molecules are in general polarizable and hence less volatile. On the other hand, in some cases, bulky groups can enhance volatility since they minimize intermolecular interaction by steric hindrance. Finally, the introduction of a $-CF_3$ group can increase the volatility of the precursor [1]. At present, the precursors for metal Chemical Vapor Deposition (CVD) techniques can be grouped in seven

families [2]: metal halides, metal alkyls, complexes with unsaturated organic ligands, metal ß-diketonates, metal alcoxides, metal carbonyls, metal trifluorophosphines.

Metal halides contain neither carbon nor oxygen, therefore they would be particularly suitable for EBID of metals. WCl_6 and WF_6 have already been used for EBID [3] [4-7]. Nevertheless volatile halides are available only for a limited number of metals, examples are $SiCl_4$, VCl_4, $TiCl_4$, MoF_6, ReF_6, WF_6, WCl_6, $AlCl_3$. If the oxidation number of the metal is smaller than the coordination number, oligomerization can occur (e.g. by bridging of halogen ligands), which leads to a decrease of volatility. Another inconvenience of these compounds is their high toxicity. In addition, some metal halides are gaseous and therefore difficult to handle.

Metal alkyls are not interesting for EBID of metals since in general they give carbon contaminated deposits. Also, they are often pyrophoric, explode on contact with water and are toxic.

Complexes with unsaturated organic ligands include alkene and alkyne adducts, metal allyls, η^5–cyclopentadienyl, η^6–arene and related complexes. The only precursor of this family used for EBID is Me_3PtCp (Trimethyl-cyclopentadienyl platinum). This precursor has already given platinum containing deposits with a high carbon contamination [8-10]. The carbon contamination is due to the stability of the M-C bond [2].

Metal ß-diketonates (or acetyl-acetonates) have the advantage that in general they have high vapor pressure. On the other hand they do not decompose to pure metals below 300°C. These complexes can be easily synthesized by adding an aqueous solution of a metallic salt to an aqueous solution of the protonated ligand in the presence of a buffer [11]. EBID deposits obtained with these precursors are possible but show high carbon and oxygen contamination. EBID has been already obtained with Dimethyl gold (β-diketonates) [12-14] and Cu [15] ß-diketonates.

Metal carbonyl (CO) and trifluorophosphine present several analogies: they are iso-electronic and stabilize metals in low oxidation states, via back bonding from the ligand to the metal; some complexes of the ligands are even iso-structural and can be obtained by substitution of one ligand by the other.

Metal carbonyls (CO) are in principle not suitable for EBID of pure metals since carbon and oxygen contamination is expected. In addition, many carbonyls are toxic. Nevertheless, because of their high volatility, these compound have been extensively used for EBID. Depositions have already been achieved from $Fe(CO)_5$ [16], $Cr(CO)_6$ [17], $Re_2(CO)_{10}$ [17], $W(CO)_6$ [18, 19] [20] [21], $Mo(CO)_6$ [15], $Ru_3(CO)_{12}$, $Os_3(CO)_{12}$ [22]. In all cases the deposited material contained carbon and oxygen as contaminants.

Metal-trifluorophosphines are potentially very interesting for EBID since they are in general volatile and release highly volatile products on cleavage of the metal-ligand bond. Furthermore, the absence of carbon and oxygen atoms in these precursors can avoid such atoms contaminating the deposit. However, free PF_3 can disproportionate before desorption with the reaction

$$5\ PF_3 \rightarrow 3\ PF_5 + 2P$$

which leads to phosphorous impurities. Another possible source for phosphorous contamination is the reaction of PF_3 on Si substrates to form P and liberate SiF_4 with the reaction:

$$Si + 4\ PF_3 \rightarrow 3\ SiF_4 + 4P.$$

In CVD, complexes with PF_3 have been used to deposit metal films at temperatures between 200 and 300 °C. EBID experiments with these precursors have been carried out until now only by our research group [23] [24] [25].

3.2 SELECTED PRECURSORS

The principal aims of this work are:

- deposition of high metal content structures
- structural and chemical characterization of the deposits
- better understanding of the deposition mechanism.

Deposition of high metal content structures can be more easily achieved for metals which do not form stable oxides, nitrides and carbides, namely Rh, Au, Pt, Ir, Pd. In addition, to minimize contamination, carbon- and oxygen-free precursors should be used. Among the metals listed above, the ones for which high volatile precursors are available are Rh and Au. These precursors are di-μ-chloro-tetrakis-trifluorophosphine-di-Rhodium, $[RhCl(PF_3)_2]_2$ and chloro-trifluorophosphine-gold, $AuCl(PF_3)$. $AuCl(PF_3)$ gives high metal content structure [24]; $[RhCl(PF_3)_2]_2$ is more chemically stable in air, in vacuum and less reactive on metal surfaces. In addition it is easier to synthesize and handle and less expensive. Therefore $[RhCl(PF_3)_2]_2$ is the selected precursor for EBID performed in this work.

The chemical stability of $[RhCl(PF_3)_2]_2$ allows to experiment on a long time scale, which means the possibility to deposit high aspect ratio structures. The low cost and the simplicity of the synthesis make the product available in large quantities for a high number of experiments, needed for mechanism investigation and chemical and structural analysis. Moreover Rh deposition is interesting since the metal has a good combination of electrical and mechanical properties and is stable to oxidation and corrosion. A more detailed description of the physical and chemical properties of Rh is presented in the Appendix (Section I.1).

$[RhCl(PF_3)_2]_2$ is a red powder at room temperature. It has been known as a volatile precursor for Rh deposition since 1971 [26]. This precursor gives high Rh content deposits by thermal CVD at 200 °C, with a small chlorine contamination [27] and has also been used for direct patterning of conductive structures in a STM [28].

The compound used for our experiments has been synthesized by P. Doppelt's group at the Ecole Superieure de Physique et Chimie Industrielle (ESPCI) in Paris, following a procedure described in the literature [26]. For comparison some deposits have also been carried out from the commercial precursors di-μ-chloro tetracarbonyldirhodium, $[RhCl(CO)_2]_2$ (Fluka, 36065) and dimethyl gold trifluoro-acetyl-acetonate $[Me_2Au(tfa)]$. Some properties of the above-mentioned precursors are reported in Table 3-1. The vapor pressures (when not taken from the literature) have been measured by means of an experimental set-up, described in the Appendix (Section I.2).

Chemical formula	M ($gmol^{-1}$)	P_{vap} (Pa)	Metal content (at.%)	n_{ox} of metal	Physical status	CAS Number
$Cl_2F_{12}P_4Rh_2$	628.59	7.47	10	+1	solid (red powder)	14876-98-3
$C_4Cl_2O_4Rh_2$	388.76	0.25	20	+1	solid (red powder)	14404-25-2
$C_7H_{10}O_2F_3Au$	380.11	7.11	4.3	+3	solid (white powder)	63470-53-1

Table 3-1: *Properties of the selected EBID precursors. M: molecular weight; P_{vap}: vapor pressure; n_{ox}: oxidation number; CAS: Chemical Abstract System. The vapor pressure value for $C_4Cl_2O_4Rh_2$ is taken from the literature [29].*

The structure of $[RhCl(PF_3)_2]_2$ is reported in Fig. 3-1[1]. The molecule basically consists of two $RhCl_2(PF_3)_2$ planes with a dihedral angle of 113.54°. The Rh-Rh distance of 2.9709 Å is shorter than in the iso-structural compound $[RhCl(CO)_2]_2$ [30]. The (PF_3) ligands are oriented toward the central axis of the dimer so that the P-F contacts are minimized. As a consequence, the Rh atom is 0.14 Å out of the main plane formed by the four ligands. The Rh-P distance is 2.12 Å, shorter than in other Rh complexes containing phosphine ligands because of strong back bonding to the PF_3 ligand. The square planar geometry of Rh in the complex $[RhCl(PF_3)_2]_2$ is typical of metal ions having a d^8 configuration, and according to Pauling's theory it can be explained with a dsp^2 hybridization of the Rh orbitals. Such complexes are an exception to the 18 electron rule and obey the 16 electron rule (eight electron from the metal, eight from the ligands) [31].

3.3 VAPOR PRESSURE MEASUREMENTS

Vapor pressure measurements for the precursors tetrakis-trifluorophosphine-dichloro-dirhodium $[RhCl(PF_3)_2]_2$ and dimethyl-gold-trifluoroacetylacetonate $Me_2Au(tfa)$ have been carried out with a set-up constructed in our laboratory during this thesis work [32]. For $[RhCl(CO)_2]_2$

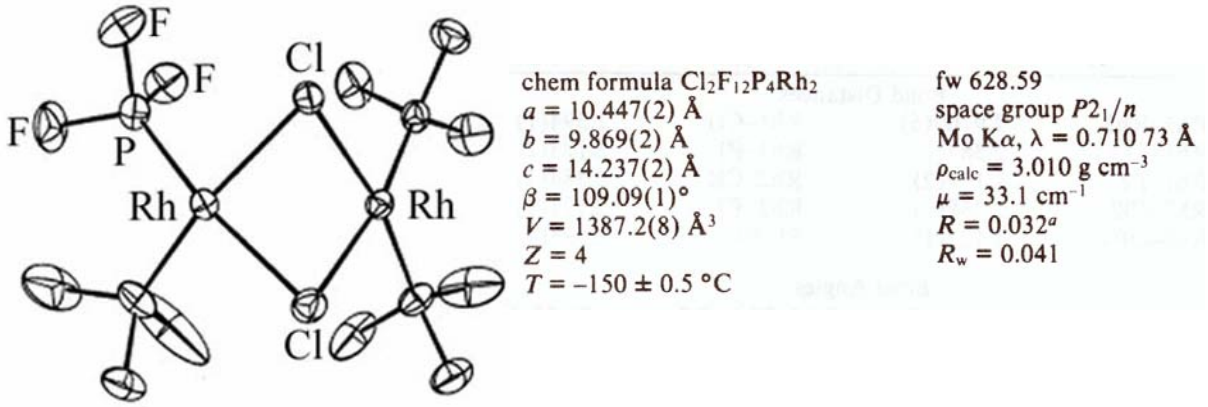

Figure 3-1: *Molecular structure and crystallographic data for $[RhCl(PF_3)_2]_2$ measured at -150 °C [1].*

vapor pressure data are available from the literature. The experimental set-up is described in the Appendix (Section I.2).

Measurements of the background pressure in the vacuum system at room temperature resulted in a stabilized constant pressure of 0.3±0.15 Pa. The statistical fluctuation corresponding to the smallest measurable value of the pressure gauge controller. The measurement of vapor pressures larger than 1Pa is, therefore, reasonably reliable. Precursor loading is carried out in a dry nitrogen purged glove box to reduce contact with air and water. After mounting onto the vacuum system, the precursor container is evacuated to a rough vacuum. Further evacuation is carried out by applying several freeze-pump-thaw cycles. To guarantee the purity of the precursor, several measurements are collected for each load until reproducible pressure values are obtained. The acquisition time ranges from 2000 to 8000 seconds. At the end of each measurement, the whole measuring volume, except the cooled container, is evacuated to about 10^{-5} Pa. At least three consecutive measurements have been carried out at each temperature. All measurements show good reproducibility.

Since the temperatures of the pressure gauge and the precursor container are different, the measured vapor pressure values are influenced by the thermal transpiration effect [33]. The detected pressures are therefore corrected to the temperature of the precursor compounds with an empirical thermal transpiration correction factor [34] [35]. The corrections are always 5% smaller than the measured values, thus resulting in a smaller than 5% correction of the sublimation and evaporation enthalpy.

The mean value of the vapor pressure of the compounds at each temperature are represented in the logarithmic pressure (in Pa) against *1/T(K)* plot. The error bars on the ordinate (pressure) indicate two times the standard deviation, whereas the error bars for the abscissa are smaller than the symbols. The data have been fitted to an integrated form of the Clausius-Clapeyron equation:

$$log P_{vap} = A + \frac{B}{T}. \quad (3.1)$$

The fitting has been weighted by the ratio of the standard deviation to the mean value. The errors for the fitting constants *A* and *B* indicate the standard error for the fitting calculation.

With a negligible condensed phase molar volume compared to the gas-phase molar volume and by applying the ideal gas law, the sublimation or evaporation enthalpy, ΔH_s, of solids or liquids can be obtained as follows:

$$\Delta H_s = -R\frac{d\,ln P_{vap}}{d(1/T)} = -2.303RB \quad (3.2)$$

where R (J/moleK) is the gas constant and B(K) is the fitting constant for the Clausius-Clapeyron equation [36]. The error for ΔH_s is derived from the error for the fitting constant, B.

3.3.1 MEASUREMENTS OF $[RhCl(PF_3)_2]_2$

The vapor pressure of $[RhCl(PF_3)_2]_2$ measured between 23ºC and 0.5ºC is shown in Fig. 3-2. The values measured by us are higher than those previously determined using an infrared transmission detection method and assuming that the optical absorption cross sections for both free PF_3 and PF_3 ligands are the same. The calculated enthalpy of sublimation of $[RhCl(PF_3)_2]_2$ is 90.8 kJ/mole, obtained from the Clausius-Clapeyron equation with the determined fitting values (listed in Table 3-2). No pressure increase with time have been observed during the measurements.

3.3.2 MEASUREMENTS OF $Me_2Au(tfa)$

Figure 3-3 shows the vapor pressure values of $Me_2Au(tfa)$ measured from 283.6 K (10.4ºC) to 297.0 K (23.8ºC). The calculated sublimation enthalpy of the compound is 81.7 kJ/mole (as reported in Table 3-2).

A color change of the solid precursor, and a blue violet deposit on the Cu gasket, exposed to the precursor vapor at room temperature, were observed. X-ray photoelectron spectroscopic analysis (XPS) of the latter deposit detected beside Cu the presence of Au, C and F. During the vapor pressure measurement a continuous pressure increase (between 3 x $10^{-4}$and 6 x 10^{-4} Pa per second) was detected. According to XPS results, the pressure increase could be a consequence of a Cu surface catalyzed decomposition of the precursor compound. Assuming the precursor has a constant vapor pressure of 7.1 Pa at 296 K (23ºC), the measured rate of decomposition corresponds to about 1% of precursor decomposed in three minutes.

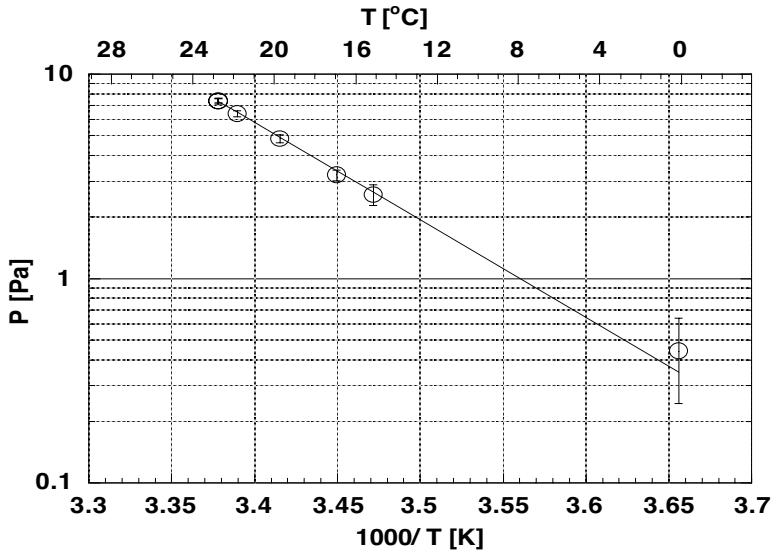

Figure 3-2: *Vapor pressure of $[RhCl(PF_3)_2]_2$, in the logP versus 1/T plot.*

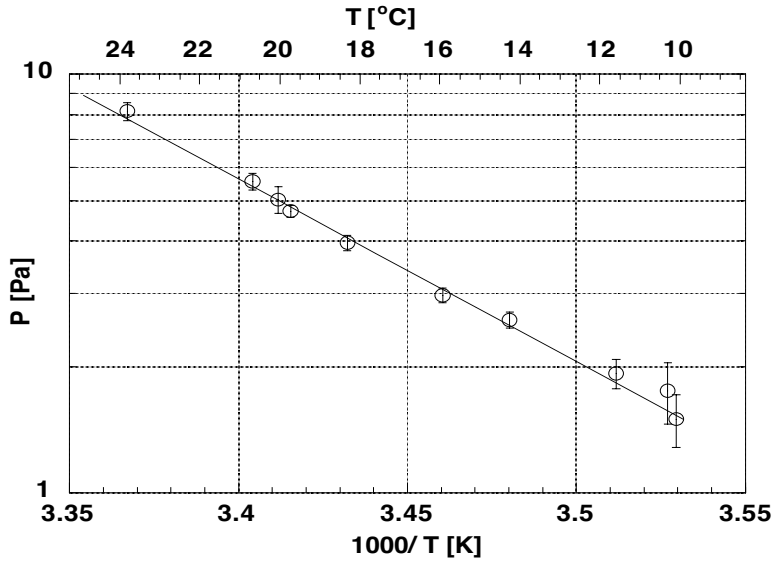

Figure 3-3: *Vapor pressure of $Me_2Au(tfa)$ in the logP versus 1/T plot.*

3.4 MASS SPECTROMETRY (MS)

Electron ionization mass spectrometry of $[RhCl(PF_3)_2]_2$ is useful to understand the fragmentation process of the compound under electron bombardment. The mass spectrum of $[RhCl(PF_3)_2]_2$ is not available from the literature, therefore the measurements have been

Compound	A	B	R	ΔH_s (kJ mol^{-1})	P at 23°C (Pa)
$[RhCl(PF_3)_2]_2$	16.9±0.41	-4757±121.5	0.998	90.8±2.3	7.47
$Me_2Au(tfa)$	13±0.37	-3559±105.2	0.997	81.7±2.0	7.11

Table 3-2: *Fitting constants, A and B, correlation coefficient R, sublimation enthalphy (ΔH_s), and the fitted vapor pressure value at 23°C for $Me_2Au(tfa)$ and $[RhCl(PF_3)_2]_2$.*

performed in our laboratory. Before these measurements the only available information about the mass spectrum of $[RhCl(PF_3)_2]_2$ was that the molecular peak and the peaks with consecutive PF_3 loss are observed [26]. The experimental set-up, designed and constructed during this work, is described in the Appendix (Section I.3).

3.4.1 MASS SPECTRUM OF $[RhCl(PF_3)_2]_2$

Mass spectra have been acquired at 10, 30 and 70 eV electron energies, with an electron current of 4.4 mA, at the pressures of 1.0 x 10^{-4} Pa (8 x 10^{-7} Torr) and 2 x 10^{-4} Pa (1.5 x 10^{-6} Torr). The highest fragmentation efficiency has been observed at 70 keV. The spectra acquired with different electron energy show the same relative peak intensity. No effect on the fragmentation has been detected increasing the precursor pressure.

The principal MS peaks have been found at the mass numbers of 50, 69, 88 and 103. These masses correspond to the ions P^+, PF_2^+, PF_3^+ and Rh^+. The ratios between the main peaks are roughly the same in the spectra measured at different energy, i.e: $PF_2^+ : PF_3^+ \approx 0.5$; $PF_2^+ : P^+ \approx 0.065$ and $PF_2^+ : Rh^+ \approx 0.02$. The mass numbers of the molecular fragments and the intensities of the peaks are reported in Table I-2 (Appendix). The intensities of the peaks are normalized at the intensity of the peak at 69 amu. The mass spectrum of $[RhCl(PF_3)_2]_2$ with the estimated fragmentation structure, acquired with an ionization energy of 70 eV and a precursor pressure of 1.5x10^{-6} Torr, is shown in Fig. 3-4 for m/z > 100.

Below 100 amu (not shown), the peaks of the ions P^+ (31), Cl^+ (35), F_2^+(38), are clearly detected. The highest peaks are measured at 69 amu (PF_2^+) and at 88 amu (PF_3^+), as already found by other authors for the spectrum of free PF_3 [37]. Furthermore, the single Rh^+ peak appears at mass 103 with a large yield. The mother peak is clearly observed at the mass 628 together with its isotopic peaks 630 and 632, due to the presence of two chlorine atoms. The peaks with consecutive loss of PF_3 from the molecular peak have been observed with increasing intensity in the order: $(PF_3)_3Rh_2Cl_2^+$, $(PF_3)_2Rh_2Cl_2^+$, $(PF_3)Rh_2Cl_2^+$ and $Rh_2Cl_2^+$. Beside these peaks, the peaks with the loss of one F atom, $(PF_2)(PF_3)_2Rh_2Cl_2^+$ and $(PF_2)(PF_3)Rh_2Cl_2^+$, have been observed. The peak at 345 amu could belong to $(PF_2)Rh_2Cl_2^+$ or to $(PF_2)_3RhCl^+$. Most of the high intensity peaks at m/z > 200, contain two Rh atoms connected by either one or

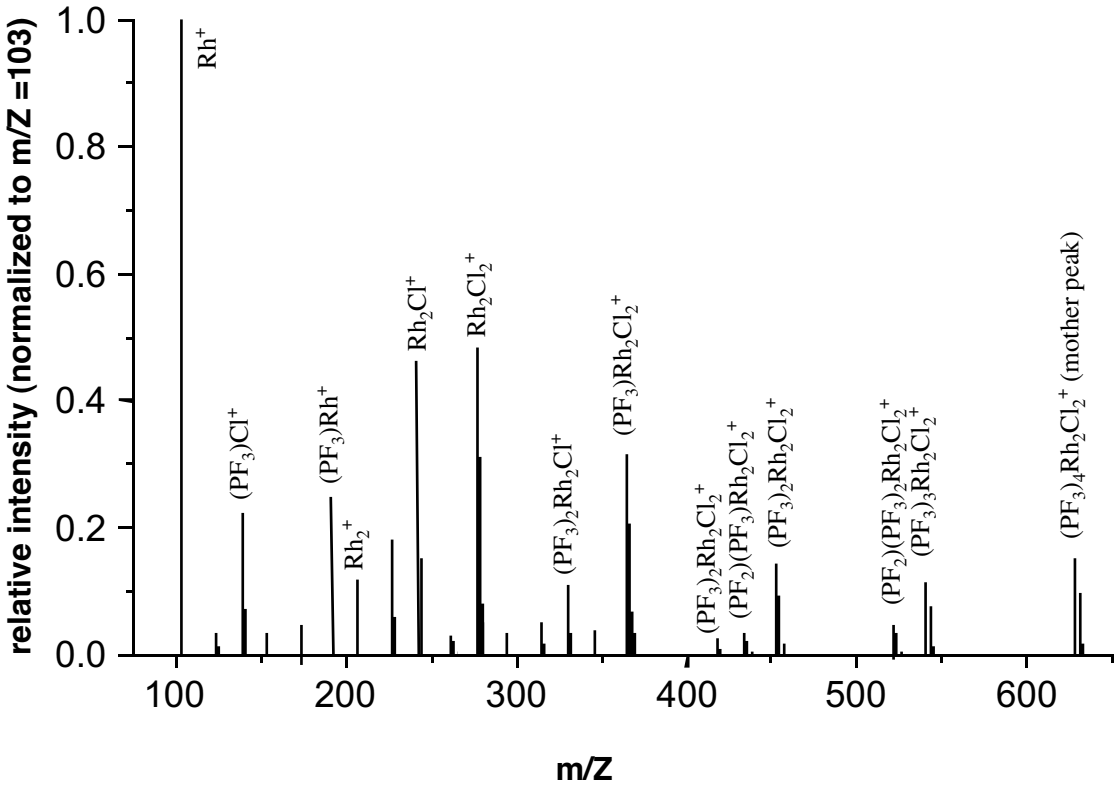

Figure 3-4: *Typical mass spectrum of $[RhCl(PF_3)_2]_2$, for m/Z > 100, with the estimated fragmentation structure. The spectrum has been acquired at 70 eV electron energy. The precursor pressure during the acquisition was $1.5x10^{-6}$ Torr.*

two bridge Cl atoms. Furthermore, at mass 314, the monomer of the molecule, $(PF_3)_2RhCl^+$ is observed as a minor peak.

The MS results prove that the decomposition of $[RhCl(PF_3)_2]_2$ starts with loss of a PF_3 group. Possible further loss of one more PF_3 indicates a weak Rh-P bond. The low intensity of the monomer peak indicate the strength of the Rh-Cl bond. Atomic F loss from PF_3 groups is monitored from the peaks, $(PF_2)_3Rh_2Cl_2^+$, $(PF_2)_2Rh_2Cl_2^+$ and $(PF_2)Rh_2Cl_2^+$, and it seems to occur after loss of one or two PF_3. The presence of an intense Rh^+ peak is an indication of the suitability of the precursor for high content Rh EBID. It can be concluded that the obtained mass spectrum allows to predict a high Rh content EBID deposit with Cl contamination.

The result of the mass spectra are confirmed by Density Functional Theory (DFT) calculations on the decomposition path of $[RhCl(PF_3)_2]_2$, carried out by the group of Prof. Weber at the university of Geneva. The calculations revealed that the removal of a PF_3 group from the molecule requires 45-50 Kcal mol^{-1} and that there is no effect of the number of previously removed PF_3 groups on the energy needed for the elimination of other PF_3 groups. This is

confirmed by the comparable intensity of the peaks of the species generated by successive loss of PF_3 groups. The calculations revealed also that no alternative path at lower energy exist for decomposition of the molecule. The energy required for the possible decomposition paths are listed in Table 3-3.

Reaction	E (Kcal/mol)	E (eV)
Single PF_3 removal from $[RhCl(PF_3)_2]_2$	44	1.9
F_2 removal from PF_3 in $[RhCl(PF_3)_2]_2$	215	9.9
free $PF_3 \rightarrow PF+F_2$	132	6.4
F removal from two PF_3 in$[RhCl(PF_3)_2]_2$ followed by F_2 formation	190	9.2

Table 3-3: *Energy of different decomposition paths for the molecule $[RhCl(PF_3)_2]_2$.*

However the processes involved in EBID are more complicated than simple gas phase ionization and can lead to different decomposition path and make possible re-arrangements of the ionized or decomposed species at the surface.

A similar MS spectrum is found in the literature [38] for the iso structural precursor $[RhCl(CO)_2]_2$. The mass spectrum of $[RhCl(CO)_2]_2$ is reported in Fig. 3-5; a lower number of fragments is present compared to $[RhCl(PF_3)_2]_2$, due to the lower number of atomic species. The most intense peak is found at 28 amu (CO); the Cl peak at 35 amu and the Rh^+ peak at 102 amu is observed. At higher m/z the mother peak and the peaks generated by successive CO losses are observed. This indicates that the decomposition of the molecule occurs for successive loss of CO groups. The comparable intensity of the peaks indicate that there are no effects of the number of previously removed groups on the energy required for the elimination of other CO groups, as found for $[RhCl(PF_3)_2]_2$ with DFT calculations.

3.5 SURFACE RESIDENCE TIME MEASUREMENTS

The chemical reactivity and the adsorption of molecules at the surfaces can be characterized by means of surface residence time and uptake coefficient measurements. The surface residence time (τ_{surf}) is defined as the time a molecule, reversibly adsorbed, spends on a surface before undergoing chemical reaction or desorption. The uptake coefficient (γ_s) is defined as the probability of a colliding molecule undergoing irreversible chemical reaction at the surface.

The knowledge of the parameters mentioned above is of primary importance in EBID. The uptake coefficient of a precursor indicates if the molecule decomposes on contact with metallic surfaces, e.g. on the substrate of capillary tubes used for precursor delivery at the surface or the substrate surface. The residence time allows to determine the activation energy for desorption

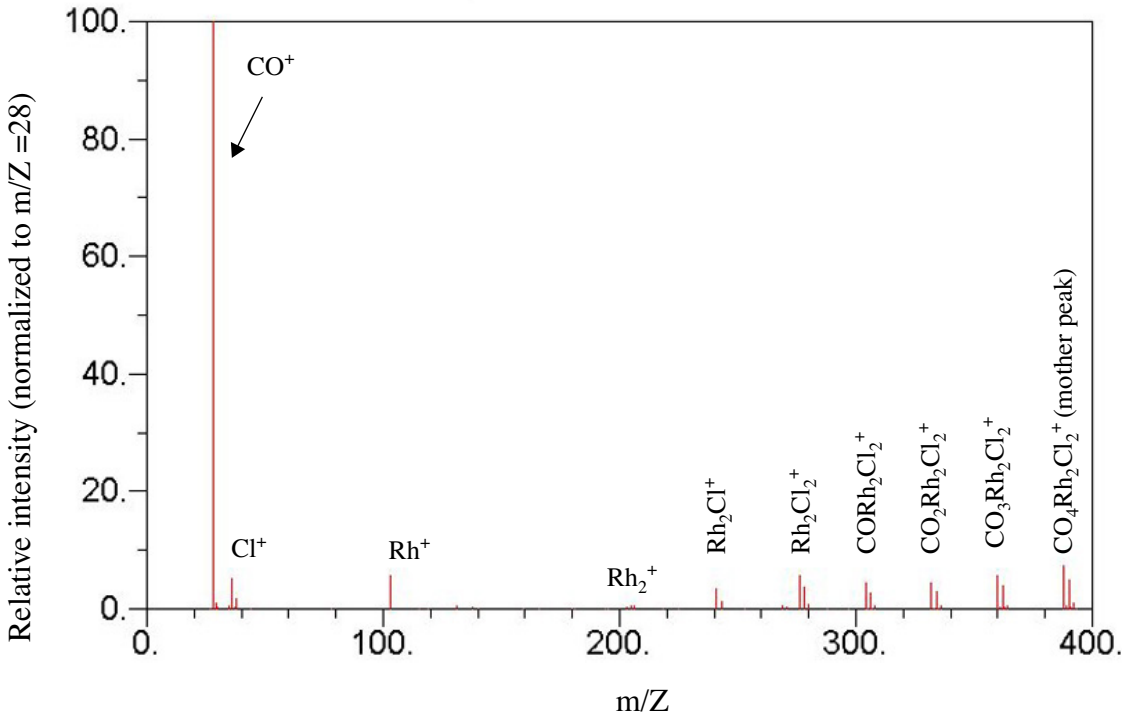

Figure 3-5: *Mass spectrum of $[RhCl(CO)_2]_2$, acquired at 70 eV electron energy* [38].

of the molecule from the surface and to estimate the maximum distance the molecule can travel by surface diffusion before being desorbed.

Surface residence time and uptake coefficient measurements have been carried out with the experimental set-up [39] described in the Appendix (Section I.4).

Residence time measurements consist on measuring the arrival time of a molecule diffusing across a a tube under molecular flow conditions. This arrival time is equal to the inverse of the decay constant (k) of the time dependent MS signal. It is determined by fitting the measured signal to a single exponential decay function in the case of non-reactive molecule-substrate interaction:

$$s = s_0 e^{-kt} \quad therefore \quad t_{arrival} = \frac{1}{k}. \tag{3.3}$$

Since the experiment operates in molecular flow conditions, the number of collisions inside the reactor tube depends only on the mass and temperature of the gas injected and on the geometry of the tube. The average surface residence time of a molecule τ_{surf} can be calculated directly by subtracting from the measured value the arrival time of an ideal system and dividing by the total number of collisions on the inner tube wall Z:

$$\tau_{surf} = \frac{1/(k_{interactive}) - 1/(k_{ideal})}{Z}. \quad (3.4)$$

An ideal system must be non-sticky and non-reactive. Stickiness and reactivity are expressed respectively by the residence time τ_{surf} and the uptake coefficient γ_s. Therefore k_{ideal} is measured on reference tubes with $\tau_{surf} = 0$ and $\gamma_s = 0$. The number of collisions on the inner tube wall Z is computed numerically by a Monte Carlo simulation.

Whether or not a molecule's behavior is ideal can be verified by measuring the arrival time of several rare gases and plotting the values against the square root of their respective molecular masses. Since the arrival time scales with the inverse of molecular velocity and thus with √M, any deviation of *1/k* from linear relationships of arrival time indicates a gas-surface interaction. The uptake coefficient can be calculated as the ratio between the integrals of the signal of a reference system and that of a reactive system.

However, in many cases experimental arrival times can only be fitted to double exponential or more complex decay, in which case the average surface residence time loses its meaning. The complex decay may be explained by a saturation effect due to a restricted number of reactive surface sites. These sites are rapidly occupied by the molecules interacting first and act as a screen for the molecules colliding later, which reach the detector earlier and give rise to a sharp initial peak in the arrival time trace. In such cases additional parameters are needed to describe gas-surface interactions. The experimental arrival time curves have to be fitted in this case with a Monte Carlo simulation using surface saturation of a given number of sites n_s, the surface residence time τ_{surf} and the uptake coefficient γ_s as fitting parameters. The model used for the Monte Carlo simulation has been described in detail in the literature [40]. It is based on the assumption that a molecule reaching a surface with a free surface site has the probability γ_{MC} to react and a probability $1-\gamma_{MC}$ to stick to the site for a time τ_s before desorbing. When the molecule reaches an occupied site, it undergoes a non-reactive collision and continues on its way looking for a free adsorption site. The tube is divided in 50 sections of equal length each containing the same number of surface sites. As the collision frequency is larger at the top of the tube close to the inlet valve than at its bottom, a gradient of saturation is observed along the tube so that the last few sections of the tube are never totally saturated.

In this work we have carried out residence time and uptake coefficient measurements of $[RhCl(PF_3)_2]_2$ on stainless steel tubes with an internal diameter of 11 mm and a length of 500 mm. The compound has been introduced in the calibrated volume by sublimation from the solid phase, after several freeze-pump-thaw cycles. The pressure in the calibrated volume is defined by the precursor vapor pressure. The number of molecules injected per pulse ranges from 9×10^{14} to about 3×10^{15}, depending on the opening time of the solenoid valve. The signal is detected on the most intense peak of the mass spectrum, at 69 amu.

The MS signal versus time curves for $[RhCl(PF_3)_2]_2$ are shown in Fig. 3-6a. The three curves with increasing maximum correspond to increasing the opening time of the valve. The shape of the curves shows that the arrival time cannot be fitted with a simple exponential decay. There-

fore the signal has been fitted by Monte Carlo simulations as explained above. The comparison between the experimental curve and the simulation is shown in Fig. 3-6b. The gray curve represents the best fit, obtained with the following fitting parameters: $\tau_{surf} = 2\ ms$, $n_s = 12x10^{12} cm^{-2}$, $\gamma_s = 0$. Variation of any fitting parameter worsens the quality of the fitting of decay part of the signal.

The result $\gamma_s = 0$ proves that, on stainless steel surfaces, $[RhCl(PF_3)_2]_2$ does not give chemical reactions but only reversible adsorption. The knowledge of τ_{surf} allows to calculate the activation energy for desorption E_d of $[RhCl(PF_3)_2]_2$ on stainless steel by applying the Frenkel's formula [41]:

$$\tau_0 \approx \tau e^{-\frac{E_d}{RT}} \tag{3.5}$$

where τ_0 is the period of vibration of a molecule at the surface, found to be about 10^{-13} s [41]. Substituting $\tau_{surf}=2\ ms$ and $T=298\ K$, Eq. 3.5 gives $E_d \approx 0.6\ eV$. The residence time is also useful to estimate the distance that molecules adsorbed at surface travel before being desorbed. The distance x a surface boundary travels in a time t, from first Fick's law of diffusion, is

$$x = D_s t \tag{3.6}$$

where D_s is the surface diffusion coefficient of the molecule. The surface diffusion coefficient of $[RhCl(PF_3)_2]$ on stainless steel is not know, nevertheless it is known from the literature that D_s for gases on solids are of the order of 10^{-3}-10^{-4} cm^2s^{-1}[41]. Substituting $D_s = 10^{-4}$ cm^2s^{-1} and $t = 2\ ms$ in Eq. 3.6, we obtain $x \approx 4\mu m$. This value represents a rough estimation of the maximum distance the precursor molecule can travel before being

The measurements presented in this section and the calculations based on them should be looked just as rough estimations, since the experimental data could not be perfectly fitted by Monte Carlo simulations. The dark grey curve reported in figure 3-6b represents the best fit obtained trying different values of τ_{surf} , n_s and γ_s. The reason of the non perfect fitting can be the high molecular weight of $[RhCl(PF_3)_2]_2$ compared to that of the molecules for which the Monte Carlo model has been developed. In addition the pressure in the calibrated volume (vapor pressure of the precursor) is close to the detection limit of the gauge; this can cause large errors in the calculation of the number of injected molecules per pulse. The possibility to improve the quality of the measurements is still under investigation.

3.6 PRECURSOR SUPPLY TO REACTION AREA

In EBID the precursor vapors can be supplied to the substrate area either through a sub-chamber or an oriented tube. A sub-chamber is a metallic box containing the precursor and the substrate. A pin hole on the top of the box allows the electron beam to reach the sample surface. The pressure in the sub-chamber is defined by the vapor pressure of the precursor,

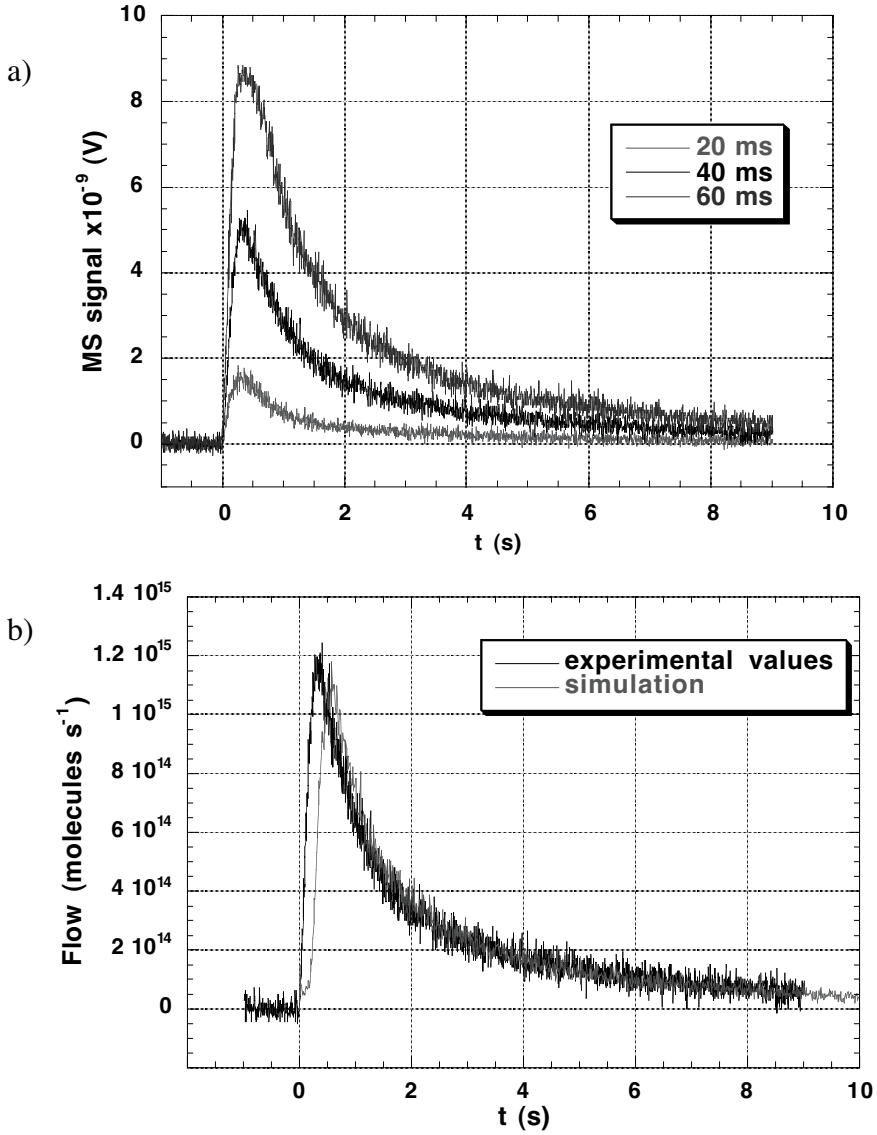

Figure 3-6: *Arrival times of $[RhCl(PF_3)_2]_2$ at different opening times of the pulse valve (a); fitting of the experimental data (40 ms opening time) with a Monte Carlo simulation (b).*

while in the SEM it can be two or three orders of magnitude lower, as required for beam operation. Another possibility is to use a capillary gas feed aimed at the surface in close proximity to the beam to produce a local gas environment. With this option the gas flow can be controlled by choosing the appropriate tube length and diameter. In this work the latter option is used. The gas flow through capillary tubes is described in the following paragraphs.

3.6.1 GAS FLOW THROUGH CAPILLARY TUBES

The transport of a precursor gas through a capillary tube is treated here with the models used in vacuum technology to study the gas flow through tubes of finite length. In this work I use the model of Smith and Lewin [42], developed for tubes of finite length with partially adsorbing walls and based on Monte Carlo simulations. The wall sorption is characterized by the sticking coefficient *s*, defined as the probability, per individual collision, that a particle is permanently adsorbed by the wall. The particles adsorbed and released after a certain time are considered as reflected; time does not explicitly enter in Smith and Lewin's model.

The model allows to determine the probability of transmission of a particle through a tube, the axial distribution of adsorbed molecules on the tube walls and the profile of the emerging beam. The following assumptions have been made in treating the problem

1. The flow is steady, transient phenomena are excluded.

2. Free molecular flow conditions prevail, collisions between particles are negligible.

3. The molecules enter the tube with a uniform distribution; the consequence of this is that the input flux through an aperture of section *A* is given by Eq. 3. 7, where *J* is the impingement rate flux per unit area, *n* the molecular density and υ the mean molecular speed of the particles in the chamber.

$$F_{IN} = JA = n\frac{\upsilon}{4}A\cdot \tag{3.7}$$

4. For each individual collision of a particle with the tube, the probability that the particle is adsorbed by the wall is given by *s* and *(1-s)* is the probability that the particle leaves the wall.

5. Reflection after collision with the tube walls is diffuse, according to the cosine law.

A molecule entering a tube of length *L* and diameter *r* can be backscattered, adsorbed or transmitted. These three options are described by the coefficients: β_S (back-scattering coefficient), γ_S (uptake coefficient) and α_T (transmission coefficient). The coefficients have to satisfy the condition

$$\beta_S + \gamma_S + \alpha_T = 1\,. \tag{3.8}$$

The output flux of a cylindrical tube is given by:

$$F_{OUT} = \alpha_T F_{IN}. \tag{3.9}$$

The transmission probability α_T, reported in Fig. 3-8 as a function of L/R, is also a function of the sticking coefficient s. For instance, for a tube with $L/R = 20$ the values of the transmission probability α_T ranges from 0.1 (for $s = 0$) to 0.001 ($s = 1$). This means that even in the absence of sticking only 10% of the molecules entering the tube reach its exit. When $s = 1$ only the particles which do not collide with the walls emerge at the tube exit. The molecular beam focusing is also a function of L/R and s of the tube. For a given value of L/R the beam becomes more collimated with increasing s. For example, if $L/R = 10$, at $x = 4R$ (if x is the axial distance along the tube measured from the exit aperture) only 32% of the beam remains within a radial distance ≤ 2R for $s = 0$, while for $s = 1$ the beam is entirely focused within this distance [42].

3.6.2 APPLICATION TO PRECURSOR FLOW THROUGH TUBES

The model of Smith and Lewin can be applied to the case of precursor molecules flow through capillary tubes in a chamber (Fig. 3-7) with some approximations if assumptions 1-5 listed in section 3.6.1, on which the model is based, are valid.

The steady state assumption is realistic since the pressure gradient between the capillary tube and the vacuum system, which determines the flux, is constant with the time.

According to the literature [33], molecular flow conditions (assumption 2) are satisfied if

$$K_n = \frac{\lambda_g}{b} \geq 1 \qquad (3.10)$$

where K_n is the Knudsen number, λ_g the mean free path of the gas molecules and b a characteristic dimension of the tube (namely the diameter). For the precursor $[RhCl(PF_3)_2]_2$

$$\lambda_g = \frac{1}{n\pi d^2\sqrt{2}} \qquad (3.11)$$

where n is the molecular density and d the estimated molecular diameter (πd^2 gives the collision cross section). The density n at room temperature (23 °C) can be calculated from the kinetic gas theory ($n = P_{vap}/kT$). For the precursor $[RhCl(PF_3)_2]_2$ ($n = 1.8\ 10^{20} m^{-3}$; $d = 5.7\ 10^{-10}$ m) we obtain $\lambda \approx 4$ mm; therefore for a tube with a diameter of 0.8 mm, $K_n \approx 5$, and molecular flow conditions are satisfied.

Assumption 3 is satisfied since the dimensions of the needle reservoir are large compared to the precursor mean free path and the molecules coming from the solid phase reach all the point in the chamber with the same probability. Assumption 4 is satisfied since a sticking coefficient s for the capillary tube can be defined and assumption 5 because the reflection of molecules after collision with an industrial stainless steel surface occurs according to the cosine law [41].

The number of molecules entering the needle orifice per unit time is given by the impingement rate flux on the section of the needle A. For a tube with a diameter of 0.8 mm the section is $5x10^{-3}cm^2$, therefore the molecular flux is

$$F_{in} = n\frac{\upsilon}{4}A = \frac{P_{vap}}{4kT}\sqrt{\frac{8kT}{\pi M}}A = \frac{N_A P_{vap}}{\sqrt{2\pi RT}}A = 7.0 \times 10^{16} s^{-1} \quad (3.12)$$

where N_A is the Avogadro number and P_{vap} the vapor pressure of the precursor. This quantity corresponds to 1.4 x 10^{19} molecules $cm^{-2}s^{-1}$. As explained schematically in Fig. 3-7, for a nozzle in a vacuum system the exit flux will be given by J_A multiplied by the transmission probability α and the net flow rate will be given by the difference between the exit ($J_1\alpha_T$) and entrance (J_2) flux:

$$F_{TOT} = (J_1\alpha_T - J_2)A\,. \quad (3.13)$$

Since in the deposition apparatus $P_1(\approx 10$ Pa) $>> P_2(\approx 10^{-4}$-10^{-5} Pa), for $L/R < 20$ and for a low sticking coefficient ($s < 0.05$), with good approximation

$$F_{TOT} \approx J_1\alpha_T A\,. \quad (3.14)$$

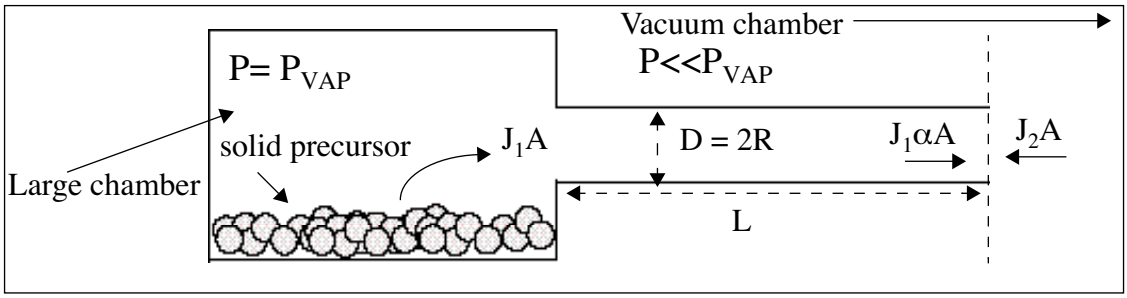

Figure 3-7: *Precursor flow through a capillary tube in a vacuum chamber (schematic drawing).*

The transmission probability for a given gas in a tube can be calculated with the model of Lewin and Smith if the tube dimensions and the sticking coefficient of the precursor on the tube material are known. An example of the variation of the flux of $[RhCl(PF_3)_2]_2$ with the tube dimensions (at s = 1 and s = 0) is shown in Fig. 3-8b. Uptake coefficient measurements have shown that for $[RhCl(PF_3)_2]_2$ $\gamma_S = 0$, which determines $s = 0$, therefore the values on the curve $s = 0$ represent a good estimation for the case treated here. In reality, since the molecules have a residence time on the stainless steel surface, the area exposed to the molecules in the tube is small and the molecular flux is high, the surface of the tube is covered by a precursor layer after some seconds of pumping. For this reason the calculation should take into account the sticking coefficient of the precursor on itself. Literature data report that for most gases the sticking coefficient declines towards 0 at monolayer coverage [41].

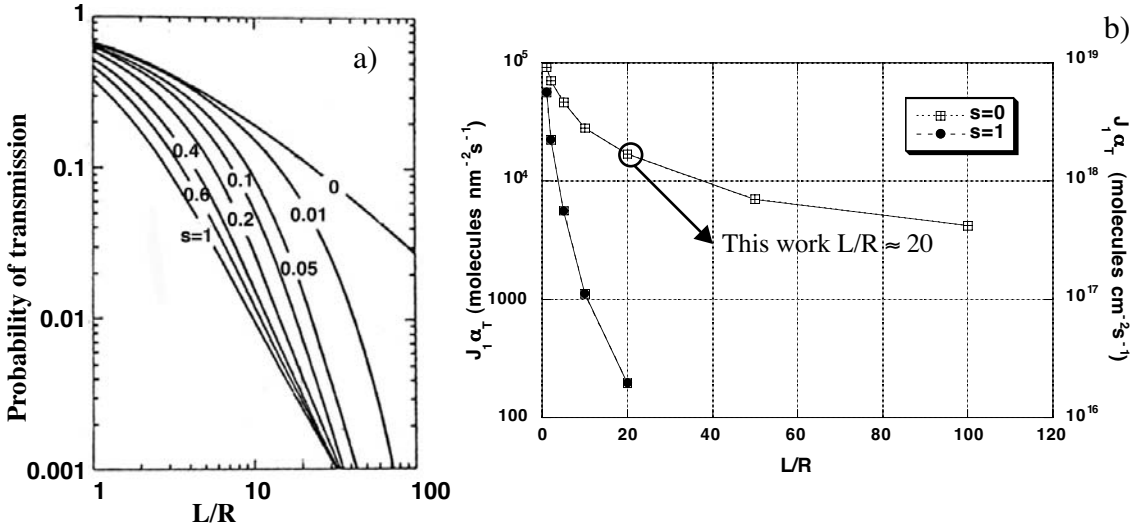

Figure 3-8: *a) Transmission probability (α_T) of a molecule through a cylindrical tube, as a function of the tube L/R and sticking coefficient [42]; b) molecular flux of $[RhCl(PF_3)_2]_2$ as a function of L/R for s=0 and s=1. Transmission coefficients are extrapolated from Fig. 3-8 a) [42].*

The calculation of the precursor flux shown above give the maximum value of the flux. Deviation from the model, resulting in a lower flux, can occur due to low Knudsen number and to a sticking coefficient larger than 0.

3.7 CONCLUSION

The precursor selected for EBID deposition is $[RhCl(PF_3)_2]_2$ because of its low carbon and oxygen content and, chemical stability and high volatility. The vapor pressure of the compound as a function of the temperature has been measured. At 23 °C the precursor has a vapor pressure of 7.5 Pa. Mass spectrometry measurements have revealed the fragmentation path of the precursor under electron beam irradiation in the gas phase. The measurements are in agreement with DFT calculations and show that the precursor is promising for deposition of high Rh content structure. Residence time measurements reveal that $[RhCl(PF_3)_2]_2$ is reversibly adsorbed on stainless steel surfaces with a residence time of 2 ms, corresponding to an activation energy for desorption of 0.6 eV. The measured residence time allows also to estimate that the maximum distance the precursor molecule can travel before being desorbed is about 4 μm. The results of vapor pressure and residence time measurements allow to estimate the number of precursor molecules flowing through a capillary tube using a modified version of the model of Lewin and Smith.

3.8 REFERENCES

[1] P. Doppelt, L. Ricard, V. Weigel; *Crystal structure and study of the volatility of* $[RhCl(PF_3)_2]_2$; Inorg. Chem., 32 (1993); p. 1039-1040.

[2] T. Kodas, M. Hampden-Smith; *The Chemistry of Metal CVD*; VCH, 1995.

[3] S. Matsui, K. Mori; *New selective deposition technology by electron beam induced surface reaction*; J. Vac. Sci. Technol. B, 4 (1985); p. 299-304.

[4] R.B. Jackmann, J.S. Foord; *Electron-beam stimulated chemical deposition of patterned tungsten films on Si (100)*; Appl. Phys. Lett., 49 (1988); p. 196-198.

[5] T. Ichihashi, S. Matsui; *In situ observation on electron beam induced chemical vapor deposition by transmission electron microscope*, in 19th Conf. Solid State Devices and Materials, 1987, Bus. Center Acad. Soc. Japan, Tokyo, p.565.

[6] D.A. Bell, J.L. Falconer, L. Zhiming, C.M. McConica; *Electron beam-induced deposition of tungsten*; J. Vac. Sci. Technol. B, 12 (1994); p. 2976-2979.

[7] H. Hiroshima, M. Komuro; *Fabrication of conductive wires by electron-beam-induced deposition*; Nanotechnology, 9 (1998); p. 108-112.

[8] H.W.P. Koops, M. Weber, C. Schössler, A. Kaya; *Three-dimensional additive electron beam lithography*; Proceedings of the SPIE, 2780 (1996); p. 388-395.

[9] C. Schossler, A. Kaya, J. Kretz, M. Weber, H.W.P. Koops; *Electrical and field emission properties of nanocrystalline materials fabricated by electron-beam induced deposition*; Microelectron. Engin., 30 (1996); p. 471-474.

[10] O. Yavas, C. Ochiai, M. Takai, A. Hosono, S. Okuda; *Maskless fabrication opf field-emitter array by focused ion and electron beam*; Appl. Phys. Lett., 76 (2000); p. 3319-3321.

[11] P. Chini; *Complementi di Chimica Generale e Inorganica*; CLUP, 1971.

[12] K.L. Lee, M. Hatzakis; *Direct electron-beam patterning for nanolithography*; J. Vac. Sci. Tech. B, 7 (1989); p. 941-946.

[13] H.W.P. Koops, J. Kretz, M. Rudolph, M. Weber; *Constructive three-dimensional lithography with electron-beam induced deposition for quantum effect devices*; J. Vac. Sci. Technol. B, 11 (1993); p. 2386-2389.

[14] M. Weber, M. Rudolph, J. Kretz, H.W.P. Koops; *Electron-Beam-Induced-Deposition for fabrication of vacuum field emitter devices*; J. Vac. Sci. Technol. B, 13 (1995); p. 461-464.

[15] M. Weber, H.W.P. Koops, M. Rudolph, J. Kretz, G. Schmidt; *New compound quantum-dot materials produced by Electron-Beam-Induced-Deposition*; J. Vac. Sci. Technol. B, 13 (1995); p. 1364-1368.

[16] R.R. Kunz, T.M. Mayer; *Electron beam induced surface nucleation and low temperature decomposition of metal carbonyls*; J. Vac. Sci. Technol. B, 6 (1988); p. 1557-1564.

[17] N.A. Kislov, I.I. Khodos, E.D. Ivanov, J. Barthel; *Electron beam induced fabrication of metal-containing nanostructures*; Scanning, 18 (1996); p. 114-118.

[18] P.C. Hoyle, M. Ogasawara, J.R.A. Cleaver, H. Ahmed; *Electrical resistance of electron beam induced deposits from tungsten hexacarbonyl*; Appl. Phys. Lett., 62 (1993); p. 3043-3045.

[19] P.C. Hoyle, J.R.A. Cleaver, H. Ahmed; *Ultralow-energy focused electron beam induced deposition*; Appl. Phys. Lett., 64 (1994); p. 1448-1450.

[20] P.C. Hoyle, J.R.A. Cleaver, H. Ahmed; *Electron beam induced deposition from $W(CO)_6$ at 2 to 20 keV and its applications*; J. Vac. Sci. Technol. B, 14 (1996); p. 662-673.

[21] H.W.P. Koops, R. Weiel, D.P. Kern, T.H. Baum; *High-resolution electron-beam induced deposition*; J. Vac. Sci. Technol. B, 6 (1988); p. 477-481.

[22] V. Scheuer, H. Koops, T. Tschudi; *Electron beam decomposition of carbonyls on Silicon*; Microelectron. Engin., 5 (1986); p. 423-430.

[23] P. Hoffmann, I. Utke, F. Cicoira, B. Dwir, K. Leifer, E. Kapon, P. Doppelt; *Focused Electron Beam Induced Deposition of Gold and Rhodium*, in Mat. Res. Soc. Symp. Proc., 2000, San Francisco, p.171-177.

[24] I. Utke, P. Hoffmann, B. Dwir, K. Leifer, E. Kapon, P. Doppelt; *Focused electron beam induced deposition of gold*; J. Vac. Sci. Technol. B, 18 (2000); p. 3168-3171.

[25] I. Utke, B. Dwir, K. Leifer, F. Cicoira, P. Doppelt, P. Hoffmann, E. Kapon; *Electron beam induced deposition of metallic tips and wires for microelectronic applications*; Microelectron. Engin., 53 (1999); p. 261-265.

[26] M.A. Bennett, J. Patmore; *Four and Five-Coordinate complexes of Rhodium and Iridium Containing Trifluorophosphine*; Inorg. Chem., 10 (1971); p. 2387-2395.

[27] P. Doppelt, V. Weigel, P. Guinot; *Mineral precursor for chemical vapor deposition of Rh metallic films*; Mater. Sci. Engin. B, 17 (1993); p. 143-146.

[28] F. Marchi, D. Tonneau, H. Dallaporta, V. Safarof, V. Bouchiat, P. Doppelt, R. Even, L. Beitone; *Direct patterning of noble mertal nanostructure with a scanning tunnelling microscope*; J. Vac. Sci. Technol. B, 18 (2000); p. 1171-1176.

[29] J.C. Hierso, P. Serp, R. Feurer, P. Kalk; *MOCVD of rhodium, palladium and platinum complexes on fluidized divided substrates: Novel process for one-step preparation of noble-metal catalyst*; Appl. Organomet. Chem., 12 (1998); p. 161-172.

[30] L.F. Dahl, C. Martell, D.L. Wampler; *Structure and metal bonding in* $[Rh(CO)_2Cl]_2$; J. Am. Chem. Soc., 83 (1961); p. 1761-1762.

[31] J.E. Huheey, E.A. Keiter, R.L. Keiter; *Inorganic Chemistry (Principles of structure and reactivity)*; Harper Collins College Publisher, 1993.

[32] T. Ohta, F. Cicoira, P. Doppelt, L. Beitone, P. Hoffmann; *Static vapor pressure measurement of low volatility precursors for molecular vapor deposition*; Advanced Materials (CVD), 7 (2001); p. 33-37.

[33] A. Chambers, R.K. Fictch, B.S. Halliday; *Basic Vacuum Technology*; Institute of Physics Publishing, 1998.

[34] K.F. Poulter, M.J. Rodgers, P.J. Nash, T.J. Thompson, M.P. Perkin; *Thermal transpiration correction in capacitance manometers*; Vacuum, 33 (1983); p. 311-316.

[35] T. Takaishi, Y. Sensui; *Thermal transpiration effect of hydrogen, rare gases and methane*; Trans. Far. Soc., 89 (1963); p. 2503-2514.

[36] P.W. Atkins; *Physical Chemistry*; Oxford University Press, 1978.

[37] D.F. Torgerson, J.B. Westmore; *Energetics of the ionization and fragmentation of phosphorous trifluoride by electron impact*; Can. J. Chem., 53 (1975); p. 933-938.

[38] NIST Mass spectrometry data center, http://webbook.nist.gov/chemistry.

[39] T.G. Koch, M. Rossi; *Direct measurements of surface residence times: nitryl chloride and chlorine nitrate on alkali halides at room temperature*; J. Phys. Chem. A, 102 (1998); p. 9193-9201.

[40] C. Alcala-Jornod, H. van den Bergh, M. Rossi; *Reactivity of* NO_2 *and* H_2O *on soot generated in the laboratory: a diffusion tube study at ambient temperature*; PCCP, 2 (2000); p. 5584-5593.

[41] P.A. Redhead, J.P. Hobson, E.V. Kornelsen; *The Physical Basis of Ultrahigh Vacuum*; American Institute of Physics, 1967.

[42] C.G. Smith, G. Lewin; *Free molecular conductance of a cylindrical tube with wall sorption*; J. Vac. Sci. Technol., 3 (1966); p. 92-95.

CHAPTER 4 *Electron beam-specimen interactions*

In this chapter I discuss the different aspects of the beam-specimen interaction, namely scattering, secondary emission, heating and charging. These phenomena can have an effect on the EBID growth process and on the properties of the deposited materials. Furthermore, this chapter allows to understand the basis of most of the analytical techniques used for deposit characterization (e.g. Auger Electron Spectroscopy and Electron Energy Loss spectrometry).

4.1 ELECTRON SCATTERING

An electron beam impinging on a solid surface undergoes a series of complex interactions with the electrons and the nuclei of the atoms of the specimen which result in elastic (no loss of energy) or inelastic scattering (some measurable loss of energy).

The chance of a particular electron undergoing any kind of scattering with an atom is determined by an interaction cross-section σ_{CS}. A cross-section has the units of area but does not represent a physical area: when divided by the actual area of the atom, it represents a probability that a scattering event will occur. The typical unit used for cross-section is the barn (10^{-24} cm^2 or 10^{-4} $Å^2$). The total scattering cross-section (σ_{CST}) for an isolated atom is given by the sum of all elastic (e) and inelastic (i) events:

$$\sigma_{CST} = \sigma_{CSe} + \sigma_{CSi}\,. \tag{4. 1}$$

For a specimen containing N atoms per unit volume, the total cross-section for scattering in the specimen Q_T can be defined:

$$Q_T = N\sigma_T = \frac{N_A \rho}{A_M}\sigma_{CST} \tag{4. 2}$$

where A_M is the atomic weight (in g mol^{-1}), N_A the Avogadro's number, ρ the density (g cm^{-3}) and σ_T the total scattering cross-section. Q_T represents the number of scattering events per unit distance that the electron travels through the specimen.

The scattering interaction can be described also by the electron mean free path, which is the average distance the electron travels between scattering events. This parameter is important

since it gives an indication of how thin a sample must be in order to make plural scattering negligible. The electron mean free path is given by the reciprocal of Q_T:

$$\Lambda_{el} = \frac{1}{Q_T} = \frac{A_M}{N_A \rho \sigma_{CST}} \tag{4. 3}$$

where A_M is the atomic weight (in g mol^{-1}), N_A the Avogadro's number, ρ the density and σ_T the total scattering cross-section.

The differential cross-section $d\sigma_{CS}/d\Omega$ describes the angular distribution of scattering from an atom. Electrons from a parallel beam that passes an area $d\sigma$ are scattered through an angle θ

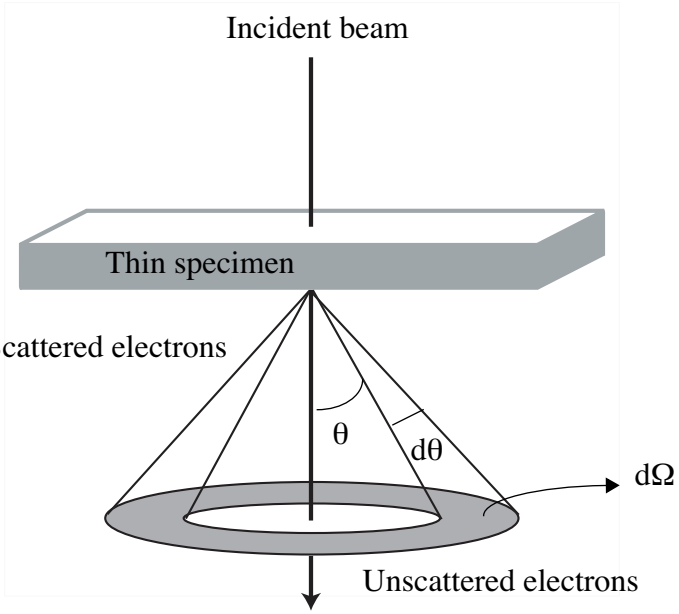

Figure 4-1: *Electron scattering by a single isolated atom. The electrons are scattered through a semiangle θ and the total angle of scattering is Ω. An incremental increase in scattering angle dθ gives an incremental increase in solid angle dΩ.*

into a cone of solid angle $d\Omega$, as shown in Fig. 4.1. Since $\Omega = 2\pi$ (1-cosθ) the differential cross-section can be written as

$$\frac{d\sigma}{d\Omega} = \frac{1}{2\pi \sin\theta} \frac{d\Omega}{d\theta}. \tag{4. 4}$$

The cross-section can be calculated by integrating Eq. 4. 4:

$$\sigma_\theta = \int_\theta^\pi d\sigma = 2\pi \int_\theta^\pi \frac{d\sigma_{CST}}{d\Omega} \sin\theta (d\theta). \tag{4. 5}$$

Since $d\sigma/d\Omega$ is often measured experimentally, Eq. 4. 5 gives a way to determine σ_{CST}.

Elastic scattering is an interaction between the electrons and the nuclei of the specimen; the total momentum and energy of the collision partner are conserved. The process can be described with classical mechanics: the electron is treated as a small particle of mass m_e and electric charge e, attracted to a nucleus of charge $+Ze$, with the coulomb force. The simplest theoretical description, given by Rutherford, allowed to obtain the following expression for the differential electron-nucleus cross-section:

$$\frac{d\sigma_{CSe}(\theta)}{d\Omega} = \frac{e^4 Z^2}{16(E)sin^4\left(\frac{\theta}{2}\right)} \tag{4. 6}$$

where E is the primary electron energy, Z the atomic number and θ the scattering semi-angle. The Rutherford formula can be corrected by a term containing the screening effect of the electron cloud surrounding the nucleus. Another correction can be introduced for relativistic energies (> 100 keV), which gives the screened relativistic Rutherford cross-section. At highest TEM voltages (300-400 keV) and for high Z (> 30) specimens, Mott cross-sections should be used.

Inelastic scattering can result in the emission of plasmons, secondary emission of radiation (electromagnetic waves), like X-rays and photons (cathodoluminescence), or particles, like secondary electrons. Each of the inelastic processes is characterized by a cross-section. As for elastic scattering a cross-section $d\sigma_i/d\Omega$ and a mean free path Λ_{inel} can be defined for all the inelastic processes. Furthermore, some of the incident electrons (40-80% of the total) are converted into heat in the specimen. The energy loss of electrons in solids is described by Bethe's continuous slow-down approximation. The interaction volume for a beam impinging on a thick solid specimen is usually described as a tear-drop (Fig. 4-2) and depends on the penetration depth of the electrons, expressed by the electron range R_E.

4.2 THE MOCASIM SOFTWARE

Monte-Carlo Simulations (MCS) are used in this work to draw electron trajectories in solids and to calculate the electron range, secondary and backscattered yield. The simulations are carried out with the commercial software Mocasim (Plano GMBH, Germany). For calculation of trajectories the program starts with a reading of the atomic number Z, atomic weight A, density ρ, and tabulated elastic cross-sections of the element of interest. The cross-sections are used to calculate the Lewis integral for multiple small angle, the cosθ (R) relations for large angle scattering, the mean free path lengths Λ between elastic scattering processes.

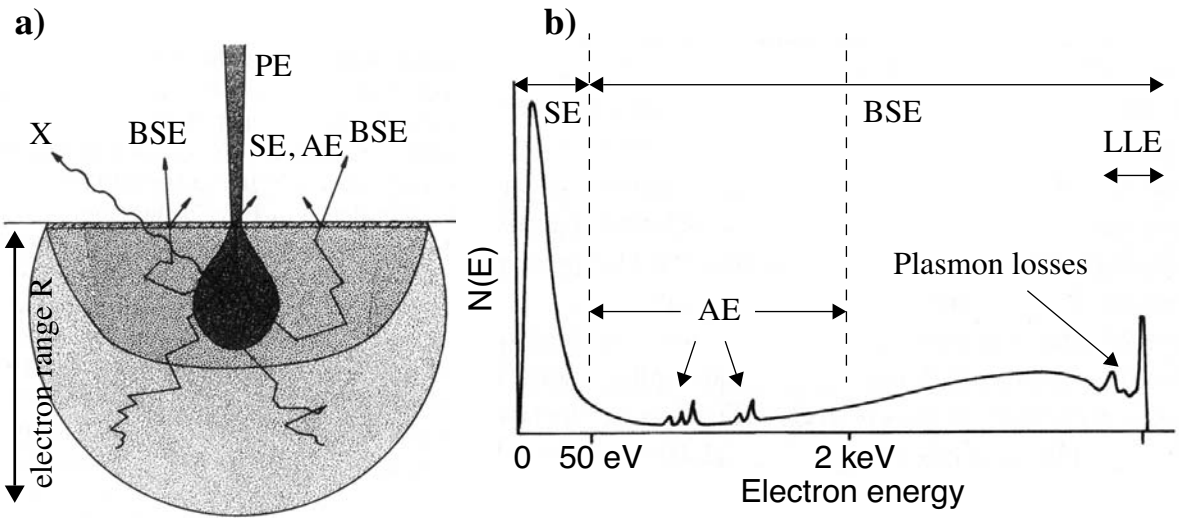

Figure 4-2: *Escape of secondary electrons (SE), backscattered electrons (BSE), Auger electrons (AE), and X-rays (X) in the diffusion cloud of electron range R (a); schematic energy spectrum of emitted electrons consisting of secondary electron (SE), backscattered electrons (BSE), low loss electrons (LLE) and peaks of Auger electrons (AE) (b) [1].*

4.3 CONTINUOUS SLOW-DOWN APPROXIMATION

The energy loss along an electron trajectory is described assuming that the energy transfer in Coulomb interaction between incident and atomic electrons is much smaller than the energy of the incident electrons. The sequence of collisions can be regarded as a continuous slowing down and to each path element of the electron trajectory can be attributed a mean energy loss - dE_m which results in the so-called Bethe loss formula [2]. The Bethe stopping power S_B for non-relativistic energies ($J << E << m_o c^2$) is given by the practical formula [3]

$$S_B = \frac{dE_m}{dx} = \frac{2\pi e^4 N_A}{(4\pi\varepsilon_0)} \times \left(\frac{Z}{A}\right)\frac{1}{E} ln\left(b\frac{E}{X}\right) = 7.8 \times 10^{10} \times \left(\frac{Z}{A}\right)\frac{1}{E} ln\left(b\frac{E}{X}\right) \qquad (4.7)$$

where S_B is the stopping power (in eV g^{-1} cm^2), E the electron energy (in eV), Z the atomic number, A the atomic mass (g mol^{-1}), X the mean ionization potential (in eV), $\varepsilon_0 = E/E_0$ with $E_0 = m_0 c^2 = 511\ keV$ and b represents the impact parameters (different values of b are reported in the literature: 1, 2 and 1.66).

The mean ionization potential increases with Z and can be described by the semi-empirical formula [4]:

$$'X = 9.76Z + 58.8Z^{-0.1} \quad \text{and} \quad JX = 11.5Z \quad \text{for} \quad Z \leq 6\,. \qquad (4.8)$$

For composite targets it can be assumed that the stopping effects of the atomic electrons combine additively (Bragg's rule). Taking into account that the number of atoms of an element *'a'* in 1g of a multi-element target is $m_a N_A / \Sigma m_i A_i$, where m_i are the atomic fractions and A_i the atomic masses, the Bethe formula for composite targets can be written, in term of the atomic fractions, as [1]

$$S_B = \frac{2\pi e^4 N_A}{(4\pi\varepsilon_0)^2 E} \frac{\Sigma m_i Z_i \ln\left(b\frac{E}{J_i}\right)}{\Sigma m_i A_i} . \qquad (4.9)$$

At low electron energy atomic shells with ionization energies higher than the incident energy E do not contribute to the energy loss. The simplest way to take this into account is to replace the mean ionization potential by an energy dependent value [5]

$$X_E = \frac{X}{1 + q(X/E)} \qquad (4.10)$$

with q values varying between 0.77 for C and 0.85 for Au. With this correction the maximum of the stopping power S is shifted to lower energies but still goes to 0 for $E = 0$.

The decrease of the mean electron energy (E_m) with increasing path length can be calculated by numerical integration of Eq. 4. 7. Extrapolation to $E_m = 0$ permits to calculate the Bethe range R_B. The values of R_B are usually expressed in g/cm^2, the range in units of length is obtained by dividing R_B by the specimen density (in units of g/cm^3). For metallic materials R_B can vary

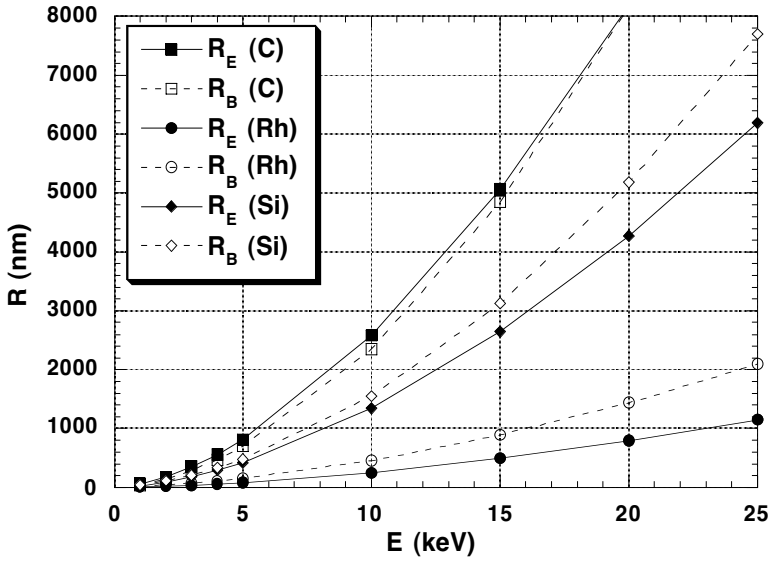

Figure 4-3: *Bethe range R_B (dashed line) and electron range R_E (solid line) as a function of the primary electron energy for C, Rh and Si, calculated by Monte Carlo simulations.*

from some tenths of nanometers to some microns, depending on the primary electron energy and the target density. The values of the Bethe range can be compared to the practical electron range (R_E), given (in mass/thickness units) by the power law [1]

$$R_E = aE^n \tag{4. 11}$$

(where 4 < a <17 and 1.3 < n < 1.7) which fits well with the data obtained from transmission measurements. Even R_E values are usually given in mass-thickness units; the range in length units is obtained by dividing the values obtained from Eq. 4. 11 by the mass density. The plot of Bethe and practical range for two materials with different Z is reported in Fig. 4-3. R_B and R_E are almost equal for low Z materials but show a discrepancy with increasing atomic number. This is because R_B represents a mean path length for complete deceleration and that the probability of large angle scattering increases with increasing Z. As shown in Fig. 4-4, in low-Z

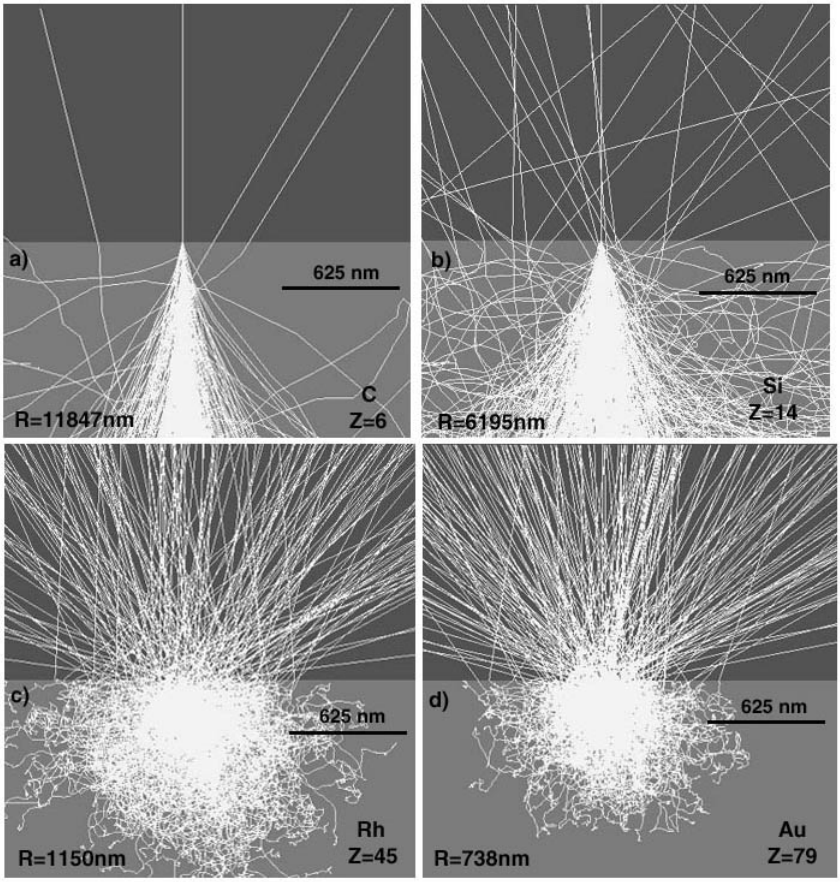

Figure 4-4: *Monte Carlo simulation of electron scattering on C(a), Si(b), Rh(c) and Au (d)). The simulations have been carried out for 500 electron trajectories with 25 keV energy. The electron range (R) and the width of backscattered electron generation decrease with increasing Z. The electron trajectories are more strongly coiled up for high-Z materials.*

materials most of the electrons are scattered only through small angles and electron diffusion

results only in a brush-like beam broadening. In high-Z materials the trajectories are more strongly coiled up. The influence of increasing electron energy on the electron range and on the backscattered electrons distribution at the surface is shown in Fig. 4-5.

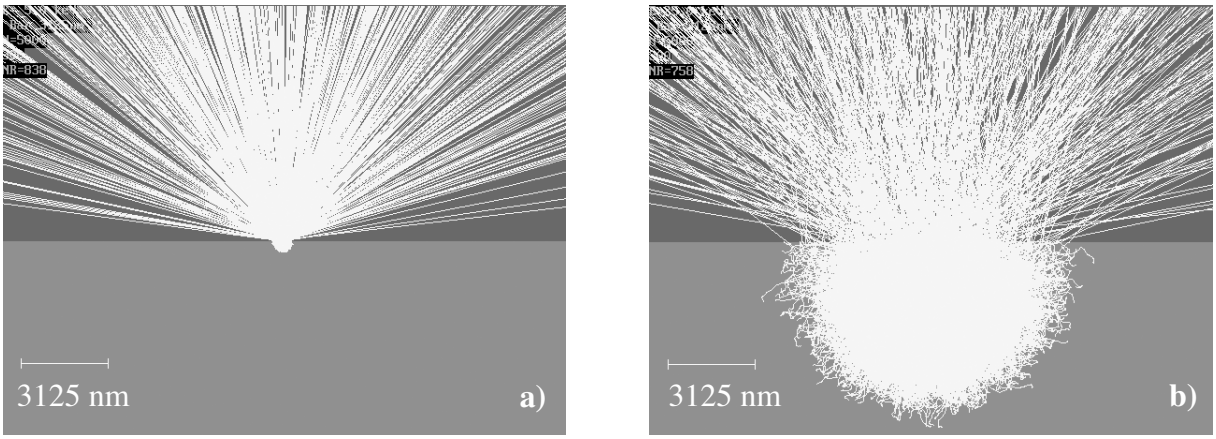

Figure 4-5: *Monte Carlo simulation of electron scattering on Si with 5 keV (a) and 25 keV (b) electron energy for 5000 electron trajectories. The electron range (R_E) and the width of backscattered electron generation increase with increasing primary electron energy.*

4.4 BACKSCATTERED ELECTRONS (BSE)

By convention, specimen-emitted electrons with $E < 50$ eV are called secondary electrons (SE) and electrons with $E > 50$ eV backscattered electrons (BSE). The integrated SE and BSE yields are indicated by δ and η respectively.

Backscattered electrons (BSE) have, on average, 60% to 80% of the primary electron energy. Because of their high energy they are not strongly adsorbed by the sample and can escape from a depth ranging from some tenths of nanometers to several micrometers. The maximum escape depth and width increase with decreasing atomic number of the sample, because of the term (Z/A) in Eq. 4. 7. The BSE yield η ranges from 0.1 to 0.5 and depends on the primary electron energy, the average atomic number Z of the sample and the specimen tilt angle ϕ. The dependence of η on the atomic number and on the electron energy is reported in Fig. 4-6. For a primary electron energy $E < 5$ keV, η increases with energy for high Z elements and decreases for low-Z elements (Fig. 4-6a)*;* there is no longer a monotonic increase and there is even a maximum at medium Z (Fig. 4-6b). For $E > 5$ keV, η is approximately independent of the primary energy and can be calculated with the empirical formula [7]

$$\eta(Z, \phi) = (1 + \cos\phi)^{-9/(\sqrt{Z})} \tag{4. 12}$$

which fits well the experimental data. The backscattered yields as a function of the primary electron energy for Au, Rh, Si and C are reported in Fig. 4-7.

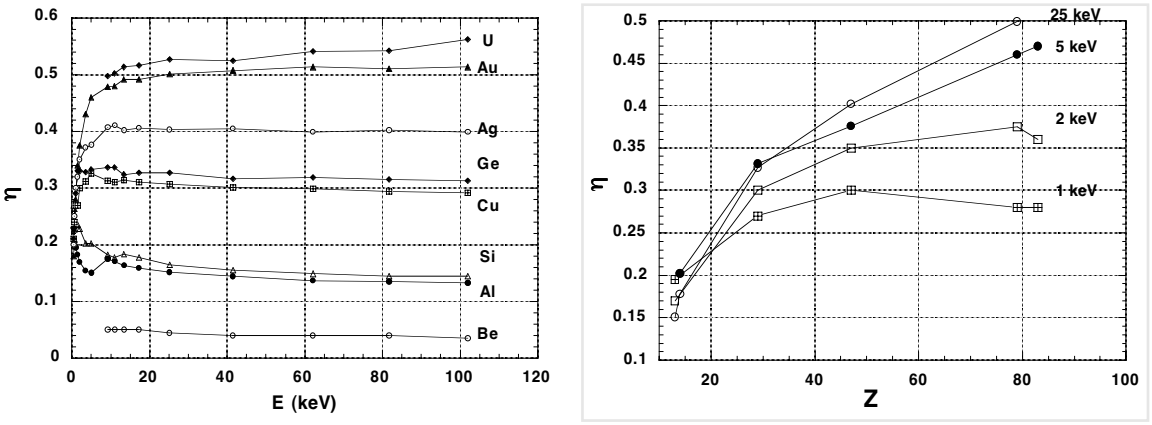

Figure 4-6: *Backscattering yield (η) as a function of the primary electron energy (E) in the range 0.5-102 keV for different elements (a) and of the atomic number (Z) for different electron energies (b). The data are taken from ref. [6].*

The width of the BSE generation around the primary beam increases with decreasing atomic number (Fig. 4-4a-c) and with increasing electron energy (Figs. 4-5a and 4-5b). Since the BSE yield increases with *Z*, at a given energy, materials with a large BSE distribution have a low BSE surface density.

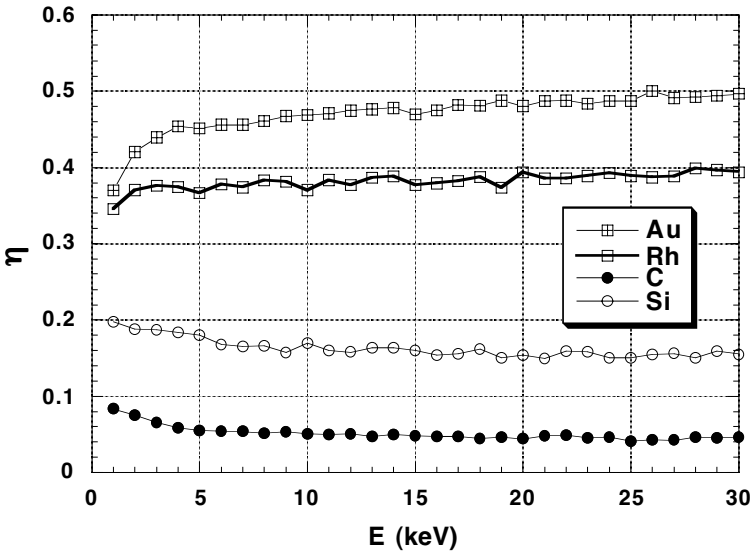

Figure 4-7: *Backscattered yield (η) as a function of the primary electron energy (E) in the range 1-30 keV for C (Z=6), Si (Z=14), Rh (Z=45), Au (Z=79), calculated by monte-carlo simulations, without specimen tilting (ϕ=0).*

Monte Carlo simulations of the electron scattering induced by a 25 keV primary beam on three different material used as substrate for EBID are shown in Fig. 4-8. Fig. 4-8a reveals that the

electron beam is totally transmitted through a 20 nm C film. Comparison of Figs. 4-8b and 4-8c shows that the BSE yield is higher on Au films than on Si. Nevertheless on Si the BSE are distributed on a larger area, due to the larger electron range (R_E), as already shown in Fig. 4-5.

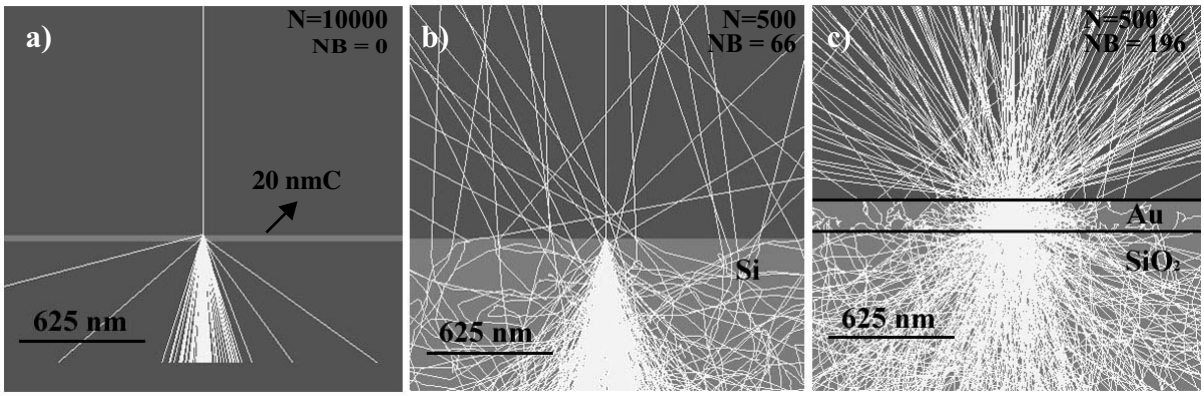

Figure 4-8: *Monte Carlo simulation of electron scattering emission on: 20 nm C thin film (a), bulk Si (b) and 150 nm thick Au film on Si (c). Simulation carried out with 100000 incident electrons in Fig. a and 500 incident electrons in figure b and c. The electron energy is 25 keV.*

4.5 SECONDARY ELECTRONS (SE)

Secondary electrons (SE) are strongly absorbed by the sample because of their low energy and thus can leave the specimen only from a small escape depth Λ_{SE}. An estimation of Λ_{SE} can be obtained using the empirical formula

$$\Lambda_{SE} = \frac{12}{\rho} \tag{4. 13}$$

where ρ is the density of the target material. The escape depth Λ_{SE} is of the order of 0.5-1.5 nm for metals, about 10 nm for carbon and 10-20 nm for insulators. The mean energy loss for excited electron is W_{SE} = 10-100 eV. The SE yield (δ) is a function of the primary electron energy, the specimen tilt angle and the atomic number. For high primary electron energies (1 keV < E < 100 keV) and straight trajectories inside the exit zone, the yield is given by:

$$\delta \propto \frac{\Lambda_{SE}}{W_{SE}} S_B(E) \tag{4. 14}$$

where S_B is the Bethe stopping power, Λ_{SE} the secondary electron exit depth, W_{SE} the mean energy loss for SE generation. The SE yield decreases with increasing primary electron energy due to the decrease of S_B (see Eq. 4-7) [1].

The dependence of the secondary yield δ on the tilt angle ϕ is expressed by a function $(\sec \phi)^n$ where $n = 1.3$ for light elements and $n = 0.8$ for heavier elements. Finally, δ increases with Z due to the contribution of SE generated by the BSE exiting the sample (SE2). The SE2, like the BSE, are characterized by a broader exit area and a lower density on the substrate surface.

The exact theory of secondary emission is very complex and can hardly be modelled exactly. In MCS a parametric model using Λ_{SE},W_{SE} and a straight line approximation with exponential decrease can be used. The probability of escape along a path length *ds* from a depth *z* below the surface can be described by the exponential law [1]

$$p(z)ds = \frac{S_B(E)ds}{W_{SE}} exp\left(-\frac{z}{\Lambda_{SE} cos\,\theta}\right) \qquad (4.15)$$

where S_B is the Bethe stopping power and θ the angle between exit direction and surface normal. A plot of secondary electron yield as a function of primary energy for Au, Rh, Si and C (flat surfaces), calculated with MCS, is reported in Fig. 4-9. MCS of SE signals can be suspicious due to the simple model of excitation, the uncertainty of Λ_{SE} and W_{SE} values and the strong influence of surface contamination.

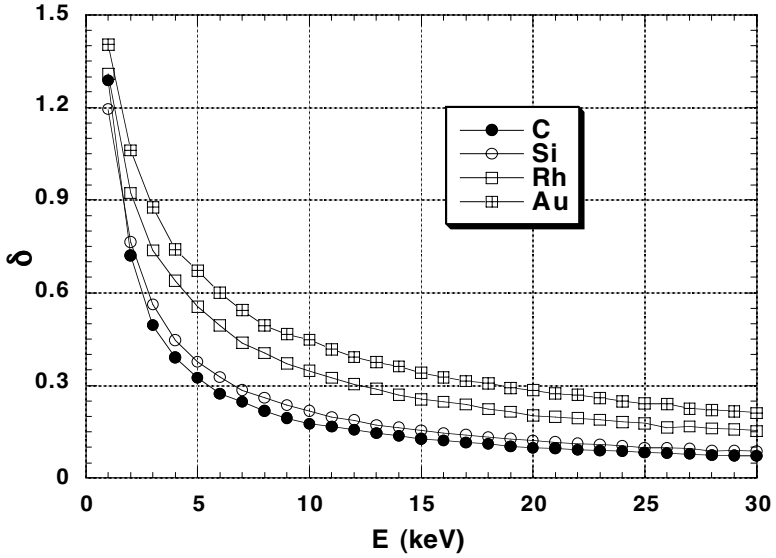

Figure 4-9: *Secondary electron yield (δ) as a function of the primary electron energy (E) for C(Z = 6), Si (Z = 14), Rh (Z = 45), Au (Z = 79) between 1 and 30 keV, calculated by Monte Carlo simulations without specimen tilting ($\phi = 0$). The exit depths Λ_{SE} are estimated using Eq. 4.13. The mean energy losses W_{SE} are taken from the literature for C, Si and Au. For Rh the value is not available, therefore W_{SE} value of Ag (Z = 47) has been used.*

4.6 X-RAY AND AUGER EMISSION

X-rays are electromagnetic waves of quantum energy $E_x = h\nu$, from 100 eV to 100 keV, they are generated by the deceleration (Bremsstrahlung) of electrons (X-ray continuum) or by electron transition from a filled electron state into a vacancy in a lower atomic shell (characteristic lines). X-rays, being photons, have a much lower probability, compared to SE and BSE, of losing their energy because of inelastic scattering in the sample, therefore they exit from the whole area of specimen-beam interaction. A typical spectrum has characteristic X-ray peaks superimposed on the background of continuum X-rays. For the continuum spectrum a short-wave cut-off λ_{min} can be defined by the relation [8]

$$E = eU = h\upsilon_{max} = h\frac{c}{\lambda_{min}}. \tag{4. 16}$$

At this limit, the most energetic bombarding electrons have all their kinetic energy converted into the energy of a photon. The cut-off λ_{min} is called the Duane-Hint limit; for U in kilovolts and wavelengths in nanometers, rearrangement of Eq. 4. 16 yields $\lambda_{min} = 1.24 / U$. The intensity distribution of the X-ray continuum is always characterized by a maximum (at 1.5-2 times λ_{min}) and a gradual drop-off towards 0 at longer wavelengths. The peak intensity of the continuum X-ray is proportional to the atomic number Z, but the shape is similar for all material. The yield for production of a continuum X-ray spectrum (η_X) for a given element is a linear function of the primary electron energy and can be estimated by the empirical formula [9]

$$\eta_x = 11x10^{-10}ZU \tag{4. 17}$$

where Z is the atomic number and U the potential of the impinging electrons in Volts. For heavy elements at 25 keV the efficiencies are of the order of some fraction of a percent. X-ray continuum yields for Au, Rh, Si and C are shown in Fig. 4-10.

Electron irradiation of solids also produces emission of characteristic X-rays and of Auger electrons [10]. When a core level of a surface atom is ionized by the primary electron beam, relaxation of the ionized atom can occur by filling the vacancy with an outer- shell electron. The relaxation energy is then dissipated in either of two ways: it can be given to a second electron, an Auger electron, which is emitted from the atom, or it can appear as a characteristic X-ray photon (X-ray fluorescence), as shown schematically in Fig. 4-11. Auger transitions are denoted by a three-letter combination, e.g. KLL, the first specifying in which shell the initial vacancy is created, the second from which shell the core level vacancy is filled, the third from which shell the Auger electron is taken. The yield of core ionization depends on the inner-shell ionization cross-section; typical values are of the order of 5 x 10^{-4}[11]. The sum of the yields of the two decay processes is unity, with the Auger process more probable for low energy transitions, as shown in the plot in the inset of Fig. 4-11.

The energy of the emitted X-rays depends on the binding energy of the core level of the substrate and can vary in a wide range of values, e.g. 284 eV for C, 1849 eV for Si, 23200 eV

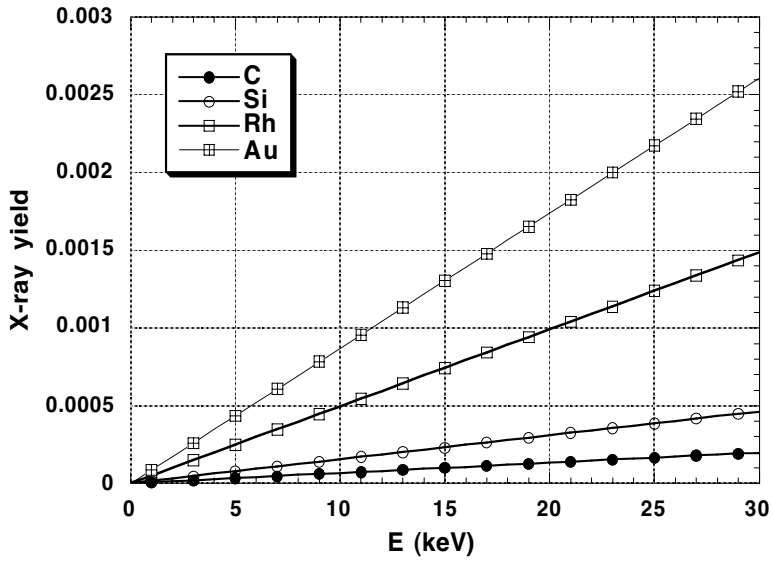

Figure 4-10: *X-ray yields as a function of the primary electron energy for C (Z = 6), Si (Z = 14), Rh (Z = 45), Au (Z = 79) between 1 and 30 keV, calculated with Eq. 4. 17.*

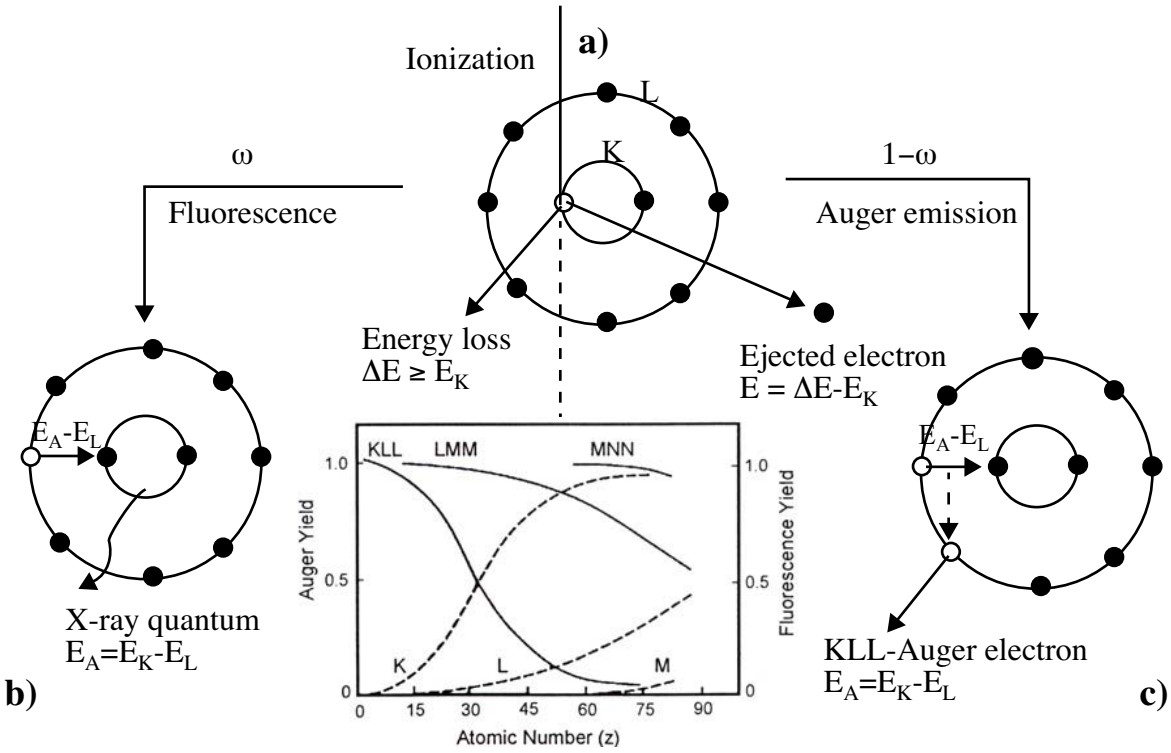

Figure 4-11: *Schematics of Auger and X-ray fluorescence processes. K-shell ionization (a) followed by either X-ray fluorescence (b) or emission of a KLL Auger electron (c). The yield for X-ray fluorescence is ω_F, for Auger emission 1-ω.*

for Rh, 80725 eV for Au [12]. Auger electron energies range from few eV to about 2500 eV [8].The kinetic energy of the emitted electron or photon is characteristic of the binding energy of the ionized core level of the target, therefore it can be used to identify a particular element. Emission of characteristic X-ray is the basis of Electron Dispersion X-ray spectroscopy (EDX) and Auger emission of Auger Electron Spectroscopy. Auger electrons, although created in the pear-shaped interaction volume between the beam and sample (Fig. 4-2), do not reach the surface unless they are created in the very top atomic layers where the lateral dimensions are given mainly by the electron probe size.

4.7 ELECTRON BEAM INDUCED CHARGING OF INSULATING SPECIMENS

The surface potential influences the trajectories of primary, secondary and backscattered electrons. Whether the surface potential of an insulating specimen is positive or negative depends on the total electron yield ε. The dependence of σ on the primary electron energy shows two crossover energies E_1 and E_2, at which $\varepsilon = 1$. E_1 is lower than 100-200 eV and it is not of great interest for EBID. If $\varepsilon > 1$ the number of emitted electrons is greater than the number of incident electrons. The excess emission results in a positive charging of the specimen surface of the order of a few Volts, which also reduces secondary emission. If $\varepsilon < 1$ there

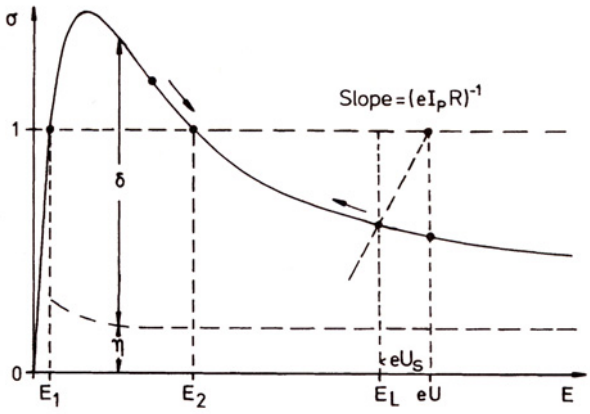

Figure 4-12: *Total electron emission yield (σ) as a function of the primary energy [1]. At E_1 and E_2 $\sigma = 1$; positive charging occurs for $\sigma > 1$ and negative for $\sigma < 1$. At $E = eU$ the potential of the sample can be constructed, according to Eq. 4. 19 as the point of intersection of $\sigma(E)$ with a straight line of slope $1/eI_PR$, which intersect at the point $\sigma_y = 1$, $E = eU$.*

are more impinging than emitted electrons and a negative space charge is produced in a region of the order of the electron range. In consequence the surface potential becomes negative and acts as a retarding field for the primary electrons, the landing energy (E_L) of which is reduced. The negative charging reaches an equilibrium when the primary electron energy is retarded to $E_L = E_2$, where $\varepsilon = 1$; it can therefore reach a few kilovolts in contrast to the positive charging.

If the increase of surface potential is treated as the charging of a capacitance C with a leak resistance R_{el} to the ground, the current equilibrium results in [1]:

$$\frac{dQ}{dt} = I_p(1-\sigma) - \frac{U_S}{R_{el}} \tag{4. 18}$$

where I_p is the probe current and U_s the surface potential. For a stationary charge $dQ/dt = 0$ and Eq. 4. 18 becomes:

$$[1-\sigma_y(E_L)]I_p = \frac{U_S}{R} \quad or \quad \sigma = 1 - \frac{E_L - E}{eI_pR_{el}}. \tag{4. 19}$$

The solution can be found graphically as the point of intersection of the curve $\sigma(E)$ with a straight line through the point $\sigma_y = 1, E = eU$ of slope (eI_pR). For an ideal insulator $R_{el} = \infty$, the intersection will be at $E = E_2$ and for a metal $R_{el} \rightarrow 0$, no charging is observed. When an insulating specimen is irradiated in spot mode below E_2 the core is charged positively but is surrounded by a region of negative charging caused by the secondary electrons retarded by the positive charge of the core. With normal incidence of the primary beam, E_2 is of the order of 1-4 keV [1]. E_2 can be estimated by Monte Carlo simulations, calculating the total yield and determining the intersection point at $\sigma_y = 1$.

4.8 ELECTRON BEAM INDUCED HEATING (STATIONARY CASE)

The power of an electron beam with a probe current I_p (in Amperes) and a voltage U (in Volts) is $P = UI$. For example, a probe current of 1 nA and an acceleration voltage of 20 kV has a power of 20 μW. The fraction of the power converted into heat in the specimen is $f = 40\text{-}80\%$ [1]. High-current electron beams can be used for melting and welding. Nevertheless in SEMs the power is so small that melting and thermal decomposition can be observed only on bulk materials with low melting point or decomposition temperature and on low thermal conductivity materials (organic substances, polymers) [1].

The temperature increase of a semi-infinite specimen can be estimated by assuming that the power $P = fVI_p$ is homogeneously dissipated inside a hemisphere of radius $R_E/2$ (R_E: *electron range*). The electron probe is assumed to be at rest and the probe diameter $d_p << R_E$. Then we have a radially symmetric problem and the stationary heat equation for thermal conduction $P = -K\Delta T$ becomes [1]

$$P\frac{r^3}{(R_E/2)^3} = -K2\pi r^2\frac{dT}{dr} \quad \text{for} \quad 0 < r < R_E/2 \tag{4. 20}$$

$$P = -K2\pi r^2\frac{dT}{dr} \quad \text{for} \quad \frac{R_E}{2} < r < \infty \tag{4. 21}$$

where $S = 2\pi r^2$ is the surface of a hemisphere of radius r and K denotes the thermal conductivity in units of $Js^{-1}m^{-1}K^{-1}$. Integration of the Eq. 4. 20 gives the temperature difference:

$$\Delta T_1 = T(0) - T\left(\frac{R_E}{2}\right) = \frac{P}{2\pi K R_E} \tag{4. 22}$$

between the centre and $r = r/2$, and integration of Eq. 4. 21 gives

$$\Delta T_1 = T(R/2) - T(\infty) = \frac{2P}{2\pi K R_E}. \tag{4. 23}$$

The total increase of temperature for compact matter becomes

$$\Delta T_c = \Delta T_1 + \Delta T_2 = \frac{3P}{(2\pi K R_E)}. \tag{4. 24}$$

The temperature increases for various materials induced, at room temperature, by an electron beam with an energy of 25 keV, a current of 1 nA and a probe diameter of about 1 μm are reported in Table 4.1. The values of ΔT are obtained assuming the electron probe at rest and supposing that all the power is converted into heat ($f = 1$). Under such experimental conditions, for metals, semiconductors and carbon the temperature increase is only a small fraction of a Kelvin, while for polymers ($0.1 < K < 0.6$) it can be enough to induce thermal damage. The temperature increases are even lower if the beam is scanned over a large area and a factor $f < 1$ is taken into account.

For thin fibers, the ΔT can be calculated by assuming that a fiber of length L and diameter D, with a cross-section $S = \pi D^2/4$ is irradiated at one end, whereas the other is connected to a heat sink of constant temperature. For this case the equation for thermal conductivity is [1]

$$P = -\frac{K\pi D^2}{4}\frac{dT}{dx} \tag{4. 25}$$

and the temperature difference between the two ends of the fiber is given by

$$\Delta T_f = \frac{4P_f L}{\pi K D^2} \tag{4. 26}$$

where P_f is the electron beam power converted into heat in a fiber. For most of the EBID three dimensional deposit $D < R_E$, therefore the fraction of the electron beam power converted into heat is lower than in the case of bulk samples, since a fraction of the incident electrons is transmitted laterally and does not contribute to sample heating. For a given electron energy, the transmitted fraction decreases with decreasing fiber aspect/ratio and increasing electron range. Assuming $P_f = P(D/R_E)^2$ and taking the ratio between 4. 24 and 4. 26 gives

$$\Delta T_f = \frac{8}{3}\frac{L}{R_E}\Delta T_c. \quad (4.27)$$

The L/R_E ratio depends on the fiber length and composition. In general for EBID columns $0.1 \leq L/R_E \leq 2$ (see Table 4-1), therefore with a good approximation, in general, $\Delta T_f \leq 10\ \Delta T_c$.

Material	Z	K ($Wm^{-1}K^{-1}$)	R_E (nm)	ΔT_c (K)	ΔT_f (K)
Au	79	315	738	0.03	0.163
Rh	**45**	**151**	**1149**	**0.042**	**0.146**
Cu	29	395	1601	0.012	0.03
Si(c)	14	15	6195	0.078	0.05
C(amorp)	6	1.5	11874	0.42	0.014
PE (c)		0.52	14193	1.02	0.207
PE (a)		0.33	16725	1.44	0.344

Table 4-1: *Temperature increase under electron irradiation for some materials of interest. Beam parameters: I_p= 1 nA, E = 25 keV. K indicates the thermal conductivity, R_E the electron range calculated by MCS. The values of ΔT have been obtained from Eqs. 4.24 and 4.27, assuming f = 0.6 for bulk materials. ΔT in the last column refer to fibers with an aspect ratio of 20. References for thermal conductivity: [13].*

Values of ΔT for bulk materials and EBID fibers of aspect ratio 20 ($L = 4000$ *nm* and $D = 200$ *nm*) irradiated with a beam of 25 μW, calculated with Eqs. 4.24 and 4.27, are reported in Table 4-1. For the calculations, decrease of the electron range in insulating materials due to charging effects is not taken into account.

The results show that the temperature rise in fibers is higher than in bulk materials for high-Z material (where in general $L/R_E > 1$), whereas it is lower for low-Z materials. Electron range effects are compensated for by thermal conductivity effects and for all the materials $\Delta T_f < 1$ K. When EBID is carried out with currents of tens of pA, the ΔT are a factor 100-1000 lower.

4.9 ELECTRON BEAM INDUCED HEATING (NON-STATIONARY CASE)

The non stationary case of electron beam induced heating has been described by Pittaway for thin foils [14]. The temperature rise, at the centre of the spot, due to a stationary Gaussian beam focused on a thin foil is described by the following equation:

$$\Delta T = \frac{P}{4\pi KB} ln\left(\frac{1 + 4\kappa t}{\sigma^2}\right) \quad (4.28)$$

where ΔT is the temperature rise, P the power liberated on the target per second, B the specimen thickness, σ the standard deviation of the gaussian electron beam, K and κ respectively the thermal conductivity and diffusivity of the target material, t the irradiation time. The theory of Pittaway has been extended to a SiO_2 bulk specimen by Hiroshima and Komuro[15]. The bulk is considered to be made of several thin slices in which the same thermal diffusion occurs. The energy deposited per unit length E_0/D, calculated by Monte Carlo simulation for an electron beam with an energy of 50 keV and a current of 100 pA on a SiO_2 substrate, is 0.54 eV/nm. Introducing the latter value for P/D in Eq. 4. 28, choosing $\sigma = 3.7$ and using the values of K and κ for SiO_2 (0.013 J $cm^{-1}s^{-1}°C^{-1}$ and 0.0083 cm^2s^{-1}, respectively) gives the plot reported in Fig. 4-13.

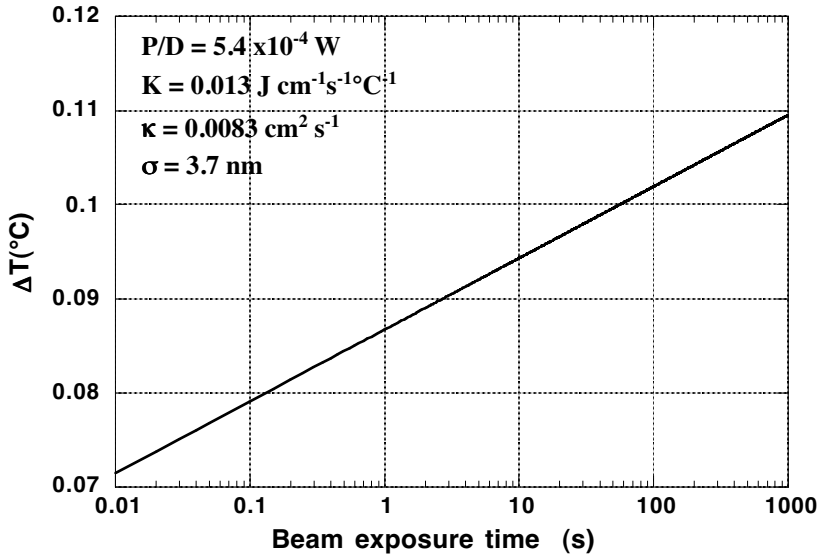

Figure 4-13: *Temperature rise versus beam exposure time for a bulk SiO_2 specimen. Beam parameters: I_p = 100 pA, E = 50 keV. Other material properties and beam parameters are reported on the figure.*

The result shows that even for exposure times of several minutes, the temperature increase is less than 1°C. This small increase in temperature allows us to consider the SiO_2 specimen as an ideal heat sink.

If an EBID column is deposited on a heat sink having a temperature T_s the electron beam energy changes into thermal energy, uniformly distributed along the column and flows through the base of the column. At equilibrium, the maximum temperature of the deposit is T_D and the deposited energy per unit time is a balance of the heat flow per unit time as described by

$$\frac{dQ}{dt} = \left(\frac{P}{B}\right) I_p h \tag{4. 29}$$

where P/B is the deposited energy per unit length, I_p the beam current, h the height of the column, t the time. The same heat flow dQ/dt is achieved by a heat source with a temperature T_C in contact with the top of the column, in the absence of electron irradiation. The relationship

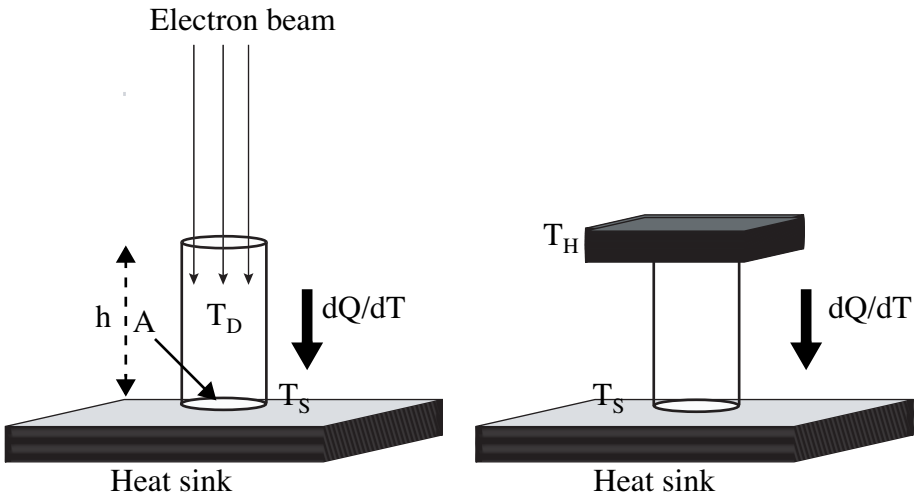

Figure 4-14: *[15] Heat flow through a pillar heated by (a) electron beam irradiation and (b) by a heat source.*

between heat flow and temperature is

$$\frac{dQ}{dt} = \kappa \frac{(T_H - T_S)A}{h} \tag{4. 30}$$

where κ is the thermal diffusivity of the deposited material and A the area of the column base. It is clear that $T_D<T_S$. Therefore, taking into account the Eq. 4. 29 and 4. 30 the temperature rise in the column during beam irradiation becomes

$$T_D - T_S < \frac{EI_p h^2}{B\kappa A} \tag{4. 31}$$

For example in a SiO_2 pillar with 3.7 nm diameter and 30 nm height the temperature rise is less than 1°C. If the thermal conductivity of the deposits is higher than that of SiO_2, the temperature increase is even smaller. In conclusion, heating effects are negligible in the EBID process.

Temperature increase in EBID three dimensional structures has been estimated by studying electron scattering by Monte Carlo simulation also by other authors [16]. The calculations

showed that at most 2% of the deposited energy is left in an EBID tip. If the deposition is carried out with an electron beam operating at 50 keV and 50pA, the amount of energy left in the tip is about 20 nW. This amount of energy, even when depositing a material with low thermal conductivity, results in a temperature increase lower than 1 K.

4.10 CONCLUSIONS

Electron beams interact with solid surface giving rise to electron scattering, secondary and backscattering electron emission, thermal and charging effects. The form of these phenomena depends on the composition of the substrate material and on the power of the electron beam.

Secondary and backscattered emission yields, electron and Bethe ranges for the element of interest in this work have been calculated by Monte Carlo simulations. SE and BSE electrons can play a role in EBID, depending on the yield of the substrate material. The effect of the Auger electrons and X-rays can be neglected because of the low yield of the processes.

Thermal effects of the electron beam are negligible at the beam power used in EBID both for electrically conducting or semiconducting substrate.

4.11 REFERENCES

[1] L. Reimer; *Scanning Electron Microscopy*; Springer, 1998.

[2] H. Bethe; *Zur Theorie des Durchgangs schneller Korpuskularstrahlen durch Materie*; Ann. Phys., 5 (1930); p. 325.

[3] R.D. Evans; *The Atomic Nucleus*; McGraw Hill, 1955.

[4] M.J. Berger, S.M. Seltzer; *Tables of energy loss and ranges of electrons and positrons*; Nat. Acad. Sci., Nat. Res. Council. Publ. 1133, 1964.

[5] D.C. Joy, S. Luo; *An empirical stopping power relationship for low-energy electrons*; Scanning, 11 (1989); p.

[6] H. Drescher, L. Reimer, H. Seidel; *Rückstreukoeffizient und Sekundärelektronen-Ausbeute von 10-100 keV Elektronen und Beziehungen zur Raster-Elektronrnmikroskopie*.; Z. Angew. Phys., 29 (1970); p. 331-335.

[7] F. Arnal, P. Verdier, P.D. Vinsensini; *Coefficient de rétrodiffusion dans de cas d'électrons monocinétiques arrivant sur la cible sous une incidence oblique*; Compt. rend. Acad. Sci. Paris, 268 (1969); p. 1526.

[8] H.A. Strobel, W.R. Heineman; *Chemical instrumentation: a systematic approach*; John Wiley and Sons, 1988.

[9] B.K. Agarwal; *X-ray Spectroscopy (an introduction)*; Springer, 1989.

[10] P. Auger; J. Physique Radium, 6 (1925); p. 205.

[11] D. Briggs, M.P. Seah; *Practical Surface Analysis*; John Wiley and sons, 1995.

[12] D. Bäuerle; *Laser processing and chemistry*; Springer-Verlag, 1996.

[13] E.A. Brandes, G.B. Brook; *Smithells Metals Reference Book*; Butterworth Heinemann, 1992.

[14] L.G. Pittaway; *The temperature distribution in thin foil and semi-infinite targets bombarded by an electron beam*; Brit. J. Appl. Phys., 15 (1964); p. 967-982.

[15] H. Hiroshima, M. Komuro; *High growth rate for slow scanning in electron-beam-induced deposition*; Jpn. J. App. Phys. 1, 36 (1997); p. 7686-7690.

[16] M. Weber, M. Rudolph, J. Kretz, H.W.P. Koops; *Electron-Beam-Induced-Deposition for fabrication of vacuum field emitter devices*; J. Vac. Sci. Technol. B, 13 (1995); p. 461-464.

CHAPTER 5 *Literature overview*

In this chapter I present a review of the previous works on EBID concerning the material properties and the growth mechanism.

5.1 HISTORY

Deposition of insulating films under electron irradiation, due to the presence of organic contaminants in vacuum systems, was detected for the first time in 1933 [1]. In 1947 the same kind of deposition was observed and studied for the first time in an electron microscope [2]. The first application of EBID for solid polymer films goes back to 1960 [3]. In 1976 Broers et al.[4] were able to deposit nanometer scale carbon contamination structures in a scanning transmission electron microscope with electrons of 45 keV energy. Matsui and Mori [5] obtained the first metal containing deposits by introducing a metal halide (WF_6) vapor in the vacuum chamber of a scanning electron microscope. The first metal-containing three-dimensional nanostructures were deposited in 1986 by Koops et al. [6], using the focused electron beam of a conventional SEM.

Since the first experiments, several EBID metal-containing structures have been deposited under a wide range of experimental conditions in the past twenty years. The literature data show that the deposits differ essentially in chemical composition, growth rate and ultimate size. In the following paragraphs I examine in detail the characteristics of the deposits according to the available literature data.

5.2 CHEMICAL COMPOSITION, STRUCTURE AND ELECTRICAL PROPERTIES

As already mentioned in chapter 1, EBID of pure metallic structures has not been performed yet. The deposits have a nanocomposite structure and contain in general, besides the element of interest, some of the elements present in the precursor molecules and other contaminating elements such as oxygen, nitrogen and carbon. Analysis of EBID structure is not straightforward, due to the high spatial resolution required, and the results depend on the sensitivity and resolution of the analytical technique employed. The chemical composition of the deposits obtained until now is discussed in detail in the next paragraphs.

5.2.1 TUNGSTEN DEPOSITION

Tungsten is the metal most deposited with the EBID technique since it is an excellent X-ray adsorber and an attractive material for X-ray photolithography masks [7]. The metal has been deposited with the precursors $W(CO)_6$,WF_6 and WCl_6. The characteristics of the deposits obtained until now and the most important deposition parameters are reported in Table 5-1.

The first W deposition (which was also the first metal-containing EBID) was carried out by Matsui et al. [5] from the halides WF_6 and WCl_6 with an unfocused electron beam (spot size of 0.5 mm), keeping constant the electron energy and the electron current and varying the substrate temperature (see Table 5-1). In situ Auger Electron Spectroscopy (AES) showed that W concentration decreases with decreasing substrate temperature. Other elements detected in the deposit were carbon and oxygen, whose concentrations decrease continuously with increasing temperature, and, in a lower amount, fluorine. AES depth profiling showed that O and C were uniformly distributed in the deposit. According to the authors this contamination could be explained by the low vacuum of the deposition system (10^{-7} Torr). An additional reason for the presence of O and C in the deposit is the stability of tungsten oxides and carbides.

The growth rate of the deposit increases with decreasing substrate temperature due to an increase of the number of condensed precursor molecules. The same authors obtained high content W deposits also from the precursor WCl_6 in a modified SEM, using a focused electron beam (see Table 5-1).

Deposition from WF_6 frozen layer with a broad electron gun was also obtained by Jackmann et al. [8]. In situ AES on the adsorbed films (non-irradiated) and on the deposit revealed that fluorine concentration drops to zero after electron irradiation.

Irradiation of a WF_6 frozen layer was also used to monitor the evolution of the film composition as a function of the irradiation time [7]. The depositions were carried out with an AES electron gun with the parameters reported in Table 5-1. The experiment revealed that the tungsten concentration increases with the irradiation time, before reaching a plateau value after some minutes of irradiation. The time needed to reach the maximum concentration decreased with increasing electron current and decreasing electron energy. The fluorine AES peak drops to zero when W concentration reaches the plateau value. According to the authors, this result proves that an intermediate decomposition product is formed during the first steps of the process.

WF_6 has been used for EBID of conductive lines between Au/Cr electrodes on an insulating SiO_2 substrate [10]. The electron gun used for deposition had an electron energy of 50 keV, an emission current of 100 pA and a spot size of 3 nm; the gas was delivered to the reaction area with a nozzle. It was shown that the line resistivity decreases with increasing electron dose down to a stable value of $6x10^{-4}$ Ωcm (a factor 100 higher than pure W). The resistivity of the deposit could be improved by about one order of magnitude by two different treatments:

Precursor	Deposit properties	*E* (keV)	I_p	*T* (°C)	Substrate	Remarks	Ref.
WF_6	56 at.% W at.% O at.% C i-(AES)	10	1.5 μA	-110	SiO_2	O, C decr. with incr. *T*	[5]
WF_6	66 at.% W at.% O at.% C i-(AES)	10	1.5 μA	25	SiO_2		[5]
WF_6	pure W	5	0.2 nA	-196	Si	no F frozen layer	[8]
WF_6	80 at.% W i-(AES) 300 s irr.	3	13 μA	-180	Ni	as above	[7]
WF_6	80 at.% W i-(AES) 80 s irr.	1	13 μA	-180	Ni	as above	[7]

Table 5-1: *Properties of W containing deposits obtained from the precursors WF_6, WCl_6 and $W(CO)_6$. AES: Auger Electron Spectroscopy; EDX: Electron Dispersive X-ray spectroscopy; i-: in situ; e-: ex situ. R_R indicates the resistivity ratio to the pure metal($\rho_{deposit}/\rho_{pure\ metal}$).*

Precursor	Deposit properties	E (keV)	I_p	T (°C)	Substrate	Remarks	Ref.
WF_6	$R_R \approx 100$	50	100 pA	25	Au/SiO_2		[9]
WF_6	$R_R \approx 10$	50	100 pA	25	Au/SiO	H_2 anneal O_2 plasma	[10]
WF_6	66 at.% W i-(AES)	10	1.5 μA	160	SiO_2		[5]
WF_6	90 at.% W i-(AES) 200 s irr.	3	18.4 μA	-180	Ni	as above	[7]
WF_6	70 at.% W i-(AES) 500 s irr.	3	5.5 μA	-180	Ni	irradiation time effect frozen layer	[7]
WCl_6	58 at.% W 6 at.% Cl, 8 at.% C, 18 at.% O e-(EDX)	15	40 pA	25	Au/Cr on SiO_2		[5]
$W(CO)_6$	55 at.% W, 30 at.% C, 15 at.% O e-(EDX) $R_R \approx 10000$	25	10 nA spot: 150 nm	-3	Si_3N_4		[6]
$W(CO)_6$	$R_R \approx 100000$	5	1 nA	20	Au/GaAs	diff. scan speed	[11]
$W(CO)_6$	$R_R \approx 100$	0.25	4 nA	20	Au/GaAs		[12]
$W(CO)_6$	$R_R \approx 3500$	2	4 nA	20	Au/GaAs		[13]

Table 5-1: *Properties of W containing deposits obtained from the precursors WF_6, WCl_6 and $W(CO)_6$. AES: Auger Electron Spectroscopy; EDX: Electron Dispersive X-ray spectroscopy; i-: in situ; e-: ex situ. R_R indicates the resistivity ratio to the pure metal($\rho_{deposit}/\rho_{pure\ metal}$).*

preliminary in situ O_2 plasma etching of the substrate or post annealing at 500°C in H_2 environment. Comparison between repeated line scanning and single slow scanning at a constant electron dose revealed that wire conductance and deposition rate are both higher when depositing in single slow scanning mode [9].

With the precursor $W(CO)_6$, the first depositions were obtained by Koops et al. [6] in a modified SEM, on Si_3N_4 membrane cooled to -3 °C with a Peltier element. The W content of the deposits, detected with EDX, reached 55 at.%. On the other hand, the measured resistivity was more than four orders of magnitude higher than bulk tungsten. The high values were attributed to the high carbon content (see Table 5-1).

The influence of the scanning speed of the electron beam on the deposit properties, at constant energy and current, was studied by Hoyle et al. with the precursor $W(CO)_6$ [11]. As in reference [10], the authors found that the material resistivity decreases with decreasing scanning speed of the electron beam. The authors explain these results by supposing the deposition of an intermediate product with higher resistivity which is converted to the final product by further irradiation. Since the deposit volume growth rate is higher for exposure at high scanning speeds, the authors concluded that the conversion of the intermediate into the final product is associated with a compaction effect.

Tungsten deposition from $W(CO)_6$ has also been studied at variable electron energies (20, 2, 1, 0.5, 0.15, 0.10, 0.06 keV) with constant electron doses [12]. In situ resistivity measurements showed a drop of four orders of magnitude when changing the electron energy from 20 keV to 2 keV or lower. The lowest resistivity value, measured at 0.25 keV, was $6x10^{-4}$ Ωcm, two orders of magnitude higher than that of bulk W. Resistivity measurements of deposits obtained at $E \leq 150$ eV were not possible due to the presence of cracks.

Other experiments with the same precursor were carried out to study the deposition rate and the material resistivity as a function of the dose per scan (scanning speed) at various electron voltages (2, 5, 10, 15 and 20 keV) [13]. The deposition rate increased with decreasing beam energy and dose per scan. The authors explain this effect by assuming that when the dose per scan decreases a higher number of precursor molecules can reach the irradiated area in the time gap between two irradiations. The maximum rate, in the investigated range, was measured at 2 keV electron energy and $3x10^{-1}$ C/m^2dose per scan. As already shown in other experiments, the deposit resistivity decreased with decreasing electron voltage and increasing dose per scan, with a maximum between 50 C/m^2 and 300 C/m^2 dose per scan. The best measured value was 0.02 Ωcm at 2 keV, 10^5 C/m^2 dose per scan (3500 times higher than pure W). TEM investigation, performed on the same deposits, revealed that the structure turns from amorphous to nanocomposite by increasing the dose per scan. This can be explained by further decomposition of the adsorbed molecules and by stabilization of the stable crystalline phase under electron irradiation.

The effect of annealing in vacuum on deposits obtained from $W(CO)_6$ has been studied by Kislov et al. [14]. W containing rods grown with a 100 keV STEM electron gun show a sharp-

ening of the electron diffraction ring after 15 minutes of in situ vacuum annealing at 600°C. Further increase of the temperature up to 800°C for one hour induced the formation of nanocrystals up to 20 nm in size.

5.2.2 GOLD DEPOSITION

Gold deposition has been until now obtained only from the β-diketonate precursors $Me_2Au(acac)$, $Me_2Au(tfa)$, and $Me_2Au(hfa)$. Differences in structure, composition and electrical properties between structures obtained from the three precursors are in general negligible.

The first Au deposition was obtained by Koops et al. [6] from $Me_2Au(tfa)$. Large areas, lines and dots were deposited on Si_3N_4 membranes, with a modified electron-beam lithography system. The deposits contained 40% Au, 55% C and 5% O.

Another work on Au deposition from the same precursor was performed by Lee and Hatzakis [15] with a focused electron beam. High resolution lines were deposited at various electron energies and exposure times on a Si substrate, at 5°C in a subchamber (experimental conditions reported in Table 5-2). The atomic percentages of Au and C (detected with AES) were found to be 75% and 25%, respectively, and did not change significantly when varying the electron energy (at 30 keV, 5 keV and 2 keV). AES depth profiling detected a stable concentration down to a depth of 0.1 μm. The best measured resistivity was 6 Ωcm (about six orders of magnitude higher than pure Au) and did not improve after annealing at 250°C in He or at 350°C in oxygen. Observation in the transmission electron microscope detected a nanocomposite structure with Au polycristallytes (5 nm in diameter) dispersed in a carbonaceous amorphous matrix.

Also from $Me_2Au(tfa)$ Koops et al. [16] constructed free-standing resistors with a resistivity ratio (to pure Au) of 2500.

TEM observation of EBID structures deposited at different electron currents from all three ß-diketonate precursors is reported in several works [17, 21, 22]. The images reveal an amorphous structure for deposits obtained at low beam current (< 50 pA) and a nanocomposite structure for deposits obtained at higher beam currents (> 50 pA). The polycristalline material shows a face centered cubic (fcc) structure with an elementary cell and lattice planes similar to the one of polycristalline gold.

The Au content in deposits obtained from $(Me)_2Au(tfa)$ could be increased by increasing the beam current [17, 22]: EDX analysis revealed a linear evolution from about 30 wt.% to 65 wt.% (2.5 at.% to 11 at.%) for beam current values included between 50 pA and 800 pA, then it remains stable at higher currents. In good agreement with the increased Au concentration, the deposit resistivity drops by five orders of magnitude by increasing the current from 100 to 900 pA [19], then stays constant for higher current values. The lowest measured resistivity is $2x10^{-2}$ Ωcm at 900 pA. The decrease of resistivity with increasing beam current can be

Precursor	Deposit properties	E (keV)	I_p	T (°C)	Substrate	Remarks	Ref.
$Me_2Au(tfa)$	40 e-(EDX) 40 at.% Au, 55 at.% C, 1.5 at.% O	25	10 nA	0.5	Si_3N_4		[6]
$Me_2Au(tfa)$	25 at.% Au 75 at.% C i-(AES) $R_R \approx 10^6$	30 5 2	50 pA	5	Si	no change with electron voltage or after annealing	[15]
$Me_2Au(tfa)$	$R_R \approx 2500$	25	1 nA	25	free standing		[16]
$Me_2Au(tfa)$	35 wt.% Au e-(EDX) $R_R \approx 10^9$	25	100 pA	25	SiO_2		[17]
$Me_2Au(tfa)$	65 wt.% Au e-(EDX) $R_R \approx 10^4$	25	>900 pA	25	SiO_2		[17]
$Me_2Au(tfa)$	80 wt.% Au e-(EDX) $R_R \approx 100$	25	120 pA	100	SiO_2		[18]
$Me_2Au(tfa)$	$R_R \approx 8500$	25	900 pA	25	SiO_2	R_R decreases with increasing current	[19]
$Me_2Au(hfa)$	50 wt.% Au e-(AES)	15		25	Si	ESEM 10 Torr Ar/O_2	[20]

Table 5-2: *characteristics of Au EBID deposits obtained from Au ß-diketonates. AES: Auger electron spectroscopy; EDX: electron dispersive X-ray spectroscopy; i-: in-situ; e-: ex-situ. R_R indicates the resistivity ratio to the pure metal($\rho_{deposit}/\rho_{pure\ metal}$). I_p: probe current, E: primary electron energy.*

explained by the closer packing of the Au crystallites, as observed in TEM investigation of EBID three-dimensional deposits.

The Au content in deposits obtained from ß-diketonates has been enhanced also working at high substrate temperature [18]. Varying the temperature from 25 °C to 100 °C induced a continuous increase of the Au concentration from 20 wt.% to 80 wt.%. The improved deposit purity with increasing substrate temperature is explained by simultaneous thermal and electron beam induced decomposition of the precursors.

EBID deposited resistor obtained from $Me_2Au(tfa)$ have been characterized at temperatures ranging from -150°C to 180°C [18, 19, 23]. The measurement showed an ohmic behavior of the resistors and a drop of the resistivity by up to two or three orders of magnitude after vacuum annealing at 180 °C.

Au deposition from $Me_2Au(hfa)$ has also been performed in an environmental scanning electron microscope (ESEM) in the presence of Ar, H_2O and of an O_2/Ar mixture at different pressures [20, 24]. The Au content in the deposits, detected ex-situ with AES, without environmental gas was around 3 at.%. In Ar atmosphere the deposited structures contained up to 15 at.% Au and were independent of the gas pressure (1 Torr, 3 Torr and 5 Torr). Deposition in H_2O environment gave deposits with 13 at.% Au at 1 Torr, 15 at.% Au at 2 Torr, 20 at.% Au at 3 Torr. A further improvement was obtained in Ar/O_2 environment: 30 at.% Au at 2.5 Torr, 40 at.% at 7.5 Torr and 50 at.% at 10 Torr. This result can be explained by reaction of oxygen radicals, created in the ESEM, with the carbon contained in the deposited material, which gives the volatile oxides CO and CO_2.

5.2.3 PLATINUM DEPOSITION

The most significant result on platinum deposition are summarized in Table 5-3. The only precursor at present used for platinum EBID is $CpPt(Me)_3$. Pt deposits have properties similar to the Au deposits described above, as explained in several papers [18, 25]. The Pt concentration in the deposits depends on the deposition current: with a constant acceleration voltage of 20 keV the concentration varies from 4 at.% at 100 pA up to 13 at.% at 1200 pA. A similar behavior was found for the electrical resistivity, which decreased by almost two orders of magnitude between 200 pA and 900 pA deposition current. The best obtained value was 10^4 times higher than that of pure Pt [19].

TEM investigation detected metal nanocrystals embedded in an amorphous matrix, with plane distance and elementary cell in good agreement with platinum. The nanocrystal dimensions decrease from the center to the edge [22].

Pt EBID was used also for the production of resistors with 30 keV electrons and 630 pA [18, 19]. The resistivity was measured from -150 °C to 180 °C. As in the case of Au deposits, the electrical resistance decreases by three orders of magnitude after ex-situ annealing at 180 °C. On the other hand, Pt deposits did not show an ohmic behavior, due to their low metal content.

Precursor	Deposit properties	E (keV)	I_p	T (°C)	Substrate	Remarks	Ref.
$CpPt(Me)_3$	$R_R \approx 10^4$	20	900 pA	23	SiO_2		[19]
$CpPt(Me)_3$	13 at.% Pt e-(AES)	20	1.1 nA	23	SiO_2	4% Pt at 100 pA	[22]
$CpPt(Me)_3$	21.5 at.% Pt, 73 at.% C 5.5 at.% O e-(AES) R ≈ 3	30	?	23	SiO_2	dual beam	[26]

Table 5-3: *characteristics of Pt EBID deposits obtained from $CpPt(Me)_3$. AES: Auger electron spectroscopy; EDX: electron dispersive X-ray spectroscopy; i-: in-situ; e-: ex-situ. R_R indicates the resistivity ratio to the pure metal($\rho_{deposit}/\rho_{pure\ metal}$). I_p: primary electron current, E: probe electron energy.*

The dominant mechanism of conduction is probably electron hopping, due to the nanostructure of the deposits.

Pt deposition has been also achieved in a dual beam system to construct a field emission device [26-28]. The deposit growth rate showed an increase with decreasing electron energy and seems to follow the secondary electron yield of the substrate (Si). With 30 keV electrons a deposit composition of 21.5 at.% Pt, 73 at.% C and 5.5 at.% O (detected with AES) was obtained. The resistivity of the same material was 30 $\mu\Omega$cm, only three times higher than for the pure metal. This value is much lower than that measured in reference [19] and cannot be explained by the 21 at.% Pt content.

5.2.4 COPPER DEPOSITION

Copper deposition has been realized from two precursors: $Cu(hfa)_2$ and (hfa)Cu(I)trimethylvinylsilane (trade name Cupra select, Schumacher, USA). The results are listed in Table 5-4.

Deposits obtained from $Cu(hfa)_2$ exhibited low growth rate and shank shape [22]. The dimension of the Cu crystallites in the amorphous matrix, according to TEM observation, were determined to be 1-2 nm. The obtained electron diffraction patterns revealed an amorphous structure. The chemical composition of the deposit was not investigated.

Deposition from Cupra select was performed in an ESEM system [29], under a precursor gas pressure of 1.2 Torr, at 30 keV electron energy and 600 pA electron current. The composition of the same deposit, studied by AES, was determined to be about 11 at.% Cu, 44 at.% C, 35 at.% Si, 9 at.% O and did not change significantly when varying the irradiation time from 1 to 8 minutes and the substrate temperature from 10 °C to 25 °C. The resistivity of lines deposited

Precursor	Deposit properties	E	I_p	T (°C)	Substrate	Remarks	Ref.
$Cu(hfa)_2$					SiO_2		[22]
Cupra select	11 at.% Cu 44 at.% C 9 at.% O 35 at.% Si $R_R \approx 150$ e-(AES)	30 keV	600 pA	10-25	SiO_2	ESEM	[29]
Cupra select	$R_R \approx 2$	50 keV	≈10 nA	25	SiO_2	EB lithography system	[29]
Cupra select	15-5% Cu 70-80% C 10% O 5-10% F i-(AES and XPS)	1-25 eV	60 μAcm^{-2}	27	Si (111) 7x7 sputter cleaned	low energy broad beam	[30]

Table 5-4: *characteristics of Cu EBID deposits obtained from $Cu(hfa)_2$ and Cupra Select. AES: Auger electron spectroscopy; EDX: electron dispersive X-ray spectroscopy; i-: in-situ; e-: ex-situ. R_R indicates the resistivity ratio to the pure metal($\rho_{deposit}/\rho_{pure\ metal}$). I_p: probe current, E: primary electron energy.*

under the same conditions was 240 Ωcm ($R_R \approx 150$). The same authors, depositing in an EB lithography system at 50 keV electron energy, obtain an EBID line with a resistivity of 3.63 $\mu\Omega$cm, only a factor two higher than pure Cu. If the chemical composition is assumed similar to the one obtained in the ESEM system, the low resistivity could be explained, according to the authors, by considering the material as a semiconductor (Si) with high dopant (Cu) concentration. Alternatively, it can be explained by a higher Cu concentration, due to the higher voltage and current used for deposition.

The electron beam induced decomposition of the precursor Cupra select has also been studied at low electron energy (1 eV - 25 eV) [30]. The threshold for electron beam decomposition was found to be around 4 eV. The deposit composition was monitored in situ by AES and XPS. The results revealed that the deposit composition is different from the one of the physisorbed layer. Compared to the precursor molecule, the deposit has a higher concentration of C and Cu and a lower concentration of Si, O and F. The Cu concentration detected by AES was higher than that detected by XPS, probably due to the further decomposition of the film by the high energy electron beam of the AES system. The C content of the deposit ranged from 70-80 at.% and the Cu content from 5 at.% to 10 at.%. Growth rate measurement indicated that the main decom-

position channel in the explored energy range is Dissociative Electron Attachment (DEA) and not direct ionization of (hfa)CuTMVS.

5.2.5 OTHER METALS

Besides W, Au, Pt and Cu some other metals have been deposited by EBID. The characteristics of the deposits and the deposition parameters are reported in Table 5-5.

Iron has been deposited from the precursor $Fe(CO)_5$ [31]. Deposition with electron energy ranging from 1 to 12 keV, with a substrate temperature of 140 °C, gave pure films, in which AES analysis did not detect the presence of C or O after sputter cleaning. The lowest resistivity value was measured at 1 keV deposition energy and it was a factor 10 higher than the one measured for pure Fe.

Os [32], Ru [32], Mo [22], Re [14], Cr [14] [31] have been deposited from their carbonyls; in all the cases the structures show a very high carbon and oxygen contamination. The metallic characteristics of the Cr- and Re- containing deposits can be improved by in situ thermal annealing, as already explained for W deposits from $W(CO)_6$ [14]. Cr has been deposited also from $Cr(C_6H_6)_2$ [5]. The chemical composition, detected by AES, was 16% Cr, 62% C and 22% O. These deposits are not removed by dry etching with CF_4.

Mo content in the deposits does not exceed 10 at.% [18] and is not very sensitive to temperature or current changes. The diffraction patterns for Mo containing deposits are similar to the diffraction patterns of MoC [22].

Si has been deposited from SiH_2Cl_2 at 120 keV in a STEM [33]. The obtained deposits showed amorphous structure; the chemical composition was not measured.

EBID tin films have been realized from frozen layers of the precursor $SnCl_4$ with 2keV electrons at a substrate temperature of 120K [34]. The deposits showed a Sn/Cl ratio of almost 1 (measured with RBS) and a resistivity 25 times higher than that of pure Sn.

Aluminum has been deposited from the precursor trimethyl aluminum (TMA) with an electron energy of 6 keV and an electron current of 10 pA [35]. Depositions were carried out for various exposure times at substrate temperatures of 28°C and 80°C. Electron-probe-micro-analysis detected signals from Al and C in all the deposited structures. The spectra show also that the deposit purity increases with exposure time and with substrate temperature.

Precursor	Deposit properties	E (keV)	I_p	T (°C)	Substrate	Remarks	Ref.
$Fe(CO)_5$	pure Fe $R_R \approx 10$	1	?	140	Si	probably thermal CVD	[31]
$Cr(CO)_6$	low C content $R_R \approx 6\text{-}12$	1	?	280 330	Si	as above	[31]
$Cr(CO)_6$ $Re_2(CO)_{10}$	nanocrystals $R_R \approx 10^8$	100	?	23	Si(111)	crystal size increases after annealing at 600 °C	[14]
$Os_3(CO)_{12}$ $Ru_3(CO)_{12}$	metallic grains 0.1 nm-20 nm	40	15 mA/cm^2	-10 -40 -105	Si	masked electron beam	[32]
SiH_2Cl_2	amorphous	120	100 A/cm^2	50	Si fine particles	TEM	[33]
$Mo(CO)_6$	10 at.% Mo 40 at.% O 50 at.% C e-(EDX)	20	1.5 nA	RT	SiO_2	no current or temper-ature effects	[22]
$Cr(C_6H_6)_2$	16 at.% Cr 62 at.% C 22 at.% O e-(AES)	15	40 pA	RT	SiO_2		[5]
$SnCl_4$	Sn:Cl = 1:1 e-(RBS) $R_R \approx 25$	2	?	-153	Si	$SnCl_4$ frozen layer	[34]
$Al(CH_3)_3$	presence of Al	6	10 pA	28 80	GaAs		[35]

Table 5-5: *Characteristics of EBID deposits containing different metals. AES: Auger electron spectroscopy; EDX: electron dispersive X-ray spectroscopy; i-: in-situ; e-: ex-situ. R_R indicates the resistivity ratio to the pure metal($\rho_{deposit}/\rho_{pure\ metal}$). RBS: Rutherford backscattering. I_p: probe current, E: primary electron energy.*

5.3 GROWTH RATE

The growth rate is in general expressed as deposited volume as a function of time or in some case as deposit height versus time (3D growth rate). The deposition parameters affecting the growth rate in EBID can be related to the precursor, the electron beam and the substrate.

The most important precursor properties influencing the growth rate are the vapor pressure and the decomposition cross section. The effect of the precursor vapor pressure on EBID growth rate can be observed when the rate-determining step of the process is the precursor transport in the reaction area. In this case an increase of vapor pressure will increase the number of precursor molecules decomposed by the electron beam in the reaction area. As already explained in Chapter 3, the number of molecules reaching the reaction area depends also on the precursor supply system. In a subchamber system the number of molecules reaching the surface is defined only by the vapor pressure of the precursor. In a needle-based system the number of molecules reaching the surface and the focusing of the molecular beam are determined by the precursor vapor pressure and by the dimensions of the needle. A localized high pressure on the sample can be produced using a conical nozzle instead of a conventional needle with a constant diameter [36]. With this system it has been possible to increase by a factor four (19 nm/s against 5 nm/s for a normal needle) the rate for W deposition from $W(CO)_6$ [9, 36], because of better focusing of the molecular beam. The decomposition cross section will be discussed later.

The electron beam parameters affecting the growth rate are the beam current, the beam energy, and the scanning mode. An increase of the electron beam current determines an increase of the deposit diameter and volume because of a broadening of the beam distribution. In the case in which the deposition rate is determined by the electron flux an increase of the electron current determines an increase of the deposit height.

The electron voltage acts on the deposition rate via the electron impact dissociation and ionization cross section. Electron decomposition cross sections depend on the electron energies and on the ligands present in the molecules; typical values are in the $Å^2$ range (10^{-16} cm^2). Measurements of this parameter require a very complicated experimental setup [37]; therefore the values are known only for simple molecules at low electron energy (< 1 keV). The values at higher energies can be extrapolated by analogy with electron impact ionization cross sections, for which more literature data are available [38]. Electron impact decomposition and ionization cross sections are reported in Fig. 5-1. The plot reported in Fig. 5-1a shows that CO ionization is about a factor of five more probable than dissociation. Both cross sections for CO have a maximum at electron energies lower than 100 eV. For example, the decomposition cross section has a maximum of 0.75 $Å^2$ at a primary electron energy of 48.5 eV, then it decreases by a factor of two at 200 eV. The plot in Fig. 5-1b shows that the ionization cross sections decrease with the electron energy by about one order of magnitude at electron energies higher than 1 keV. Since the two curves in Fig. 5-1a are almost parallel, a similar behavior is assumed for the decomposition cross section. This result shows that the secondary electrons are more efficient than primary electrons to induce the processes leading to EBID. Furthermore the deposition rate should increase by decreasing the primary electron energy since both cross sections and secondary electron yield become higher. It must however be pointed out that the

values of ionization and dissociation cross sections can be different for EBID precursor molecules, since different channels for dissociation can exist.

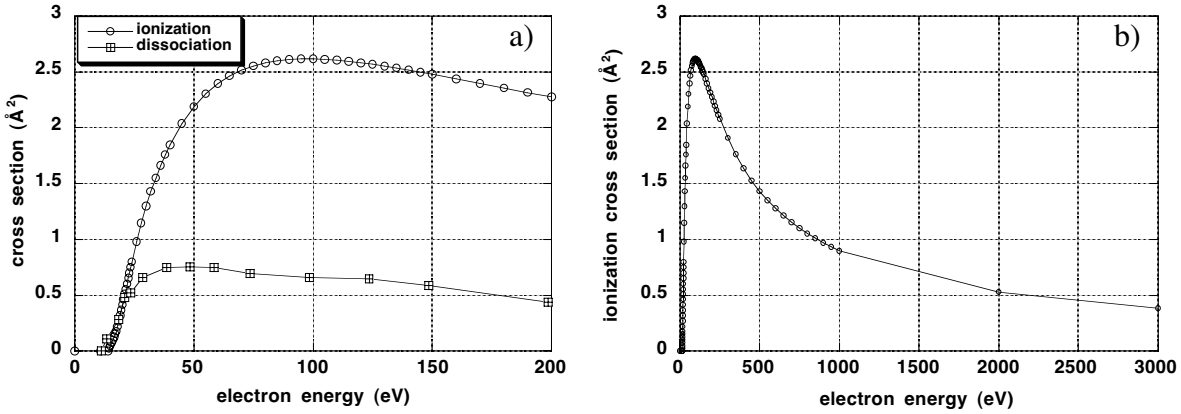

Figure 5-1: *(a) Electron impact ionization [38] and dissociation [37] cross section for CO between 10 eV and 200 eV; (b) electron impact ionization cross section for CO between 0 and 3 keV [38].*

The effect of decreasing electron voltage on the deposition rate has been studied in the work by Hoyle et al.[12] for W deposition from $W(CO)_6$. Experiments done at different electron energies from 20 to 0.06 keV exhibited a maximum deposition rate between 0.1 and 1 keV primary energy, with a drop of a factor four at 10 keV. The maximum for deposition rate matches the maximum for secondary electron yield for tungsten, with a deviation at lower energies, probably due to increasing contribution of the primary electrons to the process. The effect of secondary electrons on growth rate is confirmed by the work of Kunz et al. [39], which reported that electron beam induced oxidation of Si shows a maximum reaction rate corresponding to the maximum of the secondary electron yield for Si.

When deposition is performed by exposing moving the beam in spot mode from one point to the next, the deposit growth rate can be optimized with an appropriate setting of two characteristic parameters: the dwell time (t_d) and the loop time (t_l). t_d is the time spent by the beam on a pixel; t_l is the time taken by the beam to return to the same pixel.

With a constant loop time, the deposition rate decreases with increasing dwell time. When the dwell time is constant, the rate increases by increasing the loop time [40]. The decreasing rate with increasing dwell time is the result of the progressive decomposition of the adsorbate layer by e-beam induced decomposition. The amount of decomposed molecules per unit time is therefore larger in the beginning than in later intervals of dwell time. Another possibility is a change in the supply mechanism from diffusion at the surface to diffusion from a constant area of the grown cylinder. The higher rates obtained for longer loop time resulted from the increased adsorbate density due to longer replenishing time.

Hiroshima et al. [9] found that the rate for line deposition is higher in slow scanning mode than in fast repeated scanning mode. In slow scanning mode the electron beam strikes an inclined front of the depositing wire, while in fast scanning mode the beam strikes always a flat surface. The phenomenon was explained by a higher secondary electron yield in slow scanning mode due to a higher angle of incidence of the primary beam.

The catalytic effect of the substrate was studied by Kunz et al. [41]. They showed that spontaneous Fe deposition can be obtained at 125°C on pre-electron-beam-deposited Fe layers with a rate 900 times higher than on Si substrates.

The first theoretical description of the EBID rate was formulated by Christy in 1960 [3]. The same model, with some modifications, has been used also by other authors and showed good agreement with the experimental data [6, 32] [11]. The models distinguish two cases: growth limited by the precursor flux or growth limited by the electron beam current. A model taking into account also surface diffusion was developed by Reimer. All these models are described in the following paragraphs [42].

5.3.1 MODEL OF CHRISTY

The model of Christy [3] was developed to explain the growth of polymeric films from a silicone oil vapor with a deposition energy of 225 eV and a current density ranging from 0.05 mA cm^{-2} to 0.6 mA cm^{-2}(for a focused beam of 20 nm diameter, with a current of 50 pA, the density is about 1 Acm^{-2}). The deposition rate is calculated using a phenomenological model. The assumption is that the electron beam induces cross-linking of the molecules adsorbed at the surface transforming them into a solid film. The derivation of the model is presented for a better understanding of the physical parameters influencing the growth rate.

Let us consider a number n of molecules per unit area adsorbed on a surface, with a mean residence time τ. An electron hitting one of these molecules can incorporate it into the deposit. If P is the number of molecules per unit area which are cross linked and dP/dt is the growth rate of the film, assuming a first order rate process we obtain

$$\frac{dP}{dt} = \sigma_E n \frac{j}{e} = \sigma_E n f \tag{5. 1}$$

where σ_E is the cross section for the cross linking, j the current density, e the electron charge, f the number of electrons per unit area per unit time, as discussed in Chapter 2. Since every cross linking event removes an adsorbed molecule from the number n on the surface, the rate of concentration change is expressed by the following three term differential equation:

$$\frac{dn}{dt} = J - \frac{n}{\tau} - \frac{dP}{dt} = F - \frac{n}{\tau} - \sigma_E n f = J - n\left(\frac{1}{\tau} + \sigma_E f\right) \tag{5. 2}$$

where J is the number of gas molecules impinging on the surface per unit area and unit time (discussed in Chapter 3). Integrating Eq. 5. 2 we get

$$N = \left[\frac{J}{\sigma_E f + 1/\tau}\right]\left[1 - \Theta e^{-(\sigma_E f + 1/\tau)t}\right] \tag{5. 3}$$

where Θ is a constant depending on the number of molecules initially adsorbed at the surface. Let us now consider the case in which the surface is not completely covered with molecules (less than one monolayer adsorbed), so that $n < 1/a$, where a is the area of the molecule. This assumption requires that the number of gas molecules impinging at the surface is less than the sum of the desorbing and cross linked molecules:

$$J < (\sigma/a) f + 1/(a\tau) \tag{5. 4}$$

By inserting Eq. 5. 3 into 5. 1 and integrating we get the number of cross linked molecules:

$$P = \frac{J}{1 + 1/(\sigma_E \tau f)}\left\{t + \frac{K}{\sigma_E f + 1/\tau}\left[e^{-(\sigma_E f + 1/\tau)t} - 1\right]\right\} \tag{5. 5}$$

Unless both $\sigma_E f$ and $1/\tau$ are very small compared to unity, the exponential term can be neglected, so that

$$P \approx \left\{\frac{J}{1 + 1/(\sigma_E \tau f)}\right\} t \tag{5. 6}$$

The total thickness of the film is vP, where v is the volume of one molecule. Defining the rate of film formation by $R = vP/t$, we obtain:

$$R = \frac{vJ}{1 + 1/(\sigma_E \tau f)} \quad \text{when} \quad F < (\sigma_E/a) f + 1/(a\tau) \tag{5. 7}$$

According to this result, at high current density or low temperatures, when $\sigma\tau f >> 1$ the rate saturates at a value vF determined by the effective vapor pressure (or flux) of the precursor. At very low current density or high temperature, on the other hand, the rate is approximately $\sigma_E \tau f v F$, depending also on current density and temperature.

If the flux is so large that there is always an adsorbed monolayer of molecules, $n = 1/a$ should be put into Eq. 5. 1 so that

$$R = \frac{\sigma_E}{a}(vf) \quad \text{when} \quad F \geq \frac{\sigma_E}{a} f + \left(\frac{1}{a\tau}\right). \tag{5. 8}$$

This result is independent of the precursor pressure, since there is a molecule waiting to be hit for every impinging electron.

Since not more than one electron-molecule collision on the surface is assumed, the rate of film formation should not depend on the electron energy, unless the cross section σ is energy dependent. The length of the cross links may depend on electron energy, since more cross links may be formed in lower layers if the electrons are sufficiently energetic. If each electron produces one cross link, the number of cross links per unit area formed per unit time is f. Dividing by the rate of the film formation calculated from Eq. 5. 6, the number of cross links per molecule δ is

$$\delta = \frac{1 + \sigma_E \tau f}{\sigma_E \tau J} \tag{5. 9}$$

On the other hand, when Eq. 5. 8 applies, $\delta = 1$. If the electrons are energetic enough to produce more than one cross link each, δ will be correspondingly greater. Experimental data show that δ is in general larger than unity. For calculation of J see Chapter 3.

5.3.2 MODEL OF SCHEUER AND KOOPS

This model [32] is based on that of Christy with some modifications. The main assumption is that only molecules adsorbed at the surface undergo electron-induced dissociation, thus only a monolayer of precursor contributes to the layer growth. The rate of concentration change is expressed by

$$\frac{dn}{dt} = sJ\left(1 - \frac{n}{\eta_0}\right) - \frac{n}{\tau} - \sigma_E n f = sF - n\left(\frac{sf}{\eta_0} + \frac{1}{\tau} + \sigma_E f\right) \tag{5. 10}$$

where s is the sticking coefficient of the precursor on the substrate, F the precursor flux, N the density of the adsorbed molecules, f the electron flux, τ the adsorption time, σ_E the electron decomposition cross section, η_0 the molecular density in a monolayer. The introduction of n/η_0 limits the process to one monolayer coverage. The growth rate of the film is given by Eq. 5. 1. The steady-state growth rate is therefore

$$R = \frac{vsF}{1 + \dfrac{\eta_0 + s\tau F}{\eta_0 \tau \sigma_E f}}. \tag{5. 11}$$

The deposition efficiency is defined as the layer volume divided by the charge required for deposition. The reciprocal efficiency can be calculated as follows for the case $\tau sF < \eta$, i.e. the flux reaching the surface does not form a monolayer:

$$W^{-1} = \frac{e}{\tau q \sigma_E vsF} + f\frac{e}{vsF} = \Upsilon + f\partial. \tag{5. 12}$$

In the case in which the surface is always covered with a monolayer we get

$$W^{-1} = \frac{e}{\eta_0 \sigma_E v} + f\frac{e}{vsF} = \Xi + f\partial . \quad (5.13)$$

The reciprocal efficiency can be calculated by measuring the electron current and the volume of the deposit. Determination of the reciprocal efficiency allows to calculate some terms present in Eqs. 5. 12 and 5. 13 by plotting W^{-1} versus f. The mean relaxation time of adsorbed molecules can be calculated from

$$\tau = \frac{s\Xi\eta_0}{\Upsilon} . \quad (5.14)$$

The number of electrons to incorporate a monolayer (assuming $s = 1$) is:

$$z = \frac{f}{R\partial f} . \quad (5.15)$$

The cross section σ for layer formation (still assuming $s = 1$) can be derived from

$$\sigma_L = \frac{\partial F}{\eta_0 \Xi} . \quad (5.16)$$

For deposition from $Ru_3(CO)_{12}$, the authors found $\tau = 1.4\pm1\ s, z = 280\pm110, \sigma_L = 0.2\pm0.15\ \AA^2$. The last of these values is in good accordance with the measured data for CO (reported in Fig. 5-1). The model holds only for deposition of flat layers since for three-dimensional structures edge backscattering and secondary emission must be taken into account.

5.3.3 MODEL OF REIMER

The model developed by Reimer [42] describes contamination deposition under different irradiation conditions. Three types of irradiation conditions may be distinguished: uniform irradiation of a large area (>10 μm), irradiation of a small area with uniform current density (few μm), and irradiation with an electron probe (< 50 nm). In the first case flat thin films are obtained. When a small area is irradiated an annular contamination spot can be observed with more contamination at the periphery of the irradiated area than at the centre. The contamination rate is higher than that found with uniform illumination of a large area because the whole foil is a source which supplies molecules by surface diffusion. Irradiation with an electron probe gives a cone shaped contamination spot, broadened at the bottom by electron scattering effect. If a thin foil is used as specimen a contamination cone will be deposited also at its bottom.

The rate equation is similar to the one proposed by Christy but includes an additional term which takes into account surface diffusion of the adsorbed molecules into the reaction area:

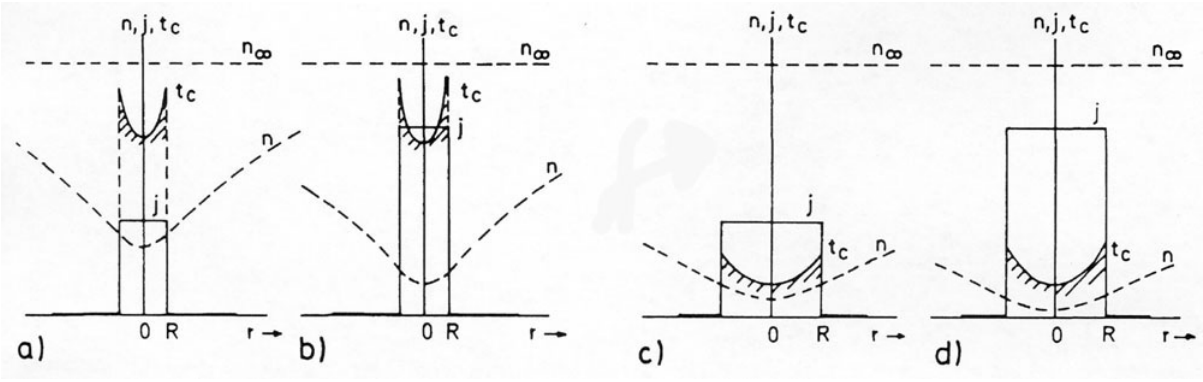

Figure 5-2: *Equilibrium of the concentration n(r) of adsorbed organic molecules [42]. The irradiated area r < R acts as a sink for mobile molecules, so that a contamination layer of thickness proportional to n(r)jt is formed. The irradiated area shows in (c) and (d) twice the diameter 2R as in (a) and (b) and the current density in (b) and (d) a factor two larger than in (a) and (c).*

$$\frac{dN}{dt} = F - \frac{N}{\tau} - \frac{j}{e}\sigma_E N + D_S \nabla^2 n \tag{5.17}$$

where D_S represents the diffusion coefficient of the precursor at the surface. Applying the equilibrium conditions and imposing rotational symmetry we obtain

$$F - \frac{n}{\tau} + l\left(\frac{\partial^2 n}{\partial r^2} + \frac{1}{r}\frac{dn}{dr}\right) - \frac{j}{e}\sigma_E n = 0\,. \tag{5.18}$$

With the abbreviations $\xi = (\tau D_S)^{1/2}$, $\chi = \sigma/eD_S$, F/l = n/ξ^2, this equation can be written as

$$\frac{dn}{dr^2} + \frac{1}{r} - \frac{1}{\rho^2}n(r) - \chi j(r) + \frac{n_\infty}{\rho\xi^2} = 0\,. \tag{5.19}$$

If uniform irradiation is assumed in the area of radius $r \leq R$, the equation can be solved in this inner area:

$$n_1 = n_\infty\left[1 - C_1 A_0\left(\frac{r}{\xi}\right)\right] \tag{5.20}$$

and in the outer non-irradiated area $r \geq R$,

$$n_2 = n_\infty \left[\frac{\rho^2_0}{\rho^2} + C_2 B_0\left(\frac{r}{\xi_0}\right) \right] \quad \text{with} \quad \xi_0 = \xi(1 + \chi^2 \xi^2 j_0)^{-1/2} \ . \tag{5.21}$$

The constants C_1 and C_2 can be determined by the boundary conditions at $r = R$: $n_1(R) = n_2(R)$ and $dn_1(R)/dr = dn_2(R)/dr$. A_0 and B_0 are the modified Bessel (Hankel) functions. An example of the resulting distribution $n(r)$ and the thickness

$$T = \frac{\sigma_E n(r) j}{e} t \tag{5.22}$$

of the contamination layer is shown in Figs. 5-2 a-d. The irradiated area acts like a sink for hydrocarbons: increasing the current density j by a factor two (a to b and c to d), the molecular density at the surface $n(r)$ decreases to almost half the value observed at lower j. At given irradiation current j and molecular density n, this results in a growth of contamination of thickness t_c, proportional only to the irradiation time t (since $\sigma n(r)j/e$ = const). For constant j, increasing the radius R of the irradiated area (a to c) results in a decrease of $n(r)$, which is approximately proportional to r^{-2}. The proportionality of $n(r)$ to $(jR^2)^{-1} = I_p^{-1}$ results in a constant total mass of contamination per unit time. There is thus a saturation effect, caused by the delayed diffusion of hydrocarbon molecules from the unirradiated part of the foil.

5.4 ULTIMATE RESOLUTION

The ultimate resolution of the EBID process is mainly determined by the primary electron beam size and distribution (i.e. by the type of electron gun and by the electron optics of the deposition system). Additional effects can arise from the distribution of the secondary and backscattered electrons emitted from the substrate or by beam broadening induced by charging effects. The best resolution in EBID has been achieved by growing the deposit laterally from WCl_6 on fine silicon particles with a 120 keV TEM electron beam, with a current density of 100 A/cm^2 and a spot size of 3 nm [33]. These conditions allowed to obtain 3D rods with a diameter of 15 nm. In more conventional applications, however, with a perpendicular impact of the beam with the surface, the ultimate resolutions of three-dimensional structures range from 100 nm to 200 nm. Assuming a Gaussian intensity distribution of the electron beam, all the reported measurements exhibit a broadening of the deposit compared to the beam diameter (2σ of the Gaussian function) [43] [15].

The ultimate resolution as a function of the beam voltage and current was studied by Kohlmann von Platen et al. [43] depositing with the precursor $W(CO)_6$. Three-dimensional needle-like structures were deposited for one minute each at electron energies of 5 keV, 20 keV and 30 keV, with the current ranging from 100 to 500 pA. The diameter of the deposit increased with increasing beam current and decreasing beam energy, according to the larger beam diameter. Extrapolation to zero beam current shows an offset of 100 nm, independently of the beam energy. To evaluate the time progression of the needle height $h(t)$ and the needle diameter at the base $b(t)$, deposits were carried out for times ranging from 5 to 180 s, at 5 keV

(25 pA), 20 keV (100 pA) and 30 keV (100 pA). The time dependence of the deposit height h(t) and width b(t) fits the functions

$$h(t) = at + v(1 - e^{\alpha t}) \quad \text{and} \quad b(t) = gt + c(1 - de^{-\beta t}) \tag{5.23}$$

where a, v, α, g, c and β are the fitting parameters. The result indicates that the needle diameter at the base continues to increase during deposition. The lateral growth rate is explained by broadening of the secondary electron distribution with increasing angle of incidence determined by the conical shape of the deposit.

The ultimate resolution for EBID three-dimensional deposits was studied also by Lee et al. for high aspect ratio tips obtained from $Me_2Au(tfa)$. Deposition with 30 keV electron voltage, 50 pA electron current and a spot size of 10 nm gave features with a column diameter of 100 nm and apex diameter of about 50 nm [15]. The column diameters were found to be independent of the substrate thickness and to decrease with increasing voltage. The discrepancy between the beam size and tip diameter was attributed to forward scattering of the electrons in the deposited column.

The cone angle, i.e. the apex diameter, of EBID tips has been extrapolated, with Monte Carlo simulations, from the spatial distribution brought into the tip by the impinging electrons [21]. The calculated spatial distribution showed good agreement with experimental cone angles of contamination tips consisting mainly of carbon. This agreement proves that the cone angle of the deposited tip is mainly determined by elastic scattering of the primary electrons. The simulations indicate also that the cone angle of the tip should increase with the average atomic number of the deposit, due to the increase of the characteristic angle for elastic scattering. Therefore, tips with small cone angles (less than 20°) should be produced with light elements using high acceleration voltages.

For three-dimensional deposits the discrepancy between the beam size and the column diameter can be explained by scattering in the deposit and by increasing the incidence angle of the primary beam which occurs with increasing deposit height. The effect of the electron scattering, simulated by a Monte Carlo method, with an electron beam of 25 keV will be discussed in Chapter 7. The electron range (R) in the deposited material is bigger than the column diameter. Therefore most of the impinging electrons do not lose their energy in the deposit and are backscattered from the lateral walls, where they induce the emission of secondary electrons (SE2). The precursor molecules adsorbed at the deposit surface can be decomposed by the emerging electrons, resulting in an increase of the deposit diameter. The region of exit of the scattered electrons is shifted upwards with increasing deposit height, therefore the ultimate diameter of three-dimensional deposits stays constant with time. The conical shape of the tip apex is explained by the fact that less BSE and SE2 participate in the decomposition process in this region.

The ultimate resolution of EBID lines as a function of the electron voltage was studied by Lee et al. [15]. The lines were deposited from the precursor $Me_2Au(tfa)$, at variable exposure times, on a Si substrate at 5°C in a subchamber. The deposits were carried out with a focused electron

beam at a constant current of 50 pA at 30 keV (10 nm resolution) and 2 keV (50 nm resolution). High voltage deposition gave lines with a thickness increasing with the electron dose with an ultimate resolution of 30 nm. Low voltage deposition gave lines with ultimate resolution close to the beam diameter and with two distinct features: a central thicker film and a roughly uniform and thinner external halo. Experimentally it was found that the halo decreased with the beam voltage, which excludes that it is deposited by the BSE.

5.5 CONCLUSIONS

EBID of pure metal has not yet been achieved and only a few metal containing structures have been deposited. In general the structure of the deposits is nanocomposite with metal nanocrystals embedded in a lighter amorphous matrix, containing contaminants coming from the precursor molecule or from the reaction environment. High purity deposits can be obtained using carbon- and oxygen-free precursors.

Other methods to improve the properties of the deposits are: increasing the electron current and decreasing the electron voltage, substrate heating during deposition, ex-situ thermal annealing in vacuum or in the presence of reactive gases, deposition in a reactive environment and preliminary O_2 plasma cleaning of the substrate.

The resolution of the process is determined by the characteristics of the electron beam distribution and by the secondary emission properties of the substrate. In general, the narrower the electron beam distribution, the higher is the process resolution. Nevertheless the ultimate resolution in EBID is always at least a factor three worse than the beam diameter. This effect has not yet been understood. A high BSE emission can induce deposition outside of the directly irradiated area.

The growth rate is influenced by the electron beam voltage and current, the precursor vapor pressure, the decomposition cross section, by the catalytic properties and the secondary emission of the substrate. Decreasing the electron energy increases the decomposition cross section and the secondary electron yield and therefore the deposition rate. An increase of the electron current determines an increase of the deposition rate, if the deposition process is current limited. The precursor vapor pressure determines the number of molecules reaching the reaction area. An increase of the reaction rate can be obtained also by selecting an appropriate *L/D* ratio for the tube used for precursor supply. The substrate can induce rate enhancement by catalytic effects or by emission of secondary or backscattered electrons.

The decomposition and ionization cross section are about a factor 10 higher for secondary electrons than for primary electrons at the energy typically used in scanning electron microscopes.

5.6 REFERENCES

[1] R. Lariviere Stewart; *Insulating films formed under electron and ion bombardment*; Phys. Rev., 45 (1934); p. 488-490.

[2] A.E. Ennos; *The Sources of Electron-Induced Contamination in Kinetic Vacuum Systems*; Brit. J. Appl. Phys., 5 (1954); p. 27-31.

[3] R.W. Christy; *Formation of thin polymer films by electron bombardment*; J. Appl. Phys., 31 (1960); p. 1680-1683.

[4] A.N. Broers, W.W. Molzen, J.J. Cuomo, N.D. Wittels; *Electron-beam fabrication of 80-Å metal structures*; Appl. Phys. Lett., 29 (1976); p. 596-598.

[5] S. Matsui, K. Mori; *New selective deposition technology by electron beam induced surface reaction*; J. Vac. Sci. Technol. B, 4 (1985); p. 299-304.

[6] H.W.P. Koops, R. Weiel, D.P. Kern, T.H. Baum; *High-resolution electron-beam induced deposition*; J. Vac. Sci. Technol. B, 6 (1988); p. 477-481.

[7] D.A. Bell, J.L. Falconer, L. Zhiming, C.M. McConica; *Electron beam-induced deposition of tungsten*; J. Vac. Sci. Technol. B, 12 (1994); p. 2976-2979.

[8] R.B. Jackmann, J.S. Foord; *Electron-beam stimulated chemical deposition of patterned tungsten films on Si (100)*; Appl. Phys. Lett., 49 (1988); p. 196-198.

[9] H. Hiroshima, M. Komuro; *High growth rate for slow scanning in electron-beam-induced deposition*; Jpn. J. App. Phys. 1, 36 (1997); p. 7686-7690.

[10] M. Komuro, H. Hiroshima, A. Takechi; *Miniature tunnel junction by electron-beam-induced deposition*; Nanotechnology, 9 (1998); p. 104-107.

[11] P.C. Hoyle, M. Ogasawara, J.R.A. Cleaver, H. Ahmed; *Electrical resistance of electron beam induced deposits from tungsten hexacarbonyl*; Appl. Phys. Lett., 62 (1993); p. 3043-3045.

[12] P.C. Hoyle, J.R.A. Cleaver, H. Ahmed; *Ultralow-energy focused electron beam induced deposition*; Appl. Phys. Lett., 64 (1994); p. 1448-1450.

[13] P.C. Hoyle, J.R.A. Cleaver, H. Ahmed; *Electron beam induced deposition from $W(CO)_6$ at 2 to 20 keV and its applications*; J. Vac. Sci. Technol. B, 14 (1996); p. 662-673.

[14] N.A. Kislov, I.I. Khodos, E.D. Ivanov, J. Barthel; *Electron beam induced fabrication of metal-containing nanostructures*; Scanning, 18 (1996); p. 114-118.

[15] K.L. Lee, M. Hatzakis; *Direct electron-beam patterning for nanolithography*; J. Vac. Sci. Tech. B, 7 (1989); p. 941-946.

[16] H.W.P. Koops, J. Kretz, M. Rudolph, M. Weber; *Constructive three-dimensional lithography with electron-beam induced deposition for quantum effect devices*; J. Vac. Sci. Technol. B, 11 (1993); p. 2386-2389.

[17] H.W.P. Koops, J. Kretz, M. Rudolph, M. Weber, G. Dahm, K.L. Lee; *Characterization and application of materials grown by Electron-Beam-Induced Deposition*; Jpn. J. Appl. Phys. 1, 33 (1994); p. 7099-7107.

[18] H.W.P. Koops, C. Schossler, A. Kaya, M. Weber; *Conductive dots, wires, and supertips for field electron emitters produced by Electron-Beam-Induced Deposition on samples having increased temperature*; J. Vac. Sci. Technol. B, 14 (1996); p. 4105-4109.

[19] C. Schossler, A. Kaya, J. Kretz, M. Weber, H.W.P. Koops; *Electrical and field emission properties of nanocrystalline materials fabricated by electron-beam induced deposition*; Microelectron. Engin., 30 (1996); p. 471-474.

[20] A. Folch, J. Tejada, C.H. Peters, M.S. Wrighton; *Electron-Beam Deposition of Gold Nanostructures in a Reactive Environment*; Appl. Phys. Lett., 66 (1995); p. 2080-2082.

[21] M. Weber, M. Rudolph, J. Kretz, H.W.P. Koops; *Electron-Beam-Induced-Deposition for fabrication of vacuum field emitter devices*; J. Vac. Sci. Technol. B, 13 (1995); p. 461-464.

[22] M. Weber, H.W.P. Koops, M. Rudolph, J. Kretz, G. Schmidt; *New compound quantum-dot materials produced by Electron-Beam-Induced-Deposition*; J. Vac. Sci. Technol. B, 13 (1995); p. 1364-1368.

[23] H.W.P. Koops, M. Weber, C. Schössler, A. Kaya; *Three-dimensional additive electron beam lithography*; Proceedings of the SPIE, 2780 (1996); p. 388-395.

[24] A. Folch, J. Servat, J. Esteve, J. Tejada, M. Seco; *High-Vacuum Versus Environmental Electron-Beam Deposition*; J. Vac. Sci. Technol. B, 14 (1996); p. 2609-2614.

[25] H.W.P. Koops, A. Kaya, M. Weber; *Fabrication and characterization of platinum nanocrystalline material grown by electron-beam-induced Deposition*; J. Vac. Sci. Technol. B, 13 (1995); p. 2400-2403.

[26] O. Yavas, C. Ochiai, M. Takai, A. Hosono, S. Okuda; *Maskless fabrication opf field-emitter array by focused ion and electron beam*; Appl. Phys. Lett., 76 (2000); p. 3319-3321.

[27] M. Takai, T. Kishimoto, H. Morimoto, Y.K. Park, S. Lipp, C. Lehrer, L. Frey, H. Ryssel, A. Hosono, S. Kawabuchi; *Fabrication of field emitter array using focused ion and electron beam induced reaction*; Microelectron. Engin., 41/42 (1998); p. 453-456.

[28] O. Yavas, C. Ochiai, M. Takai, Y.K. Park, C. Lehrer, S. Lipp, L. Frey, H. Ryssel, A. Hosono, S. Okuda; *Field emitter array fabricated using focused ion and electron beam induced reaction*; J. Vac. Sci. Technol. B, 18 (2000); p.

[29] Y. Ochiai, J. Fujita, S. Matsui; *Electron-beam-induced deposition of copper compound with low resistivity*; J. Vac. Sci. Technol. B, 14 (1996); p. 3887-3891.

[30] S. Mezhenny, I. Lyubinetsky, W.J. Choyke, J.J.T. Yates; *Electron stimulated decomposition of adsorbed hexafluoroacetylacetonate Cu(I) vinyltrimethylsilane, Cu(I)(hfac)(vtms)*; J. Appl. Phys., 85 (1999); p. 3368-3373.

[31] R.R. Kunz, T.M. Mayer; *Electron beam induced surface nucleation and low temperature decomposition of metal carbonyls*; J. Vac. Sci. Technol. B, 6 (1988); p. 1557-1564.

[32] V. Scheuer, H. Koops, T. Tschudi; *Electron beam decomposition of carbonyls on Silicon*; Microelectron. Engin., 5 (1986); p. 423-430.

[33] T. Ichihashi, S. Matsui; *In situ observation on electron beam induced chemical vapor deposition by transmission electron microscope*, in 19th Conf. Solid State Devices and Materials, 1987, Bus. Center Acad. Soc. Japan, Tokyo, p.565.

[34] H.O. Funsten, J.W. Boring, R.E. Johnson; *Low-temperature beam-induced deposition of thin tin films*; J. Appl. Phys., 71 (1992); p. 1475-84.

[35] A. Ishibashi, K. Funato, Y. Mori; *Electron-beam induced resist and aluminum formation*; J. Vac. Sci. Technol. B, 9 (1991); p. 169-172.

[36] K.T. Kohlmann, M. Thiemann, W.H. Brünger; *E-beam induced X-ray mask repair with optimized gas nozzle geometry*; Microelectron. Engin., 13 (1991); p. 279-282.

[37] P.C. Cosby; *Electron-impact dissociation of carbon monoxide*; J. Chem. Phys., 98 (1993); p. 7804-7818.

[38] Web site of the National Institute of Standard and Technology, http://physics.nist.gov/PhysRefData/Ionization/EII_table.html.

[39] R.R. Kunz, T.M. Mayer; *Summary Abstract: Surface reaction enhancement via low energy electron bombardment and secondary electron emission*; J. Vac. Sci. Technol. B, 5 (1986); p. 427-429.

[40] K.T. Kohlmann von Platen, L.M. Buchmann, H.C. Petzold, W.H. Brunger; *Electron-beam induced tungsten deposition: growth rate enhancement and applications in microelectronics*; J. Vac. Sci. Technol. B, 10 (1992); p. 2690-2694.

[41] R.R. Kunz, T.M. Mayer; *Catalytic growth rate enhancement of electron beam deposited iron wires*; Appl. Phys. Lett., 50 (1987); p. 962-964.

[42] L. Reimer; *Transmission Electron Microscopy*; Springer, 1997.

[43] K.T. Kohlmann von Platen, J. Chlebek, M. Weiss, K. Reimer, H. Oertel, W.H. Brunger; *Resolution limits in electron-beam induced tungsten deposition*; J. Vac. Sci. Technol. B, 11 (1993); p. 2219-2223.

CHAPTER 6 *Experimental setup and characterization techniques*

In this chapter I describe the EBID experimental set-up and the various techniques used for sample characterization.

6.1 EXPERIMENTAL SET-UP FOR EBID

The deposition apparatus used in this work consists of a modified scanning electron microscope, Cambridge S100 (Cambridge ltd., England), fitted with a thermionic tungsten emitter (hairpin filament). The electron energy (E) can be set to 2, 5, 10, 15 or 25 keV. The electron probe current (I_p), measured by focusing the electron beam in a Faraday cup on the sample holder, connected to a pico-amperometer (Kittel 486), can be varied from about 1 pA to some μA. Pumping is achieved with an oil-free turbo-molecular pumping station (turbo-molecular pump Pfeiffer TMH 260 with a membrane pump Vacubrand MD 4T as backing pump). The oil free-system allows reduction of hydrocarbon contamination in the sample chamber caused by pump oil vapors. The ultimate pressure in the system, measured with a Penning gauge (Edwards 8) mounted on the sample chamber, is around $1x10^{-4}$ Pa in the absence of precursor gas. The maximum working pressure of the deposition system is $1x10^{-3}$ Pa. The microscope allows in situ observation of the produced deposits.

The precursor molecules are supplied in the reaction area via a stainless steel syringe needle (Unimed SA, Lausanne, Switzerland), as shown in Fig. 6-1. The needles are available in a wide range of sections and lengths; the choice depends mainly on the precursor vapor pressure. The needles are rinsed before use first in acetone, then in an isopropanol ultrasonic bath and dried by baking in a furnace at 100°C for one hour. The precursors are introduced in the needle reservoir in a N_2 purged glove box to avoid reaction with oxygen or water vapor. After filling, the needle is closed with a rubber cap and it is opened after being attached to the sample holder in the deposition system.

The system is equipped with a computer controlled e-beam lithography software, Nano Pattern Generation System (NPGS), sold by J.C. Nabity Lithography Systems (USA), which allows to pilot the electron beam on different pre-defined computer designed patterns. NPGS can control motorized stages providing fully automated sample movement and pattern alignment. Lines, polygons, and arbitrarily shaped features are all supported.

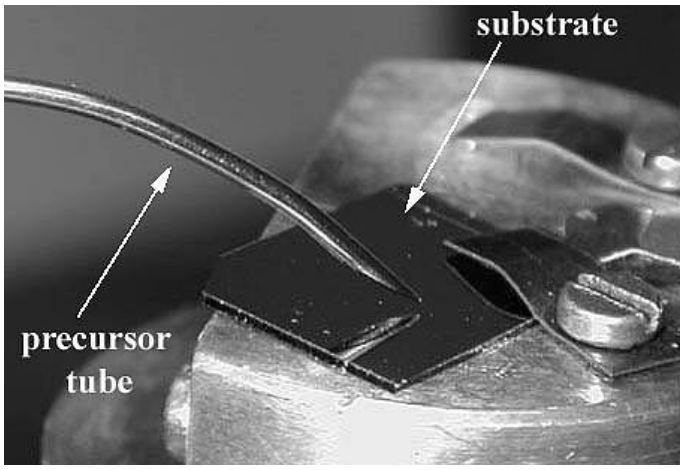

Figure 6-1: *System for precursor delivery at the substrate surface.*

6.1.1 DEPOSITION MODES

EBID can be performed by operating the electron beam in scanning or spot mode (stationary beam). In scanning mode the options: TV, VIS (1, 2 and 3) or Graph are available. In TV mode the beam is scanned along the TV frame in a standard scan of 625 lines with 50 Hz frequency. In VIS mode the same area is scanned with reduced frequency: 12 Hz in VIS1, 3.75 Hz in VIS 2, 0.2 Hz in VIS 3 [1]. In Graph mode the beam is scanned along a horizontal line between two sides of the TV frame with a frequency of 50 Hz. In spot mode the scan in the column is stopped and the beam is parked at a point indicated with a spot on the TV frame. The beam can be moved in x-y directions from the microscope control console or by means of the NPGS software.

6.2 SUBSTRATES FOR EBID

The choice of the substrate material in this work is limited to sufficiently conductive materials, since the W emitter does not allow to work with insulating materials, due to charging effects. The following substrate have been used: p-doped (boron) Si (111), thermally evaporated (150 nm thick) Au films on SiO_2 coated Si and thin carbon films (20 nm thickness) on Cu grids (for TEM).

The bulk substrates are cleaned before use by rinsing first in an acetone, than an in isopropanol ultrasonic bath and dried with a CO_2 spray. Several substrate materials have been tested in this work: they differ in electrical conductivity, surface chemistry, secondary emission (SE, BSE, SE2) and mechanical properties. In some cases the substrate choice depends on the characterization technique. (i.e. C grids for TEM-EELS, conductive substrate for AES).

6.3 DEPOSITION OF NANOSTRUCTURE: DOTS, TIPS, WIRES, SQUARES

The mechanism of EBID has been studied by morphological analysis of dots, three-dimensional columns and lines.

Dots and three dimensional columns are deposited by irradiation in spot mode with a stationary beam. Short time irradiation produces dots, long time irradiation three dimensional columns. The time of irradiation is called in this work *exposure time* and is indicated with the symbol t_e.

Line deposition can be achieved in spot or scanning (Graph) mode. In spot mode the lines are deposited by moving the beam on the substrate, with pre-defined point to point distance and dwell time, with the NPGS software. The point-to-point distance is the distance (variable from 1 to 500 nm) between two next points irradiated by the electron beam; the dwell time (variable from 1μs to 1s) the time spent by the electron beam on each visited point. Deposition in Graph mode is obtained using the Graph option described in the previous paragraph.

EBID squares (5 to 50 μm sides), mainly used for chemical analysis, are deposited operating the beam in TV or VIS mode. The parameter D_e indicates the total electron dose, given by:

$$D_e = \frac{I_p t_e}{S n_f} \tag{6-1}$$

where I_p is the probe current, t_e the exposure time, S the scanned surface and n_f the number of scanned frames per second. D_e takes into account the variations of all the parameters included in Eq. 6-1.

Other 3-D features, (arches, pyramids) can be obtained working in spot mode controlling the beam with the NPGS software.

6.4 CHARACTERIZATION OF THE DEPOSITS

Characterization of EBID structures includes morphological, structural and chemical analysis. Morphological analysis has been performed with Scanning Electron Microscopy (SEM), Transmission Electron Microscopy (TEM) and Atomic Force Microscopy (AFM). Structural characterization have been carried out with TEM. Chemical composition has been studied by Electron Energy Loss Spectroscopy (EELS) and Auger Electron Spectroscopy (AES).

6.4.1 SCANNING ELECTRON MICROSCOPY (SEM)

SEM observation allows to study the shape and the morphology of the deposits and to measure the characteristic dimensions of two- and three- dimensional deposits (height, width).

In this work the observations have been carried out with the SEMs XL 30 FEG and XL 30 SFEG (Philips, The Netherlands), both fitted with a hot field emission gun. The nominal resolution of the XL 30 FEG is around 2.0 nm at 30 kV and around 8 nm at 1 kV [2]. The XL 30 SFEG is equipped with a through lens detector and a high resolution image acquisition system, which allow higher resolution than in conventional SEMs.

6.4.2 ATOMIC FORCE MICROSCOPY (AFM)

Atomic Force Microscopy has been used to study the surface topography of the deposit and to determine the thickness and the height of EBID structures. In particular, AFM is essential to measure the section of EBID lines needed for electrical resistivity measurements. The measurements have been performed with the microscope Nanoscope III (Digital Instrument, USA), in intermittent contact mode, equipped with a NT-MDT Si cantilever.

6.4.3 TRANSMISSION ELECTRON MICROSCOPY (TEM): DIFFRACTION AND IMAGING

Transmission Electron Microscopy (TEM) has been used for characterization of EBID structures in imaging and diffraction mode.

TEM imaging in Bright Field (BF) and Dark Field (DF), has been used to study deposits obtained at short exposure times and low probe currents on thin C grids and to acquire images of three dimensional structures with higher magnification and resolution than in SEM.

TEM diffraction has allowed to determine the crystal structure of the deposit.

Z-contrast imaging in scanning mode (STEM) has been used to detect, with high resolution, differences in atomic number on various region of the same deposit.

TEMs are generally equipped with Electron Energy Loss Spectroscopy (EELS) facilities, which allows chemical analysis with high resolution.

The instrument used in this work for TEM, STEM and EELS are listed in Table 6-1. In all the models the specimen holder can be cooled to liquid nitrogen temperature, to reduce the contamination by hydrocarbons during microanalysis. The spatial resolution of the EELS systems used here is of the order of the electron probe diameter, i.e. 1-2 nm.

Further details about TEM imaging and diffraction are given in the Appendix (Section I.5).

Model	Emitter	*E* (keV)	Point resolution (Å)	Maximum tilt angle (degrees)	STEM	EELS
Hitachi HF 2000	cold FEG	200	2.3	±15	y	y
Philips EM430ST	LaB_6	300	2.0	±10	n	n
Philips CM 20	LaB_6	200	2.8	±45	y	n
Philips CM 300	Schottky FEG	300	1.7		y	y

Table 6-1: *Transmission electron microscopes used in this work.*

6.4.4 AUGER ELECTRON SPECTROSCOPY (AES)

Auger Electron Spectroscopy (AES) has been used in this work to study the chemical composition of the deposits and the distribution of the elements at the surface and in the bulk of the deposit.

AES has been performed ex situ with a PHI 660 (Perkin Elmer) Scanning Auger Microprobe (SAM) fitted with a LaB_6 electron gun with a nominal minimum beam diameter of less than 25 nm at 20 keV electron energy [3]. The system is equipped with a full Cylindrical Mirror Analyzer (CMA) [4] and a channeltron electron multiplier [4]. An Ar^+ ion sputter gun is available for sputter cleaning of the specimen. Sputter etching performed sequentially with the acquisition of Auger spectra results in sputter depth profiles, in which sample composition is measured as a function of depth. Imaging of the specimen is possible by operating the system in SEM mode.

The analysis has been performed on deposits with dimensions larger than the lateral resolution (squares with a side of 10-20 μm), in order to avoid detection of substrate elements. All the spectra shown in this work have been acquired with a primary beam energy of 3 keV and a current ranging from 1 nA to 3 nA. Sputter cleaning is achieved with a 2 keV Ar^+ ion gun in raster mode.

Further details about AES and the quantification procedure for elemental analysis are reported in the Appendix (Section I.7).

The main problem for elemental quantification in Rh EBID structure is the partial overlapping of the C and Rh Auger peaks in the region between 240 and 290 eV. This effect is visible in Fig. 6-2, showing the spectrum of a Rh standard (Rh foil 0.25 mm thick 99.8%, Alfa Aesar).

The black and the gray lines represent, respectively, the as received and the sputter cleaned (120 s, 2keV Ar^+ ions) sample. The principal features of the Rh spectrum are the MNN triplet with energies at 219 eV, 250 eV, 298 eV and the LMM singlet at 46 eV. In the spectrum of the as received sample the carbon and oxygen KLL peaks, due to the contamination layer, are visible at 265 and 510 eV, respectively. The contamination layer is totally removed after sputter cleaning. The overlap of the Rh and C peaks is better visualized in Fig. 6-2b, reporting the 200-320 eV region of the spectrum shown in Fig. 6-2a.

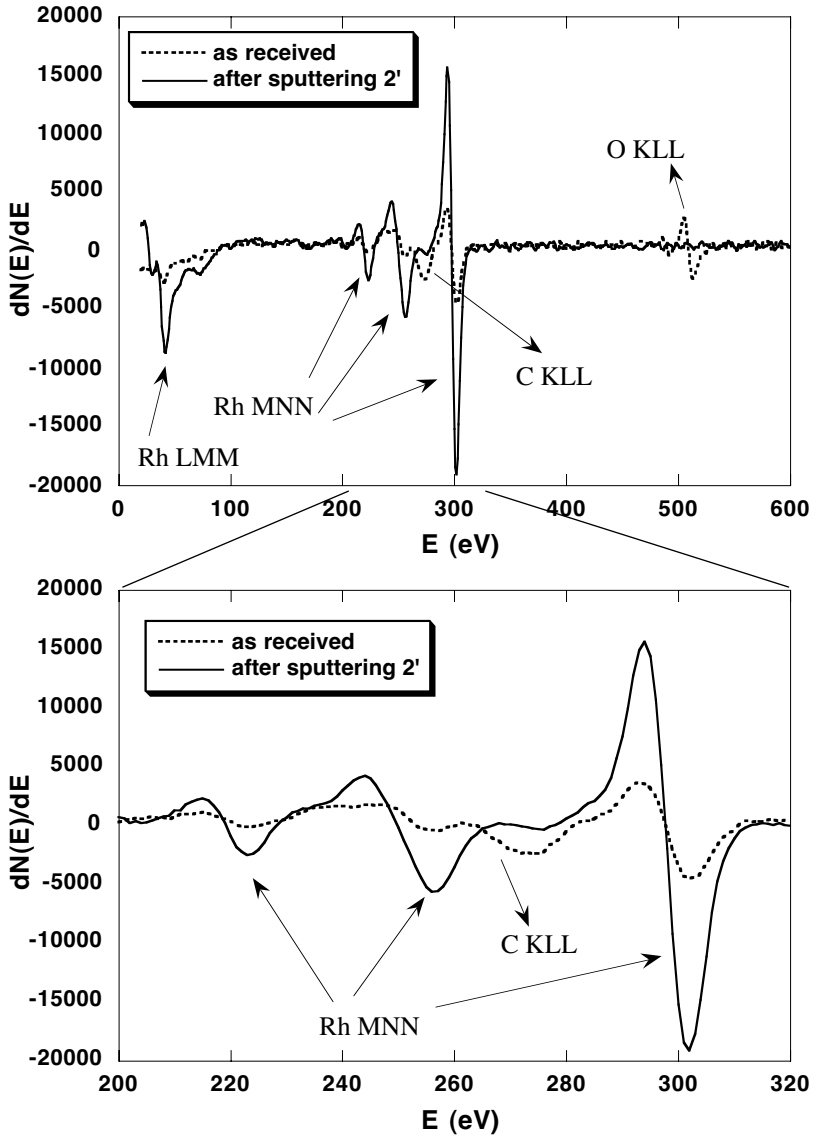

Figure 6-2: *AES spectrum of a Rh (99.8%) foil (area 6.25 cm^2, thickness 0.25 mm, Alfa Aesar 231-125-0), before (dashed line) and after (solid line) sputter cleaning (a). Same plot as between 200 and 320 eV.*

This can cause errors in the evaluation of the atomic concentration since even small peak to peak amplitudes, due to noise or tails of the Rh MNN peaks, can result in high C concentrations, because of the high sensitivity factor of the element.

In this work, to verify the carbon presence, I compare all the acquired spectra with the spectrum of the Rh standard shown above and with the spectrum of EBID C standard, consisting in the region between 240 and 300 eV. The presence of the structure of the C peak is first verified in a non-differentiated spectrum, then in a differentiated one. The procedure will be discussed in detail in Chapter 7.

6.4.5 ELECTRON ENERGY LOSS SPECTROSCOPY (EELS)

EELS analysis of EBID structures has been performed with the aim to confirm the results obtained by AES concerning the presence of C contamination in the deposit.

In addition, because of its high resolution, EELS has been used to acquire chemical mapping of deposits with sub-micrometer dimension and to determine the distribution of the elements in the deposits with nanometer-resolution.

The experiments set-ups used for EELS analysis are listed in Table 6-1. Further information about EELS and the elemental quantification procedures are presented in the Appendix (Section I.7).

6.4.6 RESISTIVITY MEASUREMENTS

Resistivity measurements have been carried out with a probe station (6000 MM, USA) using the two-point-probe method. The EBID lines are deposited between four Au electrodes (150 nm thick) pre-deposited on 450 a nm thick SiO_2 film on Si, with spacings of 5, 10 and 20 μm, as shown schematically in Fig. 6-3.

The resistance of the lines are measured between the electrodes at distances *d1*, *d2* and *d3* (see Fig. 6-3) and plotted against the distance. The equation of the plotted line is

$$R_{el} = R_0 + \alpha_{el} d \tag{6.2}$$

where R_{el} is the measured resistance, R_0 the contact resistance and α_{el} is the line resistance times the line length. The resistivity of the line is obtained by multiplying α_{el} by the line section.

For resistivity calculation the length and the section of the EBID lines must be measured. In this work the sections are measured with an AFM and the lengths with a SEM. The line sections are approximated to rectangles with a base equal to the deposit width and a height equal to the average deposit height.

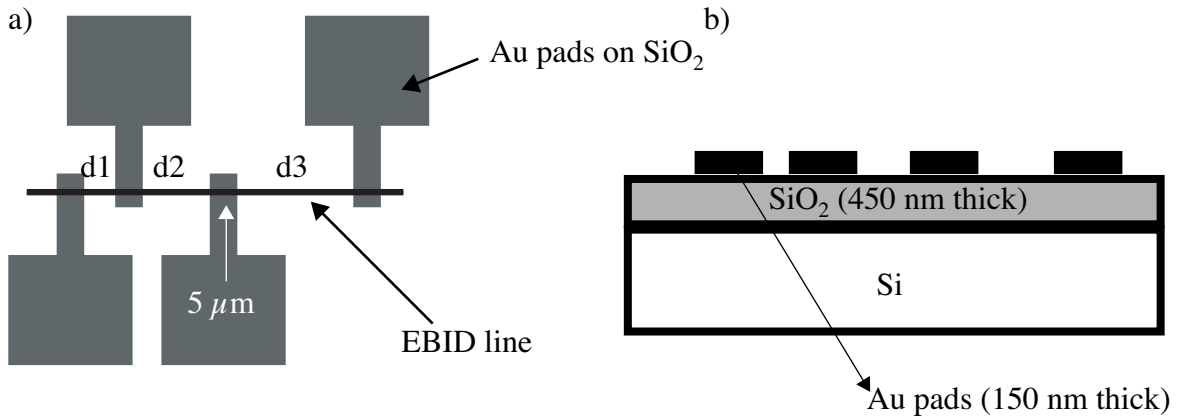

Figure 6-3: *Schematics of the system for resistivity measurements. Top (a) and side (b) view.*

6.5 CONCLUSION

EBID is performed in this work by means of a modified SEM Cambdidge S100, fitted by a thermionic electron gun.

The deposits are characterized with respect to their morphology, structure and chemical composition.

Morphological analysis is performed by means of SEM, TEM (bright and dark field) and AFM. STEM imaging in Z-contrast mode allows to identify regions with different average atomic number with nanometric resolution.

TEM diffraction patterns allow identification of the crystalline phases.

Chemical analysis are performed with AES and EELS. AES allows to know the composition of the deposit surface with a lateral resolution of the order of the μm and a depth resolution of less than 10 nm. Compositional analysis of the deposit bulk can be achieved by sputter depth profiling. EELS is used to confirm the result obtained by AES, to acquire chemical mappings of deposits of sub-micrometer size and to determine the distribution of the element in the deposit with nanometric resolution.

The electrical properties of the deposits are studied by four-point-probe resistivity measurements.

6.6 REFERENCES

[1] Operating instructions for Stereoscan 100, Cambridge ltd.

[2] Web site of CIME (EPFL), cimewww.epfl.ch/facilities/facilities_index.htm.

[3] Perkin-Elmer; *660 AES Operator's reference manual (version 5.0)*; 1988.

[4] H.A. Strobel, W.R. Heineman; *Chemical instrumentation: a systematic approach*; John Wiley and Sons, 1988.

CHAPTER 7 *Rhodium EBID: results and discussion*

In this Chapter I present and discuss the characterization of the Rh deposits obtained from the precursor $[RhCl(PF_3)_2]_2$, realized as described in Chapter 6. The characterization includes morphological, structural and chemical analysis.

7.1 MORPHOLOGY (SEM AND TEM), GROWTH PROCESS

Morphological analysis by scanning electron microscopy (SEM) and transmission electron microscopy (TEM) is the main experimental tool to study the mechanism of EBID.

EBID of three-dimensional structures can be divided in two main phases, which in this work I call nucleation and growth. During nucleation EBID takes place on the substrate, during growth on the surface of the pre-deposited material. For this reason, the parameters describing electron beam-matter interaction (SE and BSE emission, electron range) should be in the first phase referred to the substrate material, in the second to the deposit. After a certain height (depending on the composition) of the three-dimensional deposit no more electrons reach the substrate, so the process becomes independent of the substrate properties.

In this work nucleation and growth have been studied with two different techniques. Nucleation has been studied by TEM observation of deposits obtained at very short exposure times on 20 nm thick C grids. As shown by Monte Carlo simulations (Fig. 4-8a), BSE emission on such substrates is negligible, even in the presence of an adsorbed layer of precursor molecules or of a deposit with a 100 nm thickness. In addition C is one of the materials with the lowest secondary electron yield (0.08 for 25 keV primary electron energy, as shown in Fig. 4-9). Therefore the deposition process on thin C films can be in good approximation described by taking into account only the effect of primary electrons. Furthermore TEM is necessary for observation of very thin deposits which cannot be observed in SEM. Nevertheless deposits on C grids cannot always be used for deposit height evaluation, because of the effect of the transmitted electrons on the back-side of the film (as will be shown later).

Three-dimensional growth (exposure times of the order of minutes) has been studied by SEM observation of three-dimensional deposits on bulk Si(111). On this material BSE and SE yields (Figs. 4-7 and 4-9) are enhanced compared to C grids, while there is no effect of the transmitted electrons.

7.1.1 TEM OBSERVATION OF DEPOSITS ON THIN C FILMS

The deposits for TEM observation have been carried out in beam spot mode with an electron energy of 25 keV, at four different values of the beam current I_p (25 pA, 110 pA, 330 pA, 1000 pA). As substrates, commercial C films deposited on Cu grids for TEM observations (AGAR ltd., UK) have been used. The precursor has been supplied with a 15 mm long needle with an inner diameter of 0.8 mm, oriented towards the substrate with an angle of 30°; the distance between the needle exit and the irradiated area has been set to about 40μm. For each value of the beam current (I_p) an array of 16 deposits has been performed, varying the exposure time from 0.05 s to 349 s. Examples of two arrays of deposits are shown in the DF TEM micrographs reported in Fig. 7-1, for a deposition current of 25 pA (Fig. 7-1a) and 110 pA (Fig. 7-1b). The exposure times are indicated in Fig. 7-1a below each deposit.

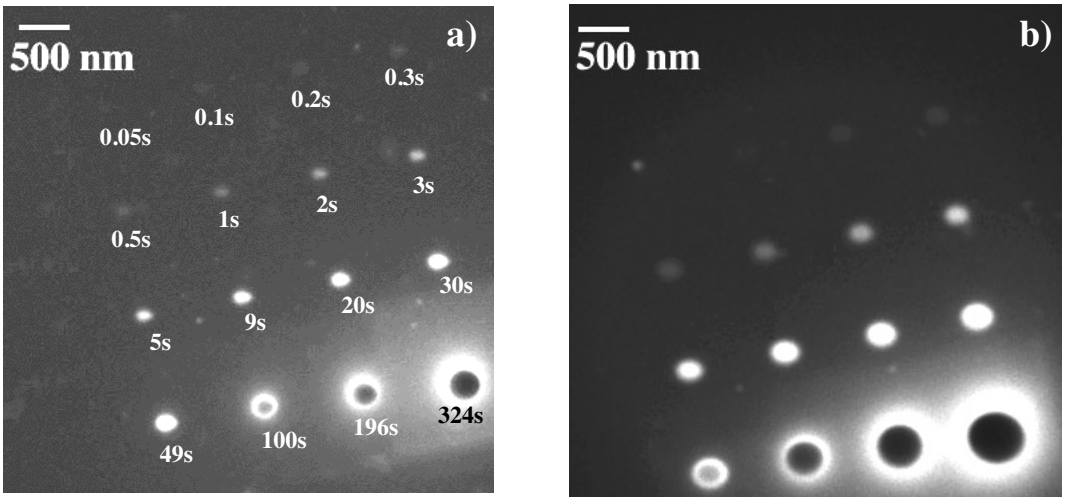

Figure 7-1: *Dark field (DF) TEM micrographs of two arrays of 16 dots deposited at I_p = 25 pA (a) and I_p = 110 pA (b). Exposure times from the first dot at the left upper corner of the square: 0.05, 0.1, 0.2, 0.3, 0.5, 1, 2, 3, 5, 9, 20, 30, 49, 100, 196, and 324 seconds. Deposits carried out on a C grid from the precursor $[RhCl(PF_3)_3]_2$; E = 25 keV.*

The images reveal that EBID is obtained even at the lowest applied exposure time and electron currents (0.05 s and 25pA respectively) indicating a high decomposition probability for the precursor $[RhCl(PF_3)_2]_2$. The total electron density at the substrate surface is given by the sum of the primary (PE), secondary (SE), backscattered (BSE) and secondary from backscattered (SE2) electron densities. For a thin C grid BSE and SE2 contributions are negligible, therefore the total electron density j_{TOT} is:

$$j_{TOT} = j_{PE} + j_{SE} = j_{PE}(1 + 0.08) \approx 1.1\, j_{PE}\,. \qquad (7.1)$$

For a 0.05 s irradiation with I_p = 25 pA the total number of electrons impinging at the surface is 7.8×10^6. Assuming that the electrons are uniformly distributed in a circle of 60 nm radius (dot

diameter) gives an average density of 800 electrons/nm^2, taking into account the secondary electrons. The maximum density of molecules impinging at the surface in the same interval of time, calculated from Eq. 3. 13 with $s = 0$, is about 900/nm^2, which gives a height of about 100 nm, taking into account the dimensions of the precursor molecule. Since the height of the deposit obtained at 0.05 s exposure time and 25 pA beam current is about 0.2 nm (as shown later), I can conclude that the ratio between the number of impinging electrons and decomposed $[RhCl(PF_3)_2]_2$ molecules is about 500. Nevertheless, this does not exclude that, after interacting with a precursor molecule, a primary electron can generate other processes.

The images in Fig. 7-1 show the effect of the probe current and of the exposure time on the deposit diameter. Comparison of Fig. 7-1a and 7-1b reveals that the deposit diameter increases with increasing probe current. Both images reveal that for a given electron current, the deposit diameter increases with exposure time.

The same images show that the contrast intensity for thin deposits increases with the deposition time; revealing growing deposit thickness. On the other hand, for thick deposits ($t_e > 49$ s) the contrast intensity in the center of the deposit decreases, due to absorption of electrons. For long exposure times (in general for $t_e > 60$ s) the deposits take the shape of three-dimensional cones, as shown in Fig. 7-2a and 7-2b, displaying the same areas as in Fig. 7-1, with the substrate tilted by 45° and rotated by 90°. Comparison of the tip curvature radii reveal that they are constant for a constant deposition current and increase for increasing deposition current.

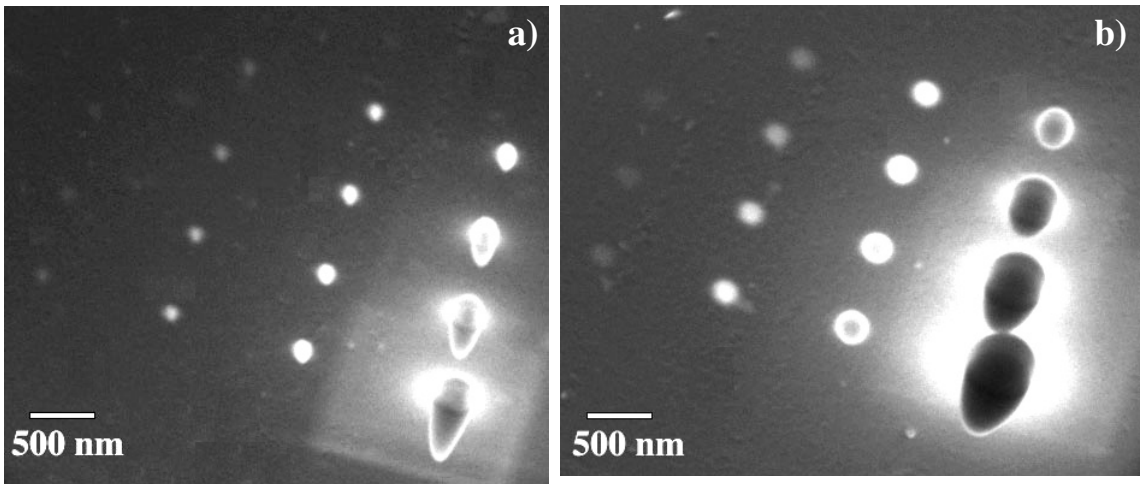

Figure 7-2: *Same deposit arrays as Fig. 7-1, 45° tilted images; upper left lowest exposure time (0.05 s); lower right-highest exposure time (324 s).*

The evolution of the deposit diameter with the exposure time, for all the investigated deposition currents (I_p), is shown in the graphs in Fig. 7-3. The graph 7-3a shows that the deposit diameter increases with the exposure time for all the applied deposition currents, with a steeper increase for exposure times between 0.05 s and 5 s. The steeper diameter increase in the short

time region is further demonstrated by the fit reported in Fig. 7-3b, (0.05 s - 5 s) and 7-3c (9 s - 324 s). The plots are close to linear in both the short and long exposure time regions, with a slope of about a factor 10 higher in the short time region.

The increase of the deposit diameter with increasing electron probe current is a consequence of the broadening of the electron beam diameter, due to a change in the electron density distribution, as shown schematically in Fig. 7-4.

The increase of the deposit diameter with increasing exposure time is explained by accumulation of deposition events in the lower electron density regions of the electron beam. When a substrate is irradiated by a Gaussian electron beam, the electron density at the substrate is higher in the central region than in the tail of the distribution function. For the decomposition process, assuming a sufficient precursor flux, in the center of the beam the number of impinging electrons is always sufficient to decompose all the impinging and adsorbed precursor molecules. In the tail regions the electron density is much smaller and the probability to decompose precursor molecules decreases. Increasing the exposure time increases the total electron density reaching the surface. As a consequence, the probability to decompose precursor molecules at a growing distance from the beam center increases. The effect of the exposure time on the electron beam density distribution at the surface for a hypothetical Gaussian beam (as calculated in Chapter 2 from the short time EBID TEM imaging), with I_p = 25 pA and 0.5 s, 1 s and 2 s exposure times, is shown in Fig. 7-5. A beam diameter of 120 nm (width at 1/e) is assumed.

The higher deposition rate in the center of the beam is confirmed by the shape of the contrast profiles of the deposits, obtained from DF TEM images. The contrast profiles of three deposits obtained with an electron energy of 25 keV, an electron current of 110 pA at 0.5 s, 1 s and 2 s exposure times are shown in Fig. 7-6a.

The plot reveals that the net contrast intensity (related to the deposit height) increases with increasing exposure time and, for a given exposure time, when moving towards the center of the beam, because of a high deposition rate, due to the higher electron density. The profiles present a close to Gaussian shape with a deviation in the zone around the peak. The deviation indicates that, in the region of highest electron flux, the EBID rate depends on the number of precursor molecules reaching the reaction region (precursor flow limited). The contrast drop on the deposit edges indicates that in the peripheral region of the beam the deposition rate depends on the electron density (electron flux limited). The contrast profiles of the deposits carried out with t_e < 2 s, at all the investigated currents, can be fitted with a Gauss function. The fit is obtained excluding the contrast values in the central part of the deposit. As already discusssed in Chapter 2, the width parameter of the Gauss functions gives an estimation of the electron beam diameter. An example of Gaussian fit, for the contrast profiles shown in figure 7-6a (I_p=110 pA), is shown in Fig 7-6b. The three contrast profiles corresonding to dots deposited at different exposure times, are fitted with Gaussian functions with different height and the same width parameter. Similar results are obtained for contrast profiles of dots deposited at different beam currents. The width parameter of the fitting Gaussian functions at 25 pA, 110 pA, 330 pA

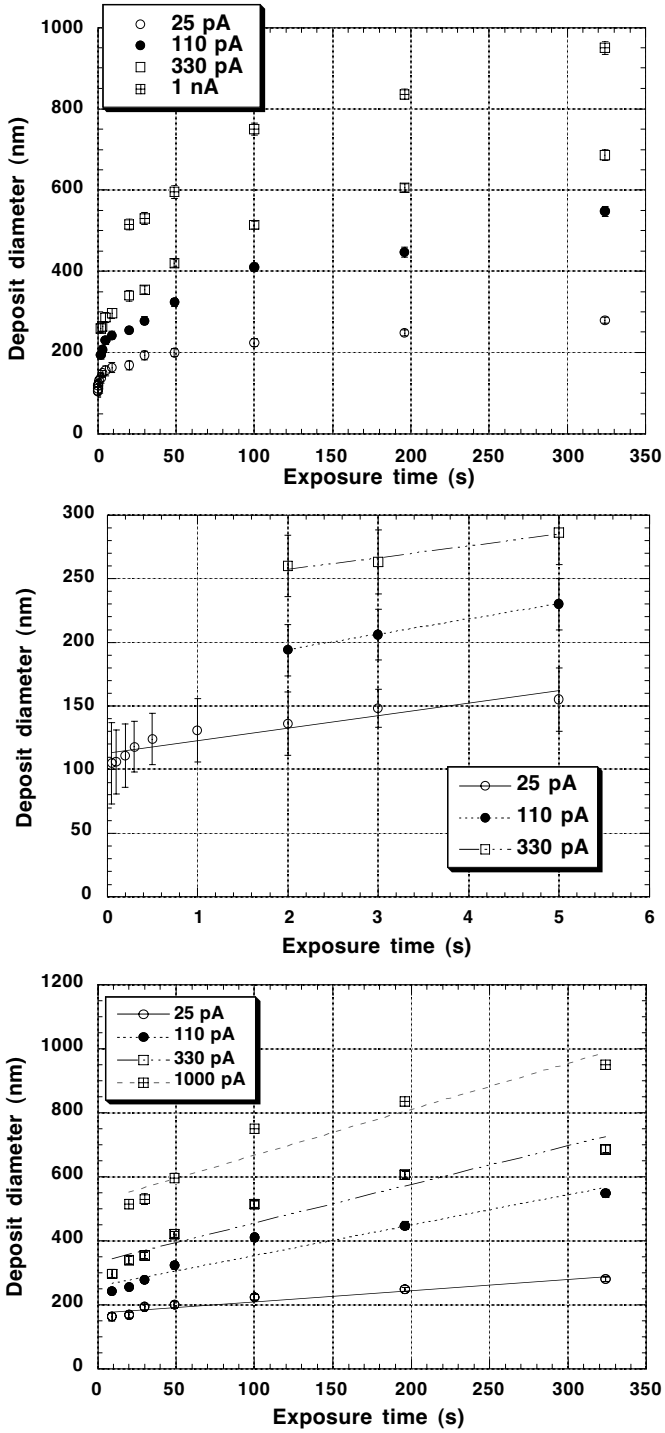

Figure 7-3: *Deposit diameter versus exposure time at four different probe currents: (a) whole time range, (b) short time range (0.05 s - 5 s), (c) long time range (9 s - 350 s). Deposits carried out on a C grid from the precursor* $[RhCl(PF_3)_3]_2$*; E = 25 keV.*

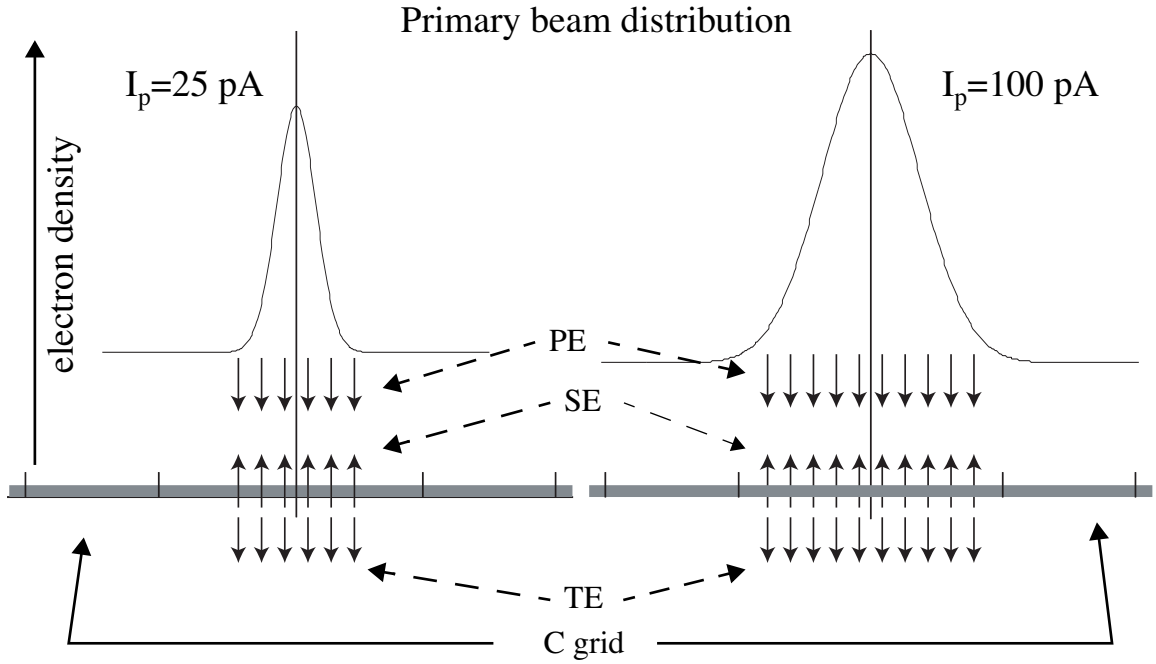

Figure 7-4: *Effect of increasing electron current for deposition on C grids for an electron beam with a Gaussian distribution. Increasing the probe current determines an increase of the surface exposed to the electron beam. PE: primary electrons, SE: secondary electrons, TE: transmitted electrons.*

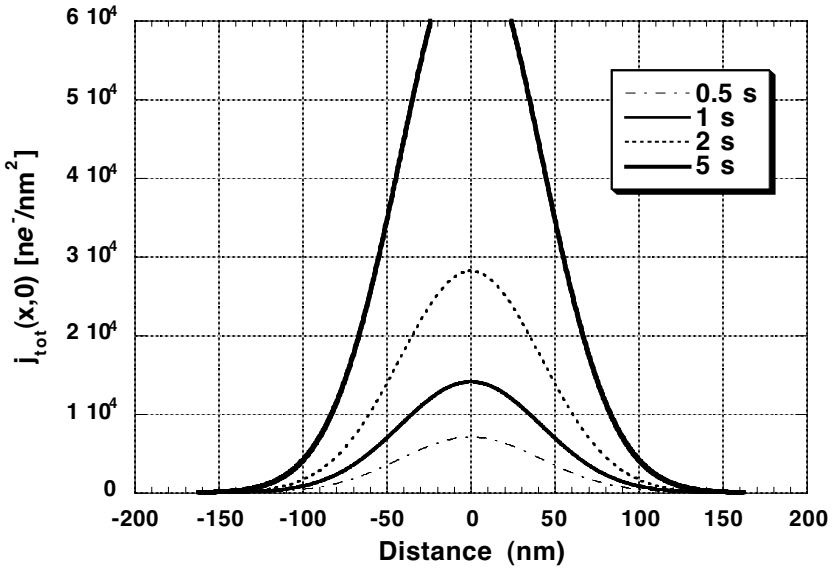

Figure 7-5: *Effect of the exposure time on the electron density. Gaussian electron beam density distributions at I_p = 110 pA with exposure times 0.5 s, 1 s, 2 s (b).*

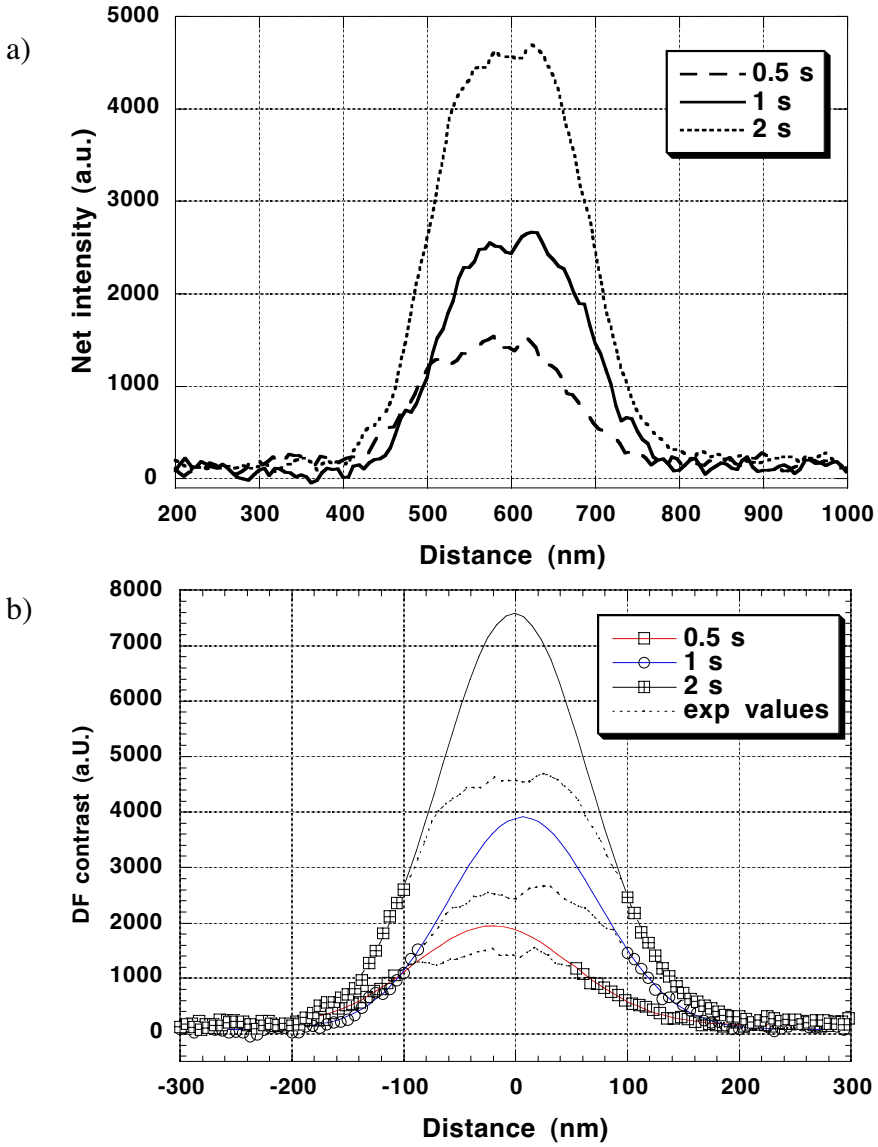

Figure 7-6: *Contrast profiles measured from TEM DF micrographs of three EBID dots deposited with I_p = 110 pA, E = 25 keV, exposure times 0.5 s, 1 s, 2 s. Deposits carried out on a C grid from the precursor $[RhCl(PF_3)_3]_2$.*

and 1000 pA are reported in Table 2-3. The Gaussian fits in Fig. 7-6b make more evident the electron flux limited and precursor limited growth region.

The different slope of the diameter versus time plots reported in Fig. 7-3b and 7-3c reveals that the effect of the exposure time on the deposit diameter decreases with increasing deposit height and with decreasing electron current. The effect has not been understood but it could be due to electron scattering by the three-dimensional structures.

The plot in Fig. 7-7a reports the deposit height versus the exposure time for $t_e > 30\ s$. The height has been evaluated from tilted TEM micrographs. The height increase is close to linear with a deviation from linearity at higher exposure times. The deposited height at a given deposition time increases between 25 and 330 pA. The height of very thin deposits, obtained at short exposure times (< 3 s), cannot be estimated from the tilted TEM micrograph, as can be observed in Fig. 7-2. Therefore the 3D growth process in the corresponding time range is analyzed by plotting the deposit DF contrast intensity versus time.

For a thin and amorphous specimen, the DF intensity is proportional to the specimen thickness. The net contrast change versus deposition time for deposits carried out at 25 pA and 110 pA, obtained from DF TEM images (e.g the ones shown in Fig. 7-1), is plotted in Fig. 7-7b. The plotted values refer to the net DF contrast, obtained by subtracting the contribution of the carbon film C^C from the total contrast C^{TOT}, measured in the center of the dot, and normalizing the values to the DF acquisition time. The plot indicates a linear increase of the thickness with time.

The linearity of the plots in Fig. 7-7b and of the first part of the one in Fig. 7-7a allows to relate the contrast intensity with the deposit height. For a current of 25 pA, the height versus time plot (Fig. 7-7a) is linear between 0 and 100 s and the corresponding DF intensity versus time plot is linear for short exposure times. From the plot in Fig. 7-7b, the measured height of 400 nm after an exposure time of 100 seconds, permits to extrapolate a deposition rate of about 4nm/s. This latter value is taken as the height corresponding to a deposition time of one second and used to plot the diagram in Fig. 7-7c. From this diagram it can be estimated that at the lowest applied exposure times the deposit height is around 2Å, assuming that before electron irradiation the precursor forms a monolayer with a thickness equal to the molecular diameter (6Å). This means that the density of the deposit is a factor of three higher than that of the precursor.

A particular feature of EBID on thin carbon films is that the deposition is observed on both sides of the irradiated film, as shown in Fig. 7-2 and, with higher magnification, in Fig. 7-8a. The growth of the back-side deposit stops at heights of about 120 nm and 180 nm at currents of 25 pA and 110 pA respectively (Fig. 7-8 b). This corresponds to front-side deposit heights of 400 and 700 nm for currents of 25 pA and 110 pA respectively. The diameter of the deposit is larger on the irradiated side. As observed also in Fig. 7-8a the back-side growth stops when the transmitted beam is completely scattered by the deposit grown on the front-side. A similar phenomenon is described in the literature with regard to carbon contamination deposition on the opposite side of thin blades [1]. This back side growth is induced by the transmitted electron beam, which decomposes precursor molecules reaching the back side of the grid through holes in the C membrane.

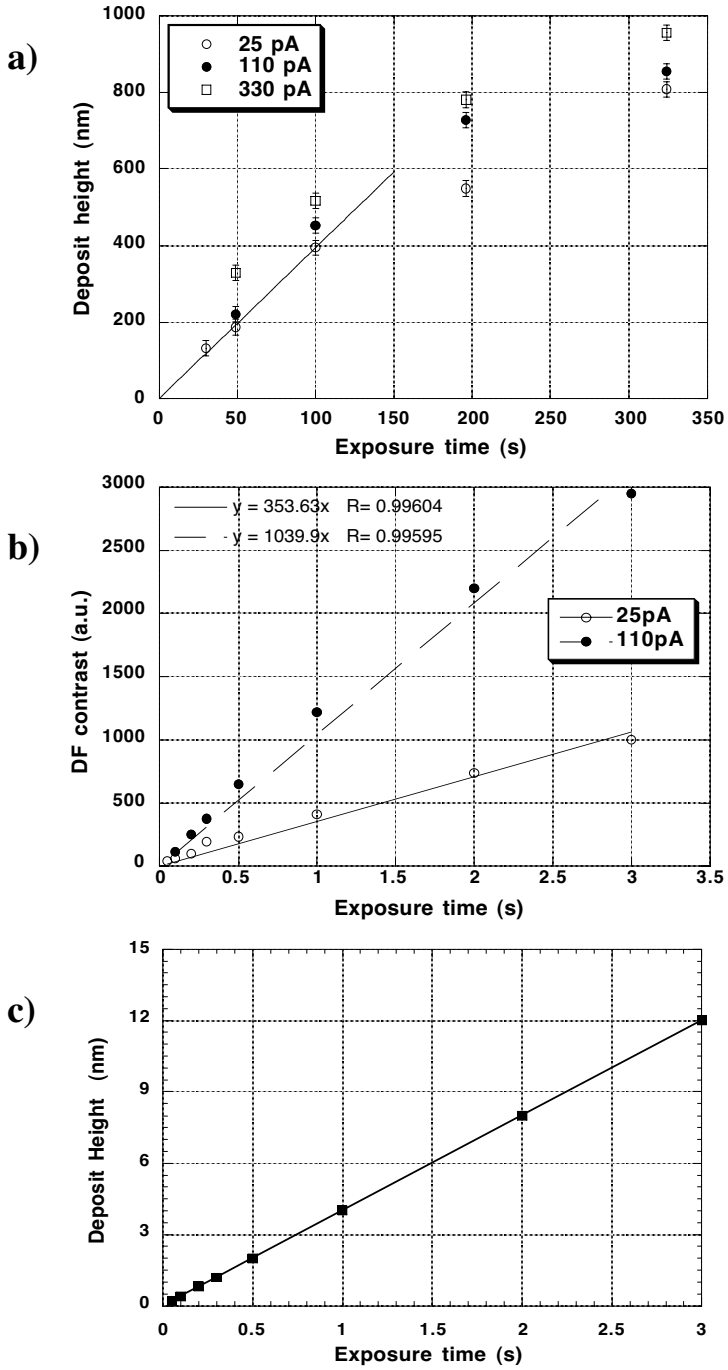

Figure 7-7: *Height (a) as a function of the exposure time at I_p = 25 pA, I_p = 110 pA and I_p = 330 pA; net DF contrast (b) as a function of the exposure time at I_p = 25 pA, I_p = 110 pA; (c) height versus time for dots deposited at I_p = 25 pA (extrapolated from curves a and b). Deposits carried out on a C grid from the precursor $[RhCl(PF_3)_3]_2$; E = 25 keV.*

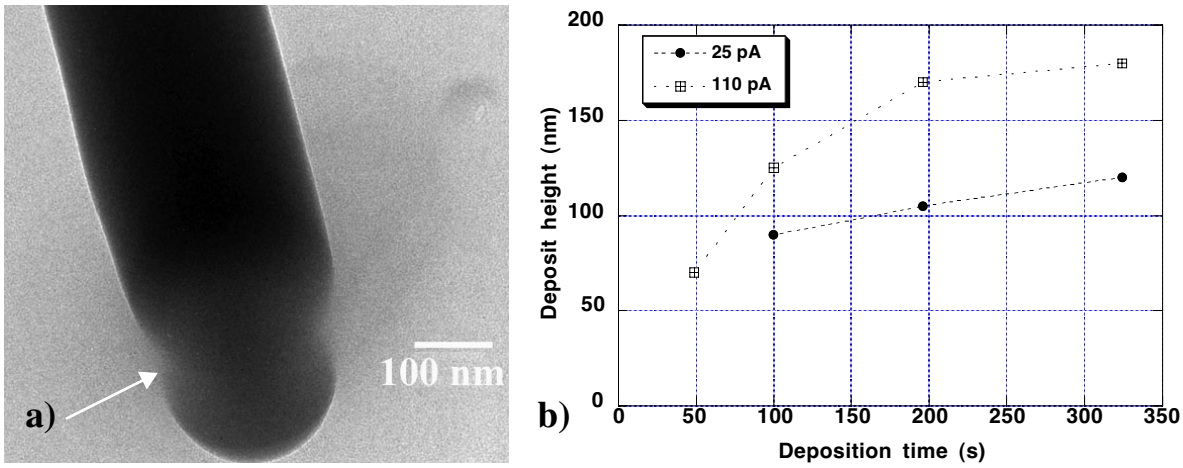

Figure 7-8: *(a) TEM image of a Rh containing three-dimensional deposit (25 keV, 25 pA, 300 s exposure time) under a tilt angle of 45°. The deposition takes places on both sides of the C grid. The white arrow indicates the region where the grid intercepts the deposit. (b) Height of the back side deposit versus exposure time at I_p = 25 pA and I_p = 110 pA. Deposits carried out on a C grid from the precursor $[RhCl(PF_3)_3]_2$; E = 25 keV.*

7.1.2 SEM OBSERVATION OF DEPOSITS ON BULK SUBSTRATES

Scanning Electron Microscopy (SEM) and Atomic Force Microscopy (AFM) imaging of EBID structures deposited on Si(111) allow to investigate the three-dimensional growth phase of EBID.

The resolution of the EBID process on Si (111) has been tested depositing a series of EBID dots at various probe currents, with an electron energy of 25 keV and an exposure time of 30 seconds. The deposit diameter as a function of the deposition current is plotted in Fig. 7-9 and compared with the diameter of dots deposited on C film, with the same electron energy and exposure times. The reported diameters are an average of three deposits obtained in identical experimental conditions. The results show that the deposit diameter increases with increasing probe current. The deposit diameter increases by a factor 3.6 for an increase of I_p of a factor 70. This result indicates that the deposit size depends on the current density rather than on the total probe current.

The results reveal also that, for the same exposure times, the diameters are larger on bulk Si(111) than on C grids, with a discrepancy increasing with increasing probe current. Since the applied electron currents are the same in the two cases, the different dot diameter can be explained by the higher deposited electron density on the bulk Si substrate. The total electron density at the silicon surface is

$$j_{TOT} = j_{PE} + j_{SE} + j_{BSE} + j_{SE2} = j_{PE}(1 + 0.15 + 0.2) \approx 1.35 j_{PE} \qquad (7.2)$$

and is therefore 1.23 times higher than on C films (see Eq. 7. 1).

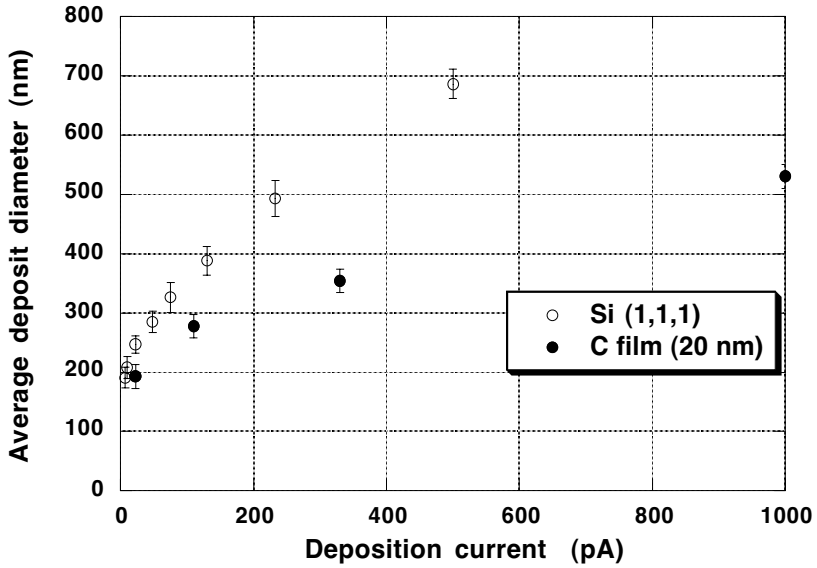

Figure 7-9: *Average deposit diameter for a 30 s deposition as a function of I_p on bulk Si(111) and on a C grid. Deposits carried out from the precursor $[RhCl(PF_3)_3]_2$; E = 25 keV.*

The three-dimensional growth phase of EBID has been studied by analyzing the dimensions and shape of deposits as a function of the exposure time. The deposits have been performed at electron probe currents of 22 pA, 46 pA, 110 pA and 500 pA, with exposure times ranging from 10 seconds to 10 minutes, with a fixed electron energy of 25 keV. The precursor has been supplied to the reaction area with a stainless steel needle with an inner diameter of 0.9 mm and a length of 15 mm. The deposition area is 20 μm from the needle exit. The height and volume of the deposits have been evaluated from tilted SEM pictures.

Figure 7-10 shows SEM images of three-dimensional EBID structures deposited at 25 keV electron energy with I_p = 22 pA (a) and I_p = 100 pA (b); the exposure times are indicated in the figure. Observation and comparison of the images reveal that:

- the diameter of three-dimensional deposits decreases with decreasing probe current;
- for a given I_p value the deposit diameter is constant with time (cylindrical growth);
- the three-dimensional deposits have a conical end, with curvature radii decreasing with the deposition current;
- the vertical growth rate increases with decreasing probe current.

The increasing column diameter with increasing probe current is a consequence of the broadening of the beam diameter, as already explained in the previous section.

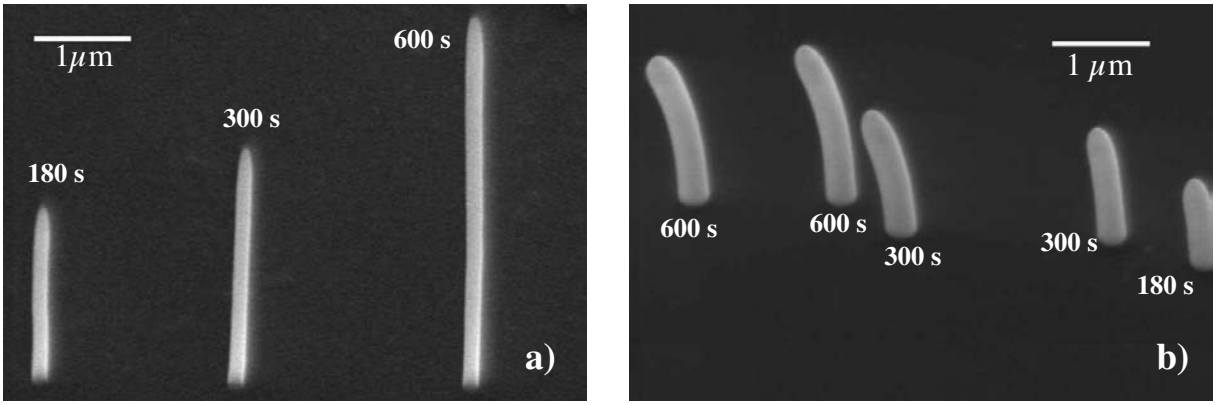

Figure 7-10: *Effect of the beam current and the exposure time on the shape of three-dimensional deposits. Tips deposited with I_p=22 pA (a) and I_p=100 pA (b). Deposits carried out from the precursor $[RhCl(PF_3)_3]_2$; E=25 keV. The bending of the tips in (b) is due to mechanical drift in the microscope.*

A further contribution to the broadening of the deposit diameter during the growth process is due to back-scattering phenomena from the deposit. This effect is demonstrated by Monte Carlo simulations of the trajectories of 100 electrons, with an energy of 25 keV, impinging on cylindrical three-dimensional deposits of different height (see Fig. 7-11). The deposit is assumed to have the shape of a top-cut cone with a diameter of 300 nm at the base and 200 nm at the top. The chemical formula of the deposited material is assumed to be $Rh_6P_{1.5}Cl_{0.5}NO$, with a density of 7 gcm^{-3}. This latter value is obtained multiplying the density of the pure elements by their concentrations detected in the deposit by AES. The simulations are carried out for 100 electron trajectories, assuming a punctual beam diameter. The simulations show that for deposit higher than 400 nm the scattering events occur mainly in the deposited material. The electrons scattered by the deposit (BSE) are deviated through different angles and transmitted through the walls, where they induce further secondary electron emission (SE2); those with a scattering angle < 90° reach the substrate surface.

The BSE and SE2 can decompose precursor molecules impinging or adsorbed on the deposit walls. This process causes a broadening of the column diameter. As is clearly visible in Fig. 7-11, the backscattering cloud shifts upwards with increasing deposit height, therefore BSE have a similar broadening effect at different column heights. This explains the cylindrical shape of the deposits. Electron scattering in the deposit can also contribute to the explanation of the conical tip of the cylindrical rods. As visible in Fig. 7-11 most of the scattered electrons leave the deposit wall with an angle > 45°. The upper extremity of deposit is therefore exposed only to primary (PE) and secondary electrons (SE1), whose distribution determines the final dimensions. The scattered electrons which reach the substrate surface can induce deposition around the deposit basis (halo), as shown in the TEM picture reported in Fig. 7-12.

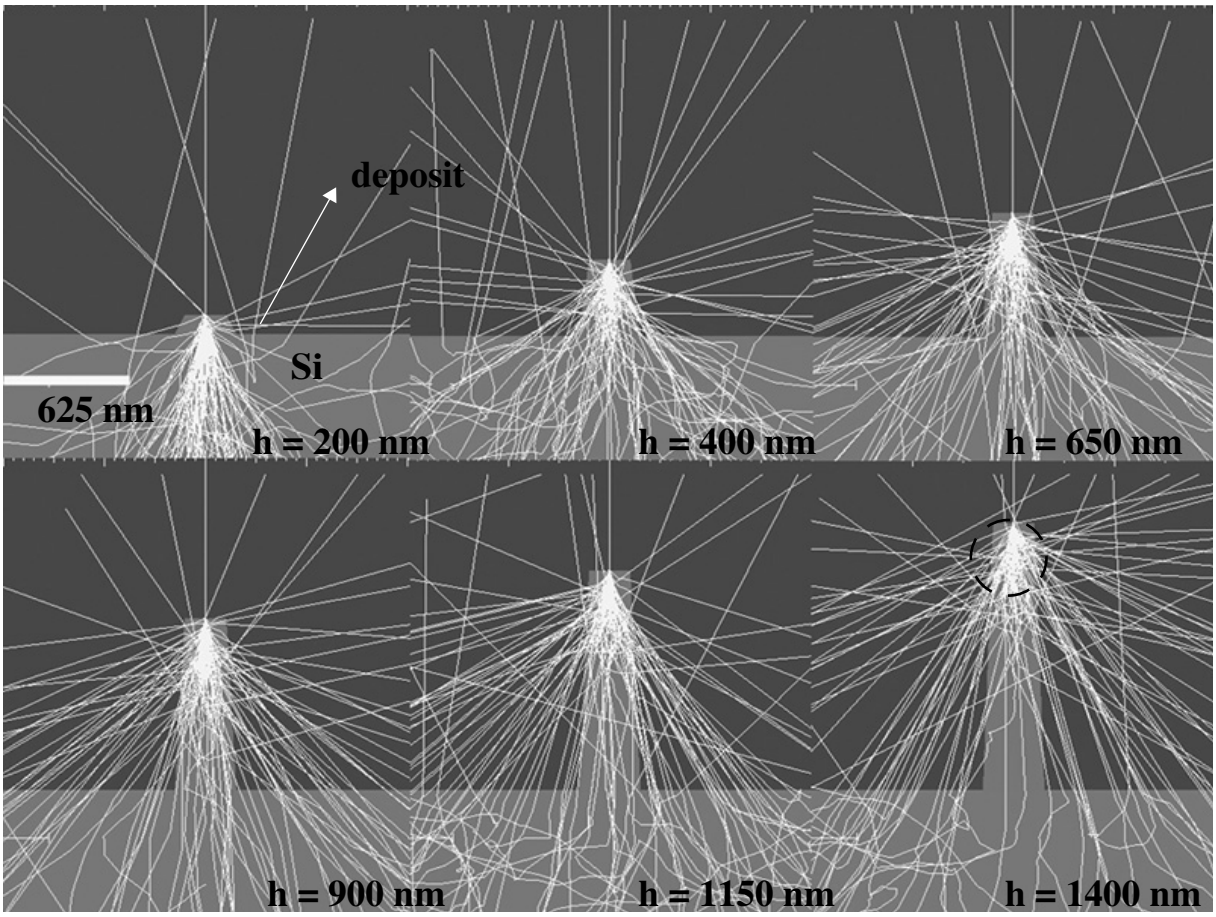

Figure 7-11: *Monte Carlo simulations of electron scattering on EBID Rh containing rods of different heights (h) on Si (111). The deposits are assumed to have a density of 7 gcm^{-3}, estimated from their chemical composition. Simulation for 100 electrons with E = 25 keV.*

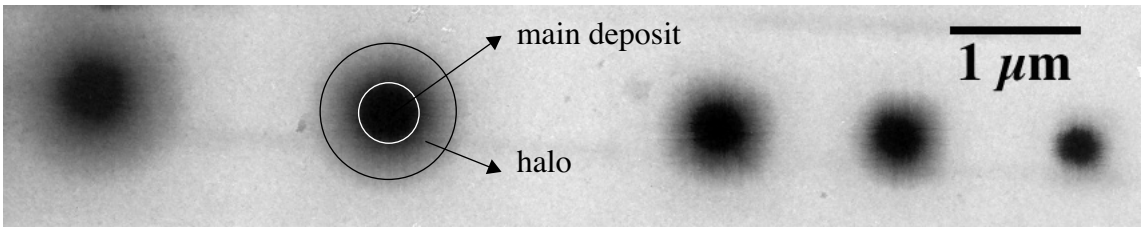

Figure 7-12: *Halo effect for Rh EBID on C grids. Exposure times (from right to left): 10 s, 20 s, 30 s, 45 s, 60 s. Deposits carried out from the precursor [RhCl(PF$_3$)$_3$]$_2$; I_p= 500 pA; E = 25 keV.*

The height of the deposits as a function of time at the electron currents of 22 pA, 46 pA, 100 pA and 500 pA, is reported in Fig. 7-13 a). At all the investigated currents the deposits have a shape similar to the one of those shown in Figs. 7-10a and 7-10b. The error bars in the graph

contain the uncertainty on the position of the starting and ending point of measurement and take into account the bending of high aspect ratio deposits during SEM observations.

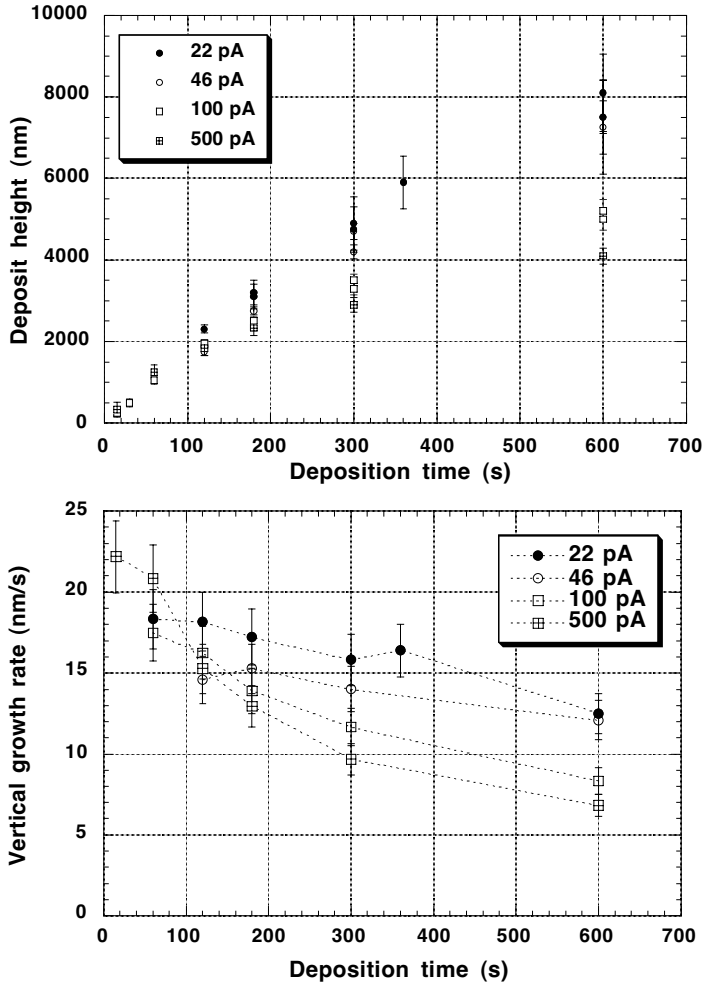

Figure 7-13: *Height (a) and three-dimensional growth rate (b) as a function of the exposure time for different I_p values (see inset). Deposits carried out from the precursor $[RhCl(PF_3)_3]_2$ on bulk Si(111); E = 25 keV.*

As already observed for deposits on C films, the height versus time plots present a close to linear behavior with a deviation from linearity at high exposure times, which becomes more pronounced with increasing deposition currents. The plot shows that, in the investigated current range, the efficiency for three-dimensional deposition increases with decreasing probe current I_p (see inset). The graph in Fig. 7-13b reports the vertical deposition rate as a function of the exposure time. The vertical deposition rate (of the order of 17 to 22 nm/s) decreases with time at all the applied deposition currents. The decrease becomes steeper with increasing beam current. This is an indication that surface diffusion contributes to the precursor transport in the reaction region.

The deviation from linearity of the height versus time plot at high deposition current and the decrease of deposition rate with time can be explained by the effect of the increasing width of the electron beam diameter. When the beam diameter increases, EBID takes places in a larger area. The precursor molecules, which reach the reaction area by surface diffusion have a higher probability to be decomposed by peripheral electrons before reaching the center of the beam and contribute to vertical growth.

The volume of deposited material as a function of time for four different values of the electron current is reported in Fig. 7-14a. For volume calculations the deposits are considered as cylinders, with a diameter equal to the EBID column diameter at half width and a height equal to the distance between the rod basis and the tip apex. The error bars are calculated from the errors on the deposit base and height measurements and take into account the approximation to a cylindrical shape. The deposited volume increases with increasing I_p, according to the increasing number of impinging electrons. For a given electron current the deposited volume increases linearly with increasing exposure time at low I_p (22 pA and 46 pA); at higher I_p (100 and 500 pA) the plots present a deviation from linearity at high exposure times.

The volume growth rate, reported in Fig. 7-14b is almost constant with time for I_p = 22 pA and I_p = 46 pA, while it decreases with time at I_p = 100 pA and more steeply at I_p = 500 pA. Since both precursor flux and electron flux (for a given deposition current) at the surface are constant during deposition, a constant volume deposition rate is expected at all the applied currents, in equilibrium conditions. The plot 7-14b shows that equilibrium conditions are reached during the deposition process for narrow electron beams and low electron densities while for wide electron beams the equilibrium conditions are reached only at the beginning of the process and not during irradiation. This is a consequence of a higher volume deposition rate which requires a longer time to reach the equilibrium conditions.

The ratio of the volume of deposits obtained at different electron currents it is not equal to the ratio between the corresponding total currents. This confirms that the quantity of the deposited material looks more related to the density than to the total electron current.

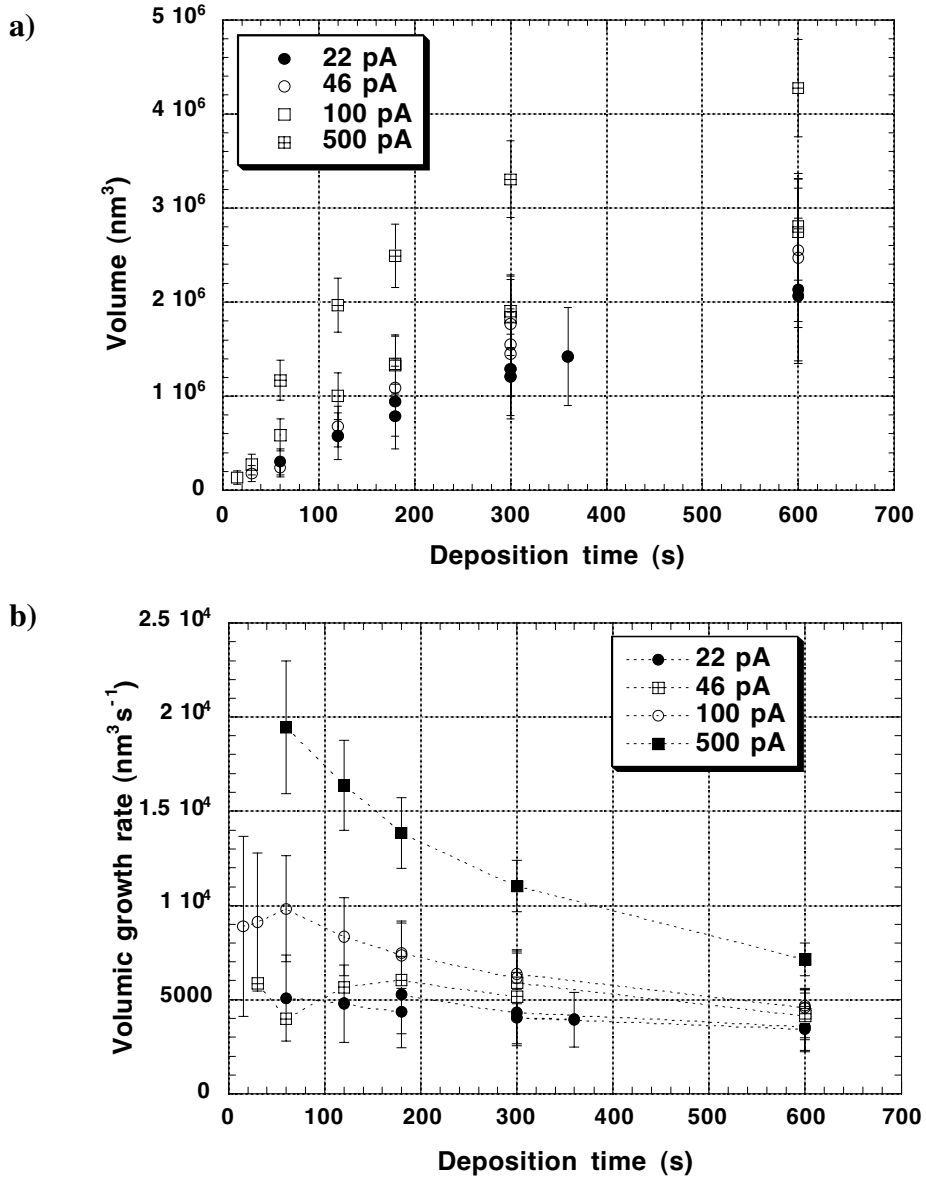

Figure 7-14: *Deposited volume (a) and volume growth rate (b) as function of the exposure time for different electron currents. Deposits carried out from the precursor $[RhCl(PF_3)_3]_2$; E = 25 keV on bulk Si(111).*

7.1.3 LINE DEPOSITION

EBID line deposition has been performed following the procedure described in Chapter 6. Observation of the morphology and the structure of lines obtained under different experimental conditions is an additional tool to understand the deposition process. In addition these structures have a potential application as connections of electrical contacts on micro- and nanometer scales.

EBID lines from $[RhCl(PF_3)_2]_2$ have been deposited by varying the electron energy, the probe current, the point-to-point distance and the dwell time. Deposition has been accomplished on Si(111), C films (20 nm thick), Au films (120 nm thickness) evaporated on SiO_2 and Au pads on thermally oxidized SiO_2 (oxide thickness 450 nm). Different substrates allow to explore the role of the BSE and SE2 in the deposition process.

The dimension and the shape of the EBID lines depend mainly on the size of the primary electron beam, as for the other EBID structures.

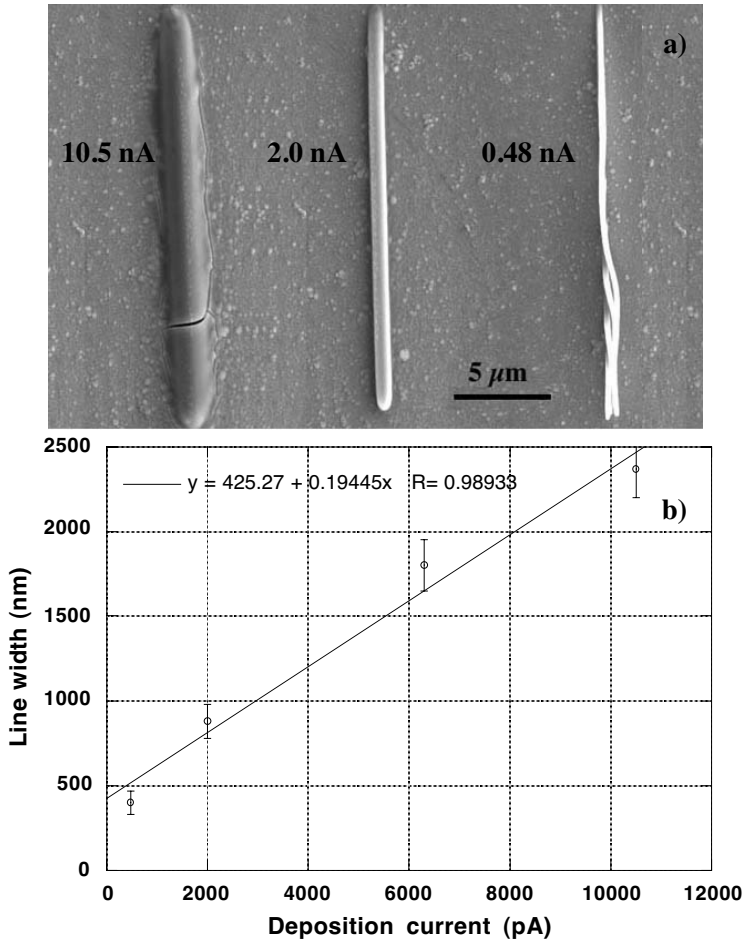

Figure 7-15: *Rh containing EBID lines on a gold substrate deposited at I_p = 10.5 nA (a), I_p = 2.0 nA (b), I_p = 480 pA (c). Line width versus deposition current (d). The data refer to the three lines in Fig. 7-15a and to a line deposited with I_p = 6.5 nA (not shown). Deposits carried out from the precursor $[RhCl(PF_3)_3]_2$; E = 25 keV; point-to-point distance 10 nm, dwell time 1 s. Substrate: thermally evaporated Au film (150 nm) on SiO_2 coated Si.*

The effect of the electron beam size on the line width has been studied by depositing at different electron probe currents and electron energies. As shown in Chapter 2, an increase of the probe current and a decrease of the electron voltage both result in a larger beam size.

The effect of the electron probe current I_p on line width is clearly observed in the SEM images (Fig. 7-15). The three lines have been deposited on a 100 nm thick Au film on thermally oxidized SiO_2 (oxide thickness 450 nm), with an electron energy of 25 keV, a point-to-point distance of 10 nm, a dwell time of 1 s, with electron currents of 10500 pA (a), 2000 pA (b), 480 pA (c). The line width increases linearly with the deposition current, as shown by the plot 7-15. The experimental results show that the line width does not increase with the current with the same law of the beam diameter, proportional to $I_p^{\,0.375}$(Eq. 2. 14).

The effect of the electron beam acceleration voltage E on the lateral width of EBID lines is shown in Fig. 7-16. The two lines have been deposited on p-doped (boron) Si (111), with identical electron probe current (10 nA), point-to point distance (10 nm) and dwell time (1 s), at E = 25 keV (a) and E = 5 keV (b). The images show that the lines deposited at E = 5 keV are a factor 4.5 larger than the lines deposited with E = 25 keV. The result is explained by the broadening of the electron beam distribution with decreasing acceleration voltage.

The two images in Fig. 7-16 explain also the role of the BSE in EBID. The lines deposited at E = 25 keV (Fig. 7-16a) present an external thinner deposit, about 7.5 μm wide, around the main line generated along the primary beam path. This deposit is not observed around the lines deposited at E = 5 keV (Fig. 7-16 b).

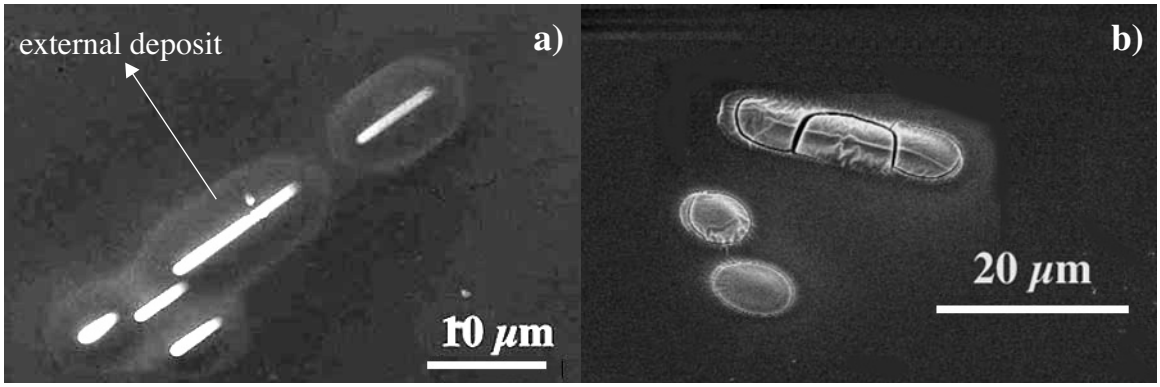

Figure 7-16: *EBID lines deposited on Si(111) at 5 keV (a) and 25 keV (b). Deposits carried out from the precursor* $[RhCl(PF_3)_3]_2$; I_p = 10 nA; *point-to-point distance 10 nm, dwell time 1 s.*

The external and thinner deposit can be explained by the decomposition of the impinging and adsorbed precursor molecules by BSE and SE2 leaving the SiO_2 surface. As shown by the Monte Carlo simulations reported in Fig. 4-5, the BSE lateral range increases with the acceleration voltage. On a Si substrate, at 5 keV the BSE are localized around the primary beam while at 25 keV the lateral BSE range has a width of about 7 μm, comparable to that of the broad area in Fig. 7-16b.

The wider external area is not visible in Fig. 7-15, partly because of the reduced BSE lateral range of Au (see Fig. 4-5) compared to Si, partly because of lower contrast between the Au substrate and the Rh deposit.

The effect of the exposure time, i.e. of the total electron density deposited at the surface, is shown in Figs. 7-17a, 7-17b, 7-17c, 7-17d. The four lines have been deposited with E = 25 keV,

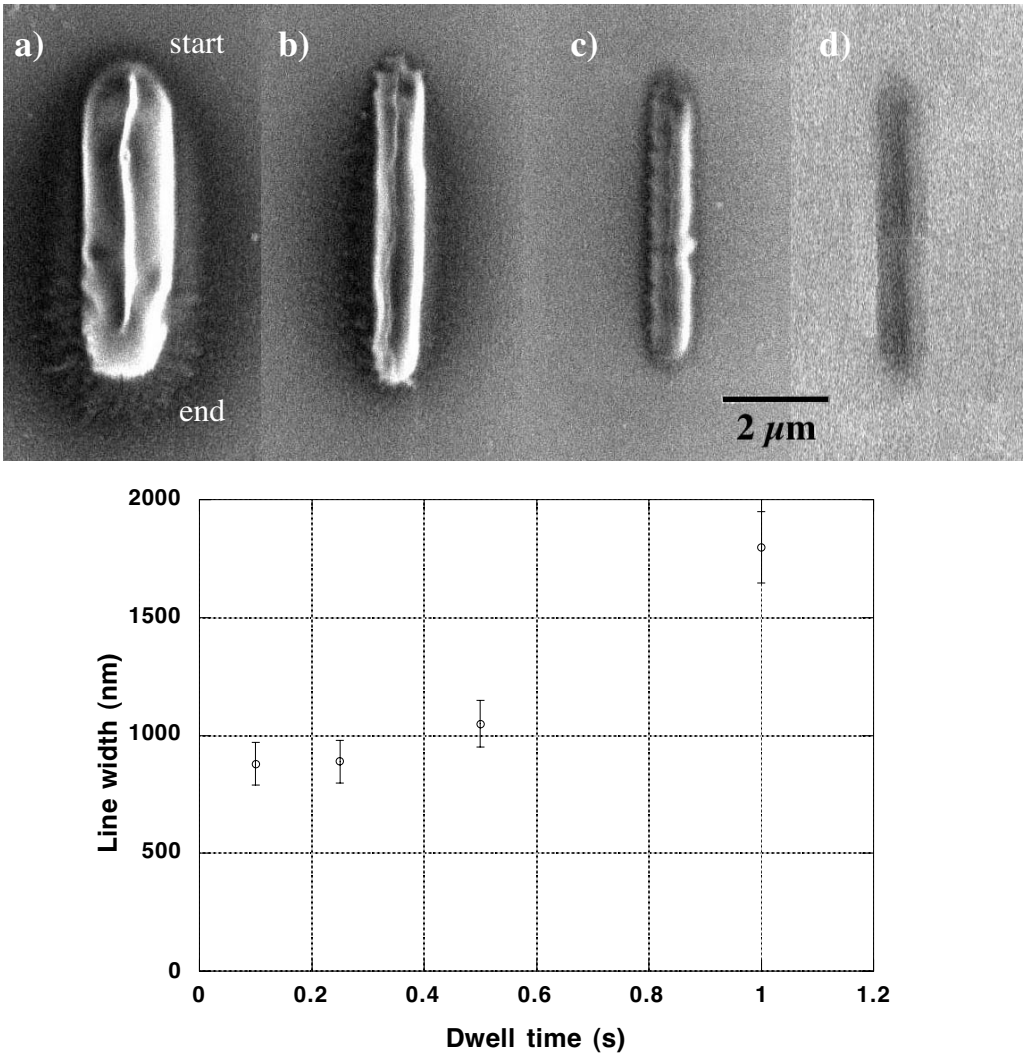

Figure 7-17: *Rh containing EBID lines deposited at different dwell times; 1 s (a), 0.5 s (b), 0.25 s (c), 0.1 s (d). Width versus exposure time for the lines shown in Fig. 7-17 a-d (e). Substrate: thermally evaporated Au film (150 nm) on SiO_2 coated Si; E = 25 keV, I_p= 8.5 nA, point-to-point distance 10 nm, precursor: $[RhCl(PF_3)_3]_2$.*

I_p = 8500 pA, a point-to-point distance of 10 nm and a dwell time of 1 s (a), 0.5 s (b), 0.25 s (c), 0.1 s (d). In all the four picture the upper part of the line represents the starting point of the deposition, as can be recognized from the shape of the line and the surrounding deposit.

Varying the dwell time while keeping all the other parameters constant allows to clarify the effect of the increasing electron dose on the peripheral regions of the electron beam.

The lines reported in Fig. 7-17 have been deposited in spot mode moving the electron beam along a line of 5 μm, with a point-to-point distance (10 nm) smaller than the beam diameter at 10 nA. For that reason every point along the electron beam path is irradiated several times and the total electron dose deposited per unit surface is given by the sum of all the electron doses to which the surface is exposed. Increasing the exposure time increases the electron dose on the irradiated regions and allows to achieve deposition at larger distances from the center of the beam, as proven by the change in line width shown in Figs. 7-17a-d. The same effect determines an increase of the line length with increasing exposure time. All the lines are longer than the distance travelled by the electron beam; this is a further confirmation that deposition takes place far from the beam center.

The lines shown in Figs. 7-17a-d have been also studied by AFM. The AFM images shown in Fig. 7-18a reveal the granular structure of the line end, better visualized at higher magnification (Fig. 7-18b). The grain size ranges from 10 to 20 nm and increases when moving from less irradiated to more irradiated regions. This indicates that the grain size increases with increasing electron dose.

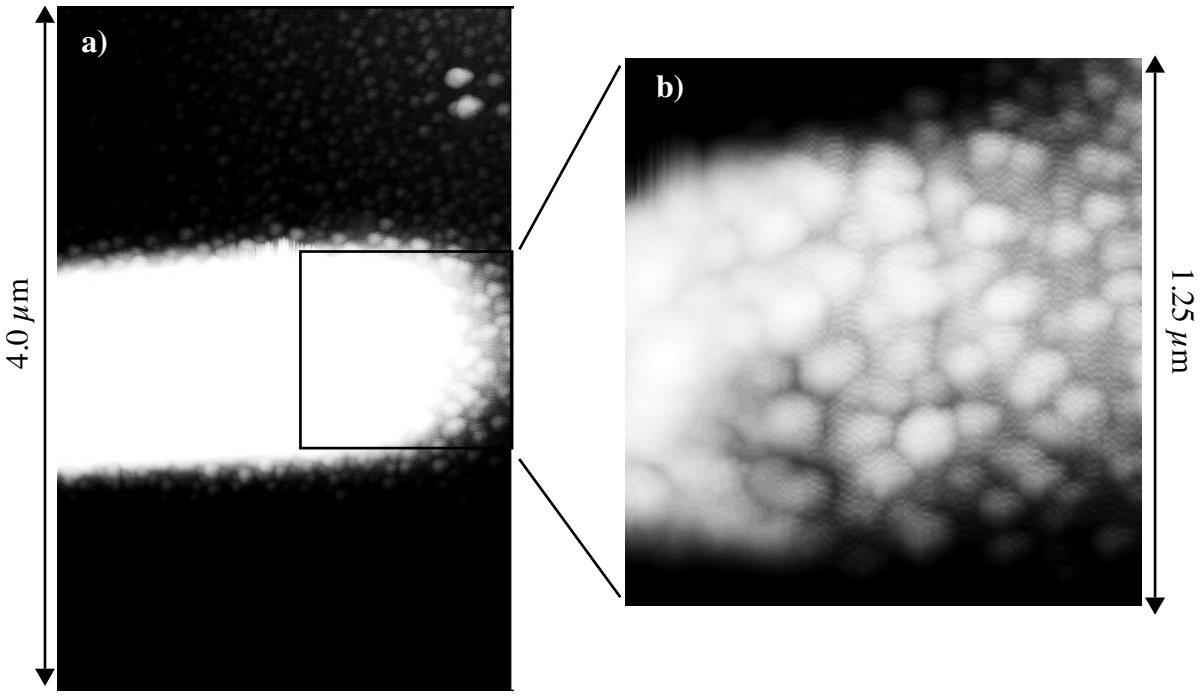

Figure 7-18: *AFM image of the end of the line shown in Fig. 7-17b (a); magnified image of the area in the black square showing the clustered structure of the line end (b). Substrate: thermally evaporated Au film (150 nm) on SiO_2 coated Si; E = 25 keV, I_p = 8.5 nA, point-to-point distance 10 nm, dwell time 0.5 s, precursor: $[RhCl(PF_3)_3]_2$.*

The AFM image of the line shown in Fig. 7-17c is shown in Fig. 7-19a and the scan profile in the center of the line in Fig. 7-19b. The profile shape confirms the decreasing thickness at the extremities of the line. The top region of the profile reveals a roughness with maximum valley depth of about 20 nm, corresponding to the observed grain size.

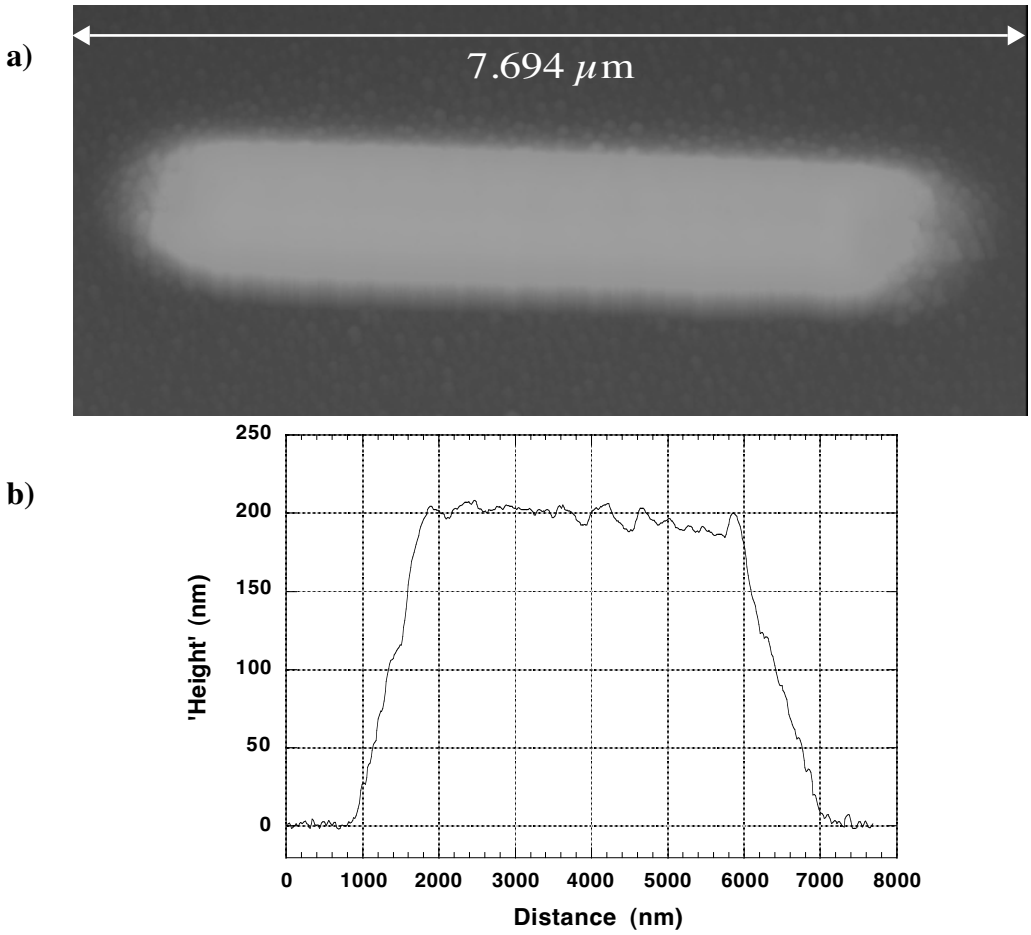

Figure 7-19: *AFM image (a) and AFM length profile (b) of the EBID line shown in Fig. 7-17c. Substrate: thermally evaporated Au film (150 nm) on SiO_2 coated Si; E = 25 keV, I_p = 8.5 nA, point-to-point distance 10 nm, dwell time 0.25 s, precursor: $[RhCl(PF_3)_3]_2$.*

The section profile of the same two lines are shown in Fig. 7-20. The graphs shows the increasing line height and width with increasing dwell time and confirm that the deposition rate during line writing is higher in the center than in the peripheral region of the electron beam.

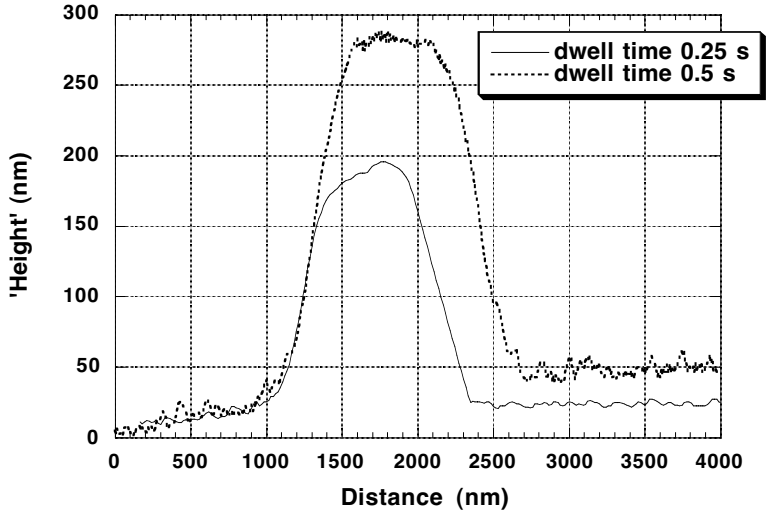

Figure 7-20: *AFM section profiles of the lines shown in Figs. 7-18a and 7-19a.*

The TEM pictures in Figs. 7-21a-d show the effect of the increasing point-to-point distance in EBID. The lines have been deposited on a 20 nm thick carbon grid, with E = 25 keV, I_p = 6 nA, a dwell time of 1 s and a point-to-point distance of 120 nm (a), 300 nm (b), 600 nm (c) and 800 nm (d). The line height increases with decreasing point-to-point distance, as proven by contrast changes. The line width in the four picture is roughly the same, because of the constant dwell time and the sufficiently large point-to point distance, which avoids strong overlap of the exposed regions.

Particularly interesting is the line in Fig. 7-21d; the periodical structure shows that every single irradiation induces deposition on a circle of about 800 nm in diameter. The regions of the line exposed more than once to the electron beam can be recognized as darker regions. The periodical structure disappears already for a point-to-point distance of 600 nm, because of dose accumulation along the line length.

For four-probe electrical resistivity measurements, EBID Rh containing lines have been deposited between Au electrodes, pre-deposited on thermally oxidized (450 nm thickness) silicon, as explained in Chapter 6 (Fig. 6-3). Line deposition has been obtained at electron energies of 2, 5 and 25 keV, at different I_p values between 350 pA to 8 nA. Examples of Rh containing lines connecting Au electrodes are shown in the SEM pictures in Fig. 7-22. The lines have been deposited with the beam operating in spot mode, with a point-to-point distance of 10 nm, a dwell time of 1s, I_p = 6000 pA (Fig. 7-22a) and I_p = 350 pA (Fig. 7-22b) and E = 25 keV. As is clearly visible from the image in Fig. 7-22a the Rh containing line deposited at high electron current present several cracks, which interrupt the contact in the line path, making impossible electrical resistivity measurements. A similar effect is visible also in Fig. 7-15a and 7-16b. Cracking of the lines on substrates for electrical conductivity measurements has been observed in about 20 cases for deposition with I_p > 1 nA, at electron energies of 25 keV, 5 keV and 25 keV. The line in Fig. 7-22a presents the thinner external deposit, already discussed earlier.

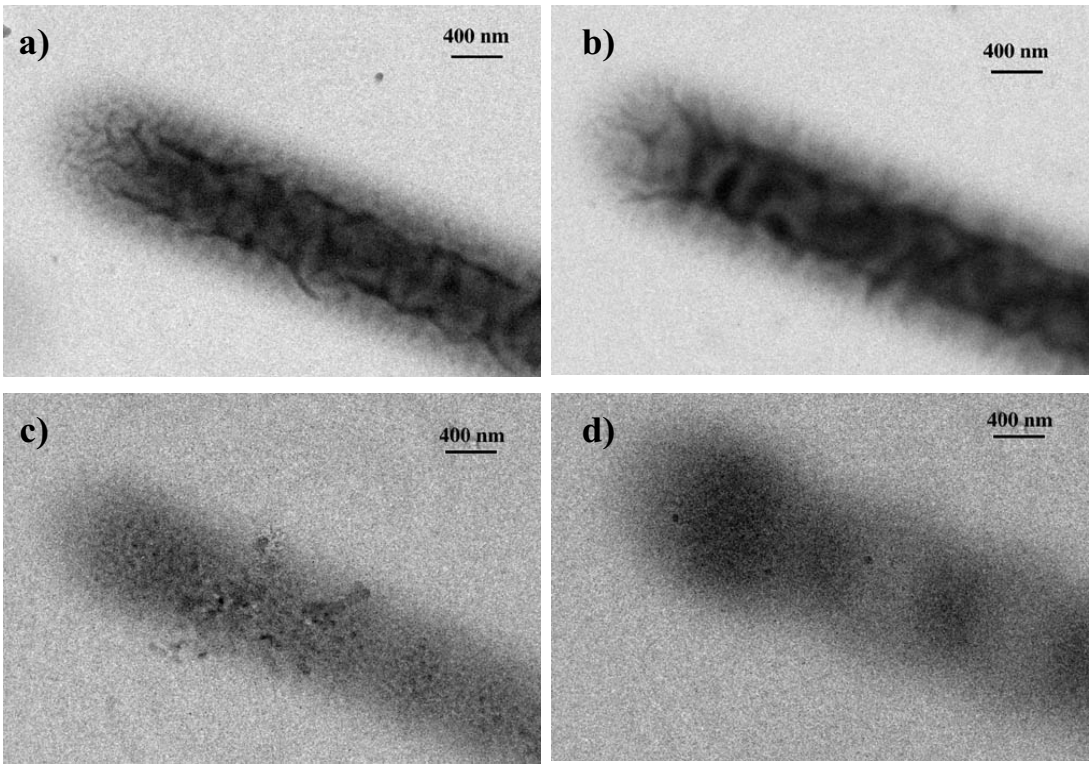

Figure 7-21: *TEM micrographs of EBID lines deposited at various point-to-point distances: 120 nm (a), 300 nm (b), 600 nm (c), 800 nm (d). Deposits carried out from the precursor $[RhCl(PF_3)_3]_2$ on a C grid; E = 25 keV, I_p = 6 nA, dwell time 1 s.*

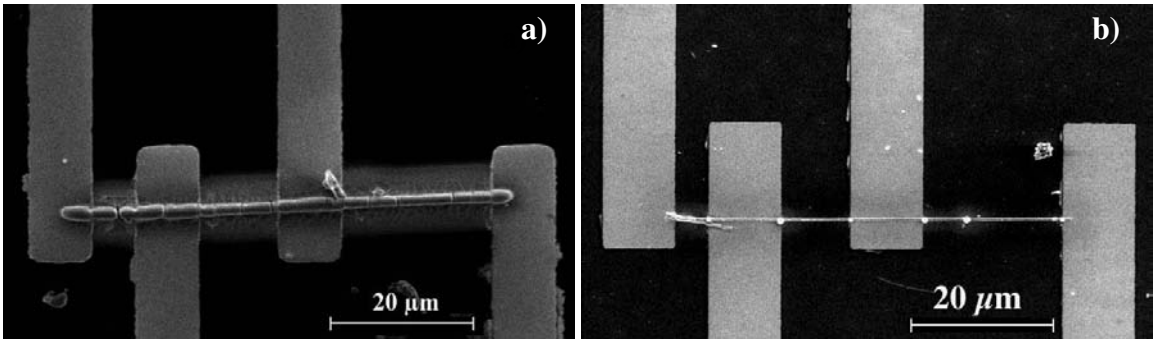

Figure 7-22: *SEM pictures of lines connecting Au electrodes pre-deposited on SiO_2 for four-point-probe resistivity measurements. Deposits carried out from the precursor $[RhCl(PF_3)_3]_2$; E = 25 keV, dwell time 1 s, point-to-point distance 10 nm, I_p= 6 nA (a), I_p= 350 pA (b).*

The cracking effects can be reduced by depositing at lower I_p, as observed for the line shown in Fig. 7-22b, deposited with I_p = 350 pA and with the same parameter as the line previously shown. The clear dots visible on the line are EBID repairs carried out after the line deposition

process. The electrical resistivity of the lines (and of other lines deposited in the same experimental conditions) is about 30 MΩ cm, resulting in a resistivity ratio to pure Rh of about 10^9. This value is higher than expected from the composition of the deposited material. In total 10 lines have been deposited without obtaining lower resistance values. Even variation of the writing speed did not improve the resistivity of the lines. The reason for the high resistivity could be that the Rh grain immersed in the amorphous matrix are not in contact, as shown by TEM observations.

To verify if the crack in the lines occurs because of an undesired reaction between adsorbed H_2O or –OH groups and the precursor, deposition experiments were performed also on surfaces modified via a gas phase silylation reaction [2]. The silylation treatment did not change the structure nor the deposition rate of the lines.

The cracking of the lines can be due to electron beam heating during irradiation or to mechanical stress between substrate and deposit. The second effect is more probable since, as already shown in Chapter 4, heating effects do not play a role in EBID.

7.1.4 DEPOSITION OF HOLLOW STRUCTURES

The deposition rate in EBID depends, at a given electron current, on the flux of precursor molecules that reach the reaction area. If the precursor is delivered with a capillary tube, the flux can be varied by changing the distance between the tube end and the irradiated area (Fig. 7-23a). As already discussed in Chapter 3, the width and the focusing of the molecular beam exiting the tube depends on the *L/R* ratio. However the gas concentration increases in proximity to the exit. In this work the precursor is delivered to the reaction area with a tube oriented to an angle of about 30° to the substrate, as shown schematically in Fig. 7-23. For a 15 mm long needle, with a diameter of 0.8 mm, the issuing molecules can reach the substrate by direct gas phase transport up to a distance of 1 mm from the needle exit. At large distances from the needle exit the precursor flux is given only by molecules flowing from the needle with a straight trajectory, when approaching the needle exit the contribution of molecules scattered from the inner tube walls increases. EBID at variable distance between the impinging electron beam and the precursor flow allows to study the process under different precursor flow conditions. These experiments are also a tool to distinguish between precursor supply to the reaction area by gas phase transport and surface diffusion.

As already explained in Chapter 3, gas phase transport occurs in all the sample regions exposed to the molecular beam, as shown schematically in Fig. 7-23. The molecules interacting with the surface can be adsorbed and then released after a certain residence time. During their residence time at the surface the molecules can diffuse according to Fick's law, before being desorbed. In Chapter 3, with an approximate model, I have estimated the maximum distance of surface diffusion for $[RhCl(PF_3)_3]_2$ molecules on stainless steel (around 4 μm). If a similar behavior on SiO_2 surfaces is detected, EBID should be detected only in substrate regions exposed to the molecular beam. In this work electron beam irradiation behind the needle exit and of other substrate regions not exposed to the molecular flux did not lead to deposition. This result

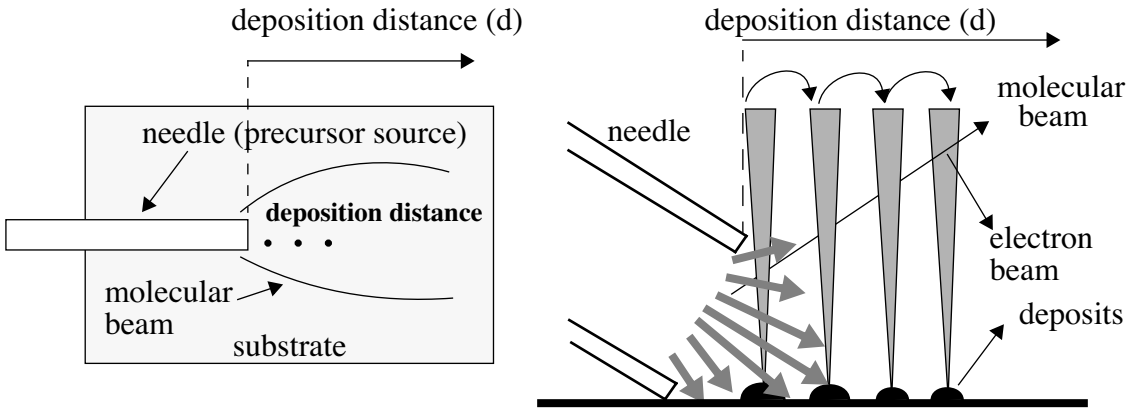

Figure 7-23: *Schematic drawing of the experiment at variable deposition distance. Top (a) and side view (b).*

proves that the precursor delivery to the reaction area occurs mainly from the gas phase. A contribution from surface diffusion is possible when the substrate is irradiated at a point within the molecular beam. The irradiation decomposes the impinging and adsorbed molecules and creates a concentration gradient between the irradiated region and the surrounding areas, which enhances surface diffusion on sub-micrometer distances. Such distances can be travelled by the precursor molecules during their surface residence time.

A confirmation of the higher contribution of the direct gas phase transport compared to surface diffusion is obtained by SEM and AFM observation of deposits carried out at increasing distance between the electron beam and the precursor source.

The results of a series of EBID deposits obtained by varying the needle-beam distance from 10μm to 1000 μm, is shown (by means of high resolution SEM pictures) in Fig. 7-24. The deposits have been carried out on SiO_2 (100 nm thick on Si), with I_p = 1000 pA, E = 25 keV and an t_e = 180 s. The precursor source during EBID was located on the left side of the deposits.

The images reveal that when increasing the beam-source distance the deposit diameter decreases and the morphology changes. The deposit obtained close to the beam exit (Fig. 7-24a) has the classical symmetrical hemispherical shape, typically obtained at high probe current. Starting from Fig. 7-24a (d = 150 μm) the deposits have an asymmetrical shape, with a higher growth rate in the direction of the precursor source. The phenomenon is emphasized in the pictures of the deposits carried out at higher values of d. In particular, for d = 570 μm or higher, the deposits are clearly made of two well-distinguished regions: an external semi-circular wall, and a central region made of nano-columnar structures. The external wall is higher in the direction of the precursor flux. The nano-columns in the center of the deposit are oriented towards the precursor source, as shown in Fig. 7-24d-f and, with higher magnification, in Fig. 7-25a. The nano-columns have a diameter ranging from 30 to 100 nm.

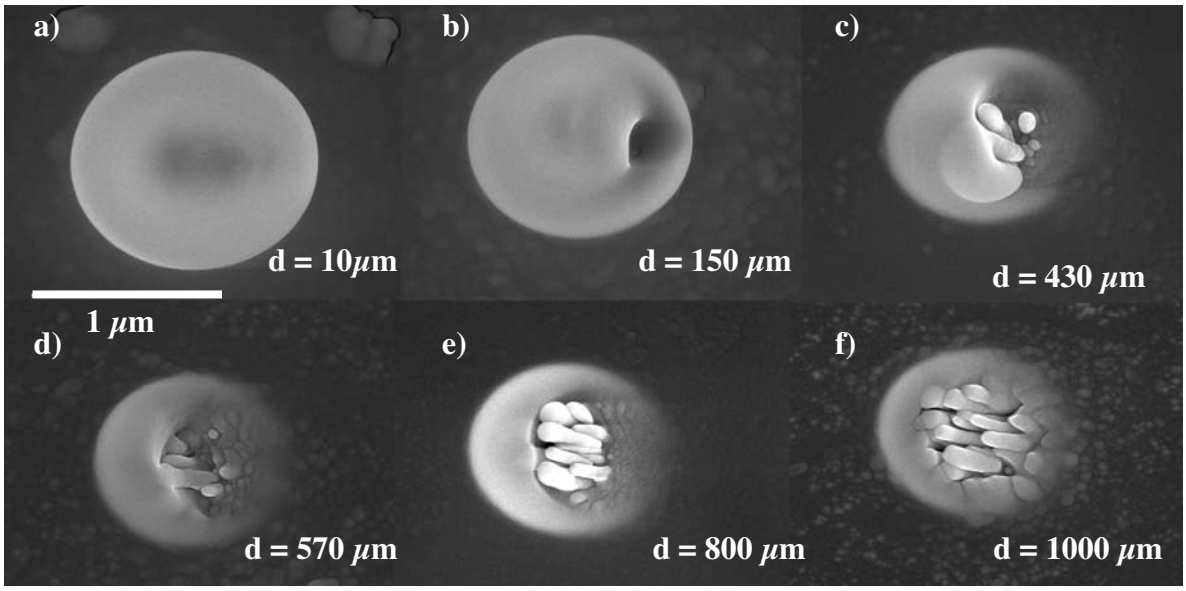

Figure 7-24: *SEM (XL30 SFEG) images of EBID deposits obtained at growing source-beam distance d (a-f). Depositions carried out on SiO_2 (150 nm on Si) from the precursor $[RhCl(PF_3)_3]_2$; E = 25 keV, I_p = 1 nA (a), 180 s exposure time.*

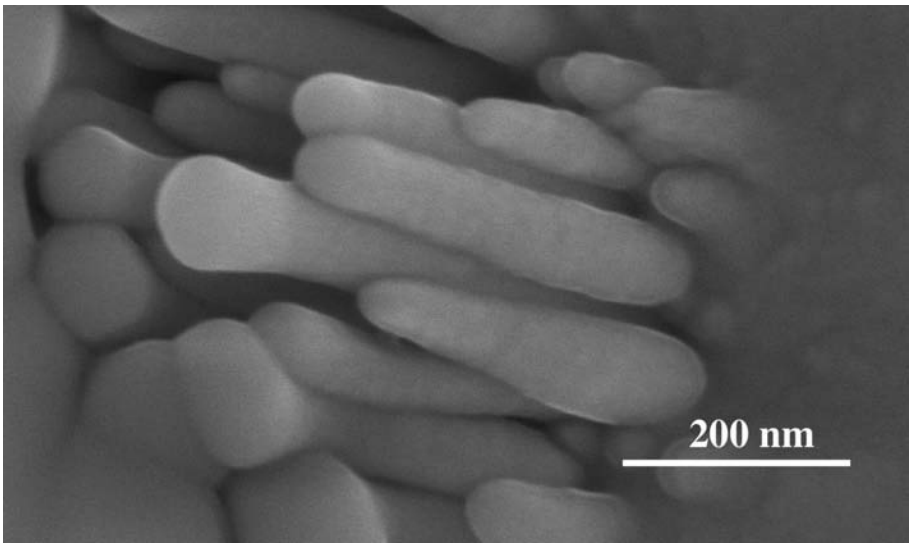

Figure 7-25: *High magnification SEM image (SFEG XL 30) of the central region of EBID hollow deposits shown in Fig. 7-24f.*

Similar results have been obtained by depositing at I_p = 500 pA, keeping constant the other deposition parameters. Examples of deposits obtained at 500 pA are shown in Fig. 7-26. The images show the effect of the increasing distance. Compared to Fig. 7-24, the deposits are smaller because of the smaller beam size. The central region of the deposit in Fig. 7-26c is shown with higher magnification in Fig. 7-27.

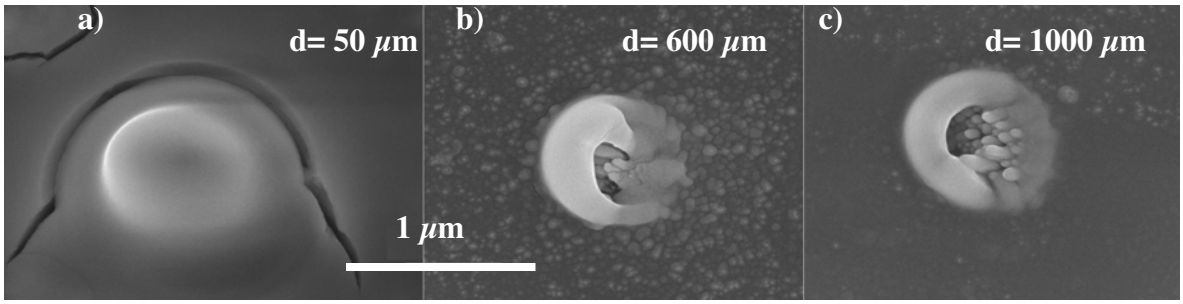

Figure 7-26: *SEM (XL30 SFEG) images of EBID deposits obtained at growing source-beam distance d (a-c). Depositions carried out on SiO_2 (150 nm on Si) from the precursor $[RhCl(PF_3)_3]_2$; E = 25 keV, I_p = 500 pA (a), 180 s exposure time.*

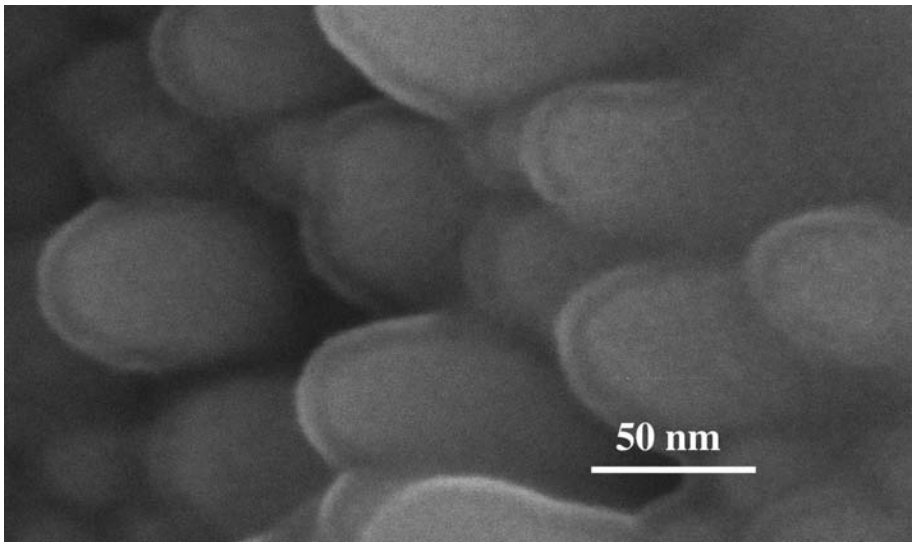

Figure 7-27: *High magnification SEM image (SFEG XL 30) of the central region of EBID hollow deposits shown in Fig. 7-26c.*

The morphology of hollow EBID deposits has also been studied with AFM. The AFM images in Fig. 7-28 show three hollow deposits carried out with I_p = 450 pA, E = 25 keV with source-beam distances of 850 μm, 1000 μm and 1200 μm. The precursor source during EBID was located on the right side of the deposit. The images show the same tendency as in Figs. 7-24 and 7-26 and reveal that a further increase of d determines a decrease of the quantity of the material deposited in the central region of the deposits. In particular, at d = 1200 μm a close to symmetrical ring shape deposit is obtained. The AFM section profiles of the hollow deposits are reported in the plot in Fig. 7-28d. The scale on the ordinate axis is magnified by a factor 10 with respect to the abscissa, for better visualization of the plot. The graph confirm that, for each deposit the external wall is higher in the direction of the precursor source and that the wall height and the quantity of deposited material decrease with increasing d.

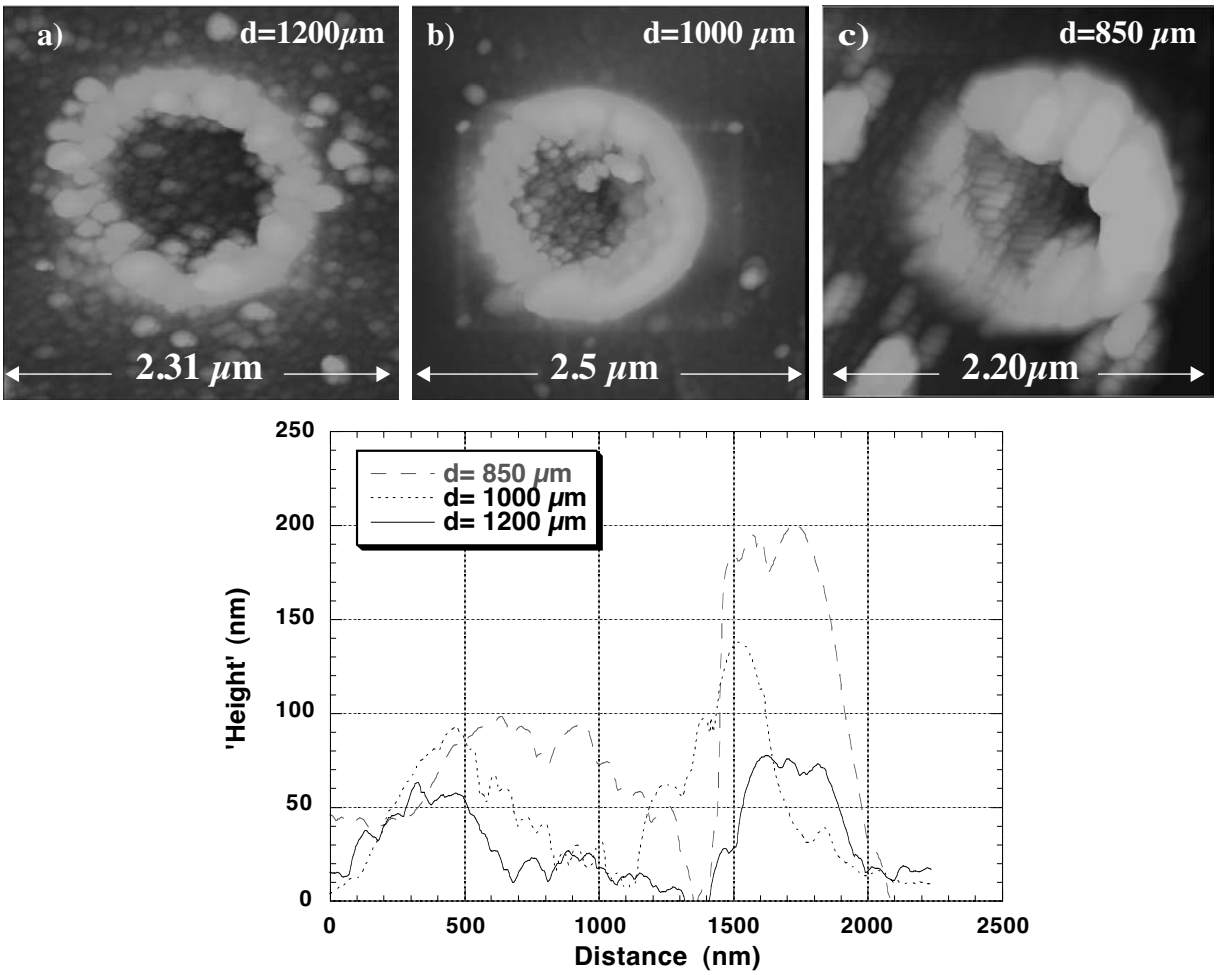

Figure 7-28: *AFM images of donut shaped EBID deposits obtained at growing source-beam distance (d): 1200 μm (a), 1000 μm (b), 850 μm (c). Deposits carried out on SiO_2 (150 nm on Si) from the precursor $[RhCl(PF_3)_3]_2$; E = 25 keV, I_p = 450 pA (a), 300 s exposure time.*

A further confirmation of the deposit thickness decrease in the center of the deposit with increasing d is obtained by analyzing the contrast intensity of TEM DF images. The images in Fig. 7-29 show EBID dots obtained at 25 keV and 1 nA, with an exposure time of one second, on C grids at a distance from the needle of 40 μm (a) and 360 μm (b). The elliptical shape of the deposits shown in Fig. 7-29a is due to non-perfect adjusting of the astigmatism. Comparison of Figs. 7-29a and 7-29b shows a decrease of the contrast in the center of the dots for increasing *d*, better visualized by comparison of the contrast profiles reported in Fig. 7-29c and 7-29d. The contrast profile of the dot deposited at d = 40 μm has a flat top while the one of the dot deposited at d = 360 μm shows a decrease moving from the edge to the center of the deposit, which corresponds to a decrease in thickness. The presence of this phenomenon on thin C film substrate excludes that the external deposit is generated by backscattered electrons.

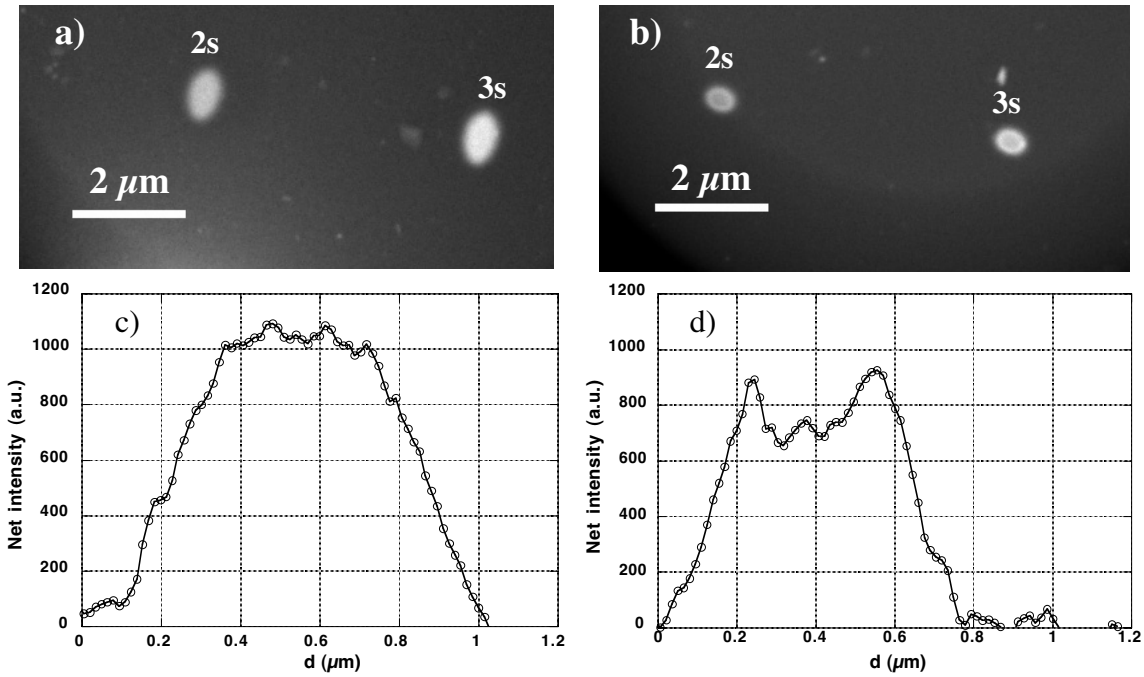

Figure 7-29: *TEM images and contrast versus distance changes of deposits obtained at different source-beam distance. Deposits carried out on C grids from the precursor* $[RhCl(PF_3)_3]_2$; *E = 25 keV,* I_p *= 450 nA (a), 300 s exposure time.*

The change in morphology of the deposits with the distance can be explained by looking at the simplified schematic drawing in Fig. 7-23b. At short source-beam distances the precursor flux from the tube exit to the surface is symmetrical with respect to the irradiated area because of the contribution of the molecules scattered in the inner tube wall. At larger distances the contribution of the scattered molecules decreases and the flux of the precursor molecules reaching the surface becomes oriented in the direction of the precursor source. Therefore the molecules reaching the irradiated area are first decomposed on the side of the electron beam which is first exposed to the flux, and form the semi-circular external wall. The remaining molecules reach the beam center and give raise to the columnar deposits. Columnar growth is observed in substrate regions reached by higher electron density and it is enhanced by increasing the electron current from 500 pA to 1000 pA. A similar effect is known from the literature on thermal CVD [3]. The structure of thermally grown deposits turns from granular to columnar when increasing the substrate temperature. These results and those obtained in this work indicate that columnar growth occurs in the points of higher energy deposited on the substrate. The orientation of the columns towards the precursor source is a geometrical effect, already known from thermal CVD [3].

7.2 NANO-STRUCTURE BY TEM

The nanostructure of the material obtained from EBID of $[RhCl(PF_3)_2]_2$ has been studied ex situ by Transmission Electron Microscopy. The observations have been carried out on EBID dots, lines and tips, deposited at different beam current and acceleration voltage.

A TEM bright field image of the tip of an EBID rod, with a curvature radius of about 50 nm, deposited on a graphite film with E = 25 keV, I_p = 40 pA and t_e = 300 s, is shown in Fig. 7-30a. The image reveals the nano-structure of the deposits:

- dark granular regions of about 5 nm in diameter are observed;
- the dark regions are separated by brighter regions showing an amorphous like pattern;
- a 4-5 nm thick bright shell surrounds the deposit.

The diffraction pattern of the same region is shown in Fig. 7-30b. The position of the diffraction rings is in good agreement with the literature values for pure rhodium [4], represented by the black dashed circles in Fig. 7-30b. This result proves the presence of poly-crystalline metallic Rh in the deposit. According to surface analysis (presented in the following sections) and TEM imaging, the outer amorphous layer can be identified as a C contamination layer formed during air exposure or SEM observation.

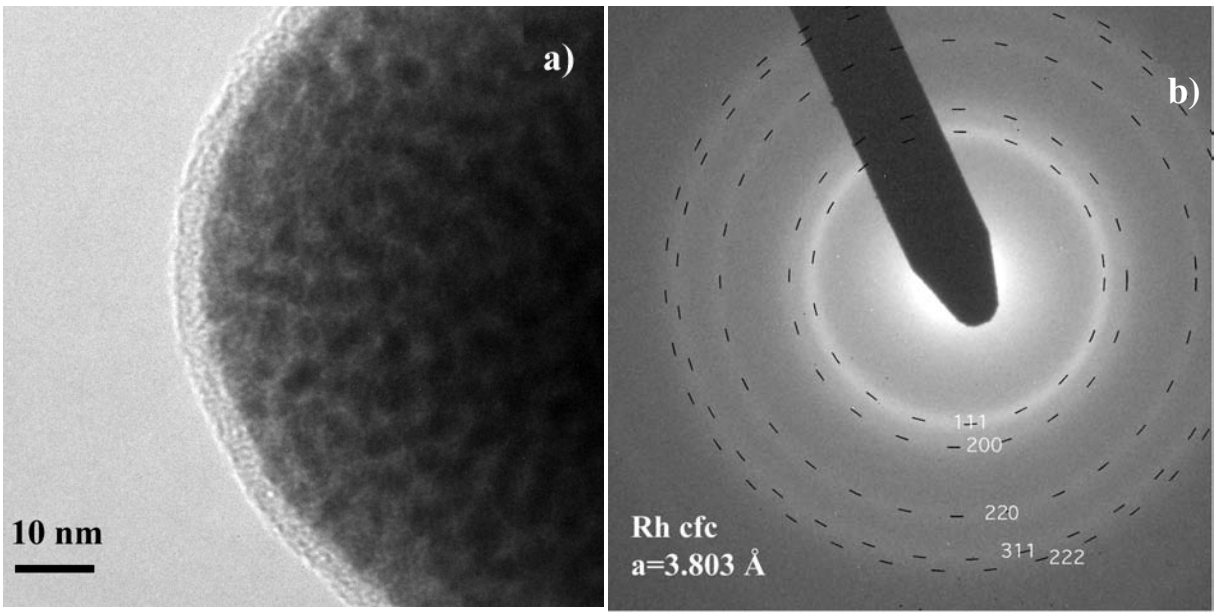

Figure 7-30: *TEM micrographs displaying (a) the apex of a tip deposited on a C grid showing the nanocomposite structure; (b) electron diffraction pattern of the same region revealing the poly-crystalline structure (the black dashed circles indicate the position of the diffraction rings for pure Rh). Precursor: $[RhCl(PF_3)_3]_2$; E = 25 keV, I_p = 40 pA, exposure time 300 s.*

High Resolution Electron Microscopy (HREM) imaging (Fig. 7-31) of lines deposited on 20 nm thick graphite films with an electron energy of 15 keV and an electron current of 8 nA gives further insight into the structure of the deposit. Lattice planes of crystallites are visible in the image. Fourier transform (low left corner of Fig. 7-30) shows that these grains have the symmetry and lattice plane spacings of poly-crystalline Rh. This confirms that the dark regions of the HREM image correspond to the poly-crystalline Rh grains.

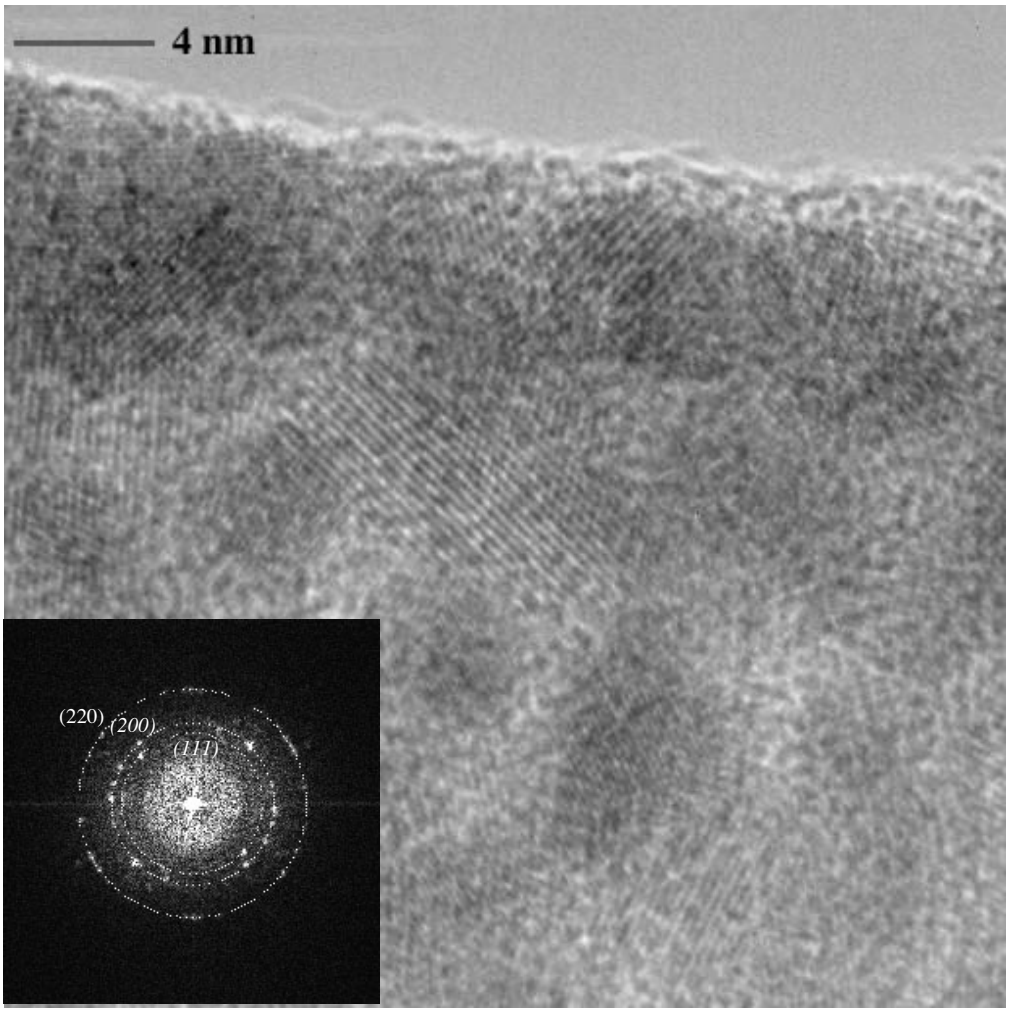

Figure 7-31: *High resolution TEM image of an EBID line, showing lattice planes of nanocrystals of 4-8 nm diameter. The diffraction pattern obtained from Fourier Transform of the TEM image is shown in the lower left corner. Precursor: $[RhCl(PF_3)_3]_2$; E = 15 keV, I_p = 8 nA, dwell time 1 s, point-to-point distance 10 nm.*

High resolution STEM images of an EBID dot deposited at E = 25 keV, I_p = 8 pA, and t_e = 60 s are reported in Fig. 7-32. The images have been acquired with different contrasts, in order to visualize zones in the center (a) and at the border (b) of the deposit. The image contrast is close to *Z*-contrast since it is obtained with electrons which are scattered by angles larger than 40

mrad. This means that the neat image intensity is proportional to Z^2. The Rh nano-grains (bright) can be clearly distinguished from the amorphous material between them (dark). The intensity of singular Rh grains of similar size changes by ±20% from one grain to another. On the other hand, the intensity of the amorphous region in the deposit is a factor 3-4 lower than the one in the Rh grains. Since for *Z*-contrast imaging contrast increases with Z^2, the result reveals that the amorphous regions are composed of low-*Z* material (i.e. P, N, O, C).

Figure 7-32b shows that Rh nanocrystals, with an average size of 5 nm, are also present on the substrate outside the dot area. These crystals may have been deposited by scattered electrons or during SEM imaging in scanning mode in the deposition system. The result proves that Rh nanocrystals are present even in deposits obtained at low electron beam current and short exposure times. Diffraction patterns acquired on deposits grown with different beam parameters and exposure times have similar line widths. This is an evidence for the stability of the grain size when the dot thickness increases, confirmed by the fact that even at higher specimen thickness the Rh deposits form a network of nanometer sized grains, as shown in Figs. 7-30, 7-31 and 7-32.

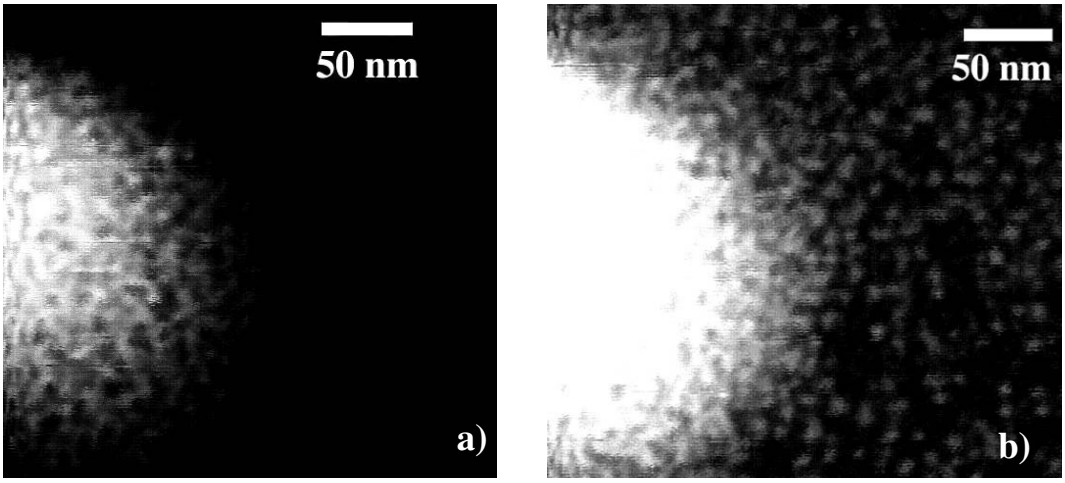

Figure 7-32: *STEM micrographs of a Rh EBID dot acquired with different contrasts. Deposit carried out on a C grid from the precursor* $[RhCl(PF_3)_3]_2$; $E = 25$ *keV,* $I_p = 8$ *pA (a), 60 s exposure time.*

A high magnification picture of Rh nanocrystals in a deposit carried out with $E = 25$ keV, $I_p = 1$ nA, $t_e = 1$ s, is shown in Fig. 7-33a. The size of the nano-crystals ranges from 2 to 4 nm, as better visualized in the contrast profile shown in Fig. 7-33b, plotted after subtraction of the C film background.

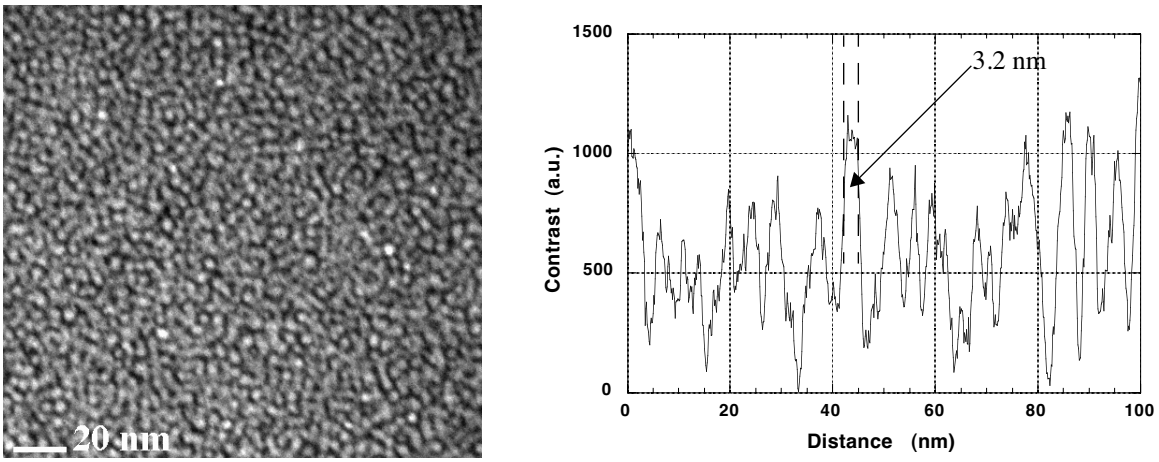

Figure 7-33: *TEM image of Rh grains in a very thin deposit (a). TEM contrast profile of the same region after subtraction of the C grid contribution (b). The image and the graph reveal that the size of the nano-crystals ranges from 2.5 to 3.5 nm. Deposit carried out on a C grid from the precursor* $[RhCl(PF_3)_3]_2$*; E = 25 keV,* I_p *= 1 nA (a), 1 s exposure time.*

7.3 AES ANALYSIS

Auger Electron Spectroscopy is used to determine the chemical composition of the deposits, the distribution of the elements and to evaluate carbon contamination.

Possible errors in AES of EBID structures can be caused by differences in morphology of the analyzed samples, by the presence of several elements in the matrix, by the nanocomposite structure of the sample, by the effect of preferential sputtering.

The concentration calculated in this work do not consider the matrix effect. Quantification methods which take into account matrix effects are known only for homogeneous binary solids and become less reliable when a high number of elements are present in the matrix [5]. This can give rise to an error in the quantification of the concentrations [6]. In addition the presence of five elements in the matrix results in a large error on the concentration calculations, because of the higher number of terms in Eq. I-3. Differences in sputtering yields can result in surface composition changes if the yields of the elements present in the deposit are different; i.e the surface results enriched of the element with the lower sputtering yield. This effect cannot be precisely quantified for the nanocomposite EBID structures since the sputtering yields are known only for pure elements. However the values found in the literature [6] for the elements Rh and P are similar (1.9 for Rh, 2.0 for P. 1.87 for P); this makes less probable a surface enrichment in one of the two elements. More problematic is the evaluation of the effect of preferential sputtering of O, Cl and N since it is not known in which form these elements are present in the deposit. The tabulated value for O is 1.87, close to those of P and Rh.

AES has been performed on EBID squares and lines of micro-meter dimensions deposited at various E, I_p and t_e. The deposition and analysis procedure have been described respectively in Sections 6.3, 6.4.4 and in the Appendix (Section I.7).

A typical AES survey spectrum in the (in the nine point differentiated form), of an EBID deposit obtained from $[RhCl(PF_3)_2]_2$ is shown in Fig. 7-34. The analyzed sample consisted in a square with a side of 12 μm, deposited in slow scanning mode (VIS2, see Section 6.3) with E = 25 keV and I_p = 2.2 nA. The dashed and solid curves indicate respectively the spectrum of the deposit as received and after sputter cleaning (2keV Ar^+, 120 s). The spectrum reveals the presence of the elements Rh, P, Cl, N and O; no F is detected even though this element is present in high concentration in the precursor molecule. The characteristic peaks of the elements present in the deposit are indicated in the plot: Rh MNN triplet (peaks at 225 eV, 256 eV and 302 eV), Rh LMM (46 eV), P LMM (120 eV), Cl (180 eV), N (375 eV) and O (500 eV) KLL. Comparison of the spectra before and after sputter cleaning reveals that sputtering induces an increase of the Rh peak and a decrease of the O peak intensity. The typical structure of the C peak, between 260 and 280 eV, is absent and the intensity in the same region is close to the noise, both before and after sputter cleaning.

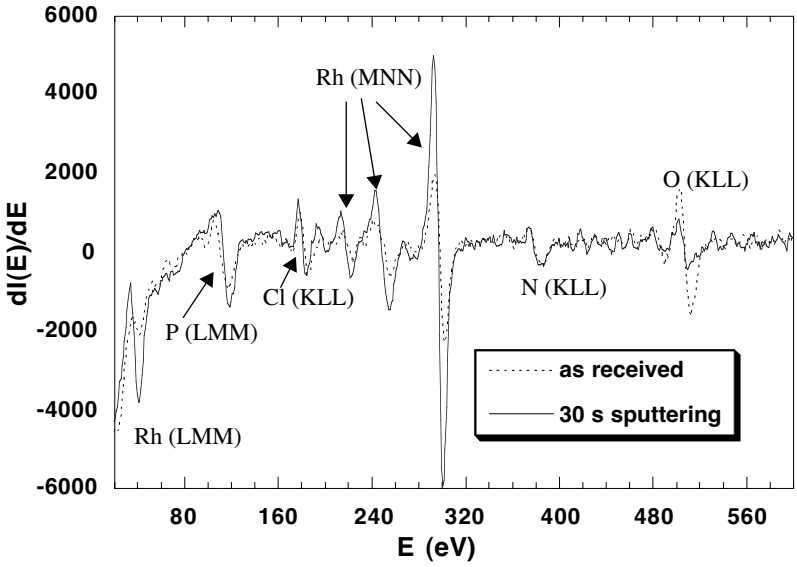

Figure 7-34: *Auger spectrum from an EBID square deposited on Si(111) from the precursor $[RhCl(PF_3)_3]_2$ before (dashed line) and after (solid line) sputter cleaning. Deposition carried out in slow scanning mode (VIS2) with E = 25 keV, I_p = 2.2 nA, 30 minutes exposure time. The characteristic peaks are at 46, 225, 256 and 302 eV for Rh, at 190 eV for Cl, at 120 eV for P and at 510 eV for O.*

To check if the detected elements are homogeneously distributed at the sample surface Auger mapping (Fig. 7-35) has been performed on the surface of the same sample. The AES images, shown in Fig. 7-35, reveal that the elements Rh, P, Cl O and N (not shown) are homogeneously

distributed on the surface of the deposits (within the AES lateral resolution limit), with the exception of the region delimited by the circle in the maps of Rh, O and P. This region shows a Rh concentration higher than in the rest of the deposit. The images reveal that rhodium and phosphorous maps are correlated between them and anti-correlated to the oxygen map. The reported maps present different intensities because of differences in concentrations and in sensitivity factors. The mapping of N is not reported since the signal is close to the noise level. This result does not exclude unhomogeneities at a smaller scale, beyond AES lateral resolution.

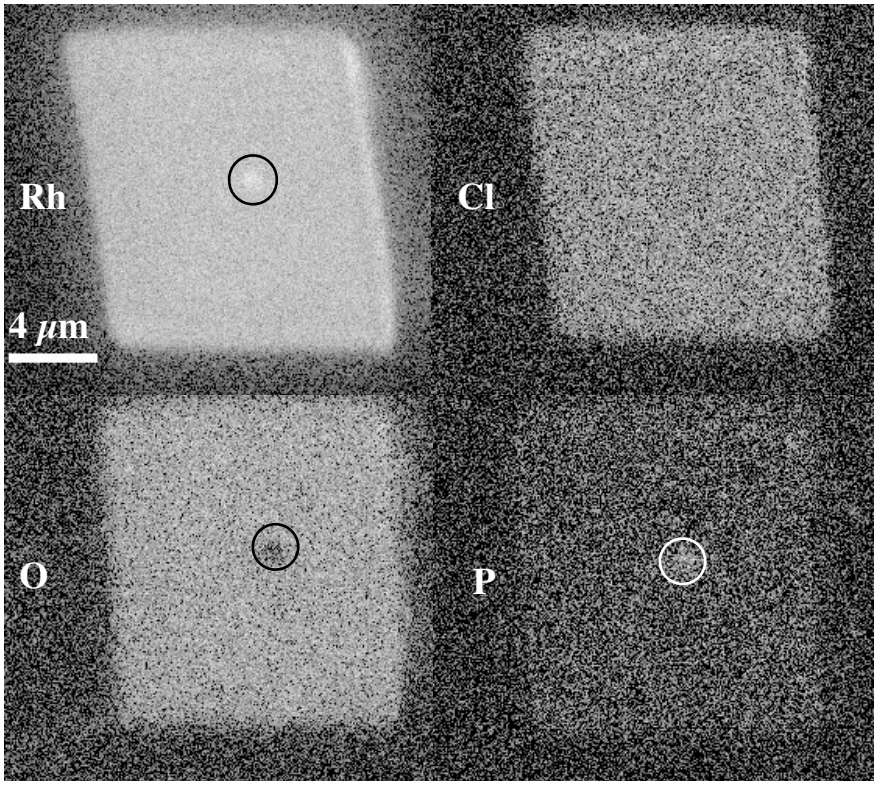

Figure 7-35: *Scanning Auger mapping for the elements Rh, Cl, O, P for an EBID square (side length about 12 µm) deposited on Si(111) from the precursor $[RhCl(PF_3)_3]_2$. The mapping has been obtained after sputter cleaning of the sample. Deposition carried out in slow scanning mode (VIS2) with E = 25 keV, I_p = 2.2 nA, 30 minutes exposure time.*

The atomic concentration of the elements present in the deposit is calculated by applying Eq. I-3, where the intensities I_x refer to peak-to-peak intensity values of the characteristic elemental peaks. A spectrum (same EBID square as for Figs. 7-34 and 7-35), acquired after 120 s sputter cleaning, is shown in Fig. 7-36. The black solid line defines the quantification intervals; the dashed line represents the spectrum of a Rh standard, normalized to the Rh (300 eV) peak intensity of the deposit. The quantification intervals of the elements are indicated in the figure. The overlap of the two spectra in the region 260-300 eV, and the absence of the C peak structure in the same interval, confirm that the C content in the deposit is close to the detection limit.

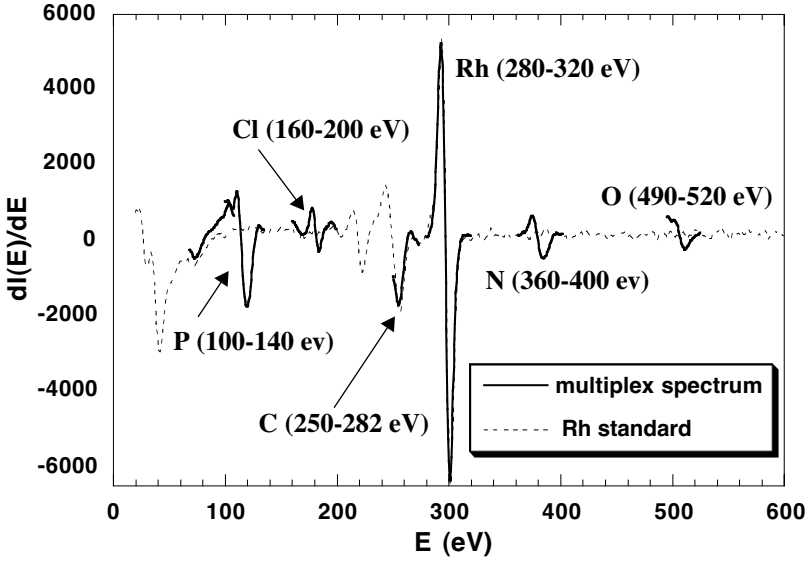

Figure 7-36: *Auger spectrum of a Rh containing deposit acquired in the quantification intervals defined by the solid line. The dashed line represents the survey spectrum of a Rh metallic standard. Same sample as above.*

A further confirmation of the absence of carbon in sputter cleaned EBID squares deposited from $[RhCl(PF_3)_2]_2$ can be obtained by comparison with a spectrum of a carbon containing EBID deposit. Such a sample has been produced by depositing an EBID square from the precursor $(CH_3)_2Au(hfa)$. The composition of the deposit, determined with AES, is 70 at.% C, 16 at.% Au and 14 at.% O. The position and the shape of the C peak in this sample can be considered as a reference for the EBID carbon peak. The differentiated survey spectra, between 220 and 340 eV, of a Rh containing deposit obtained from $[RhCl(PF_3)_2]_2$ (continuous line) and a Au containing deposit (dashed line) obtained from $(CH_3)_2Au(hfa)$, are compared in Fig. 7-37.

The asymmetrical structure of the C peak is visible in the spectrum of the Au containing deposit. Such a peak structure is absent in the spectrum of the Rh containing deposit between 265 and 280 eV. The non-zero amplitude in the spectrum of the Rh deposit between 265 and 280 eV can be due to noise or tail effects from the Rh peak. Therefore when the measured spectra show similar behavior to that reported in Fig. 7-37, the deposits are considered carbon-free.

The analysis and the comments regarding the AES spectra shown until now can be extended in general to all AES spectra of the deposits obtained by EBID from $[RhCl(PF_3)_2]_2$. Several squares have been deposited, from the same precursor, by varying the electron current, the exposure time, the irradiated surface and in some cases the electron energy. The chemical composition (in at.%) of 12 EBID squares is reported in Table 7-1. All the listed concentration values have been calculated from spectra acquired after 120 s sputter cleaning of the samples. The parameter D_e indicates the total electron dose as defined by Eq. 6-1.

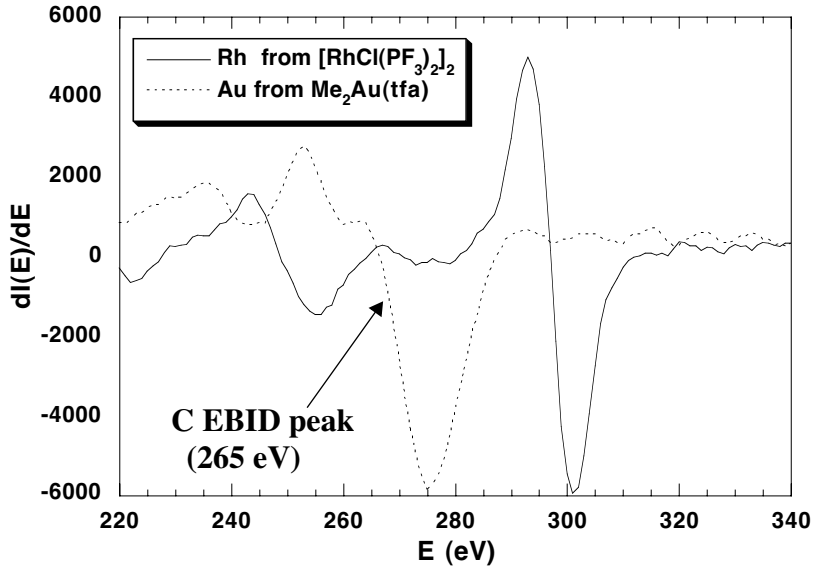

Figure 7-37: *Comparison of AES spectra of EBID squares obtained from $[RhCl(PF_3)_2]_2$ and $(CH_3)_2Au(hfa)$ between 220 and 340 eV. Deposition carried out in slow scanning mode (VIS2) with E = 25 keV, I_p = 2.2 nA, 30 minutes exposure time.*

No.	D_e (μm^{-2})	Rh at.%	P at.%	Cl at.%	N at.%	O at.%	E, I_p, t_e
1	$3.75x10^{22}$	62.0	26.0	1.8	3.6	2.7	25 keV, 10 nA, 15 min.
2	$7.5x10^{22}$	61.0	20.0	7.8	5.7	5.5	25 keV, 10 nA, 30 min.
3	$1.8x10^{23}$	63.9	16.8	6.8	6.4	6.0	25 keV, 10 nA, 75 min.
4	$3.75x10^{23}$	60.6	18.7	3.9	12.0	4.7	2 keV, 1 nA, 150 min.
5	$2.25x10^{22}$	59.7	16.9	2.1	6.0	2.8	25 keV, 1 nA, 90 min.
6	$1.4x10^{23}$	58.0	17.9	3.4	14.1	6.6	25 keV, 1nA, 140 min.

Table 7-1: *Chemical composition (in atomic percent) of EBID squares deposited from $[RhCl(PF_3)_2]_2$ under different experimental conditions. Deposition carried out in slow scanning mode (VIS2). D_e: electron dose.*

7	$2.43x10^{22}$	54.8	12.2	9.4	3.9	19.7	25 keV, 9 nA, 24 min.
8	$3.03x10^{22}$	56.9	11.56	13.22	7.32	10.97	25 keV, 9 nA, 24 min.
9	$2.73x10^{23}$	59.1	18.3	9.22	5.3	8.1	25 keV, 9 nA, 30 min.
10	$2.73x10^{23}$	60.3	18.5	8.7	5.3	7.2	25 keV, 9 nA, 30 min.
11	$2.73x10^{23}$	63.4	18.0	7.3	3.9	7.4	25 keV, 9 nA, 30 min.
12	$1.28x10^{23}$	61.6	11.4	7.9	5.8	8.8	5 keV, 1.6 nA, 80 min.

Table 7-1: *Chemical composition (in atomic percent) of EBID squares deposited from $[RhCl(PF_3)_2]_2$ under different experimental conditions. Deposition carried out in slow scanning mode (VIS2). D_e: electron dose.*

The atomic concentration data reported in Table 7-1 are plotted against the electron dose in Figs. 7-38 and 7-39. The error bars have been calculated from the noise peak-to-peak intensities in the regions of the spectrum next to the peaks of the elements; the values are, on average, ±0.55 at.% for Rh, ±1.95 at.% for P, ±0.82 at.% for Cl, ±1.62 at.% for N, ±1 at.% for O. The plot reveals that the elements Rh, P, Cl, N and O are detected in all the analyzed samples. No systematic concentration changes are observed with increasing electron dose, as better visualized in the magnified plots in Fig. 7-38. The deposit composition calculated for electron energy of 5 keV and 2 keV reveals that varying the electron energy has a weak effect on chemical composition. The scattter of the values depends on the reproducibility of the analytical technique and the deposition process.

The results indicate that a stable solid compound is formed at the lowest investigated electron doses, which remains stable under further electron irradiation. The weak effect of changes in electron energy between 25 keV and 2 keV is an indication of the low selectivity of the EBID process for electron energies in the keV range. Nevertheless this result does not exclude that an intermediate compound with different chemical composition is formed at lower electron exposure or at lower electron energy (eV range). The stability of the deposit under electron irradiation excludes that compositional changes, due to electron beam irradiation, occur during AES measurements. This is confirmed by the fact that the peak-to-peak intensities of the elements are constant during continuous irradiation (irradiation time of about 30 minutes, with $I_p = 5\ nA$).

The measurements reported until now give information only about the deposit surface, the depth of analysis of AES being less than 10 nm. Analysis of the deposit bulk is achieved by sputter depth profiling, which allows to monitor changes in chemical composition at different

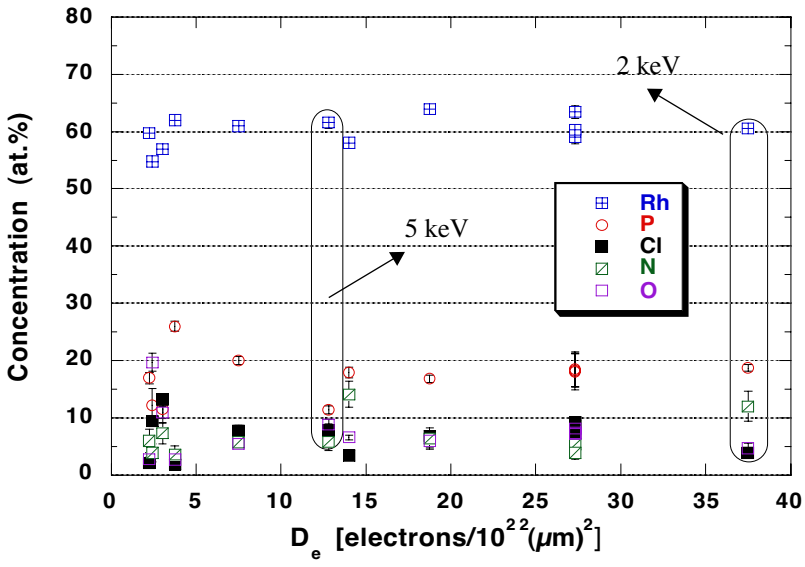

Figure 7-38: *Atomic concentrations versus electron dose of the elements Rh, P, Cl, N and O (determined by AES). The plot refers to the data in Table 7-1. The error bars for the Rh concentrations are smaller than the symbols.*

depths. An AES depth profile spectrum of a Rh square deposited with an electron energy of 5 keV and an electron current of 1 nA is shown in Fig. 7-40. Rh EBID deposit obtained with different beam parameters show a similar behavior. The spectrum shows that, after removal of the contamination layer (about 100 s sputtering), C, N and O concentration decrease while P, Cl and Rh concentrations increase. In particular, the multiplex cycles acquired between 250 and 280 eV show that the structure of the C peak is present only on the as-received sample and disappears after the first sputter cycle. After removal of the contamination layer the concentrations of the elements do not show a significant change with increasing deposit depth.

AES has been performed also on EBID lines deposited in spot mode, such as those shown in Fig. 7-16. The line have been deposited with $E = 25$ keV and $I_p = 6$ nA. Their height and width, measured with an Atomic Force Microscope are about 1.1 μm and 2.3 μm respectively, the length, measured with a SEM, is about 20 μm. These measurements allows to study the effect of the deposition mode on the chemical composition. AES has been performed also on the thin external deposit. The atomic concentration of the lines, averaged on three samples deposited under identical experimental conditions, is reported in Table 7-2. The measured concentrations show good reproducibility and are similar to those listed in Table 7-1. This result shows that the composition is not affected by the beam operation mode. The measurements revealed also that the external deposit has the same composition as the main lines. The last result is particularly interesting since it represents an indirect measurement of a deposit carried out at low electron beam current.

As shown by previous works, the chemical composition of EBID structures can be changed in some cases by ex-situ post-deposition treatments. In this work two ex-situ post-treatments have

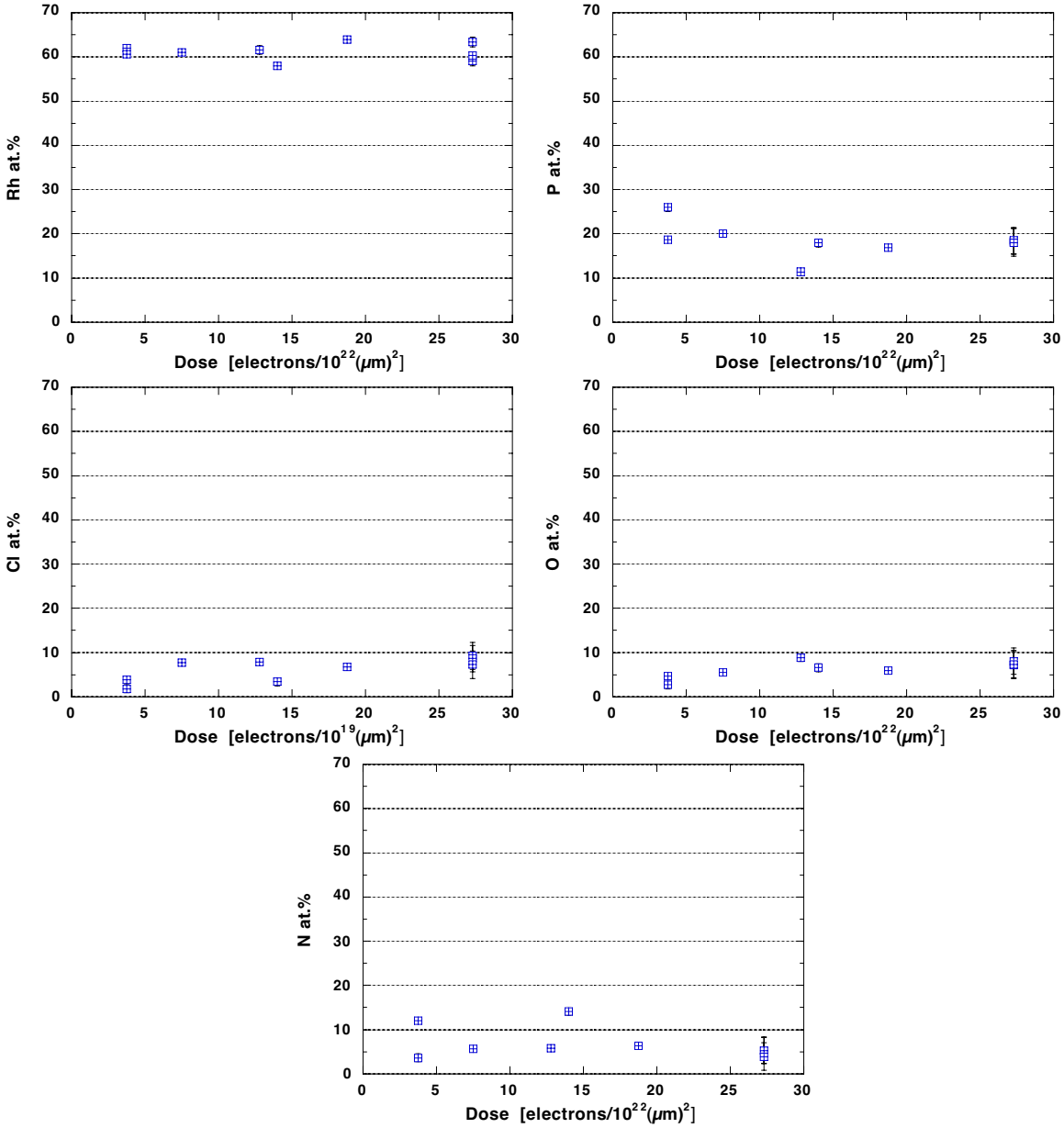

Figure 7-39: *Atomic concentration of Rh, P, Cl, O and N versus electron dose. Magnified plots.*

been performed in an attempt to increase the Rh content in the deposit: thermal annealing in air at 500 °C for two hours (heating ramp 200°C/h) in a furnace and O_2 plasma etching at 75 W plasma power for 10 minutes. The chemical concentrations of the treated samples are reported in Table 7-3. The results show that the two treatments do not induce a considerable change of the composition. The most significant effect is that thermal annealing reduces the nitrogen content to a value close to the detection limit.

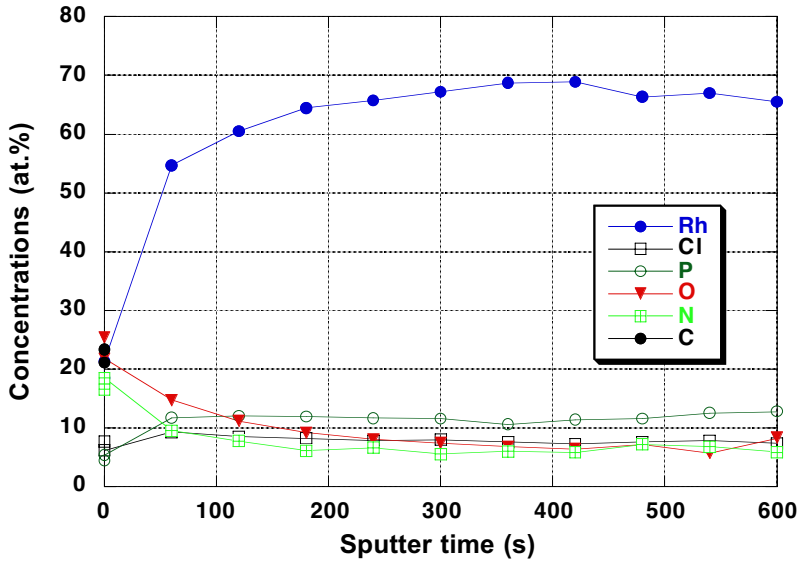

Figure 7-40: *Auger depth profile of an EBID square deposited on Si(111) from $[RhCl(PF_3)_2]_2$ in slow scanning mode (VIS 2), with E = 5 keV, I_p = 10 nA. The sputter rate is about 6 nm/s for Ta.*

comments	Rh at.%	P at.%	Cl at.%	N at.%	O at.%
EBID lines 25 keV, 6 nA	57.9 ±1.7	15.7 ±1.3	5.6 ±0.8	10.2 ±1.1	7.8 ±1.6

Table 7-2: *Chemical composition (in atomic%) of EBID lines deposited on Si(111) from the precursor $[RhCl(PF_3)_2]_2$. Deposits carried out in spot mode with E = 25 keV, I_p = 6 nA, point-to-point distance = 10 nm, dwell time = 1s. The reported values are the average on three samples deposited under identical experimental conditions.*

D_e (μm^{-2})	Rh at.%	P at.%	Cl at.%	N at.%	O at.%	Comments
$6.66x10^{22}$	60.53	19.2	4.38	10.44	4.71	annealed 500°C
$8.52x10^{22}$	56.5	24.1	7.2	3.5	8.7	annealed 500°C
$1.13x10^{23}$	61.2	22.8	5.7	2.0	8.3	O_2 plasma etched

Table 7-3: *Chemical composition (in atomic%) of EBID square after ex-situ treatments: annealing in air at 500°C (sample 1) and O_2 plasma etching (sample 2). Deposition carried out in slow scanning mode (VIS2). D_e: electron dose.*

7.3.1 DISCUSSION OF AES RESULTS

The material obtained from $[RhCl(PF_3)_2]_2$ EBID contains the elements Rh, P, Cl, N and O with the atomic percentages reported in Table 7-1. The chemical composition of the deposit is not strongly affected by variation of the electron dose (in the investigated range), the electron energy and by post-annealing treatments. The detected elements are homogeneously distributed at the surface and in the bulk of the deposit, at the scale of the AES lateral resolution. The presence of Rh, Cl and P is explained by partial decomposition of the precursor molecule, the presence of O and N by co-deposition or air uptake after exposure to the atmosphere. The N and O concentrations remain unchanged even after several days of pumping in a vacuum of 10^{-9} Torr, revealing that the elements are part of a solid stable compound. The presence of P, in almost the same amount as in the precursor, and the absence of F in the deposits indicates that the PF_3 group is decomposed under electron irradiation and it is not released as a group, as described in the proposed mechanism for thermal CVD of Rh from the same precursor [7]. Chlorine is found also in thermal CVD deposits obtained from the same precursor [7].

The deposit composition proves that the process leading to EBID are different from low-pressure gas phase ionization, as measured in mass spectrometry. According to mass spectrometry measurements, discussed in Chapter 3, electron-induced decomposition of $[RhCl(PF_3)_2]_2$ occurs mainly by successive loss of PF_3 groups or F atoms. This result is consistent with density functional calculations of the possible decomposition paths for $[RhCl(PF_3)_2]_2$, as shown in Chapter 3. On the other hand, AES of EBID squares shows that the deposition process causes complete F loss while P is detected in the deposit. This is an indication that EBID is a result of a complex reaction path, which can include multiple ionization and rearrangements of products of primary decomposition reactions.

For a comparative study, EBID squares have been deposited also from the commercial precursor $[RhCl(CO)_2]_2$, and analyzed by AES. The experiment allows to investigate if the precursor follows a decomposition path similar to $[RhCl(PF_3)_2]_2$ and if the presence of O and N in the deposit is a particular feature of Rh EBID. A survey spectrum of an EBID square deposited at E = 25keV and I_p = 2.2nA is shown in Fig. 7-41. The spectrum reveals clearly the presence of Rh, Cl (peaks already discussed previously) and C (peak is clearly visible at 275 eV, within the Rh triplet). The N peak, close to the noise level, is visible in the multiplex spectrum. No oxygen has been detected. The spectrum of the deposit, used for elemental quantification, is reported in Fig. 7-42. The atomic concentrations of two deposits obtained under the same experimental conditions, are reported in Table 7-4. The errors on chemical concentrations are, on average, ±0.55 at.% for Rh, ±3.5% at.% for C, ±0.82 at.% for Cl, ±1.62 at.% for N, ±1 at.% for O.

The Rh and Cl concentrations in deposits obtained from the two Rh precursors are similar. In both cases the most electronegative elements (F and O) are absent in the deposit, while the elements to which they are bonded (P and F) are present. This result is a further confirmation that precursor decomposition in EBID is more complicated than gas phase decomposition at low pressure. Nitrogen is found in both cases but the concentrations in the deposits obtained

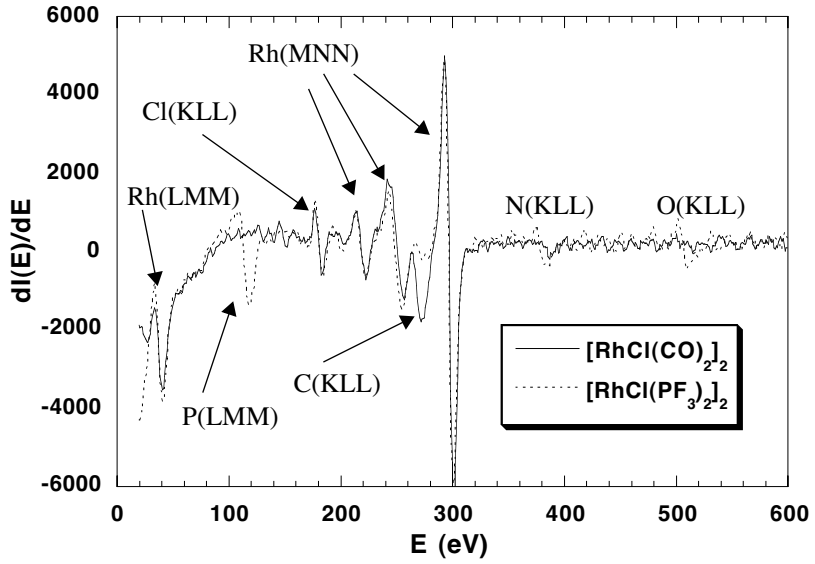

Figure 7-41: *Auger spectra of Rh EBID squares deposited from the precursors $[RhCl(CO)_2]_2$ (solid line) and $[RhCl(PF_3)_2]_2$ (dashed line). Depositions carried out in slow scanning mode (VIS2) with E = 25 keV and I_p = 2.2 nA. The characteristic peaks are indicated by arrows in the plot.*

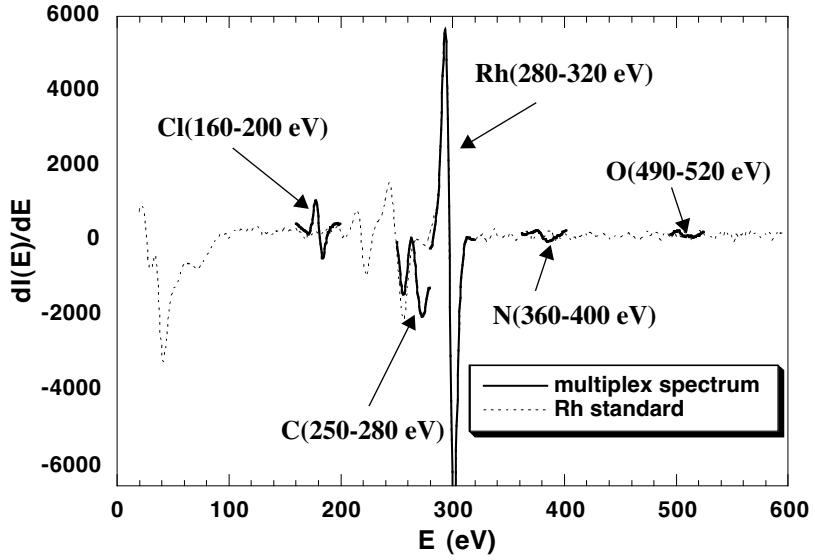

Figure 7-42: *Auger multiplex spectrum of a Rh containing deposit from the precursor $[RhCl(CO)_2]_2$ acquired in the quantification intervals defined by the solid line, same sample as above. The dashed line represents the survey spectrum of a Rh metallic standard.*

D_e (μm^{-2})	Rh at.%	C at.%	Cl at.%	N at.%	O at.%	E, I_p, t_e
$7.25x10^{23}$	56.4	33.9	4.8	2.9	1.9	25 keV, 2,2nA, 30 min.
$7.25x10^{23}$	56.7	33.7	4.8	2.9	1.8	25 keV, 2,2nA, 30 min.

Table 7-4: *Atomic concentration of two EBID squares deposited from the precursor $[RhCl(CO)_2]_2$, with E = 25 keV and I_p = 2.2 nA. Deposition carried out in slow scanning mode (VIS2). D_e: electron dose.*

from $[RhCl(PF_3)_2]_2$ are higher. The main difference between the two deposits is the lower O content in the deposit obtained from $[RhCl(CO)_2]_2$. The O presence seems therefore to be correlated to the presence of P.

7.4 EELS ANALYSIS

Electron Energy Loss Spectroscopy allows chemical analysis well beyond the resolution limit of AES. In this work EELS has been performed with the aims to prove that the presence of C is limited to the sample surface, as already found with AES, to study the chemical composition of deposits od submicrometer size and to determine the distribution of the element present in the deposits with nanometer resolution. EELS represents also a different approach compared to AES since it represent a bulk rather than a surface technique. EELS analysis has been performed on Rh EBID lines and dots, deposited from $[RhCl(PF_3)_2]_2$, with various beam parameters.

The analysis to verify the presence of C in the deposits have been performed on a Rh containing line deposited on a 20 nm C grid, with a E = 15keV, I_p= 8nA, a point-to-point distance of 10 nm and a dwell time of one second with the aim to study the evolution of the Rh/C concentration ratio as a function of the deposit thickness. The EELS spectra have been acquired, with a convergent electron beam, at six different points starting from the edge and moving towards the center of the line section, as shown schematically in Fig. 7-44b. The analyzed thickness increases moving from the edge to the center of the line. The section profile of the EBID line is similar to the one shown in Fig. 7-20.

An EELS spectrum acquired on the line is shown in Fig. 7-43. The background has been subtracted before the C edge for better visualization of the elemental edges. The spectrum reveals the presence in the deposit of the elements Rh, C, N and O. The position of the Rh (M), C (K), N (K) and O (K) edges are indicated by arrows in the spectrum. The evolution of the ratios R(C), R(O) and R(N) relative to Rh (defined by Eq. I-11), as a function of the deposit thickness, in units of mean free path (MFP), is plotted in Fig. 7-44. The plot shows that, moving from the thin to the thick region, R(O) and R(N) remain constant along the line profile, after an initial decrease, while R(C) decreases. When the presence of one element is limited to

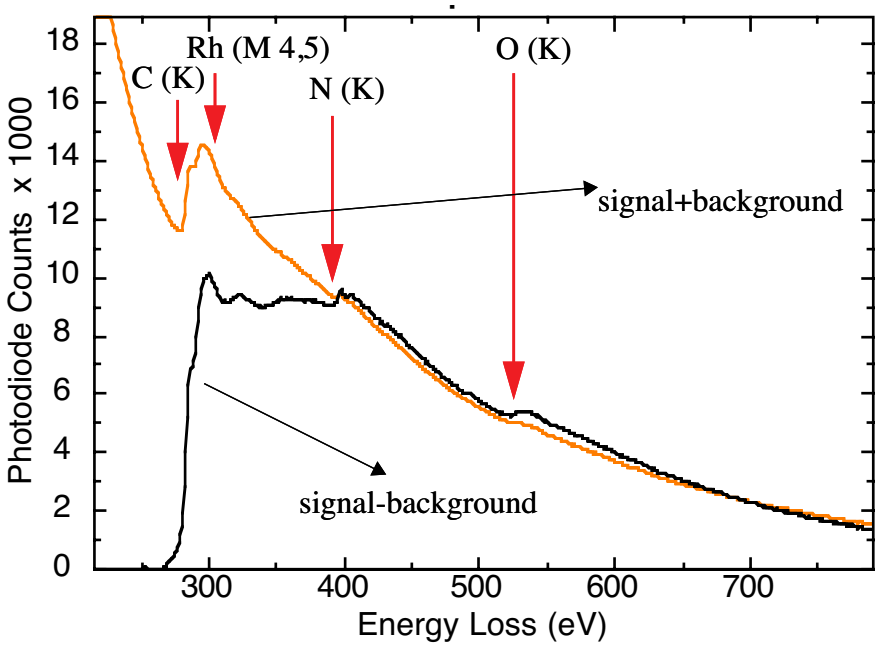

Figure 7-43: *EELS spectrum of an EBID Rh line before (gray) and after (black) background subtraction. Deposition carried out from $[RhCl(PF_3)_2]_2$ on a 20 nm thick C grid, with: E = 15 keV, I_p = 8 nA, point-to-point distance 10 nm, dwell time 1 s. The background has been subtracted before the C edge for better visualization of the elemental edges.*

the specimen surface its concentration decreases with increasing analyzed thickness. Therefore, the measurement proves that C is localized at the specimen surface, whereas O and N are homogeneously distributed in the entire specimen. This result is consistent with AES measurement and is an additional proof that the presence of C in EBID structures obtained from $[RhCl(PF_3)_2]_2$ is limited to the contamination layer.

The EELS measurements discussed above give information on the deposit chemical composition averaged on different regions of the EBID line section. In order to obtain information at a smaller scale, EELS chemical mapping (spectrum imaging) has been performed on deposits with lateral dimensions of some hundreds of nanometers.

Figure 7-45a shows a DSTEM image of a Rh dot deposited with E = 25 keV, I_p = 8 pA and t_e = 15 s. Figure 7-45b and 7-45c show respectively the edge intensities maps of Rh and P in the region delimited by the rectangle in Fig. 7-45a. These maps have been acquired on the Rh-L edge and the P-K edge at high energy losses since these two edges are less sensitive to thickness fluctuations or edge overlaps than the ones at lower energy. The images prove that rhodium and phosphorous are present in the deposit and in the more diffuse surrounding region. This result confirms that Rh and P are present also in deposits obtained at very low current and short exposure times. Furthermore an increase of the overall Rh intensity is correlated with an increase of the P intensity. Another important piece of information given by this

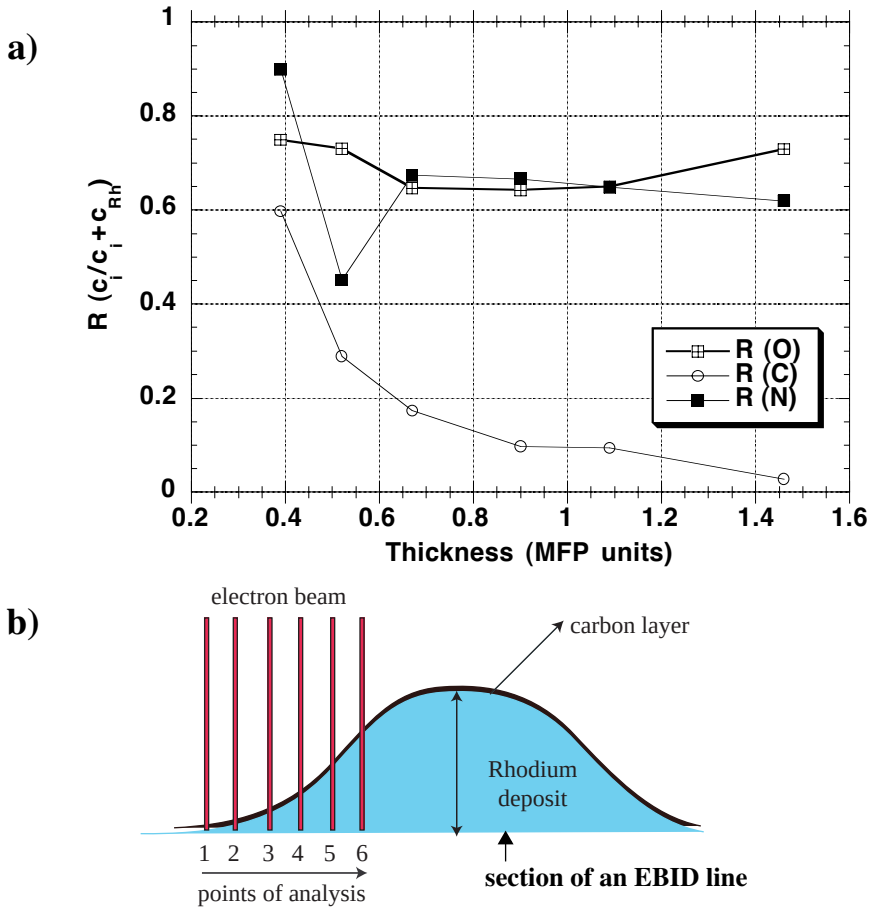

Figure 7-44: *Evaluation of the R(O), R(C) and R(N) ratios (as defined in Eq. I-11), versus deposited thickness in mean free path (MFP) units (a); schematics of the point of analysis along the section of an EBID line (b). Sample: EBID line deposited from* $[RhCl(PF_3)_2]_2$ *on a 20 nm thick C grid, with: E = 15 keV,* I_p *= 8 nA, point-to-point distance 10 nm, dwell time 1 s.*

measurement is that the presence of P is observed also for deposits on C substrates. This excludes that the element is generated by a chemical reaction between PF_3 and the Si surface.

To determine the composition at the grain size scale, edge intensity maps for Rh (M), P (K), C (K) and O (K) edges with nanometer resolution have been acquired. The spectrum images are shown in Fig. 7-46a; the 4 nm marker represents an approximate scale, deduced from the size of the Rh nanocrystals measured in Figs. 7-31 and 7-33. The images reveal that areas rich in Rh (indicated by the arrows in the figure) correlate clearly with areas poor in C and O. Therefore, we can conclude that C and O are found mainly in the gaps between Rh nano-crystallites. The P spectrum image is less clear but seems to indicate a correlation with regions rich in Rh.

This correlation between Rh and P is further clarified in Fig. 7-46b. The plots report the average intensity ratios *I(C)/I(Rh)* and *I(P)/I(Rh)*, extracted in six regions, either poor or rich in Rh. It can be clearly observed that *I(C)/I(Rh)* varies from 1.8 to 1.2, moving from Rh rich to Rh

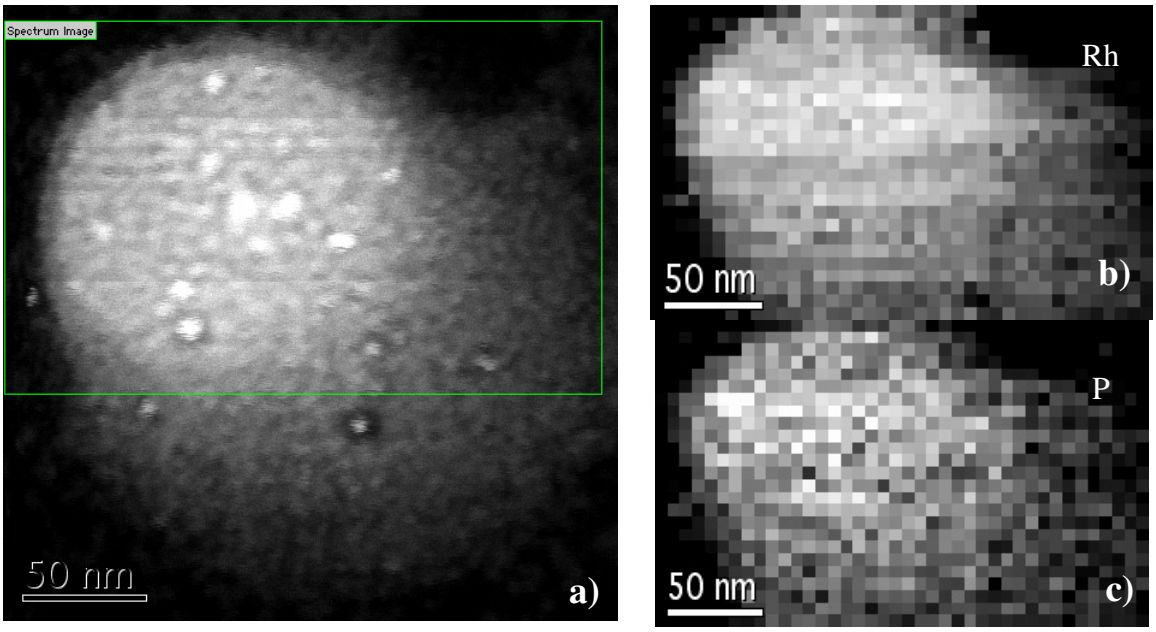

Figure 7-45: *DSTEM image of a Rh containing dot (a). Rh (b) and P (c) EELS edge intensity maps (acquired in the region delimited by the rectangle). Acquisition intervals: 3004-3146 (Rh, L);* 2196-2292 *(P,K). Dot deposited from* $[RhCl(PF_3)_2]_2$ *on a 20 nm thick C grid, with E = 25 keV,* I_p *= 8 pA, exposure time 15 s.*

poor areas. On the other hand *I(P)/I(Rh)* remains unchanged between 1.0-1.15 (with one exception) revealing that Rh rich regions correspond to P rich regions. The local correlation between Rh and P in Fig. 7-46 does not mean that P is present in the Rh grains since the Rh interstitials can accommodate some percentage of P but not the 15-20% found in the deposit. Therefore P should be present inside the amorphous zone in the close surroundings of the Rh grains.

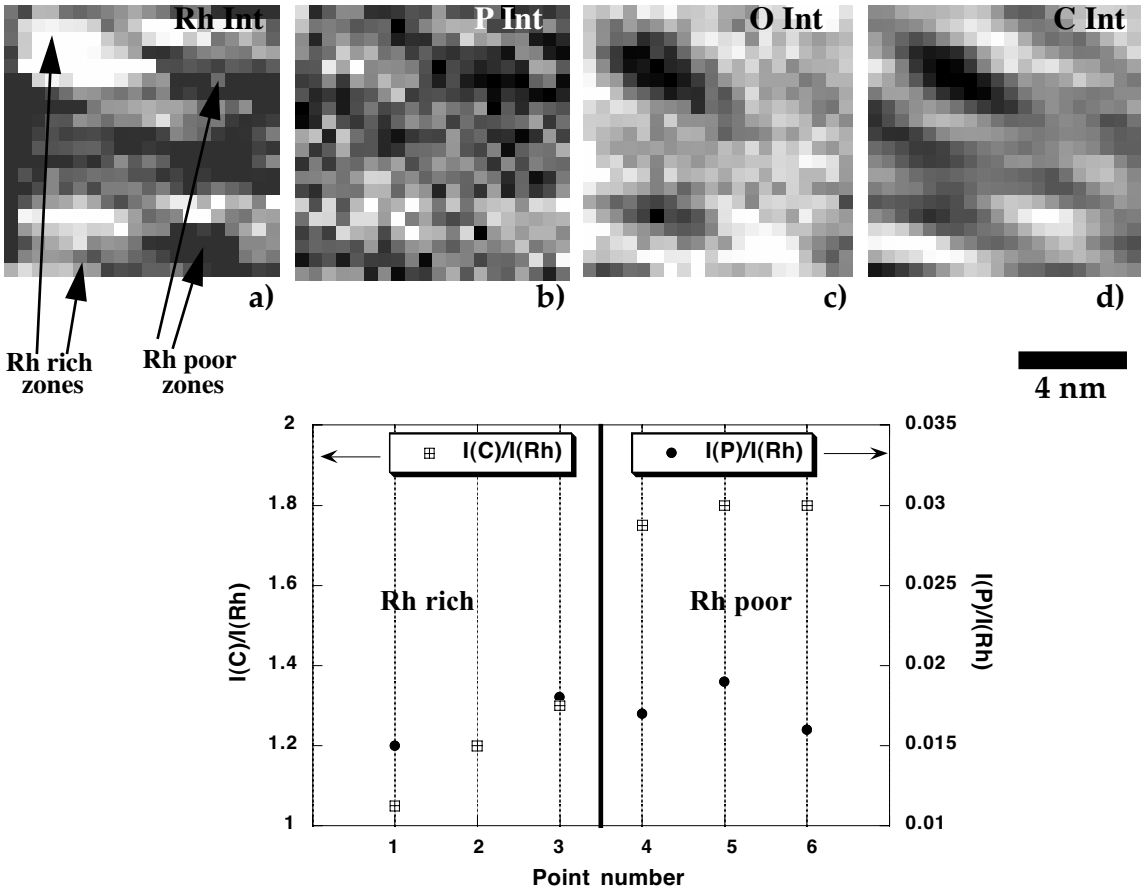

Figure 7-46: *a) High resolution EELS edge intensity maps at: 324-340 eV (Rh, M), 287-312 eV (C, K), 540-549 eV (O, K) and 2196.0-2292.0 eV (P, K); b) Carbon to rhodium and phosphorous to rhodium intensity ratios on and between Rh grains. Same sample as in Fig. 7-45. The 4 nm marker represents an approximative scale, deduced from the size of the Rh nanocrystals measured in Figs. 7-31 and 7-33.*

7.5 CONCLUSIONS

The morphology of different EBID deposits obtained from the precursor $[RhCl(PF_3)_2]_2$ have been characterized with TEM, SEM and AFM. TEM imaging of EBID dots deposited at short exposure time allowed to study the effect of the deposition current and time on the deposit dimensions (width and height) The same measurements allowed to estimate the number of electrons needed to decompose a precursor molecule. SEM observations reveal that three-dimensional growth can be achieved more easily with low electron currents. AFM imaging allowed to determine the profile of EBID lines and to detect regions of different heights in EBID hollow deposits.

Structural characterization performed by TEM imaging and diffraction has shown that the deposits are made up of Rh nanocrystals with diameters ranging from 3 to 5 nm.

Chemical analysis carried out by AES revealed the presence in the deposits of the elements Rh, P, Cl, O and N. The Rh and P concentrations are around 60 at.% and 20 at.% respectively. The remaining 20 at.% is constituted by O, N and Cl, present in concentrations ranging from 3 at.% to 10 at.%. The element C, present on the as received surfaces with a concentration of about 20 at.%, is not detected after sputter removal of the contamination layer.

The low carbon concentration in the deposit is confirmed by EELS measurements carried out at increasing sample thickness. EELS spectrum imaging confirmed the presence of Rh and P in deposit carried out at low exposure time and low electron current and allowed to determine the distribution of the elements present in the deposit with nanometric resolution.

7.6 REFERENCES

[1] L. Reimer; *Transmission Electron Microscopy*; Springer, 1997.

[2] P. Hoffmann, M. Stelzle, J.F. Rabolt; *Vapor phase self-assembly of fluorinated monolayers on silicon and germanium oxide*; Langmuir, 13 (1997); p. 1877-1880.

[3] H.O. Pierson; *Handbook of Chemical Vapor Deposition (CVD): principles, technology and application*; Park & Ride, 1999.

[4] International Center for Diffraction Data (ICDD), PDF file 05-0685.

[5] D. Briggs, M.P. Seah; *Practical Surface Analysis*; John Wiley and sons, 1995.

[6] H.J. Mathieu; *Analyse des Surfaces (Cours destiné aux étudiants en Science des Materiaux);* EPFL, Lausanne, 1999

[7] P. Doppelt, V. Weigel, P. Guinot; *Mineral precursor for chemical vapor deposition of Rh metallic films*; Mater. Sci. Engin. B, 17 (1993); p. 143-146.

CHAPTER 8 *Conclusion and future works*

In this chapter the most important results of this thesis work are discussed and some propositions for future work in EBID are presented.

8.1 RESULTS

During this thesis work the first EBID Rh containing nanostructures have been deposited from the precursor compound $[RhCl(PF_3)_2]_2$.

The deposits, independent of the deposition conditions, show the following main features.

- The structure is nanocomposite, with metallic polycrystalline Rh nano-crystals, between 2.5 nm and 5 nm in diameter, immersed in a lighter amorphous matrix.
- The Rh content is around 60 at.%.
- Contamination of P (around 20 at.%), Cl, O and N (between 2 and 10 at.%) is observed in the bulk of the deposit, the presence of C is limited to the contamination layer.
- According to EELS and AES chemical maps, phosphorous is found close to the Rh nano-crystals.
- The structure, the composition of the deposit and the nano-crystal size are independent of the deposition conditions in the investigated electron energy and current range (2 keV < E < 25 keV, 10 pA < I_p < 10 nA)

The following information results from morphological characterization by TEM, SEM and AFM.

- The ratio between impinging electrons and decomposed molecules on 20 nm thick C films is about 500.
- In the nucleation phase of the deposition process the deposit grows in height and in diameter.

- In the three-dimensional growth phase, the deposit grows in height while the deposit diameter remains constant, therefore three-dimensional EBID structures have a constant diameter.

- The deposition rate is higher in the center than in the peripheral regions of the beam.

- Precursor delivery from the gas phase is predominant compared to surface diffusion.

Measurements of the diameter of deposits obtained at very short exposure time and fitting of the TEM DF contrast profiles allow to measure the electron probe size.

Besides EBID experiments, characterization of the precursor $[RhCl(PF_3)_2]_2$, with vapor pressure, mass spectrometry and residence time measurements has been achieved. Vapor pressure and mass spectrometry measurements required the construction of two experimental set-ups, realized during this work. The most significant results are listed below:

- The vapor pressure of the compound at room temperature is 7.5 Pa, sufficiently high for deposition at room temperature.

- Decomposition of the compound by electron impact in the gas phase takes place by successive loss of PF_3 groups.

- $[RhCl(PF_3)_2]_2$ has a residence time of 2 ms on stainless steel surfaces, corresponding to an activation energy for desorption of about 0.6 eV.

The knowledge of the vapor pressure allows to calculate the number of molecules reaching the reaction area.

The mass spectrum of $[RhCl(PF_3)_2]_2$ is compatible with DFT calculations, which show that the least energetic process for the decomposition of the molecule is successive removal of PF_3 groups.

Comparison between the mass spectrum and the deposit composition proved that EBID takes place with a more complicated mechanism than low-pressure gas phase ionization. In particular, the different decomposition path is proved by the presence of P and the absence of F in the deposit. The different mechanism can be due to the high electron energy and to the high number of electrons and molecules involved in EBID. This makes possible complex phenomena such as multi-electron decomposition, post-ionization or post-decomposition rearrangements of the chemical species. The difference between low-pressure gas phase ionization and EBID is confirmed by the result of AES analysis of the deposit carried out, for comparison, from the iso-structural precursor $[RhCl(CO)_2]_2$. In this case about 30 at.% of C is found in the precursor even though the mass spectrum shows a decomposition by successive loss of CO groups.

The measured residence time indicates also that the precursor can travel by surface diffusion only for distances of some micrometers before being desorbed.

8.2 FUTURE WORK

Several aspect of EBID from $[RhCl(PF_3)_2]_2$ studied in this work have not been fully understood and require further investigation.

The origin of O and N contamination should be clarified. In-situ chemical analysis would allow to distinguish if the elements are co-deposited or uptaken after air exposure. The sputtering yield of the deposit can be calculated by measuring the height of a deposit with AFM before and after a known sputter time.

The most contradictory point of the Rh containing deposit obtained from $[RhCl(PF_3)_2]_2$ is with no doubt the low conductivity, despite the high metal content. The reason can be studied by determining the nanostructure of the inner part of the deposits. This can be achieved by preparing specimens by microtomy or FIB milling.

XPS analysis, now possible with 10-20 μm resolution should be tried to confirm the result obtained by AES and EELS. XPS is interesting since it induces less beam damage than AES. However, alternative chemical analysis techniques, which totally exclude the possibility of electron and ion beam damage should be sought.

The possibility to increase the metal content by in-situ laser heating or low voltage (below 1 keV) deposition should be envisaged.

Comparative studies with different types of electron guns can clarify how the electron probe-size limits the EBID resolution.

Comparison between fragments in the mass spectrum and deposit composition should be envisaged for all the precursor molecules to be studied in the future.

APPENDIX I

I.1 PHYSICAL AND CHEMICAL PROPERTIES OF RHODIUM

Rhodium is a hard, lustrous and silvery metal, with a color similar to that of aluminum. In nature it is found mainly with Pt, Au or Pd and it is isolated from residues after extraction. Some physical properties of the metal are listed in Table I-1 and compared to those of the 18 most conductive metals. Like the other metals of the Pt family, Rh is a catalyst for hydrogenation, dehydrogenation and oxidation.

The metal has high melting and boiling temperatures, low resistivity (only Ag, Cu, Au, Al and Be have lower values), and high Young and bulk modulus. Therefore it represents a good combination of electrical and mechanical properties.

At present the main uses of rhodium are: as alloying agent to harden platinum and palladium; as an electrical contact material (since it has a low electrical resistance, a low and stable contact resistance, and highly corrosion resistant); in jewelry; as part of the catalytic system in car catalytic converters, used to clean up exhaust gases to some extent; as an industrial catalyst; and finally for coating of optical instruments.

Metal	Z	A (amu)	Cell	ρ [g cm^{-3}]	T_M (°C)	T_B (°C)	Electrical resistivity (20°C) (μΩcm)	Bulk modulus (GPa)	Young modulus (GPa)
Ag	13	107.9	fcc	10.5	961.78	2163	1.586	103.6	82.7
Cu	29	63.55	fcc	8.92	1084.6	2560	1.678	137.8	129.8
Au	79	196.9	fcc	19.3	1064.1	2860	2.24	171	78.5
Al	13	27	fcc	2.701	660.32	2520	2.6548	70.6	75.2
Be	4	9	hcp	1.85	1287	2470	4	110	318
Rh	**45**	**102.9**	**fcc**	**12.4**	**1962**	**3700**	**4.51**	**276**	**379**
Mo	42	95.9	bcc	10.2	2615	4610	5.2	261.2	324.8
Ir	77	192.2	fcc	22.421	2446	4390	5.3	371	211.4
W	74	183.9	bcc	19.35	3420	5555	5.65	311	411
Co	27	58.9	hcp	8.9	1495	2930	6.24	181.5	211
Cd	48	112.4	hcp	8.642	321.07	767	6.83	51	62.6
Ni	28	58.7	fcc	8.9	1455	2915	6.84	177.5	199.5
Ru	44	101.1	hcp	12.3	2310	4120	7.6 (0°C)	286	432
Fe	26	55.85	bcc	7.86	1536	2860	9.71	169.8	211.4
Pd	46	106.4	fcc	12.02	1554	2960	10.54	187	121
Pt	78	195.1	fcc	21.45	1768	3830	10.6	276	170
Nb	41	92.9	fcc	8.57	2467	4740	12.5(0°C)	170.3	104.9
Cr	24	52.0	fcc	7.2	1860	2680	12.9(0°C)	160.2	279

Table I-1: *General physical properties of some metals [1]. T_M and T_B: melting and boiling temperatures.*

I.1.1 CHEMICAL REACTIONS OF RHODIUM

Rhodium metal is notably inert to reaction with acids, including aqua regia. It is, on the other hand, attacked by fused alkalis. It is largely immune to atmospheric attack in air. On heating with oxygen at temperatures higher than 600°C, rhodium metal gives rhodium (III) oxide, Rh_2O_3. The reaction is very slow (several hours) for T < 800 °C [2]. For incomplete oxidation a mixture of metal and oxide is obtained:

$4Rh(s) + 3O_2(g) \rightarrow 2Rh_2O_3(s)$ [dark grey].

Usually second and third row d-block elements show similar chemistries, except iridium (immediately below rhodium in the periodic table) which burns to give iridium (IV) oxide, IrO_2. There are reports of RhO_2, but it does not appear to be well-characterized.

No reactions of rhodium with water or nitrogen under normal conditions are known.

Metallic rhodium reacts directly with fluorine gas to form the highly corrosive rhodium(VI) fluoride, RhF_6. This material, with care, can be heated to form the dark red rhodium(V) fluoride, which has a tetrameric structure $[RhF_5]_4$.

$Rh(s) + 3F_2(g) \rightarrow RhF_6(s)$ [black].

The trihalides rhodium(III) fluoride ($RhFl_3$), rhodium(III) chloride ($RhCl_3$), and rhodium(III) bromide ($RhBr_3$), can be formed through the direct reaction of the metal with the halogen under anhydrous (dry) conditions:

$2Rh(s) + 3F_2(g) \rightarrow 2RhF_3(s)$ [red] (at 500-600°C)

$2Rh(s) + 3Cl_2(g) \rightarrow 2RhCl_3(s)$ [red] (at 250-300°C)

$2Rh(s) + 3Br_2(g) \rightarrow 2RhBr_3(s)$ [red-brown] (at 250°C, CO flow).

Binary compounds

Rh fluorides exist with the Rh oxidation state ranging from III to VI: RhF_3, RhF_4, $[RhF_5]_4$, RhF_6. Chlorides, bromides and iodides exist only with metal in the oxidation state III: $RhCl_3$, $RhBr_3$, RhI_3. Oxides and sulfides are found in the oxidation states III and IV: RhO_2, Rh_2O_3, RhS_2, Rh_2S_3. Selenides and tellurides exist in the oxidation state IV: $RhSe_2$, $RhTe_2$. Rhodium phosphides can be obtained by action of phosphorous on Rh powder at 800°C in a sealed tube. Compounds with different stoichiometry are known: Rh_2P, $RhP_{0.5}$, Rh_5P_4, RhP_3. The Rh/P ratio depends on the quantity of reactant P. These compounds are attacked by hot nitric acid, sulphuric acid or aqua regia. No Rh carbides or nitrides are known, this makes less probable C and N contamination during EBID.

I.2 SET-UP FOR VAPOR PRESSURE MEASUREMENTS

The set-up for static vapor pressure measurement of EBID precursors is shown schematically in Fig. I-1. All the parts are made in 304L stainless steel for Ultra High Vacuum (UHV) applications and equipped with Conflat (CF) flanges.

The sample (precursor) is loaded in a glass-metal adaptor connected to a bellow valve (MDC, USA), which avoids the contact of the precursor with ambient gases during mounting and allows to introduce vapor in the measuring chamber. The glass containers are silylated to

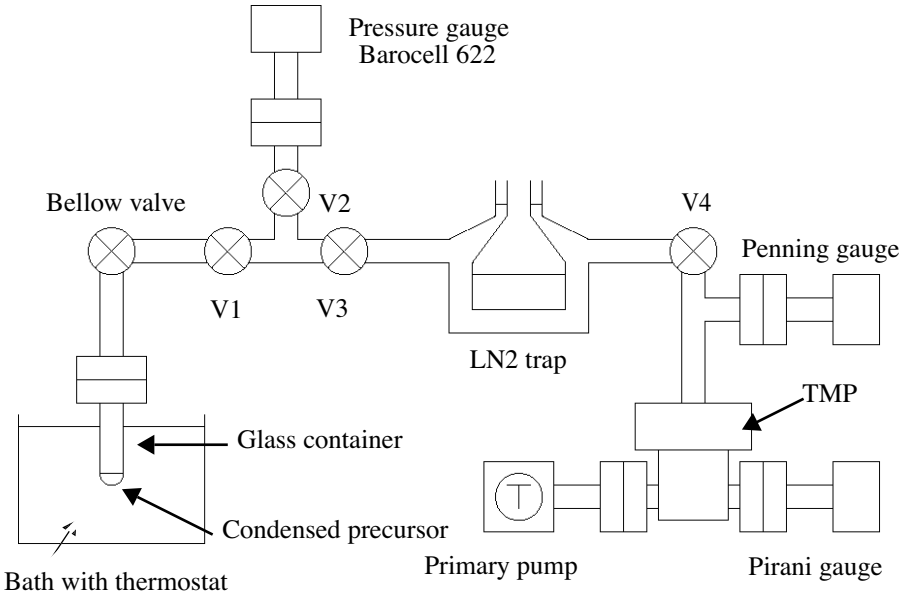

Figure I-1: *Schematic view of the apparatus for vapor pressure measurements. LN2: liquid nitrogen; TMP: turbo molecular pump; V1,V2,V3,V4: valves.*

minimize water outgassing from the walls, which could both affect the measurements and lead to hydrolysis of the precursors. To avoid light induced decomposition reactions, during all measurements the precursor container is covered by aluminum foil. Pumping is achieved by a turbo molecular pumping station (Pfeiffer TPH 110) with 100 l/s nominal pumping speed for N_2. A liquid nitrogen trap, linked to both sides of the system by means of two bellow valves, is mounted between the measuring chamber and the turbo molecular pump. The ultimate pressure in the measuring chamber is measured by a Penning gauge, mounted at the exit of the turbo molecular pump. Vapor pressure measurements are carried out by means of a capacitance gauge (Edwards Barocell 622) working in the pressure range of 0.133 Pa-1330 Pa (0.001-10 Torr), with a reading accuracy of 0.15%. The detector is protected from pressure shocks by a valve. The sample temperature is kept constant during the measurements with a temperature controlled bath operating from 240 K to 300 K. The system has been calibrated using as standard Hexamethyl-disiloxane (HMDSO) for which several vapor pressure data are available [3]. The vapor pressures measured by us, at 241 K (-32.1ºC) and 263 K (-10.6ºC), are in good agreement with the extrapolated fitting curve of literature values [3].

I.3 EXPERIMENTAL SET-UP FOR MASS SPECTROMETRY

The experimental setup for mass spectrometry (MS) measurements is shown schematically in Fig. I-2a. It includes the spectrometer head, the pumping system, the pressure gauges and the injection line. All the parts are made of UHV compatible stainless steel equipped with Conflat (CF) flanges sealed with copper gaskets. The whole system can be baked out at 200 ºC.

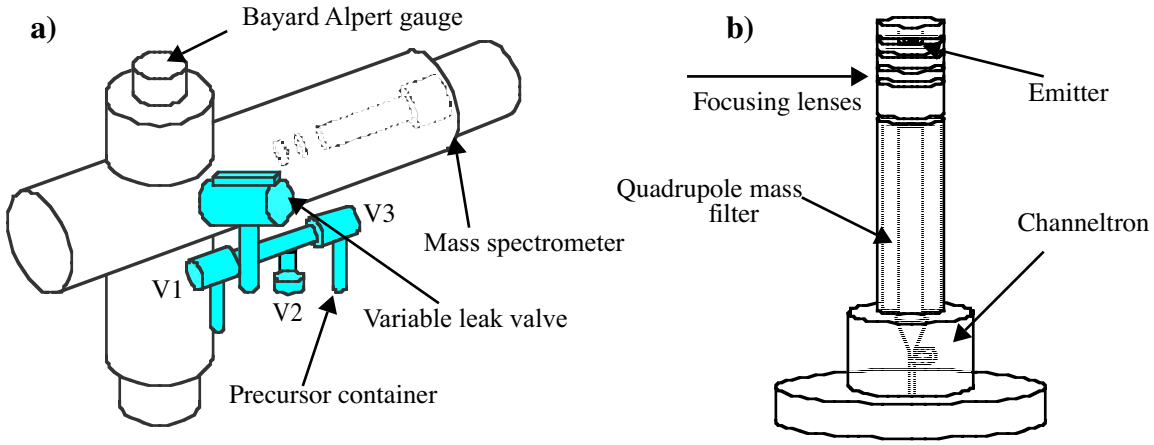

Figure I-2: *Schematic view of the system for mass spectrometry measurements (a) and of the quadrupole mass spectrometer (b).*

The mass spectrometer head (Extranuclear Laboratories Inc., Pittsburgh, USA), shown schematically in Fig. I-2b, contains the electron emitter (adjacent to electromagnetic lenses for ion collimation), the quadrupole mass filter, and the ion detectors.

The energy of the ionizing electrons can be varied from 5 eV to 90 eV, the current from 1 mA to 50 mA. The four rods of the quadrupole have a diameter (ϕ) of 9.5 mm, and a distance between the edge of two poles (L) of 0.411 cm. The two latter values define the potential which is applied between the four poles to select the desired mass/charge ratio. The ion detector used in this work is of the channeltron type. The potential applied between the entrance and the exit of the channeltron ranges from 2 to 3 kV; the amplified detected current is around 200 nA (±10 pA). Pumping is achieved with a turbo molecular pumping system (Pfeiffer TPH 170 with a nominal pumping speed of 170 l/s for N_2). The pressure is measured by means of a Pirani-Penning system and a Bayard-Alpert gauge (Balzers IMG 070). The ultimate pressure of the system, reached before introduction of the sample, is about $1x10^{-7}$ Pa ($1x10^{-9}$ Torr). During spectra acquisition all the gauges are switched off to avoid further ionization of the sample molecules. The precursor gases are injected to the detection chamber by means of a variable leak valve. The injection line is kept at 35ºC to avoid condensation of sample molecules in the introduction system while the precursor glass container is kept at room temperature (regulated at 20±1 ºC) to minimize thermal decomposition.

The current signal detected by the spectrometer is read by a pico-amperometer (Keithley 485 Autoranging picoammeter, USA). The data are acquired by a personal computer through a data acquisition card (16-bit data acquisition card PCI-M10-16XE-10, National Instrument, Austin, USA), and stored on-line with a LabVIEW program (National Instrument, Austin, USA). The control electronics can be used with two frequency resonators, High-Q Head 11 for m/Z values up to 118 and High-Q Head 15 for m/z values up to 1420. The latter frequency resonator has been used in this work. The measurements are averaged over 50 acquisitions. Figure I-3 shows the flow chart of the experimental set-up of the mass spectrometer and the control electronics.

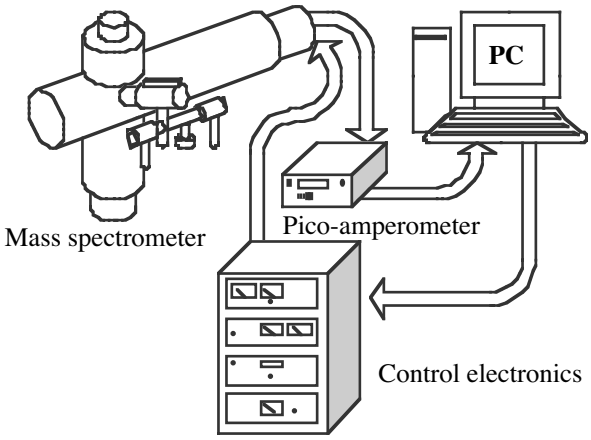

Figure I-3: *Flow chart of the mass spectrometry system.*

I.3.1 MASS SPECTRUM OF $[RhCl(PF_3)_2]_2$: MOLECULAR FRAGMENTS AND PEAK INTENSITIES

Mass number	Molecular structure of the fragmentation	10 [eV]		30 [eV]		70 [eV]	
		Intensity [%]	ΔI/I	Intensity [%]	ΔI/I	Intensity [%]	ΔI/I
31	P^+	6.55	0.06	6.71	0.19	6.854	0.19
35	Cl^+	2.94	0.23	3.35	0.71	3.020	1.00
37	Cl^+(+2)	0.95	3.52	1.09	11.2	0.98	16.6
38	F_2^+	0.87	4.18	0.98	13.6	1.07	16. 9
44	PF_2^{2+}	2.83	0.14	2.85	0.41	2.81	0.41
50	PF^+	9.25	0.13	9.01	0.13	9.35	0.12
69	PF_2^+	100	0.01	100	0.01	100	0.01
88	PF_3^+	50.77	0.02	51.10	0.02	51.65	0.02
103	Rh^+	2.24	0.01	1.93	0.01	3.05	0.03
123	PF_3Cl^+	0.06	0.95	0.06	0.65	0.10	1.54
125	PF_3Cl^+ (+2)	0.02	2.93	0.02	2.00	0.03	4.74
138	$RhCl^+$	0.46	0.13	0.43	0.09	0.68	0.22
140	$RhCl^+$ (+2)	0.15	0.39	0.14	0.28	0.22	0.68
153	$PFRh^+$	0.05	0.82	0.04	0.57	0.10	0.84
172	PF_2Rh+	0.12	0.14	0.13	0.19	0.18	0.45
191	PF_3Rh^+	0.52	0.08	0.43	0.06	0.76	0.11
206	Rh_2^+	0.24	0.17	0.20	0.12	0.36	0.23
226	PF_3RhCl^+	0.39	0.15	0.34	0.11	0.55	0.28
228	PF_3RhCl^+ (+2)	0.13	0.46	0.11	0.35	0.18	0.85
241	Rh_2Cl^+	1.00	0.06	0.83	0.04	1.41	0.11

Table I-2: *Mass number, fragmentation structure and intensity of the peaks for three different ionization energies: 10, 30 and 70 eV.*

Mass number	Molecular structure of the fragmentation	10 [eV]		30 [eV]		70 [eV]	
243	Rh_2Cl^+ (+2)	0.33	0.17	0.27	0.14	0.46	0.33
261	$PF_3RhCl_2^+$	0.04	1.43	0.04	1.02	0.09	1.84
263	$PF_3RhCl_2^+$ (+2)	0.03	2.35	0.03	1.64	0.06	2.88
265	$PF_3RhCl_2^+$ (+4)	0.01	13.6	0.00	9.61	0.01	17.7
276	$Rh_2Cl_2^+$	1.08	0.06	0.92	0.06	1.46	0.17
278	$Rh_2Cl_2^+$ (+2)	0.70	0.92	0.60	0.87	0.95	2.97
279	$(PF_3)_2Rh^+$	0.09	4.49	0.05	5.75	0.24	6.74
280	$(PF_3)_2Rh^+$(+2)	0.12	5.07	0.10	4.67	0.16	15.4
294	$PF_3Rh_2^+$ or $PF_2PF_3RhCl^+$	0.04	1.06	0.04	0.69	0.10	0.79
314	$(PF_3)_2RhCl^+$	0.09	0.67	0.08	0.50	0.16	0.96
316	$(PF_3)_2RhCl^+$(+2)	0.03	2.05	0.03	1.55	0.05	2.97
329	$PF_3Rh_2Cl^+$	0.20	0.29	0.19	0.21	0.33	0.46
331	$PF_3Rh_2Cl^+$ (+2)	0.07	0.90	0.06	0.64	0.11	1.42
345	$PF_2Rh_2Cl_2^+$ or $(PF_2)_3RhCl^+$	0.06	0.65	0.04	0.61	0.11	0.75
364	$PF_3Rh_2Cl_2^+$	0.76	0.04	0.64	0.08	0.96	0.26
366	$PF_3Rh_2Cl_2^+$(+2)	0.49	0.60	0.41	1.32	0.62	4.61
367	$(PF_3)3Rh^+$	0.01	16.7	0.03	11.3	0.20	8.22
368	$PF_3Rh_2Cl_2^+$(+4)	0.08	3.30	0.07	7.15	0.10	23.9
417	$(PF_3)_2Rh_2Cl^+$	0.05	1.11	0.04	1.01	0.08	2.01
419	$(PF_3)_2Rh_2Cl^+$(+2)	0.02	3.41	0.01	3.11	0.02	6.21

Table I-2: *Mass number, fragmentation structure and intensity of the peaks for three different ionization energies: 10, 30 and 70 eV.*

Mass number	Molecular structure of the fragmentation	10 [eV]		30 [eV]		70 [eV]	
433	$PF_2PF_3Rh_2Cl_2^+$	0.06	1.10	0.05	0.85	0.10	1.65
435	$PF_2PF_3Rh_2Cl_2^+$ (+2)	0.04	1.81	0.03	1.37	0.07	2.59
437	$PF_2PF_3Rh_2Cl_2^+$ (+4)	0.01	10.4	0.01	7.98	0.01	15.3
452	$(PF_3)_2Rh_2Cl_2^+$	0.32	0.19	0.25	0.17	0.44	0.39
454	$(PF_3)_2Rh_2Cl_2^+$(+2)	0.21	0.32	0.16	0.27	0.28	0.61
456	$(PF_3)_2Rh_2Cl_2^+$(+4)	0.03	1.81	0.03	1.61	0.05	3.71
521	$PF_2(PF_3)_2Rh_2Cl_2^+$	0.10	0.60	0.08	0.51	0.16	1.07
523	$PF_2(PF_3)_2Rh_2Cl_2^+$ (+2)	0.07	0.99	0.05	0.82	0.10	1.68
525	$PF_2(PF_3)_2Rh_2Cl_2^+$ (+4)	0.01	5.71	0.01	4.79	0.02	10.0
540	$(PF_3)_3Rh_2Cl_2^+$	0.25	0.25	0.22	1.93	0.35	0.49
542	$(PF_3)_3Rh_2Cl_2^+$ (+2)	0.16	0.40	0.14	0.31	0.23	0.76
544	$(PF_3)_3Rh_2Cl_2^+$ (+4)	0.03	2.32	0.02	1.82	0.04	4.60
628	$(PF_3)_4Rh_2Cl_2^+$	0.38	0.16	0.26	0.16	0.46	0.37
630	$(PF_3)_4Rh_2Cl_2^+$ (+2)	0.25	0.27	0.17	0.26	0.30	0.58
632	$(PF_3)_4Rh_2Cl_2^+$ (+4)	0.04	1.53	0.03	1.51	0.05	3.48

Table I-2: *Mass number, fragmentation structure and intensity of the peaks for three different ionization energies: 10, 30 and 70 eV.*

I.4 SET-UP FOR SURFACE RESIDENCE TIME MEASUREMENTS

The experimental apparatus for measurement of the uptake coefficient and surface residence time, already described in the literature [4], is shown in Fig. I-4. Two tubes are mounted in parallel between a gas inlet system and a detection chamber. To reach molecular flow conditions, the detection chamber and the tubes are pumped with a turbo-molecular pumping

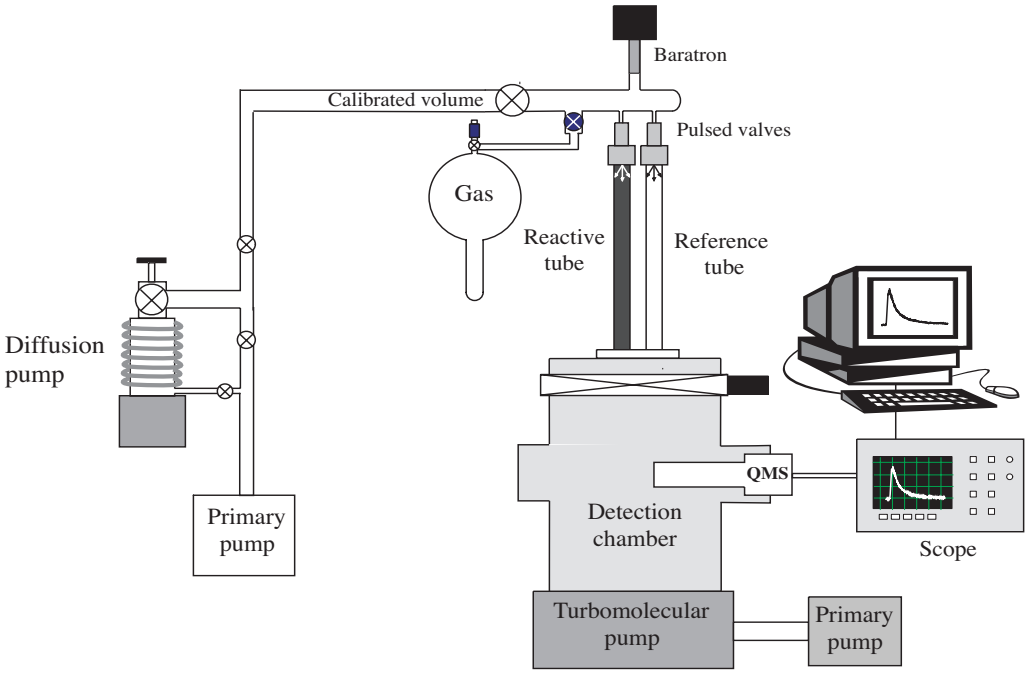

Figure I-4: *Schematic view of the system used for residence time measurements.*

system. The background pressure in the system is of the order of 5 x 10^{-6} Pa. The precursor gases are injected from a calibrated volume, previously evacuated with a diffusion pumping system, across a pulsed solenoid valve. The pressure in the calibrated volume is measured with a capacitance gauge. The number of molecules injected per pulse (dose) is calculated from the observed pressure drop on the basis of the ideal gas law. The arrival time traces, collected with a mass spectrometer, are recorded and averaged over several pulses with an oscilloscope and transmitted to a PC.

I.5 TEM DIFFRACTION AND IMAGING

Transmission Electron Microscopy allows to obtain structural information well beyond the resolution limit of a SEM. A TEM can be operated in conventional or in scanning mode. In conventional transmission mode the whole imaged specimen area is illuminated using a close to parallel electron beam, and the intensity at the exit plane of the specimen is magnified using the objective lens. In scanning transmission mode (STEM) the specimen is scanned in a raster point by point with a focused electron probe. This latter option is used in combination with an annular detector which collects scattered electrons, giving rise to a *Z*-contrast image. The resolving power of a TEM is about 0.1 nm in conventional mode. In STEM mode the spatial resolution depends on the probe size, which can reach 0.2 nm at 100 keV electron energy [5]. The instruments can be equipped with Electron Energy Loss Spectroscopy facilities.

TEM diffraction patterns are formed by elastic scattering of the electron beam by the specimen atoms. The most common illumination mode is Selective Area Diffraction (SAD), in which the specimen is illuminated through an aperture introduced in the image plane of the objective lens. Diffraction patterns allow to determine if a specimen is crystalline or amorphous. If it is crystalline, they allow to determine:

- the crystallographic characteristics (lattice parameters, symmetry etc); the orientation of the grains with respect to the beam;
- if it is mono- or poly-crystalline;
- if there is more than one phase present in the specimen.

No matter what kind of sample is analyzed, the SAD pattern will contain a bright central spot generated by the direct electrons and some scattered electrons. If a crystalline area of the specimen is observed, the scattering occurs in a regular manner, giving a pattern of sharp spots; if it is poly-crystalline, the spots are distributed to produce sharp lines; if it is amorphous the pattern gives very diffuse rings [6]. The crystal structure is determined by using the Bragg relation.

In TEM imaging we observe phase and amplitude changes that the uniform electron beam undergoes while propagating through the specimen. The specimen is magnified by the objective lens and by a system of projector lenses before it is detected on a phosphorous viewing screen, a photo plate or a CCD camera. When the beam interacts with the specimen, a transmitted beam and some scattered electrons are created. TEM images can be formed either by the central spot, or by the scattered electrons. If the direct beam is selected the resultant image is called Bright Field (BF) image, if the scattered electrons are selected it is called Dark Field (DF) image.

Diffraction patterns and images can also be obtained by operating the beam in STEM mode: the beam is scanned on the specimen by adjusting two pairs of scan coils, which are used at the same time to scan the cathode ray tube (CRT). The electron detector acts as an interface between the electrons coming from the specimen and the image viewed in the CRT. Detectors in STEM mode are used as apertures in TEM mode: the BF detector is positioned into the direct beam, while DF imaging is usually obtained using an annular detector (ADF), which surrounds the BF detector and collects all the scattered electrons. Being a serial process, STEM imaging is much slower than TEM imaging. The different TEM operational modes are compared in Fig. I-5.

The most important parameter in TEM imaging is the mass-thickness contrast, which arises from incoherent (Rutherford) elastic scattering of electrons. The cross section for elastic scattering is a function of the atomic number Z (i.e. the mass and density) and, as the thickness of the specimen increases, there will be more elastic scattering. Therefore high-Z regions of a specimen scatter more electrons than low-Z regions of the same thickness; similarly, thicker region scatter more electrons than thinner regions of the same average Z. For a BF image, thicker and /or lower Z images will appear darker than the thinner and /or lower mass areas; the

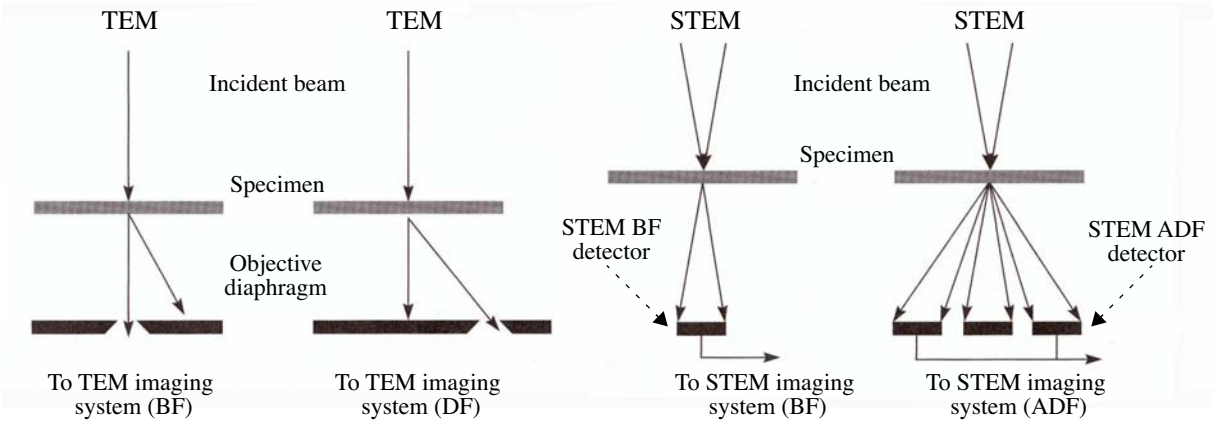

Figure I-5: *Use of an objective aperture in TEM to select (a) the direct or (b) the scattered electrons forming BF and DF images, respectively. In STEM ,an on-axis detector (c) or annular detector (d) is used to perform the equivalent operation [7].*

reverse will be true for a DF image. The overall intensity of the DF images is much lower than that of BF images (hence the relative terms dark and bright) because the objective aperture will select only a small fraction of the scattered electrons. Contrast is defined quantitatively as the difference of intensity between two adjacent areas:

$$C = \frac{(I_1 - I_2)}{I_2} = \frac{\Delta I}{I_2}. \qquad \text{(I-1)}$$

Therefore DF images show in general excellent contrast.

STEM BF images show little more than BF images. On the other hand the use of the ADF detector gives rise to a fundamental difference between TEM and STEM mode DF images. DF TEM images are usually formed by permitting only a fraction of the scattered electrons to enter the objective lenses while STEM images are formed by collecting most of the scattered electrons on the ADF. Therefore STEM ADF images, compared to TEM DF images, are less noisy and do not suffer from lens aberrations, but show in general lower resolution. Therefore STEM is more useful when contrast is more important than resolution.

I.6 AUGER ELECTRON SPECTROSCOPY (AES)

Auger Electron Spectroscopy (AES) is a surface spectrometry technique based on the Auger process, first described in Chapter 4. AES owes its high surface sensitivity and lateral resolution to the high probability of energy loss for electrons travelling in a solid. The inelastic electron mean free path (IMFP) is about 1-5 nm in solids for the most frequently used Auger transitions [8].

The major virtues of AES are [8]:

- possibility to detect all elements (for Z>3) in the periodic system;
- high surface sensitivity, approximately 1 nm;
- good lateral resolution (about 10 nm);
- perfect correlation between the secondary electron image and point analysis;
- good sensitivity throughout the periodic table (detection limit 0.02-0.2 at%), particularly high for low *Z* elements;
- possibility to combine AES with noble gas ion sputtering for depth profiling;
- possibility of high magnification imaging (in SEM mode).

The main disadvantages are:

- overlapping of the peaks in some regions of the spectrum;
- low signal to noise (S/N) ratio;
- only conductive specimen can be analyzed;
- specimen damage during analysis irradiation.

This last effect, more pronounced if the beam is focused in a small spot, can be critical for analysis of EBID materials, since the irradiation can induce further transformations in the deposited material [9]. Anyway, because of its high resolution, AES is the most interesting analytical technique for analysis of EBID materials.

The main components of an AES system are:the vacuum system, an electron source and optical column to create the incident electron probe for specimen excitation, an electron energy analyzer and detector for the measurement and collection of the emitted electrons and a sample manipulator to locate the area of interest at the analyzer focal point.

An Auger electron spectrum plots the number of detected electrons, N(E), as a function of electron kinetic energy E_k. Auger peaks are more easily detected by differentiating the energy distribution function N(E), therefore the conventional Auger spectrum is the function $dN(E)/dE_k$. The peak-to-peak magnitude of a differentiated Auger spectrum is related to the surface concentration by the relations [10]

$$C_X = \frac{I_X}{I_{st} S_X} \tag{I-2}$$

where I_X and S_X are respectively the peak-to-peak amplitude and the sensitivity factor of the element X and I_{st} is the peak-to-peak amplitude of a standard for the element. An alternative way to express the atomic concentration is

$$C_X = \frac{(I_X/S_X)}{\Sigma(I_\alpha/S_\alpha)} \tag{I-3}$$

where the summation is over one peak per element present in the specimen. The elemental sensitivity factors (S) are found in the literature for all pure elements at primary beam energies of 3, 5, and 10 keV for KLL, LMM and MNM transitions. For the element of interest in this worlk the sensitivity factors are listed in Table I-3 [10].

Peak	Peak energy (eV)	S (3 keV)	S (5 keV)	S (10 keV)
Rh1 (MNN)	305	0.640	0.680	0.470
C1 (KLL)	275	0.180	0.140	0.080
O1 (KLL)	510	0.500	0.400	0.350
P1 (LMM)	123	0.530	0.470	0.300
N1 (KLL)	389	0.350	0.230	0.160
Cl1 (LMM)	184	1.100	1.050	0.690
F (KLL)	659	0.480	0.400	0.220

Table I-3: *Peak energies and sensitivity factors (S) of the elements present in Rh containing EBID structures.*

AES spectra can be obtained either at a point on the specimen or over an area. In point analysis, a stationary electron beam is positioned on a specific point. In area analysis, the beam is rapidly scanned over an area of the surface. Two data collection modes are available for Auger spectra: survey and multiplex. Survey is a high sensitivity mode with a wide energy range, with quick scan and rapid data collection (1eV/step), to survey the elements present in the sample. Multiplex is a high resolution mode for a narrow energy range, typically 30 eV, with data collection at higher data density (0.5 eV/step). In this mode, only selected energy regions, containing the peak of interest, are scanned to obtain enhanced sensitivity and spectral details. Multiplex data can be quantified to obtain atomic concentration values. Auger depth profiles are obtained by collecting spectra in multiplex mode at various sample depths and are plotted as atomic concentration versus number of etching cycles.

In this work the elements are quantified according to Eq. I-3, taking as I_x, the peak to peak intensities of the elemental peaks in differentiated multiplex spectra, and as S_x the sensitivity factors (Table I-3). To avoid the contribution of the surface contamination layer (rich in C and O), elemental quantification is carried out usually after 120 s sputter cleaning. The error on

each concentration is evaluated by measuring the ratio between the peak to peak intensity in the quantification interval and the noise peak-to-peak intensity in a region out of the interval.

I.7 ELECTRON ENERGY LOSS SPECTROSCOPY (EELS)

Electron energy loss spectroscopy uses the loss on primary electron energy caused by inelastic scattering of the primary electron beam by the electrons of the specimen atoms.

The EELS detector is usually placed in a TEM so that it can intercept and disperse the inelastically scattered electrons as they are transmitted through the specimen. The most common commercial spectrometer is the Gatan magnetic prism spectrometer. The Gatan spectrometer (shown in Fig. I-6 a, b and c) can be installed beneath the camera system of a TEM or after the ADF detector of a STEM. The electrons, selected by a variable entrance aperture, travel down a drift tube through the spectrometer and are deflected through an angle > 90° by a magnetic field. Electrons with greater energy loss are deflected further than those suffering zero loss. The instrument used in this work acquires the spectra with a parallel acquisition (PEELS) system, which gathers the whole energy spectrum simultaneously. The PEELS detector consists of a YAG scintillator coupled via a fiber optics to a semiconductor photodiode array in the dispersion plane of the spectrometer, as shown in Fig. I-6 c. The spectrum accumulates

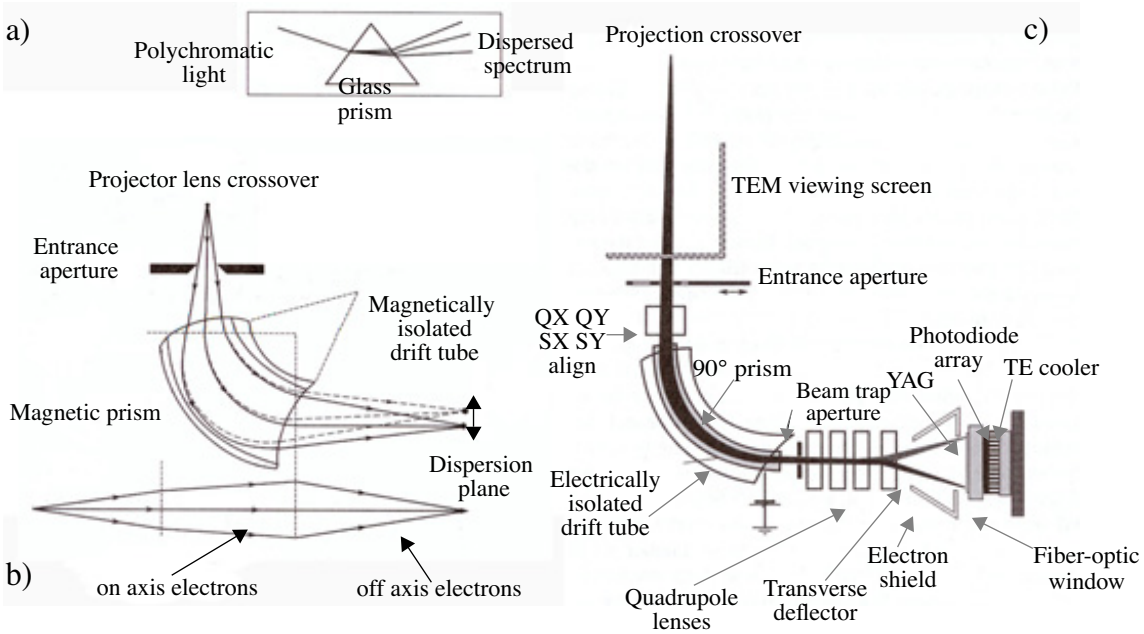

Figure I-6: *(a) Ray paths through a magnetic prism spectrometer showing dispersion and focusing of the electrons in the plane of the spectrometer and (b) the lens focusing action in the plane normal to the spectrometer; comparison of the nonfocusing action of a glass prism on visible light (inset); c) a parallel EELS (PEELS) collection onto a YAG scintillator fiber-optically coupled to a thermoelectrically cooled (TE) semiconductor diode array [7].*

across the whole energy range simultaneously, with an integration time ranging from a few ms to several hundred of seconds.

A typical EELS spectrum, recorded on a thin GaAs specimen is shown in Fig. I-7. The spectrum consists of a distribution of electron counts (*I*) versus energy loss (*ΔE*). It starts with the zero loss peak, which consists of the electrons that retain completely the beam energy E_0. After the zero loss peak the dominant features of the energy-loss spectrum are the plasmon peaks, which represent the energy lost by the electrons when they generate a plasmon and form the low loss spectrum (< 50 eV). The energy loss due to ionization of the inner shells occurs at higher energy (>50 eV) and form the so called high-loss spectrum. At higher energy loss, the electron intensity decreases according to some fairly high power of energy loss. Superimposed on this smoothly decresing intensity are features which represent inner shell exitation; they take the form of edges rather than peaks. The sharp rise occurs at the ionization threshold, whose energy-loss coordinate is the binding energy of the corresponding atomic shell. Since inner-shell binding energies depend on the atomic number of the scattering atom, the ionization edges present in a EELS spectrum indicate which elements occur in the spectrum. Further-

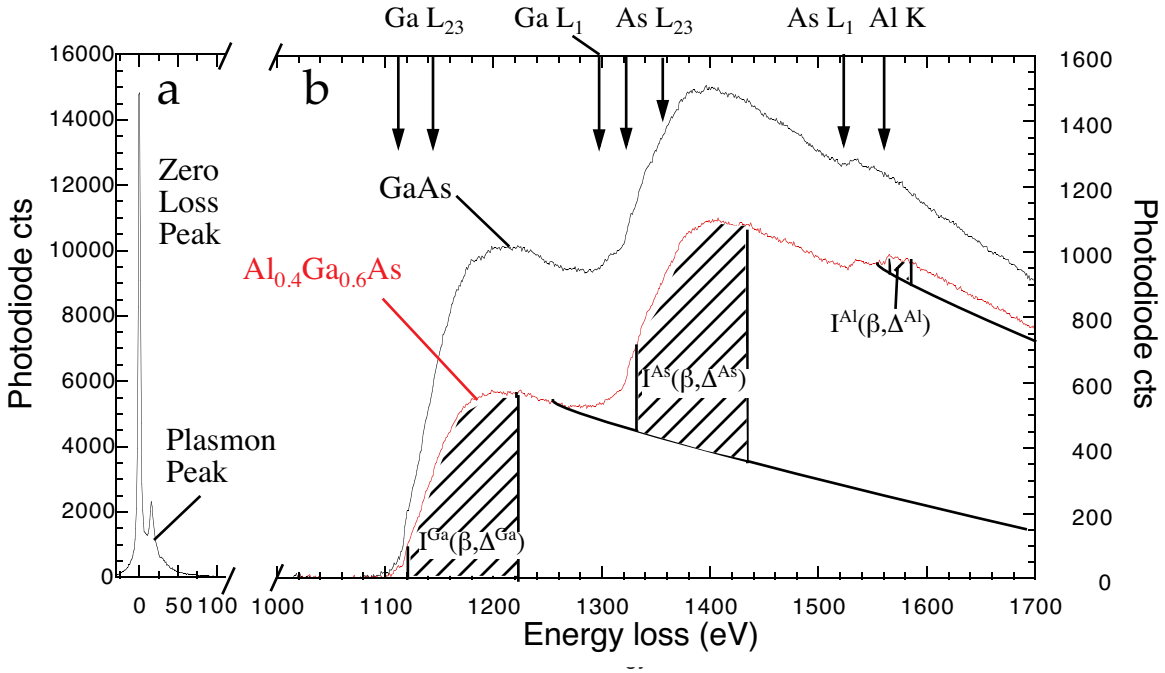

Figure I-7: *EELS spectra of GaAs and Al0.4Ga0.6As. The zero-loss peak (ZLP) and the plasmon peak are visible in the left of the plot, the high-loss region in the right part.*

more, the primary electron transmits a part of its energy as kinetic energy E_{kin} to the core electron. This additional energy gives rise to edge intensities with energies beyond E_a, i.e. $E_T = E_a + E_{kin}$.

Another process that modifies edge intensities is plural scattering. In a sufficiently thick specimen there is a reasonable probability that a transmitted electron will be inelastically scatterred more than once, giving a total energy loss which is the sum of the individual losses. The resulting edge profile is a convolution of the edge profile taken in a thin specimen region (i.e. no plural scattering) with the low-loss region. The parameter which describes sufficiently thick and thin specimens is the mean free path of plasmon scattering Λ_{MFP}. A specimen is thin if its thickness $t_h < 0.1\text{-}0.2\ \Lambda_{MFP}$. One of the advantages of the EELS technique is that the specimen thickness can be measured in multiples of Λ_{MFP} directly from the EELS spectrum in the low loss region. In the case of EBID deposits the mean free path cannot be calculated precisely since the density of the material is not known precisely. For a reasonable range of densities, or primary electron energies of 200 keV, Λ_{MFP} is of the order of 50-150 nm at 100 keV incident energy [11].

The edge intensities due to single scattering processes (i.e. the cross sections) can be described using the Hartree-Slater formalism. The resulting cross-sections $\sigma(E, \alpha)$ are a function of the excitation energy E and scattering angle α. Here all the electrons up to the maximum collection angle α_C enter the spectrometer and we replace thus $\sigma(E, \alpha)$ with

$$\sigma(E, \alpha_C) = \int_0^{\alpha_C} \sigma(E, \alpha) d\alpha . \tag{I-4}$$

The intensity is extracted by fitting a power-law function to the pre-edge background and then extrapolating this model under the edge. The subtraction of the background intensity (I^b) from the total intensity (I^{tot}) results in the edge intensity $I(\Delta E^Q, \alpha_C)$, as shown in Fig. I-8. In a thin specimen, this edge intensity $I(\Delta E^Q, \alpha_C)$ is proportional to the partial cross section:

$$\sigma^p(\Delta E, \alpha_C) = \int_{(E_A + E_{off})}^{(E_A + E_{off} + \Delta E^Q)} \alpha(\Delta E, \alpha_C) . \tag{I-5}$$

The number of atoms N_{at} of the element A in a specimen is then proportional to:

$$N_A \propto \frac{I_A(\Delta E^Q, \alpha_C)}{\sigma_A^p(E, \alpha_C)} . \tag{I-6}$$

Finally, we can obtain elemental concentration from this formula:

$$\frac{c_A}{c_B} = \frac{N_A}{N_B} = \frac{I_A(\Delta E_A^Q, \alpha_C)}{I_B(\Delta E_B^Q, \alpha_C)} \times \frac{\sigma_B(\Delta E_B, \alpha_C)}{\sigma_A(\Delta E_B, \alpha_C)} \tag{I-7}$$

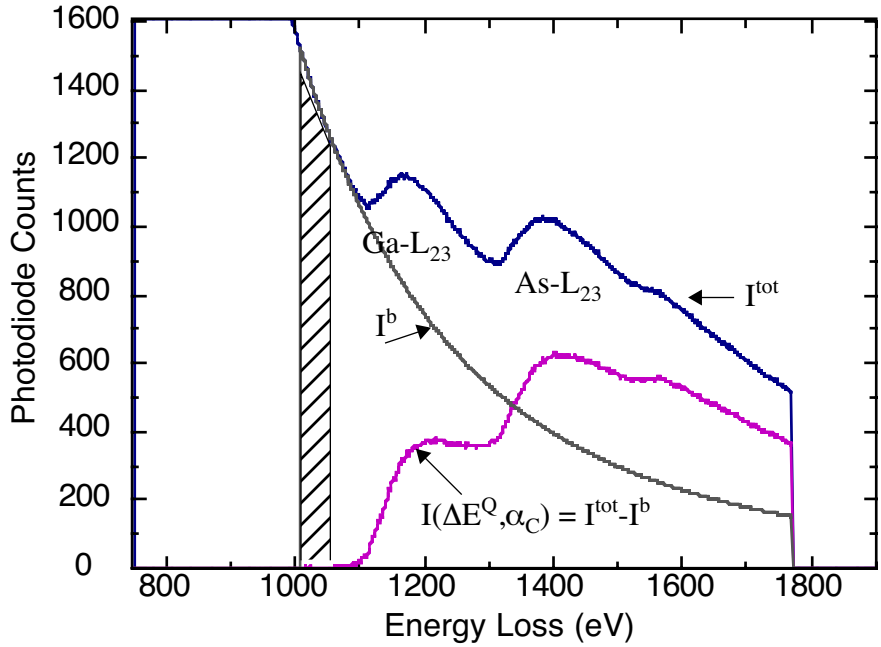

Figure I-8: *Example of background subtraction from an EELS spectrum of GaAs.*

if ΔE_A and ΔE_B are chosen with the same offsets. In the case of Rh, N, O, C concentrations the theoretical $\sigma^{Rh}(\Delta E, \alpha)$ is not well known. Therefore a Rh_2O_3 standard was used to determine $\sigma^{Rh}(\Delta E, \alpha)$, as will be explained in the next paragraph.

When the elemental distribution in a specimen shows a variation in two dimensions, an alternative way of collecting and displaying EELS data is the spectrum image [12]. The spectrum image is a 3D array of numbers: the first two axes correspond to the x-y position on the specimen as for any image, while the third is associated with the complete energy-loss spectrum, as shown in Fig. I-9. Spectrum images allow to obtain chemical maps simultaneously from different edges and different elements in one acquisition.

One of the first aims of the EELS measurements in this work is the quantification of the Rh/C concentration ratio. As shown before, the Rh/C concentration ratio can be obtained from the edge intensities I and cross sections σ:

$$\frac{c(Rh)}{c(C)} = \frac{\frac{I(Rh)}{\sigma_{Rh}}}{\frac{I(C)}{\sigma_C}}. \qquad \text{(I-8)}$$

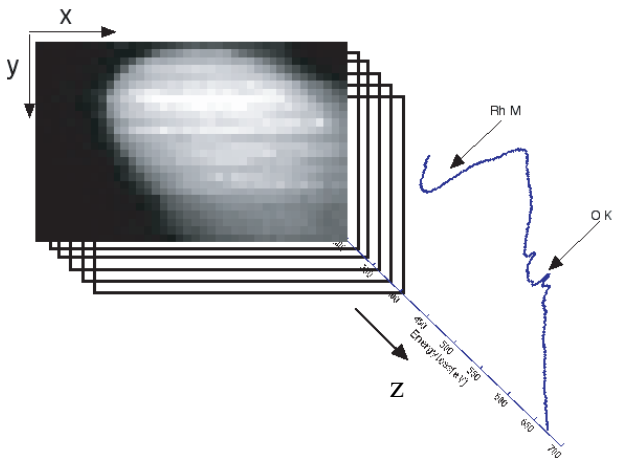

Figure I-9: *Pattern of the spectrum image data, for more details see text.*

Since the Rh-K edge is not well known, its cross section is determined from a Rh_2O_3 standard. An EELS spectrum of Rh_2O_3, with indicated Rh M 4,5, Rh M 3 and O K edges, is shown in Fig. I-10. The Rh and O edge intensities are extracted from this spectrum as described above.

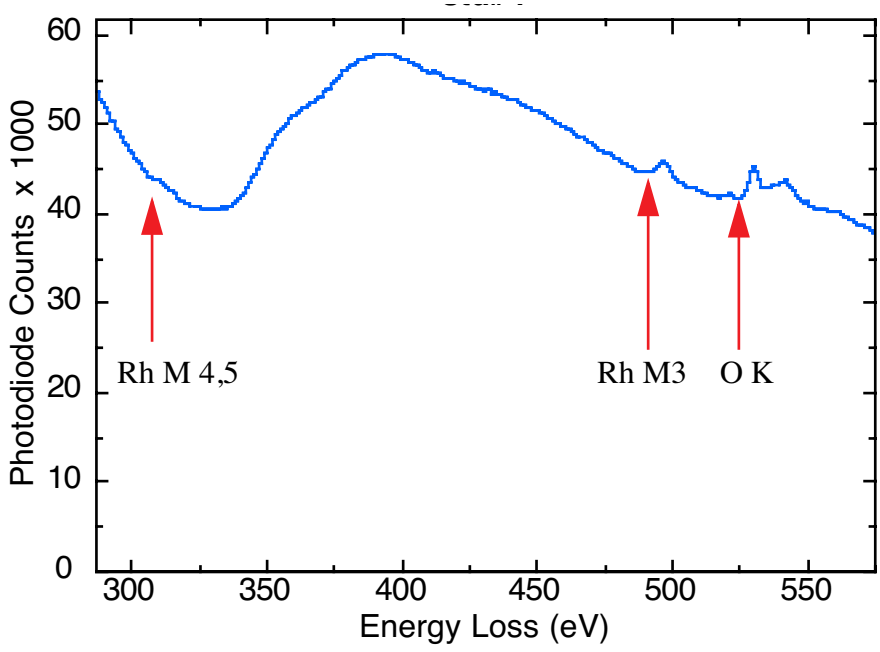

Figure I-10: *EELS spectrum of Rh_2O_3. The specimen thickness at the analysis point was 0.3 times the mean free path of the primary electrons.*

For the Rh_2O_3 standard Eq. I-8 becomes

$$\frac{c(Rh)}{c(O)} = \frac{I(Rh)}{I(O)} \frac{\sigma_O(\Delta(E, \alpha_C))}{K(Rh)} \tag{I-9}$$

where *K(Rh)* is a constant representing the Rh cross section.

The atomic concentration in the standard is known and *I(Rh)/I(O)* can be measured, therefore the constant *K(Rh)* can be calculated. The O and Rh intensities, measured at four different points on the specimen, are reported in Table I-4. On average, using Eq. I-9, we obtain $\sigma^O(\Delta E, \alpha_C)/K(Rh) = 1/11.4$.

	I(O)	*I(Rh)*
point 1	266168	2308000
point 2	170262	1146000
point 3	65030	495000
point 4	114052	853500

Table I-4: *Evaluation of Rh_2O_3 standard*

The ratio *c(Rh)/c(C)* can then be obtained by

$$\frac{c(Rh)}{c(C)} = \frac{I(Rh)}{I(C)} \frac{\sigma_O(\Delta E^Q, \alpha_C)}{K(Rh)} \frac{(\Delta E^Q, \alpha_C)\sigma_C}{(\Delta E^Q, \alpha_C)\sigma_O}. \tag{I-10}$$

The ratio σ_O/σ_C is determined to be 1.27 from theoretical values, the intensities are measured from the acquired spectra. The characteristic energies for the edges of the detected elements and the energy quantification intervals are reported in Table I-5.

Element	Edge	Energy (eV)	Spectrum image interval (eV)	Quantification interval (eV)
Rh	M4,5	307	324-340	327-377
Rh	L3, L2	3004-3146	3004-3146	-
O	K	532	540-549	552-282
C	K	284	287-312	291-301
P	K	2146	2196-2292	-
N	K	401	-	407-430

Table I-5: *Energy of the characteristic edges of the elements present in the deposit.*

From Eq. I-10 we obtain directly the Rh concentrations *R(i)* relative to C, O and N:

$$R(i) = \frac{c(i)}{c(i) + c(Rh)} \quad \text{(I-11)}$$

where the index i represents oxygen, carbon or nitrogen.

It should be noted that for P spectrum imaging we used the P-K edge at 2146 eV. This edge is more suited for quantitative work than the P-L edge at 132 eV since: 1) the power low background model gives excellent results for the P-K edge and only poor results for the P-L edge; 2) the K-edge intensity is much less sensitive to specimen thickness variations than the P-K edge.

I.8 LIST OF SYMBOLS AND ACRONYMS

I.8.1 SYMBOLS

A_M: atomic weight

B: constant for cathode material

C: capacitance

C_o,C_d, C_s, C_c : zero (0), diffraction (d), spherical (s), chromatic (d) aberration coefficients

D_e: electron dose

D_s: surface diffusion coefficient

d: molecular diameter

d_p: electron probe diameter

d_s, d_c, d_d: spherical, chromatic, difraction disc of least confusion

d_{CR}: crossover diameter

E: primary electron energy

F: molecular flux

f: electron flux

f_i: focal length

H: Henthalpy

ΔH_s: sublimation enthalpy

h: Planck's constant

I_p: electron probe current

j: electron beam current density

J: molecular impingment rate flux per unit area

K: thermal conductivity

K_n: Knudsen number

k: Boltzmann's constant

L: distance betwen electron lenses in QMS

m: demagnification

m_i: atomic fraction

M: molecular weight

N_A: Avogadro's number

n_{ox}: oxidation number

P: pressure

P_{vap}: vapor pressure

Q: heat

Q_T: total cross section for electron scattering

R: gas constant

R_{el}: electrical resistence

R_R: resistivity ratio

R_B: Bethe's range

R_E: electron range

S_B: Bethe's stopping power

s: sticking coefficient

T: temperature

t_e:exposure time

t: time

U: voltage

V: volume

v: molecular volume

y: potential gradient

W_{SE}: mean energy loss for SE generation

X: ionization potential

Z: atomic number

α: electron beam aperture angle

α_T: transmission coefficient gas transport in tubes

β: brightness

β_S: back-scattering coefficient for gas transport in tubes

γ_s: uptake coefficient

δ : secondary electron yield

ε: total electron yield

η: back-scattered electron yield

η_X: X-ray emission yield

θ: electron scattering angle

κ: thermal diffusivity

Λ_e: electron mean free path

Λ_{SE}: secondary electron escape depth

Λ_p: plasmon mean free path

λ: wavelength

λ_g: mean free path of gas molecule

ρ: density

ρ_0,ρ_d : electrical resistivity of a pure metaland of an EBID deposit

σ: width parameter of a Gauss function

σ_{CS}: cross section for electron scattering

Φ_W: work function

ϕ: tilt angle

σ_E: cross section for EBID

τ_{surf}: surface residence time

ω_f: fluorescence yield

Ω: electron scattering solid angle

I.8.2 ACRONYMS

ADF: Annular Dark Field Detector

AES: Auger Electron Spectroscopy

AFM: Atomic Force Microscopy

BF: Bright Field

BSE: Backscattered Electrons

CVD: Chemical Vapor Deposition

CMA: Cylindrical Mirror Analyzer

DEA: Dissociative Electron Attachment

DF: Dark Field (TEM)

DFT: Density Functional Theory

EELS: Electron Energy Loss Spectroscopy

EBID: Electron Beam Induced Deposition

EDX: Electron Dispersive X-ray

FEG: Field Emission Gun

FIBID: Focused Electron Beam Induced Deposition

LICVD: Laser Induced Chemical Vapor Deposition

LN2: liquid nitrogen

MCS: Monte Carlo Simulations

MEMS:Micro Electro-Mechanical Systems

MFP: Mean Free Path

MS: Mass Spectrometry

SE: Secondary Electrons

SEM: Scanning Electron Microscopy

STEM: Scanning Transmission Electron Microscopy

STM: Scanning Tunnelling Microscope

TEM: Transmission Electron Microscopy

XPS: X-ray Photoelectron Spectroscopy

UHV: Ultra High Vacuum UHV

YAG: Yttrium Aluminum Garnet

ZLP: Zero Loss Peak

I.9 REFERENCES

[1] E.A. Brandes, G.B. Brook; *Smithells Metals Reference Book*; Butterworth Heinemann, 1992.

[2] P. Pascal; *Nouveau Traité de Chimie Minerale, tome XIX*; Masson, 1958.

[3] I.I. Skorokhodov, V.E. Ditsent, N.A. Terent'eva, M.N. Zolotarev; *Vapour Pressures of Polydialky(aril)-siloxanes and Polydimethylsiloxanes*; Russian J. Phys. Chem., 45 (6) (1971); p. 902-905.

[4] T.G. Koch, M. Rossi; *Direct measurements of surface residence times: nitryl chloride and chlorine nitrate on alkali halides at room temperature*; J. Phys. Chem. A, 102 (1998); p. 9193-9201.

[5] S. Flegler, J.W.J. Heckman, K.L. Klomparens; *Scanning and Transmission Electron Microscopy, an Introduction*; Oxford University Press, 1993.

[6] D.B. Williams, C. Barry Carter; *Basics*, in *Transmission Electron Microscopy*; Kluwer Academic/Plenum Publisher, 1998, p. 5-83.

[7] D.B. Williams, C. Barry Carter; *Imaging*, in *Transmission Electron Microscopy*; Kluwer Academic/Plenum Publisher, 1998, p. 349-366.

[8] C.O.A. Olsson; *AES for characterisation of oxide films on stainless steels*, in Proc. Int. Conf. on microstruct. and function of materials, 1996, Tokyo, p.301-308.

[9] S. Mezhenny, I. Lyubinetsky, W.J. Choyke, J.J.T. Yates; *Electron stimulated decomposition of adsorbed hexafluoroacetylacetonate Cu(I) vinyltrimethylsilane, Cu(I)(hfac)(vtms)*; J. Appl. Phys., 85 (1999); p. 3368-3373.

[10] K.D. Childs, B.A. Carlson, L.A. LaVanier, J.F. Moulder, D.A. Paul, W.F. Stickle, D.G. Watson; *Handbook of Auger Electron Spectroscopy*; Physical Electronic, Inc., 1995.

[11] R.F. Egerton; *Electron Energy-Loss Spectroscopy in the electron microscopy*; Plenum Press, 1996.

[12] C. Jeanguillaume, C. Colliex; *Spectrum-Image: the next step in EELS digital acquisition*; Ultramicroscopy, 28 (1989); p. 252-257.

Acknowledgments

First of all I express my profound gratitude to Dr. MER Patrik Hoffmann who gave me the opportunity to do my Ph.D. at the Institute of Applied Optics and who supervised this work with steady encouragements, interest and optimism. I appreciated very much his way of transmitting his knowledge and leading a research group and his human qualities.

I am also very grateful to all the people who made this work possible, in particular to:

- Dr Benjamin (Benny) Dwir (EPFL/DP) and Dr Ivo Utke (EPFL/IOA), for the fruitful scientific discussions and for their collaboration in EBID experiments and theoretical aspects.
- Dr Klaus Leifer (EPFL/DP), with whom I spent some days and nights doing Transmission Electron Microscopy and Electron Energy Loss Spectroscopy.
- Dr Hans Koops (Nawotec GmbH, Darmstadt, Germany) who first introduced me into the fascinating world of Electron Beam Induced Deposition.
- Nicolas Xanthopoulos and Dr Claes Ollson (EPFL/DMX) for having taught to me practical and theoretical aspects of Auger Electron Spectroscopy.
- Taisuke Ohta (University of Washington, Seattle, USA) for having shared with me experimental work in vapor pressure measurements and mass spectrometry for almost two years.
- Prof. Philippe André Buffat, Danièle Laub, Brian Senior (EPFL/CIME) for their support in Transmission Electron Microscopy and Scanning Electron Microscopy.
- Dr Gerit Jaenchen for the conribution in AFM measurements.
- Dr Pascal Doppelt (Ecole Superieure de Physique et Chimie Industrielle, Paris) for having supplied the rhodium precursor.
- Dr Michel Rossi and Carine Alcala (EPFL/DGR) for their contribution in Residence Time measurements.

- The members of the *comitè de parrainage* Prof. Eli Kapon (EPFL/DP), Dr Wolfgang Harbich (EPFL/DP), Dr Raymond Houriet (EPFL/DMX).

- Paolo Chiggiato (CERN Geneva) for the frequent fruitful discussions about vacuum physics and technology.

- Ronald Gianotti who gave a strong contribution to the accomplishment of this work by repairing several times the EBID deposition system.

- The prince of the McIntosh Simon Benjamin for his kind and precious help in computing (hardware and software) and for having accepted me as office mate.

- Master Claude Amendola for the high-level technical support.

- Dr Clara Santato (University of Geneva and CNR Roma, Italy) and Ruggero Paraventi (Ion Energy Resources, Bologna, Italy) for their support and their advices about science and life.

- Prof. Pio Picchi (University of Torino, Italy), Aleksandra Sefanovic, Antoine Luisier, Florian Dürr, Jelena Mitic, Marcel Zeller, Marija Blagojevic, Simone Amorosi, Valeria and Francesco Pietropaolo for the precious advices they gave me to improve my thesis presentation.

- All my wonderful friends from Calitri, Bologna, Geneva, Lausanne and wherever.

- All the collegues working at the Institute of Applied Optics for the frequent scientific discussions and for the warm and friendly atmosphere I could share with them. I owe special thanks to my teammates Estelle and Frank Wagner, Giacomo Benvenuti, Tristan Bret, Laura Barbieri and to Maria Pilar Bernal, Moustapha Hafez and Sebastian Favre.

- Whoever has been with me during these years.

Dulcis in fundo un immenso grazie alla mia famiglia (Mamma, Papà, Valeria, Francesco), a cui dedico questa tesi, per avermi sempre incoraggiato e sostenuto nello studio, nel lavoro e nella vita.

Fabio Cicoira
fabio.cicoira@epfl.ch
born 3/9/1970 in Napoli (Italy)
Italian citizen

Education

1984 - 1989	Liceo Scientifico Statale L. Da Vinci, Calitri, Italy. **Scientific Baccalaureate (Maturità scientifica).**
1989 - 1996	University of Bologna, Italy, Chemical Department. **Degree in Chemistry (Laurea in Chimica).**
1998-2002	EPFL Lausanne, Switzerland, Institute of Applied Optics. **Ph.D. (Docteur és Science).**

Career History

1998 - present	**- Micro-engineering department, EPFL Lausanne, Switzerland** **• Research assistant, Ph.D. Student.** - Focused electron beam deposition of nano-structures, in collaboration with the company Deutsche Telekom. - Conception and construction of two vacuum systems to measure spectroscopical and thermodynamical properties of metal complexes. - Responsible of the chemical laboratory of the institute. Purchasing of chemicals and equipment.
1995-1998	**- Surfaces and Materials Group, European Organization for Nuclear Research (CERN), Geneva, Switzerland.** **• Technical student, research assistant.** - Diploma work and post degree research on new materials for chemical pumping systems for particle accelerators. The materials studied in this work will be applied for the pumping system of the future particle accelerator LHC (Large Hadron Collider).
1989-1995	**- Chemical Department 'G. Ciamician' , University of Bologna, Italy.** **• Student of Chemistry.**

Languages

Italian	Maternal tongue
English	Very good knowledge (spoken and written)
French	Very good knowledge (spoken and written)
Spanish, German, Serbo-croatian	Basic knowledge

Technical skills

Analytical techniques	Mass spectrometry, Scanning Electron Microscopy (SEM), Auger Electron Spectroscopy (AES).
Material deposition	Sputtering, Focused Electron Beam Induced Deposition, Silylation.
Vacuum technology	Measurements, conception and assembling of systems..
Computing	Knowledge of MacOS and Windows systems. Software: MS Office, Frame Maker, Photoshop, Digital Micrograph, Kaleidagraph.

Courses and stages

2000	Advanced English Course for 1 year in Lausanne. Cambridge Certificate in Advanced English (CAE).
1998	Four month stage at the research center of Deutsche Telekom in Darmstadt (Germany). Basic German course in Lausanne.
1995	Advanced French Course in Geneva
1992-1994	Advanced English Courses at the Linguistic Center at the University of Bologna.
1987 and 1992:	Intensive English courses for 1month in Cambridge and Dublin

Publications

C. Benvenuti, P. Chiggiato, F.Cicoira, Y. L'Aminot; *Nonevaporable getter films for ultrahigh vacuum applications*; J. Vac. Sci. Technol. A 16 (1998), p. 148-154.

C. Benvenuti, P. Chiggiato, F. Cicoira, V. Ruzinov; *Decreasing surface outgassing by thin film getter coatings;* Vacuum, 50 (1998) p. 57-63.

C. Benvenuti, J.M. Cazeneuve, P. Chiggiato, F. Cicoira, A. Escudeiro Santana, V. Johanek, V. Ruzinov, J. Fraxedas; *A novel route to extreme vacua: the non-evaporable getter thin film coatings;* Vacuum, 53 (1999), p. 219-225.

I. Utke, B. Dwir, K. Leifer; F. Cicoira, P. Doppelt, P. Hoffmann, E. Kapon; *Electron beam induced deposition of metallic tips and wires for microelectronics applications;* Microelectron. Engin., 53 (2000), p. 261-264.

P. Hoffmann, I. Utke, F. Cicoira, B. Dwir, K. Leifer, E. Kapon, P. Doppelt; *Focused electron beam induced deposition of gold and rhodium;* Proc. MRS Symp. (2000), vol. 624, p. 171-181.

P. Doppelt; R. Even, F. Marchi, V. Bouchiat, H. Dallaporta, S. Safarov, D. Tonneau, P. Hoffmann, F. Cicoira, I. Utke, B. Dwir, K. Leifer; *Nanostructures by CVD assisted methods using mineral precursors;* Proc. 197th Meeting of Electrochemical Society (2000); p. 112-125.

T. Ohta, F. Cicoira, P. Doppelt, L. Beitone, P. Hoffmann; *Static vapor pressure measurement of low volatile precursors for Molecular Vapor Deposition below ambient temperature;* Advanced Materials CVD, 7 (2001), p. 33-36.

F. Cicoira, P. Hoffmann, B. Dwir, D. Laub, H. J. Mathieu, N. Xanthopulos, E. Kapon, P. Doppelt; *Focused electron beam induced deposition of rhodium wires and tips: chemical composition and nanostructure;* Physica E: Low-dimensional Systems and Nanostructures; in press.

I. Utke, F. Cicoira, G. Jaenchen, P. Hoffmann, L. Scandella, B. Dwir, E. Kapon, D. Laub, P. A. Buffat, N. Xanthopulos, H. J. Mathieu;*Focused electron beam induced deposition of high resolution magnetic scanning probe tips;* Proc. MRS Symp. (2002), in press.